



**HAL**  
open science

# Modèles d'articulations dissipatives en dynamique multi-corps

Rafael Penas Ferreira

► **To cite this version:**

Rafael Penas Ferreira. Modèles d'articulations dissipatives en dynamique multi-corps. Mécanique des matériaux [physics.class-ph]. HESAM Université, 2021. Français. NNT : 2021HESAE039 . tel-03678828

**HAL Id: tel-03678828**

**<https://pastel.hal.science/tel-03678828>**

Submitted on 25 May 2022

**HAL** is a multi-disciplinary open access archive for the deposit and dissemination of scientific research documents, whether they are published or not. The documents may come from teaching and research institutions in France or abroad, or from public or private research centers.

L'archive ouverte pluridisciplinaire **HAL**, est destinée au dépôt et à la diffusion de documents scientifiques de niveau recherche, publiés ou non, émanant des établissements d'enseignement et de recherche français ou étrangers, des laboratoires publics ou privés.

**ÉCOLE DOCTORALE SCIENCES ET MÉTIERS DE L'INGÉNIEUR**  
**Laboratoire PIMM - Campus de Paris**

# THÈSE

*présentée par :* **Rafael PENAS FERREIRA**

*soutenue le :* **17 novembre 2021**

*pour obtenir le grade de :* **Docteur d'HESAM Université**

*préparée à :* **École Nationale Supérieure d'Arts et Métiers**

*Spécialité :* **Mécanique-Matériaux (AM)**

## Models of dissipative bushings in multibody dynamics

**THÈSE dirigée par :**  
**M. BALMÈS Étienne**  
**M. MECHBAL Nazih**

**et co-encadrée par :**  
**M. GAUDIN Arnaud**  
**M. KREIS Adrien**

**Jury**

<b>M. David RYCKELYNCK</b>	Professeur des universités - Mines, PSL	Président
<b>M. Marcelo TRINDADE</b>	Professeur des universités - EESC, USP	Rapporteur
<b>M. Gaël CHEVALLIER</b>	Professeur des universités - EIPHI, UBFC	Rapporteur
<b>M. Benoît PETITJEAN</b>	Ingénieur expert - ArianeGroup	Examinateur
<b>M. Étienne BALMÈS</b>	Professeur des universités - ENSAM, HESAM	Examinateur
<b>M. Nazih MECHBAL</b>	Professeur des universités - ENSAM, HESAM	Examinateur
<b>M. Arnaud GAUDIN</b>	Ingénieur de recherche - Stellantis	Examinateur



# Acknowledgments

D'abord je voudrais remercier Etienne, pour m'avoir accueilli comme stagiaire juste en sortie de l'école d'ingénieur, et de m'avoir pris comme doctorant, en plus d'avoir proposé ce projet à Stellantis. Je m'inspirerai de ton encadrement à niveau humain et professionnel pour toute ma vie.

Je voudrais aussi remercier énormément à Arnaud, qui a accepté de participer à ce projet et qui a aussi été un super encadrant et a toujours trouvé des solutions quand j'étais bloqué et m'a aussi donné tout le support que j'avais besoin.

Je remercie également Adrien et Nazih de faire partie aussi de l'encadrement de la thèse.

Tous les stagiaires qui ont travaillé en parallèle avec moi pendant la thèse - Goustan, Enora, Moad, Jad - un grand merci à tous.

Un grand merci à Vibracoustic, en spécial à Pierre et Wilfried. Sans votre aide et sans les essais, la thèse serait forcément moins intéressante.

Mon encadrant de bureau, Florian, merci pour tous les déjeuners et les discussions de foot. Merci aussi aux derniers collègues de bureau - les motivateurs pour la rédaction, Guillaume et Guilherme.

Un grand merci aussi à tous les collègues du laboratoire, et aussi à ceux du service SMMS de l'ancienne PSA.

A nível pessoal, não tenho como agradecer mais do que a parceira mais incrível que eu poderia sonhar em ter. Sem você, Julia, eu nem teria chagado até aqui. Amo muito você.

Mãe e Lulu, muito obrigado por estar sempre do meu lado, por toda minha vida. Sem vocês eu nunca teria tido coragem de vir até aqui, e vocês não têm ideia da falta que fazem.

Crabbé e Bruna, obrigado por terem aparecido e terem se tornado parte de minha família em Paris. Thiago, obrigado por ter me ajudado tanto desde o começo.

Obrigado também Fernando, Ana, Manuel, Manoly, Brañas, Flora, Divina, Benigno e toda a família na Espanha, que esteve aqui, e que sempre me acolheu durante as férias.

Agradeço também a todos os amigos que me acompanharam aqui - Danilo, Menegotto, Delage, Daniella e também Amanda (sempre me ouvindo do outro lado do celular). Finalmente, obrigado a todos os amigos que deixei no Brasil, especialmente do fórmula, da federal e do Joana.



# Contents

<b>List of tables</b>	<b>11</b>
<b>List of figures</b>	<b>19</b>
<b>Résumé long (in French)</b>	<b>21</b>
Introduction . . . . .	21
Modèles système d'articulations 0D . . . . .	22
Modèles matériau 3D . . . . .	29
Identification . . . . .	31
Du 3D au 0D . . . . .	35
Simulations multi-corps . . . . .	39
Conclusion . . . . .	44
<b>Introduction</b>	<b>51</b>
Industrial background . . . . .	52
Outline and contributions . . . . .	54
<b>1 0D system models of bushings</b>	<b>59</b>
1.1 Introduction . . . . .	60
1.2 Hyperelasticity or non-linear static gain . . . . .	62
1.2.1 Instantaneous modulus . . . . .	64
1.3 Viscoelasticity . . . . .	65
1.3.1 Non-parametric transfer: complex and relaxation modulus . . . . .	67
1.3.2 Selected order base representation: rational complex modulus . . . . .	68
1.3.3 Order independent parametric models : fractional derivatives . . . . .	71

## CONTENTS

---

1.4	Rate independent hysteresis . . . . .	73
1.4.1	A non-parametric model: hysteretic relaxation . . . . .	74
1.4.2	Selected order base representations : Iwan series model . . . . .	76
1.4.3	Order independent parametric forms . . . . .	79
1.4.4	Regularity in first order hysteretic cells . . . . .	81
1.5	Unified perspectives through environmental factors . . . . .	82
1.5.1	Classical temperature modeling . . . . .	83
1.5.2	Intermediates between viscoelasticity and rate independent hysteresis . . . . .	84
1.5.3	Combined behavior . . . . .	86
1.6	Experiment design perspectives and conclusions . . . . .	88
<b>2</b>	<b>3D material models</b>	<b>91</b>
2.1	Introduction . . . . .	92
2.2	Continuum mechanics . . . . .	92
2.2.1	Kinematics . . . . .	92
2.2.2	Invariants, strain rates . . . . .	93
2.2.3	Stress, equations of motion, time integration at a material point . . . . .	94
2.3	Hyperelasticity . . . . .	95
2.3.1	General properties: potential, polyconvexity . . . . .	95
2.3.2	Compression or volume change behavior . . . . .	96
2.3.3	Deviatoric behavior . . . . .	96
2.3.4	Basic deformations used for material characterization . . . . .	98
2.4	Viscoelasticity in finite strains . . . . .	100
2.4.1	Finite strain deviatoric viscoelasticity - Simo formalism . . . . .	100
2.4.2	Bulk viscoelasticity . . . . .	101
2.4.3	Non-linear transition between viscoelasticity and hysteresis . . . . .	102
2.5	Perspectives and conclusions . . . . .	103
<b>3</b>	<b>Identification</b>	<b>105</b>
3.1	Introduction . . . . .	106
3.2	Tests conception . . . . .	106

## CONTENTS

---

3.2.1	Introduction: test objectives . . . . .	106
3.2.2	Specimen and testing machine . . . . .	107
3.2.3	Test parameters . . . . .	109
3.2.4	Low speed test: filtering . . . . .	111
3.2.5	Sine tests: instantaneous modulus and 1st harmonic . . . . .	113
3.2.6	Mullins and long term effects . . . . .	115
3.3	Classical material identification procedure . . . . .	116
3.3.1	Hyperelastic coefficients . . . . .	117
3.3.2	Hysteretic rate independent dissipation . . . . .	118
3.3.3	Viscoelasticity . . . . .	120
3.3.4	Identification results . . . . .	122
3.4	Non-parametric and selected order identification . . . . .	123
3.4.1	Hyperelastic behavior . . . . .	124
3.4.2	Hysteretic relaxation . . . . .	125
3.4.3	Viscoelastic frequency evolution . . . . .	127
3.5	Synthesis and perspectives . . . . .	129
3.5.1	Test synthesis . . . . .	129
3.5.2	Perspectives and conclusions . . . . .	136
<b>4</b>	<b>From 3D to 0D</b>	<b>137</b>
4.1	Introduction . . . . .	138
4.2	Finite element method . . . . .	138
4.2.1	Principles . . . . .	138
4.2.2	Implicit schemes . . . . .	141
4.2.3	Explicit schemes . . . . .	142
4.3	Kinematic reduction . . . . .	143
4.3.1	Motivation . . . . .	143
4.3.2	Learning methods . . . . .	144
4.3.3	Basis generation . . . . .	145
4.4	Hyper reduction: lower cost integration of non-linear terms . . . . .	147
4.4.1	Discrete Empirical Interpolation Method (DEIM) . . . . .	147

## CONTENTS

---

4.4.2	Energy Conserving Sampling and Weighting (ECSW) . . . . .	148
4.5	Sample application . . . . .	149
4.5.1	Model description . . . . .	149
4.5.2	Performance and accuracy of base implementation . . . . .	150
4.5.3	Extrapolations . . . . .	152
4.6	Perspectives and conclusions . . . . .	153
<b>5</b>	<b>Multi-body simulations</b>	<b>155</b>
5.1	Introduction . . . . .	156
5.2	Dissipated power: Powertrain suspension case . . . . .	156
5.2.1	Model description . . . . .	156
5.2.2	Bushing models . . . . .	157
5.2.3	Dissipated power . . . . .	160
5.2.4	Stop/start transient . . . . .	163
5.2.5	Modal responses . . . . .	164
5.3	Steps for a complete multibody integration: rear twist beam axle bushing case . . . . .	165
5.3.1	Current model description . . . . .	166
5.3.2	Integrating 0D models . . . . .	168
5.3.3	Integrating 3D hyper-reduced models . . . . .	169
5.3.4	Validation data for consistence checks . . . . .	170
5.3.5	Consistence of mount forces . . . . .	173
5.4	Perspectives and conclusions . . . . .	176
	<b>Conclusion</b>	<b>179</b>
	Outcomes and contributions . . . . .	180
	Perspectives . . . . .	183
	<b>Bibliography</b>	<b>185</b>
	<b>Appendix</b>	<b>193</b>
	<b>A Rate independent 3D models</b>	<b>193</b>
	A.1 Plasticity formalism . . . . .	194

## CONTENTS

---

A.2	Kinematic hardening model - infinitesimal strains . . . . .	195
A.3	Finite strains . . . . .	197
A.4	Kinematic hardening model + viscoelastic model in series . . . . .	200
<b>B</b>	<b>Test parameters</b>	<b>205</b>

## CONTENTS

---

# List of Tables

1	Temps d'implémentation des modèles, transitoire de 3 cycles. . . . .	39
3.1	Identification results. . . . .	123
4.1	Material constants used in simulation. . . . .	150
4.2	Model characteristics. CPU time is for 3 cycle transient. . . . .	151
5.1	Model parameters . . . . .	160
5.2	Powertrain suspension modes . . . . .	164
5.3	Viscous coefficient value for each direction . . . . .	167
B.1	Matrix of test conditions on specimens . . . . .	206
B.2	Individual part tests . . . . .	206

## LIST OF TABLES

---

# List of Figures

1	Localisation des articulations élastomères dans les liaisons au sol avant, arrière et dans la suspension GMP. . . . .	21
2	Stratégies pour l'implémentation de modèles d'articulations élastomères dans des modèles multi-corps. . . . .	22
3	Raideur hyper-élastique, relaxation hystérétique et module complexe viscoélastique. . . . .	23
4	Gauche : Réponse contrainte/déformation des essais sinus. Droite : Réponse contrainte/déformation des essais triangulaires. . . . .	24
5	Modèle de Maxwell généralisé avec composants linéaires et sa réponse dans le domaine fréquentiel. . . . .	25
6	Illustration des règles de Madelung rules. Gauche : schéma; Droite : essai. . . . .	26
7	Modèle d'Iwan et sa réponse en termes de relaxation hystérétique et dans le plan contrainte-déformation. . . . .	27
8	Gauche : Différence entre les modules hystérétiques et viscoélastiques, et le module hyper-élastique. Droite : Ratio. . . . .	28
9	Réponse à sollicitation sinus à 1Hz, 2.5 et 10% de déformation. Gauche : essais. Droite: modèle. . . . .	29
10	Eprouvette de cisaillement simple et son tenseur gradient de déformation. . . . .	30
11	Eprouvette de traction/compression et son tenseur gradient de déformation. . . . .	30
12	Articulation de traverse déformable. . . . .	32
13	Relaxation hystérétique et identification graphique pour le matériau 1. Gauche : cisaillement simple, droite: traction/compression. . . . .	33
14	Comportement viscoélastique et identification graphique pour le matériau 1. Gauche : cisaillement simple, droite : traction/compression. . . . .	33
15	Synthèse des essais traction/compression pour le matériau 1 <a href="#">mit</a> . Haut : Module de stockage. Bas : Module de perte. . . . .	34

## LIST OF FIGURES

---

16	Synthèse des essais cisaillement simple pour le matériau 1 <b>m1s</b> . Haut : Module de stockage. Bas : Module de perte. . . . .	35
17	Interprétation graphique de la SVD. . . . .	37
18	Premiers vecteurs de la base réduite et amplitude des valeurs singulières. . . . .	38
19	Comparaison de contraintes sur trois points différents. Gauche : zone comprimée. Centre : zone cisailée. Droite : coin de la zone comprimée. . . . .	39
20	Réponse de l'articulation à une impulsion. . . . .	39
21	Modèle 3D de la suspension GMP. . . . .	40
22	Réponse en force/déplacement pour les trois articulations testées. . . . .	41
23	Energies modales pour chaque modèle. Gauche : modèle visqueux. Droite : Modèle hystérétique. . . . .	41
24	Obstacles testés et simulés, <b>BM</b> à gauche, <b>TR</b> à droite. . . . .	43
25	Comparaisons pour les efforts simulés pour <b>BM</b> . Gauche : axe x. Droite : axe z. . . . .	43
26	Comparaisons pour les efforts simulés pour <b>TR</b> . Gauche : axe x. Droite : axe z. . . . .	43
27	Forces inélastiques (gauche) et puissance injectée (droite) pour <b>BM</b> selon l'axe z. . . . .	44
28	Localization of elastomeric bushings and mounts in front suspension, rear suspension and engine suspension. . . . .	53
29	Examples of engine suspension mounts. . . . .	54
30	Strategies for the incorporation of rubber mounts and bushings models in multibody simulations. . . . .	55
1.1	Tangent hyperelastic stiffness, hysteretic relaxation modulus, viscoelastic complex modulus . . . . .	60
1.2	Left: Multi-step test profile and response. Right: Extracted hyperelastic behavior. . .	63
1.3	Left: stress/strain response of sine tests. Right: stress/strain response for triangular tests. . . . .	63
1.4	Amplitude dependence on uniaxial test for different amplitudes and preloads. . . . .	65
1.5	Left: Stress relaxation for a strain step. Center: Estimated transfer or complex modulus. Right: Sine testing with different initial strains. . . . .	66
1.6	Triangular tests . . . . .	67
1.7	Generalized Maxwell model with linear components and associated frequency domain response. . . . .	69
1.8	Impact of order on accuracy of storage modulus and loss factor . . . . .	70

LIST OF FIGURES

---

1.9	Storage and loss moduli evolution for fractional derivative model. . . . .	71
1.10	Numeric implementation of truncated Grünwald’s approximation of a fractional derivative model. . . . .	73
1.11	Triangular traction tests. Left: stress. Right: tangent modulus. . . . .	74
1.12	Illustration of Madelung rules. Left: Principles; Right: large deformation traction test. . . . .	75
1.13	Hysteretic force/displacement cycle (left) and hysteretic stiffness (right) for model verifying Masing’s law and Madelung rules. . . . .	76
1.14	Scheme for Iwan model and respective response in terms of hysteretic relaxation and on force/displacement domain. . . . .	77
1.15	Difference (left) or ratio (right) of hysteretic and hyperelastic moduli. . . . .	78
1.16	Simulated triangular test. Left: force displacement cycle, right: hysteretic relaxation modulus . . . . .	79
1.17	Standard triboelastic solid . . . . .	80
1.18	Masing curve for continuous hysteretic models. . . . .	82
1.19	Amplitude dependence of shear test at 10 Hz with stress and strain divided by amplitude. . . . .	83
1.20	Utilization of master curves for polymeric materials. Source: [1] . . . . .	84
1.21	Damping force evolution for different values of $x_f$ . . . . .	85
1.22	Branch stress and stiffness contributions for 1 Hz excitation, 10% strain amplitude and 0 and 15% static strain . . . . .	86
1.23	Left: viscoelastic and hysteretic modulus <i>difference</i> with hyperelastic modulus, right: modulus <i>ratio</i> . . . . .	87
1.24	Sine test at 1Hz, 2.5 and 10% strain. Left: test. Right: model. . . . .	87
1.25	Sine test at 0.5, 1 and 10Hz at 10% strain. Left: test. Right: model. . . . .	88
2.1	Simple shear specimen and respective deformation tensor. . . . .	98
2.2	Tension/compression specimen and respective deformation tensor. . . . .	99
2.3	Evolution of invariants with deformation for standard tests. . . . .	100
2.4	Pseudo algorithm for constitutive law integration. . . . .	103
3.1	Specimens used and tested part illustration . . . . .	108
3.2	Strain profiles for each test: Multi-step, triangular and sine (columns) for shear and tension/compression specimen (lines). . . . .	110
3.3	Detail on sine profile: changing frequency after amplitude sweep. . . . .	110

LIST OF FIGURES

---

3.4	Displacement profiles for part tests: Multi-step, triangular and sine. . . . .	111
3.5	Difference between considered filters and unfiltered data. . . . .	112
3.6	Triangular wave test results: underlying hyperelasticity and hysteretic relaxation . . .	112
3.7	Failed HF tests . . . . .	113
3.8	Stress-strain curves for failed HF tests. . . . .	114
3.9	Instantaneous modulus extraction from sine tests. . . . .	114
3.10	Mullins effect illustration for two materials in shear (left) and in tension/compression (right). . . . .	115
3.11	Relaxation modulus extraction for multi step tests. . . . .	115
3.12	Maps for relaxation modulus in function of step amplitude. Top: tension/compression specimen. Bottom: shear specimen. . . . .	116
3.13	Comparison between hyperelastic identification and reference multi-step tests. Left: shear, right: tension/compression. Top: material 1, bottom: material 2 . . . . .	118
3.14	Comparison between tested and identified secant modulus softening with amplitude for tension/compression specimen. Left: material 1, right: material 2 . . . . .	119
3.15	Comparison between tested and identified behavior for triangular solicitations. Top: material 1, bottom: material 2, left: shear specimen; right: tension/compression specimen.	120
3.16	Comparison of tangent modulus evolution with frequency between identified model and experimental results. Left: shear specimen, right: tension/compression specimen. Top: material 1, bottom: material 2 . . . . .	121
3.17	Comparison of tangent modulus evolution with amplitude between identified model and experimental results. Left: shear specimen, right: tension/compression specimen. Top: material 1, bottom: material 2 . . . . .	122
3.18	Non-parametric hyperelastic material models. Left: shear, right: tension/compression.	125
3.19	Non-parametric hyperelastic part models. . . . .	125
3.20	Hysteretic relaxation. Left: shear , right: tension/compression. Top: material 1, bottom: material 2 . . . . .	126
3.21	Hysteretic relaxation for part tests. Left: x axis, right: z axis. . . . .	127
3.22	Viscoelastic fitting for materials. Left: shear , right: tension/compression. Top: mate- rial 1, bottom: material 2 . . . . .	128
3.23	Viscoelastic fitting for part. Left: x axis, right: z axis. . . . .	128
3.24	Summary of tension/compression tests for material 1 <a href="#">mit</a> . Top: Storage modulus. Bottom: loss factor. . . . .	130

LIST OF FIGURES

---

3.25 Summary of shear tests for material 1 [m1s](#). Top: storage modulus. Bottom: loss factor. 131

3.26 Summary of tension/compression tests for material 2 [m2t](#). Top: storage modulus. Bottom: loss factor. . . . . 132

3.27 Summary of shear tests for material 2 [m2s](#). Top: storage modulus. Bottom: loss factor. 133

3.28 Stiffness and loss summary for part test in x [px](#). Top: storage stiffness. Bottom: loss factor. . . . . 134

3.29 Stiffness and loss summary for part test in z [pz](#). Top: storage stiffness. Bottom: loss factor. . . . . 135

4.1 Implementation of the implicit Newmark scheme in SDT . . . . . 141

4.2 Implementation of the explicit Newmark scheme in SDT. . . . . 142

4.3 Visual interpretation of a singular value decomposition. . . . . 146

4.4 Implemented hyper reduction scheme . . . . . 149

4.5 First 5 vectors from the reduced model base and singular values amplitudes . . . . . 150

4.6 Localization of integration points selected by the hyper-reduction. . . . . 151

4.7 Comparison between the force displacement diagram and the displacement on time for full and hyper-reduced models. . . . . 152

4.8 Stress comparison on three different points. The first on the center of the compressed zone, the second on the sheared zone and the last in the edge of the compressed zone. 152

4.9 Articulation response to high frequency and low amplitude: global behavior on the left and localized stress on the right. . . . . 153

4.10 Articulation impulse response. . . . . 153

5.1 Left: Schematic positioning of engine mounts. Source: [2]. Right: 3D model of the engine suspension . . . . . 157

5.2 Force/displacement response for the three tested mounts . . . . . 157

5.3 Non-linear elastic response (left) and dissipative forces (right) for the tested mounts . 158

5.4 Stiffness as function of the distance to the last turning point without non-linear elastic component. . . . . 158

5.5 Nonlinear elastic force and stiffness as function of turning point with new extraction strategy. . . . . 159

5.6 Dissipated power for a STS model and a viscous model under harmonic sollicitation . 159

LIST OF FIGURES

---

5.7	Rubber mount test data and fitting with non linear stiffness and hysteretic or viscous dissipation. . . . .	160
5.8	Dissipation as function of cycle position for different solicitation frequencies for 1Hz solicitation. . . . .	161
5.9	Instant dissipation on an Iwan model under sine solicitation . . . . .	162
5.10	Dissipated power on a half cycle, supposing perfect closure. . . . .	162
5.11	Measured engine torque used as an engine for the simulation. . . . .	163
5.12	Measured and computed forces at the mounts. Left: Left mount. Middle: Anti-torque mount. Right: Right mount . . . . .	163
5.13	Dissipated energy for each model . . . . .	164
5.14	Modal energies for each model. Left: Viscous model; Right: Hysteretic model . . . . .	165
5.15	Twist beam axle with highlighted bushings. . . . .	166
5.16	Full vehicle multibody model and suspension substructure (screenshots taken from Simpack). . . . .	166
5.17	Force and stiffness as function of displacement from bushing in the MBS. . . . .	167
5.18	Torque and rotational stiffness as function of angle from bushing in the MBS. . . . .	167
5.19	Hyperelastic models compared for <b>x</b> axis (left) and <b>z</b> axis (right). . . . .	168
5.20	Tested and simulated obstacles <b>BM</b> (left), <b>TR</b> (right). . . . .	171
5.21	Comparison of tested ( <b>red</b> ) and Simpack (black) results in <b>x</b> (left) and <b>z</b> (right) directions. Top: <b>BM</b> . Bottom: <b>TR</b> . . . . .	172
5.22	Responses from simulation of passing over a metallic bar <b>BM</b> . . . . .	173
5.23	Responses from simulation of three left turns <b>TR</b> . . . . .	173
5.24	Comparisons for simulated forces. Solid lines: post-processed forces. Dotted line: Simpack results. . . . .	174
5.25	Comparisons for simulated forces for <b>BM</b> test. Left: x axis. Right: z-axis. . . . .	175
5.26	Comparisons for simulated forces for <b>TR</b> test. Left: x axis. Right: z-axis. . . . .	175
5.27	Inelastic forces (left) and injected power (right) for <b>BM</b> simulation in z direction. . . . .	176
A.1	Kinematic and isotropic hardening surface evolution. . . . .	194
A.2	Kinematic hardening scheme on the stress space . . . . .	197
A.3	Response for uniaxial stress and simple shear for kinematic plasticity model. . . . .	197

## LIST OF FIGURES

---

A.4	Response of described finite strain kinematic hardening model in shear and uniaxial strains. . . . .	200
A.5	Österlöf model . . . . .	200
A.6	Österlöf flow model. . . . .	201
A.7	Payne effect in Österlöf model . . . . .	203

## LIST OF FIGURES

---

# Résumé long (in French)

## Introduction

L'industrie automobile utilise les simulations multi-corps pour les itérations de conception. Ainsi, des modèles plus précis dès les premières phases peuvent générer d'importantes économies avant les phases d'essai et aussi éviter des changements tardifs qui peuvent s'avérer assez coûteux.

Les articulations élastomères sont normalement utilisées pour relier des pièces plus rigides. La figure 1 détaille les endroits où ces articulations sont le plus souvent utilisées. La plupart de ces articulations sont dans la liaison au sol, et dans le groupe motopropulseur, faisant la liaison entre différentes pièces métalliques dans une sous-structure, ou entre des sous-structures et la caisse.



Figure 1: Localisation des articulations élastomères dans les liaisons au sol avant, arrière et dans la suspension GMP.

En termes de conception, le plus habituel est que le constructeur automobile définisse les paramètres clés, comme la raideur, l'amortissement et l'interface structurelle, pendant que le fournisseur conçoit et teste l'articulation. Cela signifie que le fournisseur naturellement possède plus de connaissance sur la pièce, malgré le fait qu'une partie de ces connaissances soit nécessaire pour générer des modèles système précis.

La procédure actuelle pour modéliser ces articulations dans les routines multi-corps est de faire des essais dans plusieurs directions pour générer des modèles 0D pour chacune de ces directions, qui sont

directement introduits dans les modèles multi-corps. Cette approche, malgré son efficacité, présente quelques problèmes : on ne considère pas la sensibilité à des chargements transverses, les non-linéarités et les couplages ne sont pas complètement caractérisés du fait d'essais incomplets, il n'existe pas de lien entre la géométrie de la pièce et les modèles extraits, une modification de la pièce demande la réalisation de nouveaux essais pour obtenir le modèle 0D correspondant, et le choix du modèle 0D a un impact direct sur le comportement du système.

L'objectif de cette thèse est de clarifier les stratégies utilisées pour passer des essais à des modèles d'articulation appropriés aux simulations multi-corps. La figure 2 illustre la décomposition du problème en objectifs intermédiaires : conception d'essais, choix de modèle au niveau matériau ou niveau pièce, identification du modèle, optimisation du modèle en termes de temps de calcul et analyse des simulations par rapport à des différentes métriques de performance et d'autres indicateurs, qui ne sont pas forcément mesurables comme la dissipation matériau ou modale.

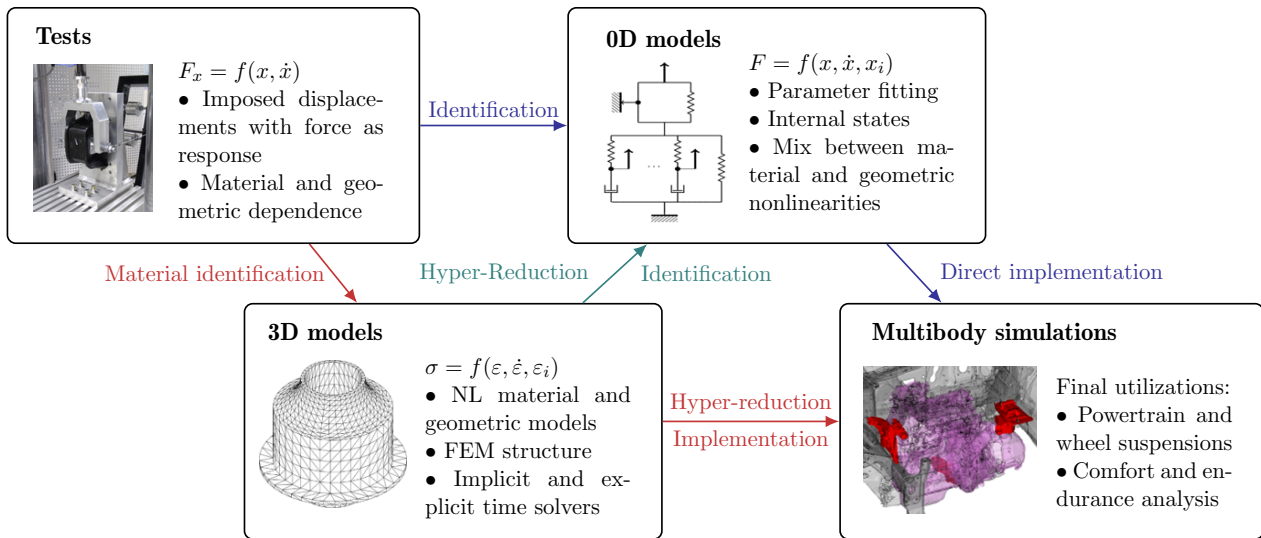


Figure 2: Stratégies pour l'implémentation de modèles d'articulations élastomères dans des modèles multi-corps.

La thèse se divise en cinq chapitres, une introduction et une conclusion. Le premier chapitre porte sur les modèles 0D qui sont utilisés, le deuxième sur l'extension de ces modèles en 3 dimensions, le troisième sur les essais réalisés pour valider les propositions, le quatrième détaille les implémentations réalisées en éléments finis, tout comme la réduction de temps de calcul et le dernier sur les modèles multi-corps utilisés comme exemples.

## Modèles système d'articulations 0D

Trois mécanismes de base sont notamment importants dans le comportement élastomère, et seront pris comme référence pour définir les modèles et étudier le comportement :

- L'**hyper-élasticité**, ou la dépendance non-linéaire de la contrainte à long terme à la valeur courante de la déformation;
- La **viscoélasticité**, ou la dépendance dynamique de la contrainte à la vitesse;
- Un dernier effet, pour lequel il n'y a pas de consensus sur le fait qu'il doit être catégorisé comme un effet de très long terme, ou comme choisi ici, une **hystérésis indépendante de la vitesse**, qui caractérise la dépendance de la contrainte au parcours des déformations.

De plus, ces trois comportements sont couplés.

La figure 3 illustre ce qu'on souhaite qu'un modèle représente. Le comportement hyper-élastique sous-jacent est visible sur la ligne rouge. A ce comportement, une contribution associée au comportement hystérétique vient se rajouter, visible en vert pointillé. Finalement, les essais sinus ont permis la construction des cartes colorés (basse fréquence en bleu, haute fréquence en jaune), qui montrent encore une augmentation du module complexe avec la fréquence, du aux effets viscoélastiques.

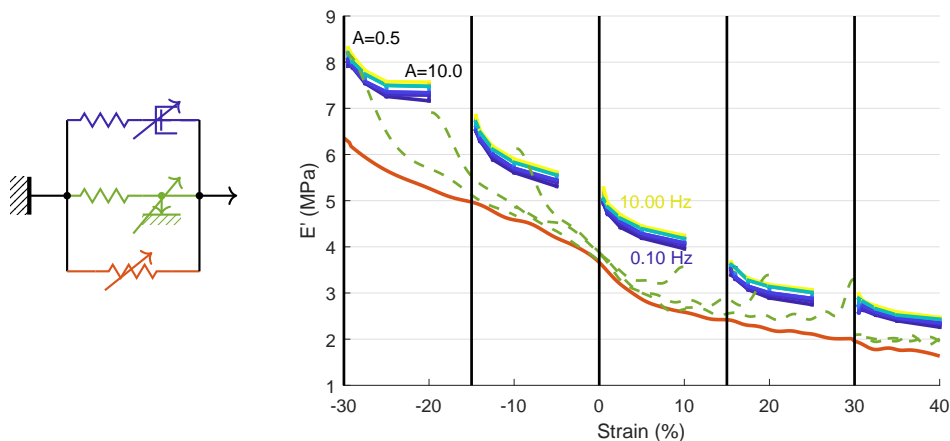


Figure 3: Raideur hyper-élastique, relaxation hystérétique et module complexe viscoélastique.

L'élasticité non-linéaire peut être assez difficile à extraire et isoler, mais sur tous les essais cet effet est présent. Pour illustrer cette idée, dans les essais montrés dans la figure 4, il est clair que la courbe maîtresse hyper-élastique est présente, même si les essais sinus ont été pensés pour extraire les effets viscoélastiques, et les essais triangulaires pour extraire le comportement hystérétique.

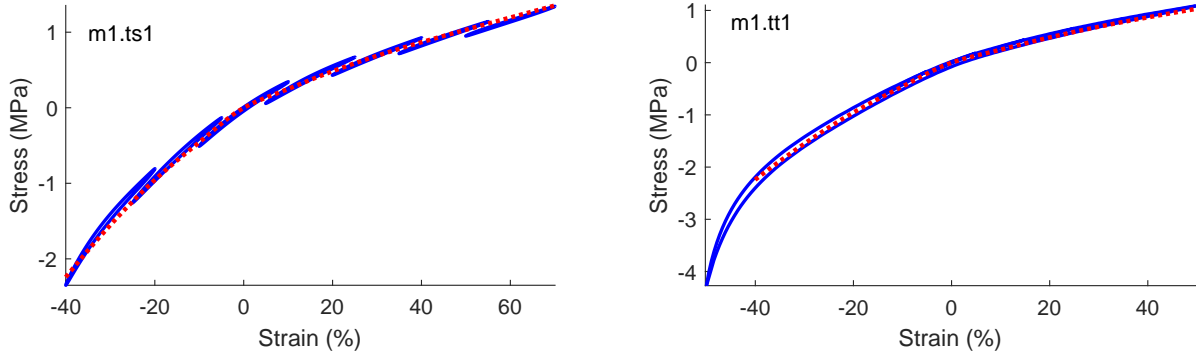


Figure 4: Gauche : Réponse contrainte/déformation des essais sinus. Droite : Réponse contrainte/déformation des essais triangulaires.

Etant donné que le modèle est non-linéaire, classiquement dans la méthode de balance harmonique on considère que la réponse est composée d'harmoniques de la sollicitation  $e^{ik\omega t}$ . Mais il est aussi possible de considérer que le système est linéaire et varie dans le temps. Ainsi, on peut définir un signal à moyenne nulle

$$\bar{u}(t) = u(t) - \frac{\omega}{2\pi} \int_0^{2\pi/\omega} u(t) dt \quad (1)$$

et construire une fenêtre glissante de  $N$  points pour calculer l'amplitude de ce signal complexe en résolvant le problème au sens des moindres carrés

$$\min_{u_1(t_1)} \left\| \begin{bmatrix} \cos(t_1) & -\sin(t_1) \\ \vdots & \vdots \\ \cos(t_N) & -\sin(t_N) \end{bmatrix} \begin{Bmatrix} \Re(u_1(\omega)) \\ \Im(u_1(\omega)) \end{Bmatrix} - \begin{Bmatrix} \bar{u}(t_1) \\ \vdots \\ \bar{u}(t_N) \end{Bmatrix} \right\| \quad (2)$$

Le module instantané est obtenu par le ratio  $E(\omega, t_1) = \sigma(\omega, t_1)/\varepsilon(\omega, t_1)$ .

A partir de l'hyper-élasticité, on doit évaluer aussi la dépendance à la vitesse de déformations. Quand elle est prise comme linéaire, cela s'appelle de la viscoélasticité dans la communauté des matériaux et un système linéaire invariant dans le temps dans la communauté du contrôle des systèmes. La réponse des essais peut être considérée comme une représentation *non paramétrique*, qui caractérise ces systèmes à travers d'une fonction de transfert, ou module complexe,

$$\sigma(\omega) = E(\omega)\varepsilon(\omega) \quad \text{or} \quad F(\omega) = K(\omega)x(\omega) \quad (3)$$

La représentation sous forme de fractions rationnelles est classiquement donnée par des pôles et des zéros dans le domaine fréquentiel, ou séparée en sommes de fractions avec des numérateurs constants appelés résidus et dénominateurs associés aux pôles. Dans la communauté mécanique, ce modèle est appelé modèle de Maxwell généralisé et illustré sur la figure 5. La force totale pour ce modèle est donnée par la somme d'une série de forces sur toutes les branches

$$F = \sum_{i=0}^N F^i \quad (4)$$

où chaque  $F^i$  peut être calculé en utilisant l'asymptote à haute fréquence,

$$\dot{F}^i + \omega^i F^i = g^i \dot{F}^\infty(x) = g^i K^\infty(x) \dot{x} \quad (5)$$

dont l'implémentation peut se faire par le schéma explicite

$$F_n^i = e^{-\omega^i \Delta t} F_{n-1}^i + g^i e^{-\frac{\omega^i \Delta t}{2}} (F_n^\infty - F_{n-1}^\infty). \quad (6)$$

Ce modèle peut être classé dans la catégorie des modèles paramétrique avec ordre. La notion d'ordre fait référence au nombre de cellules de Maxwell ou au nombre de pôles et d'états internes qui influent directement sur la précision du modèle.

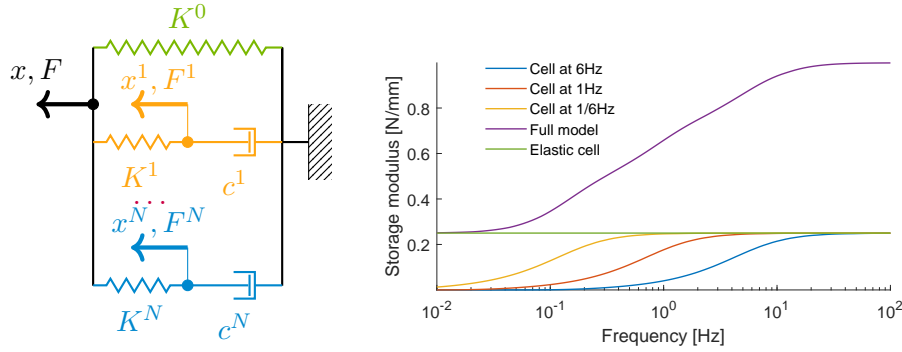


Figure 5: Modèle de Maxwell généralisé avec composants linéaires et sa réponse dans le domaine fréquentiel.

Un deuxième type de dissipation, l'hystérésis indépendante du temps a été prise en compte, mais dans ce travail, seulement les hypothèses les plus basiques sur l'hystérésis seront appliquées sur les modèles d'articulations : les règles de Madelung, qui imposent que chaque boucle dans le diagramme contrainte-déformation doit se refermer, peu importe combien de boucles internes sont réalisées, et la loi de Masing qui affirme que la première charge a la même forme que les suivantes mais avec moitié d'intensité. La figure 6 illustre le respect des règles de Madelung.

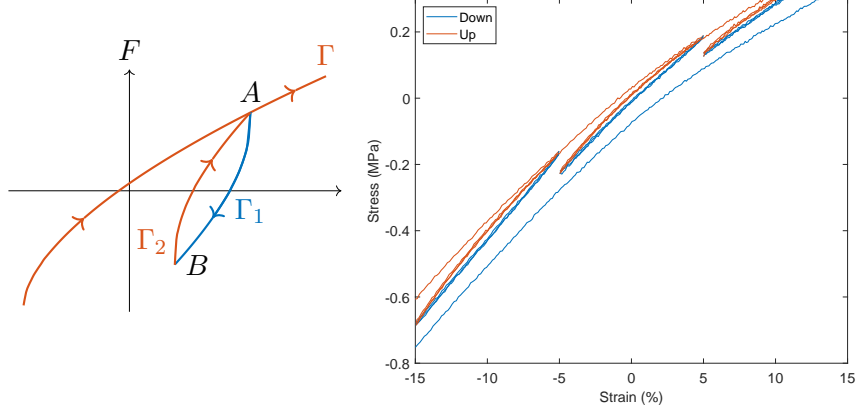


Figure 6: Illustration des règles de Madelung rules. Gauche : schéma; Droite : essai.

Comme la discrétisation viscoélastique à partir de cellules de Maxwell, une discrétisation du comportement hystérétique peut être réalisée par une série de frotteurs de premier ordre. Dans une terminologie rhéologique, l'équivalent d'une cellule de Maxwell pour un modèle hystérétique est une cellule de Jenkins, où l'amortisseur est remplacé par un frotteur, ainsi l'état interne peut être toujours la force  $F^i$  ou le déplacement  $x^i$ . Le modèle complet est un modèle de Iwan et, pour chaque cellule l'équation différentielle est remplacée par un système d'équations d'évolution non-linéaires

$$\begin{aligned} \dot{F}^i &= \frac{g^i}{g^0} \dot{F}^0, \text{ si } F^i \text{sign}(\dot{x}) < F_f^i = \frac{g^i}{g^0} K^0 x_f^i && \text{état collé} \\ \dot{F}^i &= 0, \text{ si } F^i \text{sign}(\dot{x}) = F_f^i && \text{état glissant/saturé} \end{aligned} \quad (7)$$

La courbe de raideur en fonction de la distance du point de rebroussement peut être vu comme une représentation non-paramétrique de l'hystérésis. La figure 7 illustre deux discrétisations avec différents ordres du modèle STS continu. Les modèles hystérétiques partent d'un point de rebroussement avec une raideur tangente  $\sum_{i=0}^{N_{cell}} K^i$  et tendent vers l'asymptote plus basse  $K^0$ .

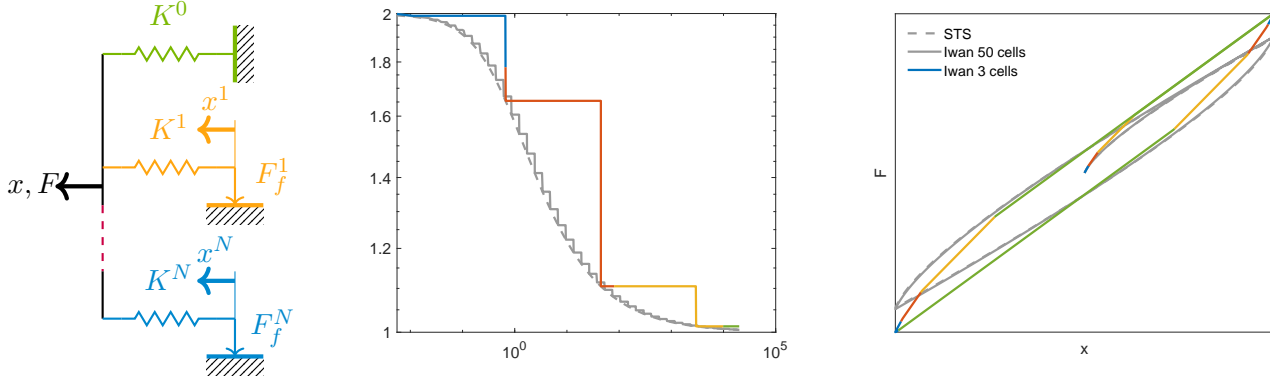


Figure 7: Modèle d'Iwan et sa réponse en termes de relaxation hystérétique et dans le plan contrainte-déformation.

On peut aussi considérer la raideur hystérétique comme dépendante de l'asymptote petites amplitudes. Ainsi la formulation (7) peut être révisée pour utiliser un gain  $g$  qui dépend de la distance du point de rebroussement

$$\dot{F}^i = g^i(|x - x_{Turn}|)\dot{F}^\infty. \quad (8)$$

Au delà des représentations non paramétriques et celles paramétriques où l'on choisit l'ordre, comme les modèles d'Iwan et de Maxwell, il existe des modèles paramétriques indépendants de l'ordre. Ces modèles, comme les dérivées fractionnaires pour la viscoélasticité et le STS continu pour l'hystérésis, diffèrent des modèles à sélection d'ordre, et sont basés sur d'autres connaissances sur le matériau et ainsi demandent moins de paramètres. En revanche, ils sont normalement plus complexes et peuvent être représentés par les modèles à sélection d'ordre.

Le premier couplage d'intérêt est entre les dissipations et l'hyper-élasticité. Quand on vient rajouter des branches hyper-élastiques, il est important de savoir quelle forme de relaxation entre déformation et contrainte est la plus appropriée. Avec l'utilisation de relaxation en déformation, les efforts visqueux ne sont pas proportionnels au module hyper-élastique, qui varie avec la précharge. Sur la figure 8 à gauche, on voit que le module augmente d'un facteur proche de 2 entre -30% et 30% de déformation statique. Cependant, dans la partie droite de la figure, le ratio avec le module hyper-élastique ne varie que  $\pm 15\%$ . Ainsi, le modèle proposé par l'équation (5), qui est basé sur les fractions de la partie hyper-élastique donne la meilleure représentation, même si considérer des fractions comme légèrement non-linéaires serait encore plus précis.

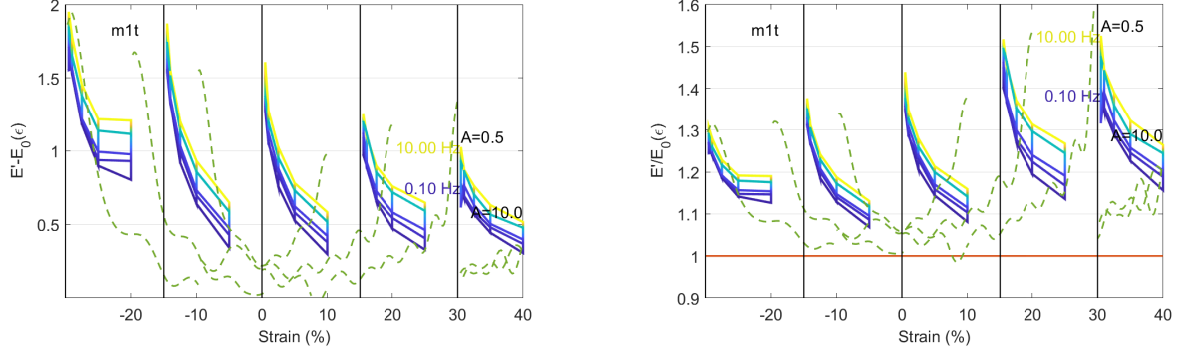


Figure 8: Gauche : Différence entre les modules hystérétiques et viscoélastiques, et le module hyperélastique. Droite : Ratio.

Une deuxième modélisation d'intérêt est la transition entre les dissipations viscoélastique et hystérétique. Avec l'idée classique de dépendance des pôles visqueux à l'état du matériau, on peut utiliser des temps de relaxation réduits. Cette formulation pourrait se réécrire comme l'équation de relaxation non-linéaire

$$\dot{F}^i + \omega^i(1 + \beta \|\dot{x}\|)F^i = g^i \dot{F}^\infty \quad (9)$$

avec un facteur de correction qui dépend de la vitesse  $\alpha(\|\dot{x}\|) = (1 + \beta \|\dot{x}\|)$ , lié à la température structurelle. Si on assume une branche de base linéaire  $F^0 = K^0 x = g^0 K^\infty x$ , et  $\beta \|\dot{x}\| \gg 1$ , on obtient une valeur asymptotique pour la force de friction,

$$F^i \approx \frac{g^i K_\infty}{\beta \omega^i} \frac{\dot{x}}{\|\dot{x}\|} \quad (10)$$

ainsi, on obtient la valeur pour l'expression de la constante hystérétique

$$\beta = \frac{1}{\omega^i x_f^i} \quad (11)$$

et la formule physiquement plus claire,

$$\dot{F}^i + \left( \omega^i + \frac{\|\dot{x}\|}{x_f^i} \right) F^i = g^i K^\infty \dot{x} \quad (12)$$

où les paramètres qui contrôlent le comportement sont les fractions  $g^i$ , la fréquence  $\omega^i$  et la distance de relaxation hystérétique  $x_f^i$  qui donne le déplacement pour lequel la cellule viscoélastique sature. Cette expression est équivalent au modèle de Bouc pour  $\omega^i = 0$ . La reproduction des résultats par le modèle, vue dans la figure 9 est assez claire. Cela confirme que l'effet Payne (assouplissement avec l'amplitude) est lié à l'hystérésis, qui est difficilement distinguable des effets de viscosité non-linéaires à très basse fréquence.

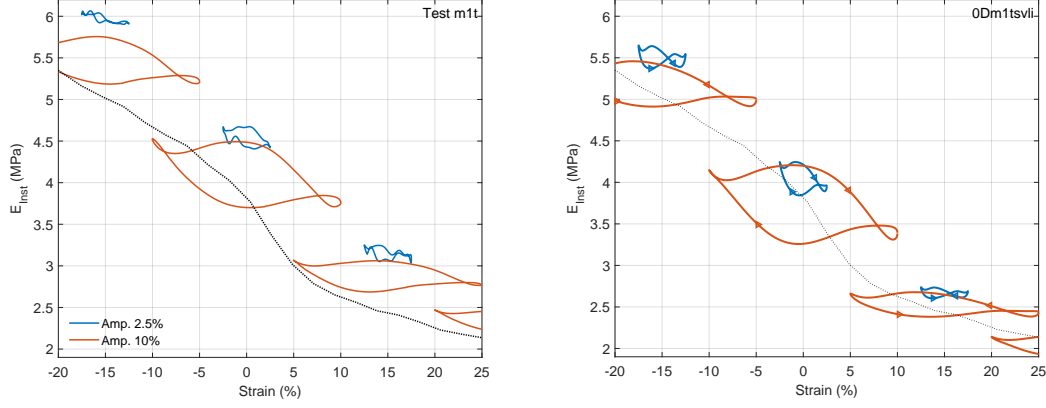


Figure 9: Réponse à sollicitation sinus à 1Hz, 2.5 et 10% de déformation. Gauche : essais. Droite: modèle.

## Modèles matériau 3D

Pour étendre le modèle proposé dans le premier chapitre à 3 dimensions, il faut aborder la généralisation d'un modèle hyper-élastique. Pour un matériau isotrope, le comportement doit être indépendant de la rotation. Cela peut être utilisé pour démontrer que le comportement peut toujours être décrit comme dérivé d'un potentiel des invariants de déformation. La contrainte peut ensuite être décrite par

$$S_{ij} = \frac{\partial \psi}{\partial e_{ij}} = 2 \frac{\partial \psi}{\partial C_{ij}} = 2 \frac{\partial I_k}{\partial C_{ij}} \frac{\partial \psi}{\partial I_k} \quad (13)$$

Les matériaux utilisés pour les articulations sont normalement incompressibles. La compressibilité est décrite par la partie isotrope des déformations et demande une discussion spécifique sur ses lois. Le potentiel qui a été retenu pour la modélisation est celui de Ciarlet-Geymonat, gère la compressibilité avec un terme de pénalisation logarithmique,

$$\begin{aligned} \psi^I &= \frac{\kappa}{2} ((J-1)^2 - \ln(J^2)) \\ \frac{\partial \psi^I}{\partial J} &= \kappa \left( J + \frac{1}{J} \right) = p \\ \frac{\partial^2 \psi^I}{\partial J^2} &= \kappa \left( 1 - \frac{1}{J^2} \right) \end{aligned} \quad (14)$$

Pour que le modèle soit stable, il faut que  $\partial^2 \psi^D / \partial C^2$  soit défini positif. Un potentiel assez simple

qui assure la stabilité, en gardant un bon accord avec les essais, est celui de Carroll,

$$\begin{aligned}
 \psi^D &= \alpha \bar{I}_1 + \beta \bar{I}_1^4 + \gamma \bar{I}_2^{1/2} = \alpha I_1 I_3^{-1/3} + \beta I_1^4 I_3^{-4/3} + \gamma I_2^{1/2} I_3^{-1/3} \\
 \frac{\partial \psi^D}{\partial I_i} &= \left\{ \alpha I_3^{-1/3} + 4\beta I_1^3 I_3^{-4/3} \quad \frac{\gamma I_2^{1/2} I_3^{-1/3}}{2} \quad -\frac{\alpha I_1 I_3^{-4/3}}{3} - \frac{4\beta I_1^4 I_3^{-7/3}}{3} - \frac{\gamma I_2^{1/2} I_3^{-4/3}}{3} \right\} \\
 \frac{\partial^2 \psi^D}{\partial I_i \partial I_j} &= \left[ \begin{array}{ccc} 12\beta I_1^2 I_3^{-4/3} & 0 & -\frac{\alpha I_3^{-4/3}}{3} - \frac{16\beta I_1^3 I_3^{-7/3}}{3} \\ 0 & -\frac{\gamma I_2^{-3/2} I_3^{-1/3}}{3} & -\frac{\gamma I_2^{-1/2} I_3^{-4/3}}{3} \\ -\frac{\alpha I_3^{-4/3}}{3} - \frac{16\beta I_1^3 I_3^{-7/3}}{3} & \frac{\gamma I_2^{-1/2} I_3^{-4/3}}{6} & \frac{4\alpha I_1 I_3^{-7/3}}{9} + \frac{28\beta I_1^4 I_3^{-10/3}}{9} + \frac{4\gamma I_2^{1/2} I_3^{-7/3}}{9} \end{array} \right] \quad (15)
 \end{aligned}$$

Comme le comportement déviatorique est décrit par au moins 2 invariants, un seul essai n'est pas suffisant pour parcourir l'espace généré par ces deux invariants. Ainsi, au moins deux essais différents sont nécessaires pour bien caractériser ce comportement.

Le **cisaillement simple** est un état de déformation qui est obtenu sur une éprouvette de type "sandwich". La figure 10 illustre l'éprouvette et le tenseur gradient de déformation associé en supposant une variation linéaire de la déformation à travers l'épaisseur.



Figure 10: Eprouvette de cisaillement simple et son tenseur gradient de déformation.

La **contrainte uni axiale** est un état caractérisé par l'étirement dans une direction pendant que les autres sont libres d'efforts. La figure 11 illustre l'éprouvette en traction/compression et le tenseur gradient de déformation qui caractérise cet état.

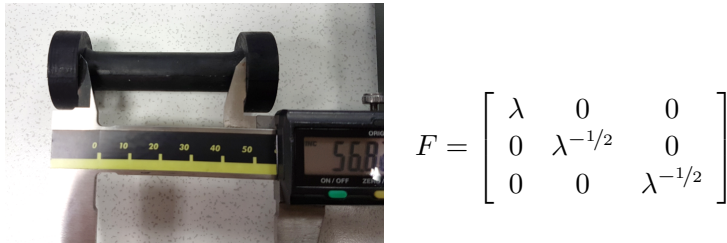


Figure 11: Eprouvette de traction/compression et son tenseur gradient de déformation.

La généralisation du modèle de Maxwell à 3 dimensions passe par la définition d'un modèle hyper-élastique qui remplace la branche non dissipative, en séparant les contributions déviatorique et isotrope. Ainsi, la contrainte totale peut s'exprimer comme la somme d'une partie hyper-élastique déviatorique

$S^0$ , d'une partie déviatorique visqueuse  $S^i$  et de la partie isotrope  $S^p$

$$S = S^0 + \sum_{i=1} S^i + S^p. \quad (16)$$

Si on considère une relaxation analogue à celle décrite pour le modèle 0D, comparable à l'équation (5), on peut avoir le schéma

$$S_{n+1}^i = e^{-\omega^i \Delta t} S_n^i + g^i e^{-\omega^i \Delta t/2} (S_{n+1}^\infty - S_n^\infty) \quad (17)$$

Comme pour un modèle 0D, la modélisation de l'hystérésis serait intéressante pour les modèles 3D. Cela correspondrait à des modèles de plasticité cinématique, mais ce sujet est assez complexe dans le domaine de grandes déformations. Comme la conclusion sur les modèles 0D était que la viscoélasticité non-linéaire était suffisante pour avoir des bons résultats, la voie de la plasticité n'a pas été approfondie.

La relaxation non-linéaire peut être décrite à nouveau par le facteur de correction  $\beta$ , mais aussi avec une saturation en déformation donnée par

$$\epsilon_f^i = \frac{1}{\beta^i \omega^i \sqrt{2/3}} \quad (18)$$

ce qui conduit à une relaxation de contrainte donnée par

$$[\dot{S}^i] + \left( \omega^i + \frac{\|d\|}{\epsilon_f} \right) [S^i] = g^i [\dot{S}^\infty] \quad (19)$$

En simplifiant, on peut utiliser

$$\hat{\omega}^i = \omega^i \left( 1 + \sqrt{\frac{2}{3}} \beta^i \|d\| \right) = \omega^i + \frac{\|d\|}{\epsilon_f^i} \quad (20)$$

Pour avoir le schéma récursif

$$S_{n+1}^i = e^{-\hat{\omega}^i \Delta t} S_n^i + g^i e^{-\hat{\omega}^i \Delta t/2} (S_{n+1}^\infty - S_n^\infty) \quad (21)$$

## Identification

L'idée initiale des essais était d'identifier la partie hyper-élastique avec une séquence de relaxations en plusieurs pas (essais multi-pas). Pour le comportement hystérique, des essais à très basse vitesse constante (essais triangulaires) ont été retenus pour vérifier l'insensibilité au taux de déformation. Pour capturer les effets viscoélastiques, les essais sinusoïdaux sont le choix le plus habituel et ont été aussi retenus pour ce travail. Pour les effets d'amplitude et précharge, les essais triangulaires ont été réalisés à plusieurs amplitudes et précharges.

Pour les essais pièce, une articulation de traverse déformable illustrée sur la figure 12 a été choisie. Ses deux matériaux élastomères ont aussi été testés avec les éprouvettes "sandwich" et traction/compression décrites précédemment, par le fournisseur Vibracoustic.



Figure 12: Articulation de traverse déformable.

Les techniques d'identification classiques sont normalement basées sur quelques courbes de référence. Aussi, une routine basée sur quelques résultats a été élaborée pour un modèle 3D avec un potentiel hyper-élastique de Carroll et quatre cellules viscoélastiques non-linéaires. Même si les résultats étaient acceptables pour une première implémentation, les extrapolations des courbes n'étaient pas satisfaisantes. Ainsi, une voie différente, basée sur les résultats d'identification non-paramétrique a-t-elle été développée.

D'abord, l'obtention de la courbe hyper-élastique a été réalisée avec les résultats des essais triangulaires, donnant une représentation non paramétrique de ce phénomène. Ensuite une deuxième exploitation des résultats des essais triangulaires a donné également une représentation non paramétrique de la relaxation hystérétique, qui a été normalisée par la courbe hyper-élastique. La discrétisation de cette courbe avec un modèle à sélection d'ordre a été réalisé simplement avec le recalage par niveaux, en choisissant les distances aux points de rebroussement et les pertes de raideur associées. Le placement des cellules de Jenkins est détaillé dans la figure 13 pour le premier matériau, sur les deux éprouvettes.

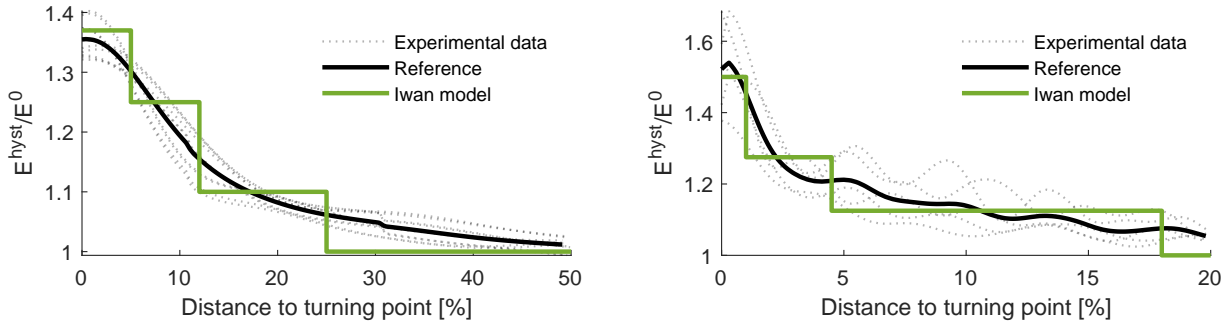


Figure 13: Relaxation hystérétique et identification graphique pour le matériau 1. Gauche : cisaillement simple, droite: traction/compression.

Pour les essais sinus, le comportement est toujours influencé par l’hystérésis. Pour contourner les effets de l’hystérésis, on a réalisé la normalisation du module par rapport au module hyper-élastique, et enlevé les contributions à 0.1Hz. Alors, les courbes de  $(E(s) - E_{(0.1Hz)})/E^0$  ont été retenues comme la représentation non paramétrique de la viscoélasticité, et l’identification à sélection d’ordre basé sur les gains et fréquences a été réalisée, et illustrée dans la figure 14.

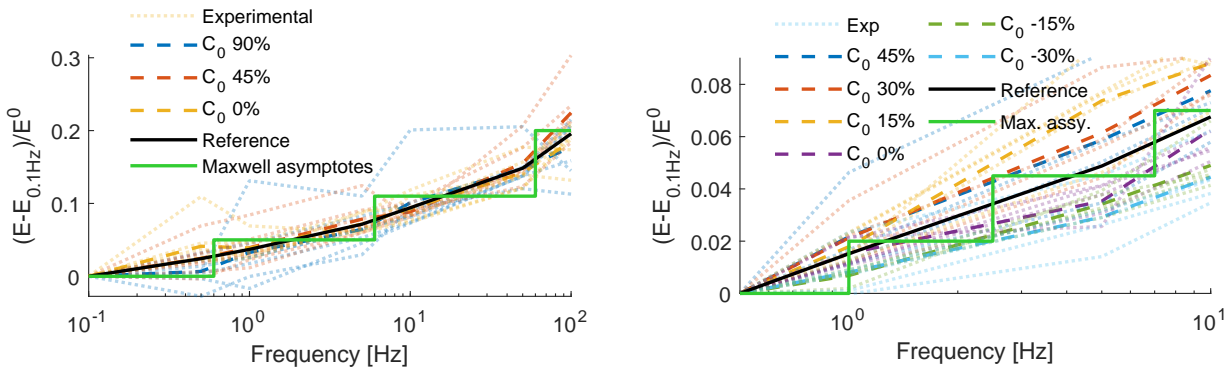


Figure 14: Comportement viscoélastique et identification graphique pour le matériau 1. Gauche : cisaillement simple, droite : traction/compression.

La synthèse de tous les résultats a été réalisé pour tous les essais, et ceux du matériau 1 peuvent être vus sur les figures 15 et 16. En bas et en rouge, le comportement hyper-élastique est illustré à partir des réponses des essais triangulaires avec une valeur moyennée sur plusieurs essais. En vert en traits discontinus, la relaxation hystérétique est illustrée, avec les valeurs utilisés pour obtenir la courbe non paramétrique. Dans la partie haute, comme une sorte de “filet”, on voit le comportement associé aux essais sinus, avec l’amplitude désignée par l’axe x et les fréquences illustrées par l’échelle de couleurs. Les lignes pointillées illustrent la relaxation visqueuse associée aux essais multi-pas pour deux fréquences différentes.

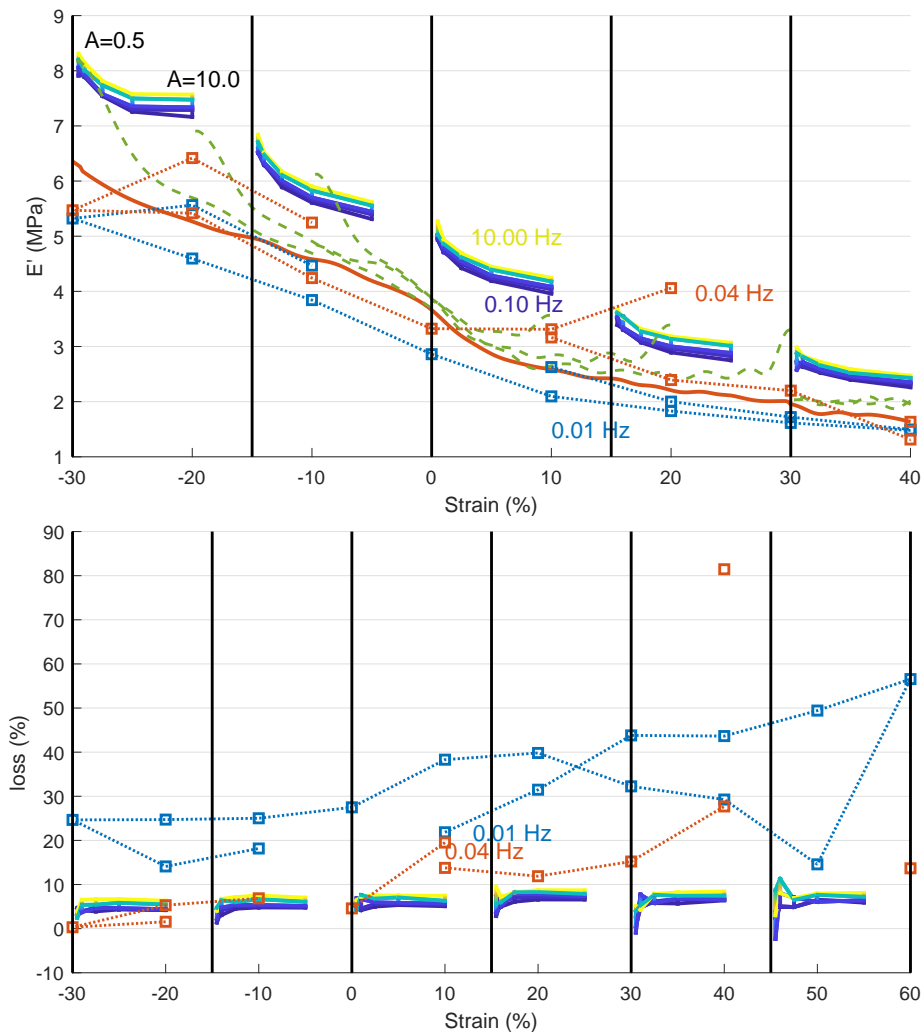


Figure 15: Synthèse des essais traction/compression pour le matériau 1 *m1t*. Haut : Module de stockage. Bas : Module de perte.

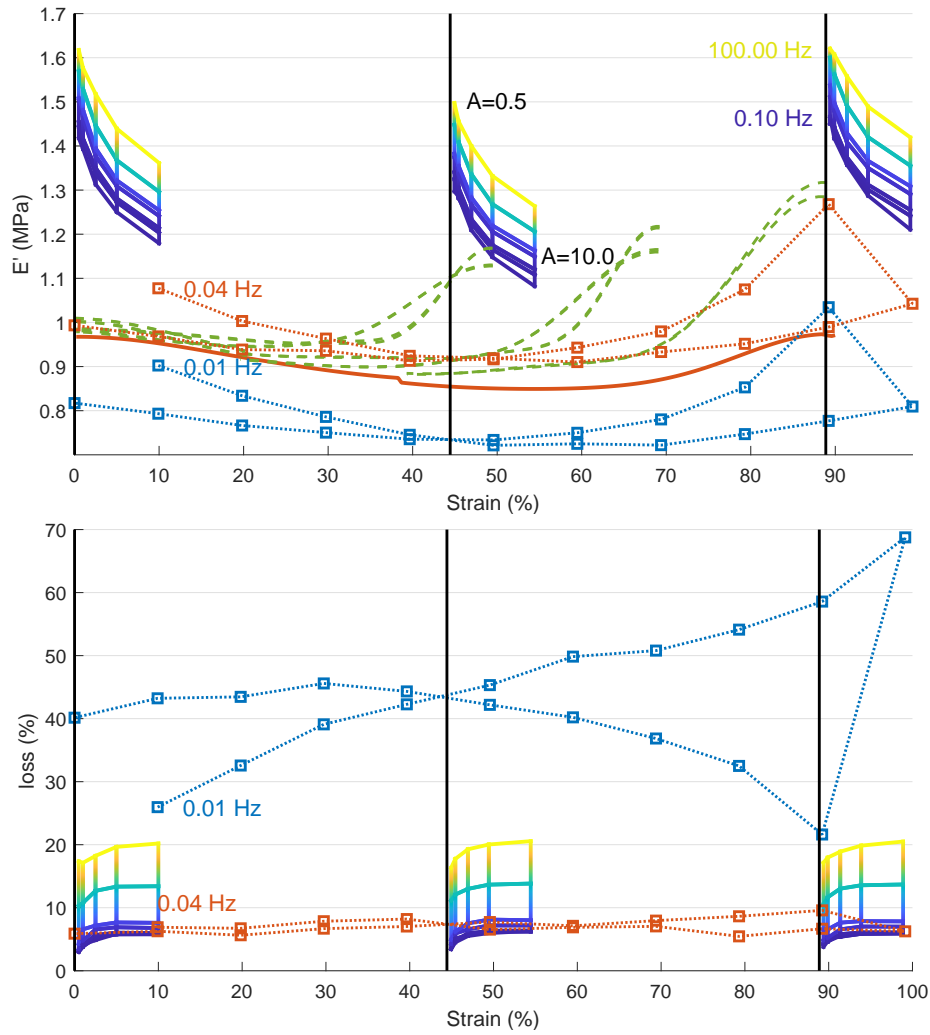


Figure 16: Synthèse des essais cisaillement simple pour le matériau 1 `m1s`. Haut : Module de stockage. Bas : Module de perte.

## Du 3D au 0D

L'implémentation des modèles 3D qui prennent en compte la géométrie passe par l'implémentation en éléments finis. A la fin, la réponse du problème structural se base sur la résolution du principe des travaux virtuels, qui peut être écrit comme un système d'équations donné par

$$[M] \{\ddot{q}\} + [\mathbb{B}] f_{material}([\mathbb{C}] \{q\}, \{\mathcal{U}^I\}) = \mathcal{F}^{ext} \quad (22)$$

avec  $M$  la matrice de masse,  $q$  les degrés de liberté,  $\mathbb{B}$  la matrice de commande tel que  $\mathbb{B}S = \mathcal{F}^{int}$ ,  $f_{material}$  la fonction matériau,  $\mathbb{C}$  la matrice d'observation tel que  $\mathbb{C}q = \nabla u$ ,  $\mathcal{U}^I$  les états internes,  $\mathcal{F}^{ext}$  les forces externes. Ces équations peuvent être résolues par deux types de solveurs.

Les schémas implicites sont ceux qui ne dépendent pas seulement des pas de temps précédents mais aussi de celui d'après, ce qui permet l'utilisation de pas de temps assez grands. En revanche la convergence est un sujet beaucoup plus complexe et l'évaluation des pas de temps peut aussi être assez longue. Les schémas explicites dépendent seulement des pas de temps précédents et l'utilisation de la matrice de masse comme jacobien rend l'évaluation des pas de temps assez rapide. Par contre, la stabilité du schéma dépend de la taille du pas de temps qui doit être relativement petit.

Pour accélérer le temps de calcul, la première approche est de réduire le nombre de degrés de liberté du modèle. La réduction cinématique, aussi connue comme réduction d'ordre du modèle, consiste à définir une base  $T$  telle que

$$\{u(t)\}_N = [T]_{N \times NR} \{q(t)\}_{NR}. \quad (23)$$

Le choix d'un sous-espace approprié restreint la réponse  $u$  au sous-espace généré par  $T$  en utilisant les coordonnées réduites  $q$ . Il a été historiquement utilisé avec des techniques combinant réponses statiques, modes et plusieurs approches itératives, mais aujourd'hui ce problème est placé dans la catégorie de problèmes de classification de sous-espaces. Les modèles éléments finis sont déjà un premier niveau de réduction, où  $T$  est construite comme l'union de polynômes par morceaux. D'autres techniques peuvent être utilisées en considérant une phase d'apprentissage, une phase de génération de base et possiblement des méthodes itératives qui combinent les deux phases.

Avec le sous-espace sélectionné, la même approche de Ritz que celle utilisée pour la MEF est reprise. L'équation (23) donne la réduction cinématique et le principe des travaux virtuels (22) est réutilisé pour obtenir un système d'équations de la même forme.

$$[M_R] \{\ddot{q}_R\} + [\mathbb{B}_R] f_{material}([C_R] \{q_R\}, \{\mathcal{U}^I\}) = \mathcal{F}^{ext} \quad (24)$$

A partir d'un ensemble de vecteurs, possiblement provenant d'une combinaison d'analyses statique, valeurs propres et analyses transitoires, la phase suivante est la construction d'une base. Des algorithmes de génération de bases doivent assurer l'indépendance des vecteurs, même en présence d'erreurs machine et possiblement d'autres contributions pour permettre la troncature ou imposer qu'une matrice soit creuse avec la génération de vecteurs disjoints. Pour l'indépendance de la base, les algorithmes de Gram-Schmidt ou décomposition LU partielle sont les approches classiques. Pour combiner des bases orthonormales avec l'idée d'organiser les contributions, la décomposition en valeurs singulières (SVD) est l'approche classique. La combinaison d'utilisation d'aperçus instantanés de la réponse (snapshots) avec la SVD est typiquement connue comme décomposition orthogonale en modes propres (POD).

Après la phase d'apprentissage qui donne  $n$  aperçus instantanés des déplacements  $q_l$ , avec  $m$  degrés de liberté, la SVD donne

$$[q_l]_{m \times n} = \sum_i U_i(x) (\Sigma_i V_i(t)), \quad (25)$$

où  $U^T U = \mathbb{1}_m$ ,  $\Sigma$  est diagonale, et  $V^T V = \mathbb{1}_n$ . Chaque vecteur des formes singulières gauches  $U_i$  est une base spatiale, et le produit des valeurs singulières  $\Sigma$  avec les formes singulières droites  $V$

décrit l'évolution des formes singulières gauches dans le temps. Une interprétation graphique de cette procédure se trouve dans la figure 17.

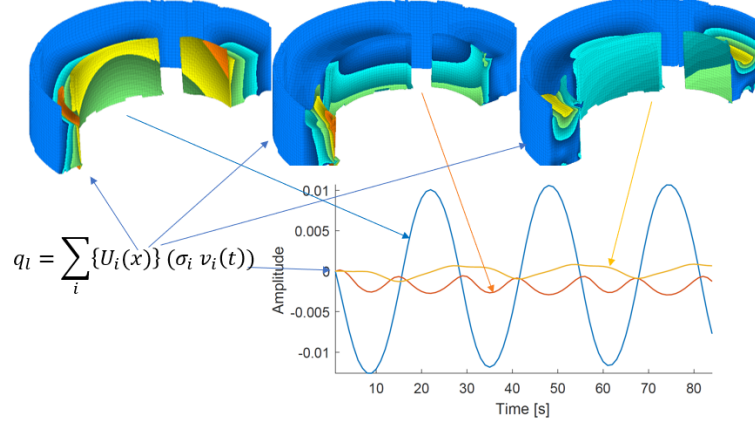


Figure 17: Interprétation graphique de la SVD.

Dans la méthode des éléments finis, le calcul du résidu implique l'évaluation de la loi matériau sur tous les points d'intégration, même après la réduction cinématique. Pour cette raison, une deuxième couche de réduction est nécessaire pour réduire sensiblement le temps de calcul, et cette réduction est appelée hyper-réduction. L'idée générale de la méthode implémentée est de sélectionner seulement quelques points d'intégration pour calculer les efforts internes, en gardant approximativement, le même travail des déformations dans la base réduite pour le modèle complet dans les conditions d'apprentissage.

Des conditions d'apprentissage, on garde les contraintes  $S_l$  et les matrices d'assemblage  $\mathbb{B}$  et  $\mathbb{C}$ . De la réduction cinématique sur les conditions d'apprentissage, vient la base  $[T]_{NR \times NR}$ . Les travaux  $\{b^r\}$  pour les  $NR$  degrés de liberté réduits aux  $NT$  aperçus instantanés peuvent être écrits de différentes manières

$$\begin{aligned}
 \{b^r\}_{NR \times NT} &= [T^T \mathbb{B}]_{NR \times NG} \{S_g^l\}_{NG \times NT} \\
 &= [[\mathbb{C}T]^T J_g S_g(t)]_{(NR \times NT) \times NG} \{w_g\}_{NG \times 1} \\
 &= [G]_{(NR \times NT) \times NG} \{w_g\}_{NG \times 1}
 \end{aligned} \tag{26}$$

La première forme est celle utilisée par les routines éléments finis, avec  $T^T \mathbb{B}$  donnant le travail sur chaque composante de déformation dans la base réduite. La deuxième forme explicite la relation entre  $\mathbb{B}$  et les poids  $w_g$  associés à chaque point d'intégration. La dernière forme réécrit le même travail comme une combinaison linéaire des poids. Cette dernière forme motive l'algorithme d'hyper-réduction choisi. On cherche l'ensemble minimal  $E$  de colonnes de  $G$  (ou également les hyper points d'intégration), et ses nouveaux poids associés  $w_g^*$ , qui donnent une bonne approximation du travail

calculé dans l'apprentissage projeté sur la base réduite  $\{b^r\}$ . Dans un langage mathématique, on a

$$\text{Trouver } w_g^* \text{ qui minimise } \|w_g^*\|_0, \text{ restreint à } \|\{b^r\} - [G] \{w_g^*\}\|_2 < \varepsilon_{tol} \text{ and } w_g^* > 0. \quad (27)$$

Même si une minimisation à norme 0 est un problème avec complexité NP, une approche sous-optimale appelée méthode des moindres carrés creux non négatifs (SNNLSQ) est utilisée. Cette méthode consiste à trouver à chaque étape le point qui contribue le plus pour représenter la matrice  $G$ , et alors réaliser la méthode des moindres carrés non négatifs avec tous les points rajoutés préalablement, jusqu'à ce que la contrainte de précision soit satisfaite.

Comme cas d'étude, le modèle est basé sur l'articulation de traverse déformable, montré dans la figure 12. Elle mesure 77mm de diamètre extérieur et 45.5mm de diamètre interne, et est composé de deux matériaux élastomères, qui ont été testés et identifiés par les essais décrits auparavant, entourés par des coques métalliques. Les parties métalliques ont été considérées rigides et l'élastomère est modélisé par un potentiel hyper-élastique de Mooney-Rivlin, avec des fractions viscoélastiques.

La SVD des résultats d'apprentissage ne prend que quelques secondes, vu que seulement une centaine d'aperçus instantanés ont été retenus. Pour la réduction cinématique, 6 formes sont gardés, avec une précision de 1% sur la valeur singulière la plus importante. Les cinq premières formes sont illustrés sur la figure 18 avec la décroissance des valeurs singulières.

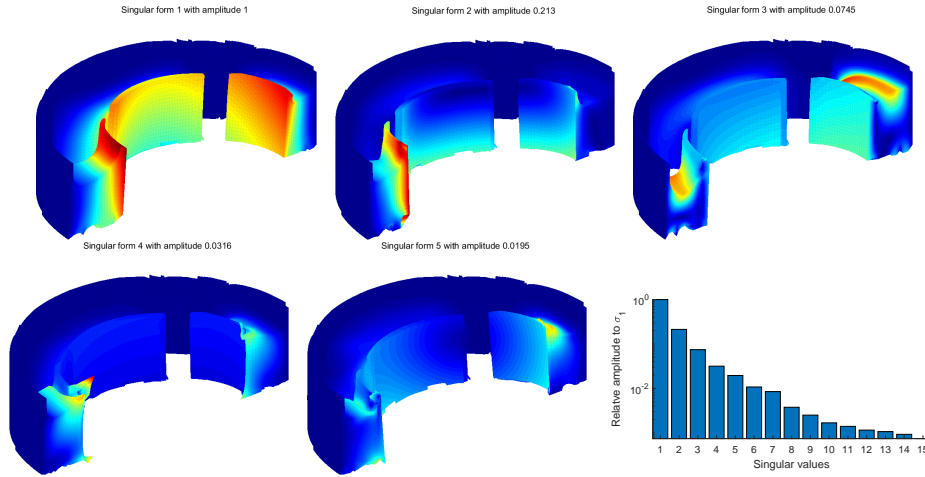


Figure 18: Premiers vecteurs de la base réduite et amplitude des valeurs singulières.

Pour l'hyper-réduction, quelques minutes sont nécessaire pour atteindre la convergence à  $10^{-4}$  de précision sur les travaux du modèle d'apprentissage. A la fin, 139 points des 196240 ont été retenus. Ces trois ordres de grandeur sont directement traduites en temps d'implémentation, comme détaillé dans le tableau 1.

Table 1: Temps d'implémentation des modèles, transitoire de 3 cycles.

	DDL	Points d'intégration	Temps de calcul
Modèle complet	76084	196240	27.7h
Modèle HR avec 3 cycles	6 ( $10^{-2}$ de précision)	139 ( $10^{-4}$ de précision)	29s
Modèle HR avec 1/2 cycle	4 ( $10^{-2}$ de précision)	48 ( $10^{-4}$ de précision)	12s

Le modèle hyper-réduit est aussi précis pour retrouver les déformations locales et contraintes dans les points d'intégration choisis, comme l'illustre la figure 19.

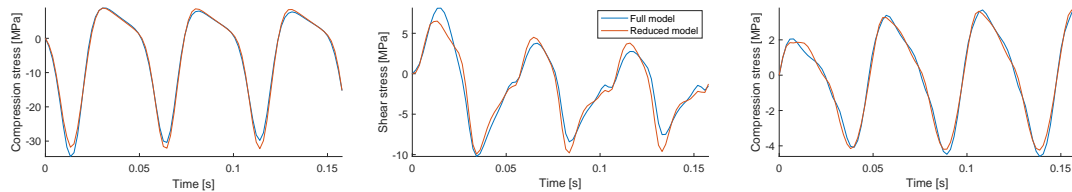


Figure 19: Comparaison de contraintes sur trois points différents. Gauche : zone comprimée. Centre : zone cisailée. Droite : coin de la zone comprimée.

Un dernier bénéfice de la réduction cinématique pour l'intégration explicite est la stabilité sur des pas de temps plus grands, vu que l'élément le plus petit (la restriction majeure pour la taille du pas de temps) n'est plus pris en compte car les modes hautes fréquences ne sont pas représentés dans la base réduite. Pour illustrer cet argument, la réponse à une impulsion, présentée sur la figure 20 a été calculé pour le modèle hyper-réduit avec un pas de temps 20 fois plus grand, sans différence visible.

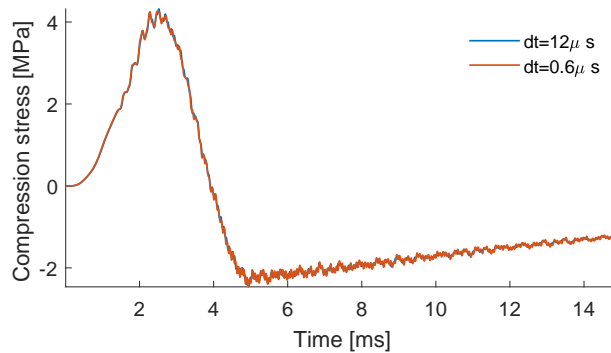


Figure 20: Réponse de l'articulation à une impulsion.

## Simulations multi-corps

Les simulations multi-corps sont une méthode numérique où les systèmes sont composés de plusieurs corps, comprenant quelques DDL (pendant que sur la MEF, des centaines de milliers de DDL sont

habituels). La connexion entre ces corps est habituellement modélisée par des contraintes cinématiques, ou des éléments de force. Il est aussi possible d'imposer des conditions de bord à chaque corps et joint. Ce type de modèle supporte aussi plusieurs types de solveurs (statique, dynamique, cinématique, etc.), ce qui enrichit la généralité de ce type de modèle.

La première application multi-corps a été réalisée sur la suspension d'un groupe motopropulseur (GMP) thermique. Pour le cas choisi, la suspension GMP comprend 3 articulations, localisées à droite, à gauche et au-dessous du GMP. Celles qui sont au-dessus du GMP supportent son poids, pendant que celle qui est au-dessous sert à reprendre le couple moteur sur la caisse. Le modèle 3D de ce montage est présenté dans la figure 21.

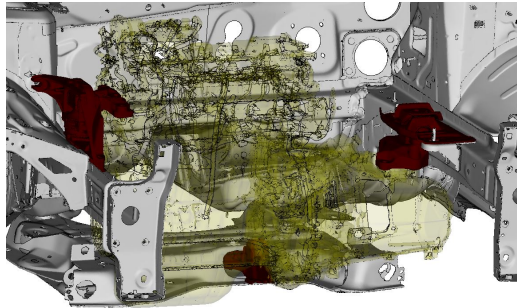


Figure 21: Modèle 3D de la suspension GMP.

La suspension GMP a pour but de filtrer les vibrations moteur au-dessus du ralenti du moteur, et ainsi limiter le bruit et les vibrations dans l'habitacle. Pour cette raison, les fréquences des modes de découplage du GMP déterminés par ces articulations sont placées au-dessous de la fréquence fondamentale de ralenti du moteur. En revanche, au démarrage et à l'arrêt du moteur, les excitations transitoires viennent exciter les modes de découplage et peuvent causer des problèmes de confort. Les paramètres de réglage pour résoudre ce problème sont la vitesse de montée/descente et l'amortissement modal, ce qui implique que la dissipation dans les articulations soit bien modélisée pour prédire précisément les vibrations dans l'habitacle.

Les essais sur les trois articulations qui composent la suspension GMP ont été réalisés avant ce travail, et ne sont pas forcément les plus adaptés, mais sont toujours pertinents. Pour chaque articulation un essai a été réalisé avec déplacement imposé de forme triangulaire à 10mm/min, et les résultats sont donnés sur la figure 22.

Un modèle élastique non-linéaire a été construit avec la force moyenne entre charge et décharge. Pour simuler la dissipation, deux modèles ont été placés en parallèle de la raideur élastique non-linéaire : une dissipation visqueuse de la forme  $f(u) + c\dot{u}$  et une dissipation hystérétique sous la forme d'un modèle STS. Les deux modèles ont été recalés pour dissiper la même quantité d'énergie à la fréquence de 10Hz (proche du mode de roulis du moteur), avec la même amplitude que les essais.

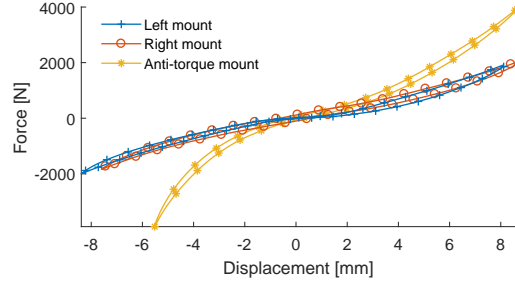


Figure 22: Réponse en force/déplacement pour les trois articulations testées.

Les résultats en temporel sur chacune des articulations ne semble pas demander plus d'efforts sur l'identification. Ainsi, les résultats sont exploités au niveau système.

Une analyse modale a été réalisée pour savoir par quels modes l'énergie passe avant d'être dissipée. L'évolution de l'énergie modale est illustrée dans la figure 23, pour les modèles hystérétique et visqueux. La différence entre les deux cas au niveau système justifie l'investissement d'efforts en caractérisation et modélisation de ces articulations.

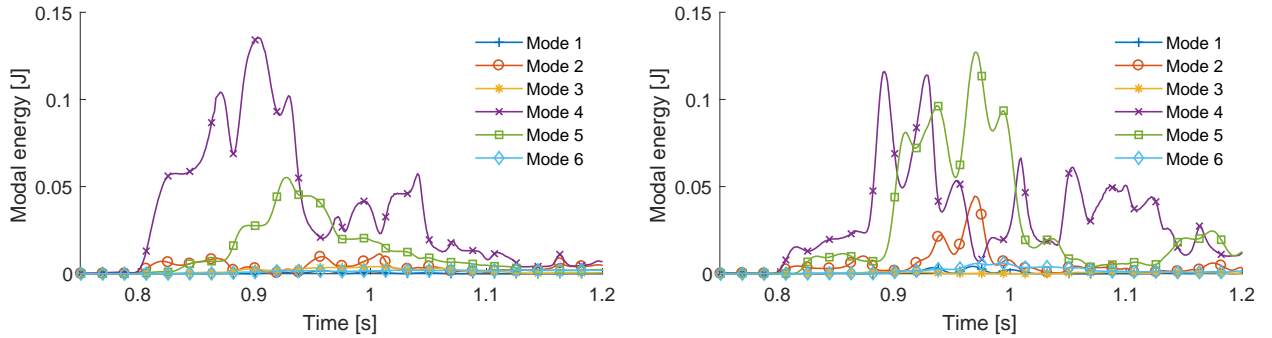


Figure 23: Energies modales pour chaque modèle. Gauche : modèle visqueux. Droite : Modèle hystérétique.

La représentation typique dans un modèle multi-corps considère un référentiel qui subit de larges rotations et de petites déplacements par rapport à cette référence. Le champs de position d'un nœud  $X(t)$  dans le référentiel de coordonnées du corps est donné par

$$\{X_B(t)\}_{3Np} = \{x_B\} + [I_F] \{q_F(t)\} \quad (28)$$

où l'indice  $B$  désigne les coordonnées du corps et l'indice  $F$  désigne le corps flexible. La position globale est ainsi obtenue par la translation et rotation des positions dans le référentiel du corps

$$\{X_{Global}(t)\}_{3Np} = \{u_B(t)\} + [R_B(t)] \{X_B(t)\} = \{u_B(t)\} + [R_B(t)] \left( \{x_B\} + [I_F] \{q_F(t)\} \right) \quad (29)$$

où  $\{u_B(t)\}$  donne la translation de l'origine du corps et  $[R_B(t)]$  sa rotation non linéaire. Si on considère l'interface corps/articulation comme rigide, le mouvement d'un point peut être décrit avec un marqueur

$$\{X_{Global}(t)\} = \{u_{Marker}(t)\} + [R_{Marker}(t)] \{x_{Local} - x_{Marker}\} \quad (30)$$

où la position relative  $x_{Local} - x_{Marker}$  est constante dans le référentiel du marqueur.

La possibilité d'introduire des modèles hyper-réduits dans les simulations multi-corps dépend de la compatibilité des équations (28) à (30), où en d'autres mots, réécrire (30) avec une base constante. Cela est possible en réordonnant le produit linéaire de (29). Les variables dépendantes du temps, utilisées comme DDL, forcés par l'interface du modèle d'articulation hyper-réduit sont donnés par

$$\{q_{LR}\}^T = \{u_i \quad R_{ij}\}^T = \{x \quad y \quad z \quad \cos(\alpha) \cos(\beta) \quad \cos(\beta) \sin(\gamma) \quad \dots\}^T \quad (31)$$

et la base constante qui combine tous les termes constants de (5.12) est donnée par

$$[T^A]_{3Np \times 12} = \begin{bmatrix} \delta_x & \delta_y & \delta_z & \delta_{i1x1p} & \delta_{i2x1p} & \delta_{i3x1p} & \delta_{i1x2p} & \delta_{i2x2p} & \delta_{i3x2p} & \delta_{i1x3p} & \delta_{i2x3p} & \delta_{i3x3p} \end{bmatrix} \quad (32)$$

L'implémentation finale aurait la forme

$$\{q\} = \begin{bmatrix} T^A & 0 & 0 \\ 0 & T^C & 0 \\ 0 & 0 & T^B \end{bmatrix} \begin{Bmatrix} q_{LR}^A \\ q_R \\ q_{LR}^B \end{Bmatrix} \quad (33)$$

où  $T^A$  avec 12 colonnes donne l'interface entre le premier marqueur et le modèle EF de l'articulation,  $T^B$ , aussi avec 12 colonnes donne l'interface entre l'articulation et le deuxième marqueur, avec une structure similaire, et  $T^C$  maintient les mouvements internes, résultant de la réduction cinématique.

Le deuxième cas multi-corps étudié est celui de l'articulation de traverse déformable. Cette pièce a été décrite dans les autres sections et sera utilisée ici à nouveau. La traverse déformable est un poutre qui a pour objectif changer le comportement entre roulis et pompage pour donner plus de manœuvrabilité au véhicule.

Le modèle d'articulation combine des raideurs non-linéaires sur les trois directions et les trois rotations, et une dissipation visqueuse sur chacun de ces 6 DDL. L'identification de chaque direction était très similaire à celle réalisée pour les articulations de la suspension GMP. Ce modèle est comparable à celui qui a été testé et identifié dans ce travail, donc des comparaisons ont été réalisées.

On a choisi de représenter seulement deux parties des simulations : une qui fait saturer l'articulation (dans la direction verticale, avec le passage du véhicule sur 3 barrettes métalliques **BM**), et une où l'articulation est forcé dans différentes directions (trois courbes à gauche avec accélération latérale maximale **TR**). Les obstacles sont illustrés dans la figure 24.



Figure 24: Obstacles testés et simulés, **BM** à gauche, **TR** à droite.

Pour la simulation **BM**, les résultats sont comparés sur la figure 25. Pour l'axe  $x$ , les pics ne sont pas bien corrélés car le modèle identifié ne prend pas en compte les mises en butée. Pour l'axe  $z$ , les réponses sont beaucoup mieux corrélés.

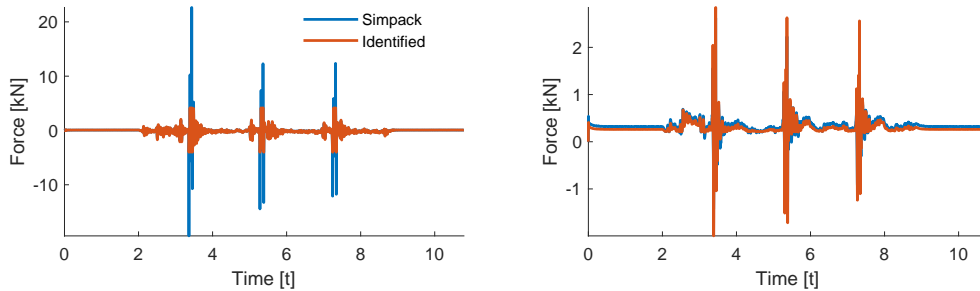


Figure 25: Comparaisons pour les efforts simulés pour **BM**. Gauche : axe  $x$ . Droite : axe  $z$ .

Les réponses pour la simulation **TR** sont affichées dans la figure 26. Pour l'axe  $x$ , le modèle est plus souple que celui identifié avant. Pour la direction  $z$ , le modèle identifié dans ce travail est beaucoup plus rigide que celui d'avant.

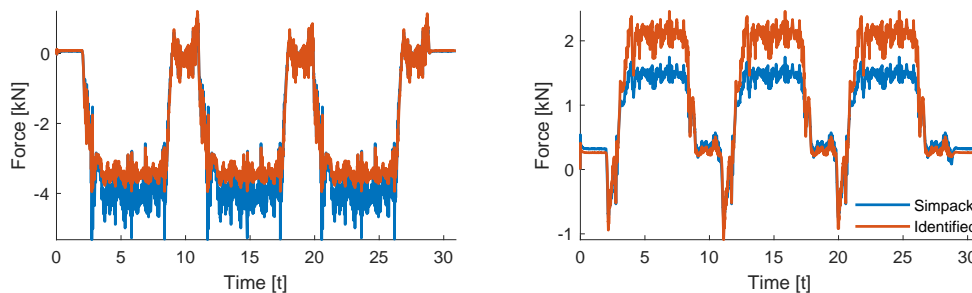


Figure 26: Comparaisons pour les efforts simulés pour **TR**. Gauche : axe  $x$ . Droite : axe  $z$ .

Un dernier résultat est lié à l'analyse des forces inélastiques (forces totales moins les hyper-élastiques), dont la puissance associée donne une indication de la dissipation instantanée. La figure 27 illustre ces quantités pour les simulations **BM** sur l'axe  $z$ . Il est intéressant de voir qu'une des cellules est bloquée dans un état déformé ce qui entraîne un décalage d'environ  $-200\text{N}$ . Ce blocage pourrait

être résolu avec l'utilisation d'un modèle viscoélastique non-linéaire, si les temps de stabilisation ne sont pas trop longs. Une confrontation avec d'autres essais semble nécessaire pour valider si cet effet est vraiment présent sur les articulations ou si c'est juste l'effet d'une sélection d'ordre grossière.

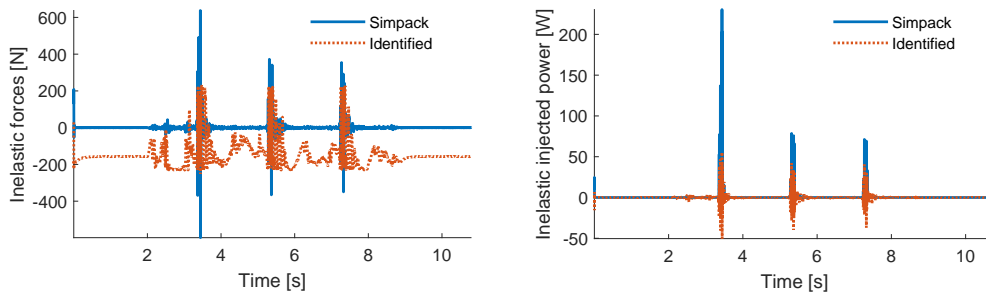


Figure 27: Forces inélastiques (gauche) et puissance injectée (droite) pour BM selon l'axe z.

La puissance inélastique injectée montre qu'avec la cellule purement visqueuse, toute l'énergie est dissipée, alors que pour le modèle identifiée, il y a d'autres modalités de stockage d'énergie qui peut ainsi revenir sur le système. Cet écart pourrait entraîner des différences notables en simulations transitoires.

## Conclusion

Pour tous les modèles, le premier pas est de déterminer le type de relation entrée/sortie qui doit être représenté. Basé sur l'expérience de Stellantis et des rapports internes, dont les résultats sont illustrés dans l'introduction, il a été établi qu'il est important de représenter l'hyper-élasticité, la viscoélasticité et la dépendance au parcours de déformation, et aussi de coupler les différentes directions de sollicitation. Cela demande un changement notable des procédures de conception actuels, qui ne considèrent que des modèles d'élasticité non-linéaire avec viscosité en parallèle.

Pour aborder cette problématique, la décomposition en problèmes plus simples a été réalisée : optimisation des procédures d'essais pour caractériser et identifier les comportements sélectionnés, investigation des modèles 0D capables de représenter tous les effets souhaités, l'élaboration de modèles compatibles avec les simulations multi-corps en passant par des modèles 3D, et finalement l'évaluation de ces modèles dans une routine multi-corps.

## Résultats et apports

La modélisation 0D discuté dans le chapitre 1, a été largement développée avec la disponibilité des résultats des essais réalisés par Vibracoustic. Les résultats moyennement satisfaisants de la première phase d'identification ont conduit à tracer les courbes non paramétriques pour tous les essais et par

conséquent le cadre qui unifie le comportement non-linéaire à partir d'une courbe maîtresse hyper-élastique à laquelle on vient rajouter le comportement hystérétique, ou viscoélastique saturé, et des forces viscoélastiques pour les hautes fréquences. Une version réduite de ce chapitre a été l'objet d'une publication à la revue MSSP [3], sous revision.

D'un autre côté, une nouvelle proposition sur ce chapitre est d'utiliser les essais *triangulaires* à basse vitesse pour extraire les modèles non paramétriques de l'hyper-élasticité et de la relaxation hystérétique. Cette représentation non paramétrique de l'hystérésis associée à un module de relaxation est originale et permet d'établir un clair parallèle avec le concept de la relaxation viscoélastique.

Un deuxième apport associé aux essais était l'introduction du calcul du module instantané en utilisant le ratio entre les signaux analytiques d'entrée et de sortie. L'implémentation de cette proposition sur essais sinus classiques était fondamentale pour la compréhension du couplage entre les trois comportements de base, et le choix final pour un modèle basé sur la relaxation de la dérivée de la force, avec viscoélasticité non-linéaire pour représenter l'hystérésis. Pour ce dernier aspect, une contribution notable était l'interprétation de saturation de charge plutôt que le concept de temps réduit. L'analyse de l'effet Payne comme le couplage entre la viscoélasticité et l'hystérésis est donc plus claire que l'analyse du module complexe au premier harmonique. L'hypothèse de fractions constantes pour tout le domaine n'est pas parfaite, mais donne des résultats raisonnables pour les essais réalisés.

Pour l'évaluation des modèles, il a été prouvé que ceux à sélection d'ordre correspondent à une discrétisation générique qui s'applique au modèle classique de viscoélasticité et au modèle proposé de relaxation hystérétique. Les stratégies graphiques d'identification ont été utilisées et donnent une manière simple de contrôler le compromis entre ordre et précision.

La contribution associée aux modèles indépendants de l'ordre était la démonstration que la sélection d'ordre est le résultat de l'implémentation numérique, donc l'intérêt de ce type de modèle réside dans la séparation des phases de paramétrisation et discrétisation, ce qui permet un accès plus simple à des problèmes de conception comme la définition d'une catégorie de matériaux réalistes pour une application donnée.

Le chapitre 2 est une suite naturelle du chapitre 1, étant donné qu'il étend à trois dimensions et aux grandes déformations les modèles 0D proposés. Un problème dans cette transition est que le modèle purement hystérétique a un équivalent tridimensionnel (plasticité cinématique) qui n'est pas complètement établi pour les grandes déformations. Comme une des contributions du chapitre 1 était la constatation que l'hystérésis est une idéalisation de la viscoélasticité non-linéaire, cette dernière a été implémentée avec des résultats satisfaisants, sans passer par des formulations plastiques. Pour cette raison, la recherche sur ce sujet a été placée dans l'annexe A.

En termes de développements de logiciel, la contribution était l'implémentation, les essais et la participation à l'optimisation des routines de lois matériau de grandes déformations dans le logiciel

d'éléments finis SDT pour simulations 3D. Cela a impliqué la gestion de détails d'implémentation, comme le schéma numérique, la taille du pas de temps, l'analyse de la dissipation... Le chapitre est donc une première documentation de l'implémentation finale.

Le chapitre 3 détaille la campagne d'essais conçue pendant le déroulement de la thèse, réalisée par Vibracoustic, dont le post traitement a engendré beaucoup de propositions formulées dans le chapitre 1. Dans le chapitre, les choix de conception des essais qui ont permis de confirmer la généralité des propositions réalisées dans le chapitre 1 sont documentés.

Des nouvelles directives peuvent être données à partir des résultats exploités. Les essais triangulaires à basse vitesse se sont révélés très pertinents car ils ont permis l'identification de la relaxation hystérétique et une description plus fine du comportement hyper-élastique. Rétrospectivement, un échantillonnage plus fin juste après les points de rebroussement pourrait être utile pour les identifications non paramétriques. Les petites boucles ont aussi permis la vérification des règles de Madelung, mais un échantillonnage plus fin sur ces essais et possiblement une transition plus subtile seraient nécessaires pour une meilleure compréhension du comportement proche du point de rebroussement. Les essais qui ont pris le plus de temps, les multi-pas, n'ont pas été les plus utiles car la partie hyper-élastique a été mieux décrite par les essais triangulaires. Ils pourraient être plus appropriés pour caractériser les effets très long terme ou l'effet Mullins. Les essais sinus ont été bien choisis, mais l'utilisation de données en plus du premier harmonique doit être une priorité.

Une routine d'identification classique a été réalisée et même si les résultats modélisaient raisonnablement le matériau, ils n'ont pas été complètement satisfaisants. En effet une grande quantité de données n'a pas été utilisée pour générer la fonction objectif et l'extrapolation du modèle obtenu vers les points d'opération qui n'ont pas été utilisés était assez grossière. Pour cette raison, basé sur les développements du chapitre 1, une nouvelle identification non paramétrique a été réalisée avec stratégies de discrétisation de courbes non paramétriques des comportements viscoélastique et hystérétique. Les résultats ont été analysés pour le matériau et pour la pièce. Cette identification fournit des résultats directement implémentables dans un code multi-corps mais il faut encore apporter des clarifications pour l'implémentation sur des modèles 3D.

Après l'illustration des enjeux concernant les modèles 0D et matériau, le chapitre 4 considère les formulations éléments finis, nécessaires pour permettre la prédiction de l'impact du changement de géométries ou de considérer le couplage directionnel. Vu que ces calculs prennent plusieurs heures, alors que les simulations multi-corps demandent des calculs réalisés en secondes, l'objectif était de montrer que les techniques de réduction peuvent atteindre le gain de performance nécessaire, en gardant l'utilisation de géométries et matériaux arbitraires. La conclusion est que cette approche est viable et la contribution associée est la documentation de l'utilisation de techniques de réduction cinématique pour diminuer sensiblement le nombre de DDL et de l'hyper-réduction pour arriver à

une approximation rapide des travaux internes sur matériaux non linéaires. Le développement suit l'originalité de SDT où les non-linéarités sont exprimés à travers de la notion de matrices de commande et d'observation, qui sont classiques dans la théorie de contrôle, mais assez rares dans le domaine de la mécanique, et donnent une image assez directe de l'implémentation.

La validation de cette implémentation pour l'articulation utilisée pour les essais avec un modèle hyper-viscoélastique a été présenté à la conférence ISMA 2020 [4]. La conclusion est que le modèle hyper-réduit a une performance compatible avec les simulations multi-corps et que les extrapolations réalisées sur les paramètres matériau, la forme de la sollicitation et l'amplitude donnent toujours des bons résultats.

Le chapitre 5 revient sur l'objectif final que sont les analyses multi-corps, avec deux cas d'étude : un sur la suspension d'un groupe motopropulseur (GMP) et l'autre sur une articulation de traverse déformable.

Le premier cas, réalisé au début de la thèse et présenté à la conférence ECCMR 2019 [5], donne une motivation claire pour la thèse. Une caractérisation insuffisante des articulations a mené à deux modèles équivalents au premier regard, mais différents en poussant l'analyse des réponses. Pour une simulation transitoire les profils de dissipation et les réponses modales sont complètement différents. Comme cela peut affecter les choix de conception, il est important de placer plus de ressources dans la caractérisation et l'identification de ces articulations.

Le deuxième cas de l'articulation de traverse déformable correspond à la pièce testée par Vibracoustic, et démontrer la capacité d'utiliser les résultats issus des autres chapitres était nécessaire pour la finalisation du travail. Comme une intégration avec Simpack n'était pas possible à cause de contraintes temporelles, l'accent a été mis sur la clarification des besoins pour les implémentations futures, et l'analyse des articulations de façon isolée en regardant les forces et puissances. L'extraction de déplacements, angles, forces et couples imposés sur l'articulation à partir d'une simulation du passage d'un véhicule complet sur différents obstacles a permis la vérification de la cohérence entre le modèle et les résultats sur Simpack. De façon surprenante, les prédictions de force n'étaient pas parfaitement consistantes avec le modèle embarqué, ce qui indique des transformations supplémentaires dans le solveur de Simpack.

Les modèles qui résultent de l'identification du chapitre 3 sont notablement différents de ceux qui sont déjà implémentés sur Simpack. Le calcul de la puissance inélastique pour les deux modèles indique que la conclusion issue du premier cas est aussi valable : un modèle plus détaillé des articulations est important pour simulations des transitoires.

## Perspectives

Les résultats de la campagne d'essais ouvrent plusieurs perspectives. La procédure standard devrait inclure au-delà des essais sinus classique, des essais triangulaires à basse vitesse et grandes amplitudes, sans besoin d'essais multi-pas, sauf si la caractérisation de temps plus longs est souhaitée. Le traitement des données devrait automatiser les techniques d'extraction du module hyper-élastique, du module de relaxation, et de son ratio associé, mais aussi développer l'utilisation du module instantané sur les essais sinus, au moins sur les graphiques de synthèse des matériaux. L'incorporation de cette stratégie dans les routines d'essai DMA devraient améliorer sensiblement la caractérisation des matériaux et des articulations.

Pour les essais triangulaires, une analyse plus détaillée proche des points de rebroussement, avec un échantillonnage plus fin et des transitions plus adoucies peuvent être une voie pour mieux comprendre la transition entre l'hystérésis indépendante du temps ou la viscoélasticité saturée et la relaxation viscoélastique. Les essais à petite amplitude introduits pour vérifier les règles de Madelung seraient les plus appropriés pour réaliser ce type d'étude.

La notion de module instantané ouvre aussi la porte pour beaucoup d'applications à des systèmes non-linéaires. L'estimation des signaux dans le temps par des filtres de Kalman étendus a déjà donné des bons résultats. L'application à d'autres formes de non-linéarité au niveau structure avec des coordonnées modales semblent être de bonnes perspectives. La liaison avec les systèmes LPV (linéaires à paramètres variables) dans la théorie du contrôle doit aussi être établie.

Pour les modèles matériau 3D, le point manquant le plus visible est la capacité d'utiliser de multiples courbes non paramétriques directement dans les modèles 3D par la séparation des invariants associés aux configurations d'essai. Cela est la clé pour étendre les modèles non paramétriques à trois dimensions avec des cellules séparées.

L'analyse de la cohérence des essais matériau à travers des simulations en éléments finis est aussi nécessaire pour comprendre ses limitations. En effet dans l'éprouvette traction/compression on suppose que la section centrale présente un état constant, que le matériau est parfaitement incompressible, et que la dissipation peut être approchée par le comportement de cette section, malgré qu'elle ait lieu sur toute l'éprouvette. Cela revient à réaliser une hyper-réduction sur un point de la section centrale, et la validité de cette approche doit aussi être démontrée. Pour l'éprouvette en cisaillement, on a négligé les contraintes transversales et on assume aussi l'incompressibilité. Ces analyses de cohérence doivent particulièrement mener à des corrections géométriques dans les courbes hyper-élastiques.

Il y a aussi d'autres problèmes moins critiques pour les implémentations décrites dans cette thèse. L'implémentation d'une routine stable qui représente l'hystérésis pure a ses intérêts, même si le modèle hyper-viscoélastique non linéaire représente mieux le matériau. Cela pourrait s'appliquer pour la modélisation d'autres effets : effet Mullins, effets plastiques, endommagement, cristallisation induite

par déformation, effets de précharge sur fatigue... L'implémentation de ce type d'approche sur des modèles 0D est plus simple que sur des modèles 3D, mais il faudrait des essais qui soient conçus pour les caractériser et aussi des groupes de travail intéressés par les résultats.

Pour l'implémentation de modèles hyper-réduits compatibles avec des simulations multi-corps, il y a plusieurs voies de développement. La phase d'apprentissage basée sur l'intégration explicite est assez coûteuse en temps (l'application décrite n'a utilisé qu'un quart du modèle total). Des méthodes implicites et/ou itératives qui considèrent des linéarisations locales, des réductions cinématiques par morceaux... sont des voies de développement très claires et doivent être appliquées. La conception d'une stratégie d'apprentissage qui prend en compte la présence de précontraintes et la construction d'un schéma d'intégration généralisé demande la résolution de plusieurs détails d'implémentation.

Tester la robustesse de modèles hyper-réduits pour la simulation de l'articulation complète dans des conditions qui ne sont pas facilement reproductibles sur des machines d'essai ou qui sont en dehors des conditions d'apprentissage semble être aussi important. D'autres extrapolations sur les paramètres de loi matériau (ou même le modèle matériau), la sensibilité des cellules, la fréquence de sollicitation, les chargements transitoires... pour le même sous-espace d'apprentissage doivent être aussi investiguées.

Dans une perspective plus long terme, la modélisation du contact doit être considérée. Les articulations présentes dans les véhicules intègrent des mises en butée qui font que la raideur augmente fortement grâce au contact avec le caoutchouc en grandes déformations, ce qui cause des changements de comportement assez brusques.

Enfin, pour les applications multi-corps, des modèles 0D à grandes rotations sont déjà implémentés sur SDT pour le cas de la suspension GMP n'incluant que deux corps et a bien été testé. En revanche, la généralisation vers un solveur plus générique est nécessaire pour le cas de l'articulation de traverse déformable. La cosimulation semble être la route la plus simple, mais la communication entre logiciels peut toujours générer des soucis, même avec des nouveaux standards. L'augmentation du nombre de cas d'étude facilement accessibles comme celui de la suspension GMP doit permettre d'évaluer avec plus de précision l'importance de la modélisation des articulations et l'utilisation de critères inhabituels comme la dissipation et les énergies modales.

La confrontation entre modèles 0D et les modèles hyper-réduits doit aussi être faite pour mieux comprendre les effets géométriques, et préparer à très long terme la mise en place d'une configuration idéale, où les essais fournissent les caractéristiques matériaux alors que les géométries pourraient être modifiées librement dans la phase de conception.

RESUME

---

# Introduction

This work was elaborated in a CIFRE PhD contract between the Structural Mechanics and Material Sciences (SMMS) division of the Scientific Department and Disruptive Technologies (SD2T) of Group Stellantis, SDTools and Laboratoire Procédures et Ingénierie en Mécanique et Matériaux (PIMM), from the engineering school Arts et Métiers Institute of Technology (ENSAM).

The main objective of this work is to propose a coherent procedure for building, identifying and validating models to represent the dynamic behavior of rubber bushings and mounts in multibody simulations. This project is at the crossroads of several engineering domains from material modeling to numerical implementation. This introduction provides a broad vision of the subject as well as some essential definitions.

### Industrial background

The automotive industry relies heavily on simulations for design iterations. Accurate models during early design stages may save a lot of resources before testing stages and avoid very costly late design changes. The vehicle performance can be evaluated in different metrics:

- dynamic behavior;
- endurance estimation;
- comfort under vibrations.

**Dynamic behavior** refers to the vehicle responses when subjected to different requirements, such as different road obstacles and driver solicitations, or even for active safety issues. The simulations are made with functional models by multibody simulations, where it is crucial that the bushing and mount models emulate properly the evolution of dissipation with nonlinear elasticity.

**Endurance estimation** seeks to reproduce the harshest operation conditions for an automobile, where a multibody model from the vehicle goes through severe road models. The main objective is to extract and predict maximal forces that each component may undergo. For this evaluation, it is essential that bushing and mount models accurately capture nonlinear elasticity, contact and dissipation.

**Comfort under vibrations** targets the attenuation of undesired noises and vibrations. In the large list of sources, a few stands out: engine cyclic solicitations, wheel unbalance, road generated trepidation. Often, this kind of evaluation is made in frequency domain, where linearized conditions are required. But when nonlinear effects gain importance, their pertinence may be questionable, motivating the use of multibody time simulations.

For the three different performance aspects, multibody dynamics is a tool of interest, where the whole vehicle is modeled by several simple bodies (mostly rigid, but they may also be considered as flexible), connected by different kinematic or dynamic link models, which are the object of interest of

this thesis. A poorly modeled articulation may induce different system behavior, possibly leading to incorrect conclusions.

Real mounts and bushings are normally used to link relatively rigid parts. Figure 28 shows a schematic representation of where this type of bushings and mounts are used. In the figure, one sees that most of the articulations are in the wheel suspension and on the powertrain, linking metal parts within the substructures or the whole substructure to the chassis, and more specifically which bushings and mounts are made of rubber in the front suspension, rear suspension and the powertrain.



Figure 28: Localization of elastomeric bushings and mounts in front suspension, rear suspension and engine suspension.

The use of flexible links between relatively rigid bodies, induces a number of demands on their behavior:

- to compensate mounting errors and permanent loads, they must allow permanent large deformations without degradation;
- to act as filtering elements limiting load transmission to low frequencies in suspension mechanisms which are key to comfort performance, they must have low stiffness and considerable damping in their standard operating range - normally up to 100Hz;
- to limit motion in extreme loading conditions linked to rapid braking, steering, and other maneuvers or speed bumps, the stiffness must increase in a controlled manner. The engine must always stay within its enclosure and not touch the body, or the twist beam axle must not touch any other components, for instance. Even though the stiffness of a material increases under compression, this is often insufficient and higher stiffness is obtained through contact and thus very specific geometries.

The first two characteristics are the main features of elastomers, the class of materials used for most automotive mounts and bushings. These articulations are often built with two metallic shells linked by elastomeric material. Figure 29 shows examples of two powertrain mounts that illustrate the mechanical stop and how the stiffness and resting positions are controlled by geometry.

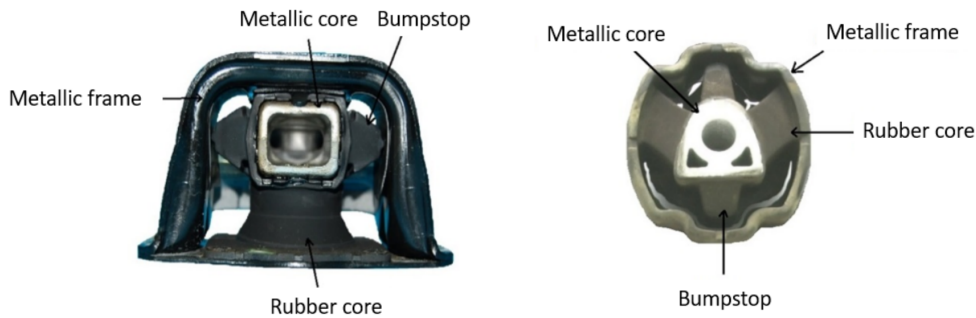


Figure 29: Examples of engine suspension mounts.

In terms of design, the most common practice is for the automobile manufacturer to define the desired stiffness, damping, structural interface and mainly fatigue life, while the supplier designs and tests the bushings and mounts. This means that the supplier normally has most of the knowledge on the part, though part of this knowledge is necessary to generate accurate system level behavior models.

The current procedure to model these mounts in multibody is to test the bushings and mounts in multiple directions and generate a 0D model for each direction, which are directly injected into the multibody model. Such approach, despite being very effective, presents a few issues: there is no consideration of transverse sensitivity, the nonlinearities are not fully characterized due to partial tests, the requirement of sample parts may be costly, there's no link between geometry and behavior, the choice of the 0D model has a direct impact on the modeled system behavior.

## Outline and contributions

The global thesis objective is to clarify strategies used to go from tests to accurate rubber mount models that can be used in multibody simulations. Figure 30 illustrates the declination into intermediate objectives: test design, model choice at the part or material level, model identification, optimization of model implementation for computational objectives, analysis of simulations in terms of performance metrics and other indicators such as material and modal dissipation that are not directly measurable.

The first step of model building is to obtain data that covers a sufficient range of behavior to be representative. The tests typically used to characterize both rubber as a material and rubber mounts are uni-axial relaxation, constant speed and sine tests. From these uniaxial tests, one classically builds 0D models which can be both used directly as a mount model for multibody simulation or indirectly to create a 3D material model later incorporated in a FEM model to account for both material and geometric effects in the mounts.

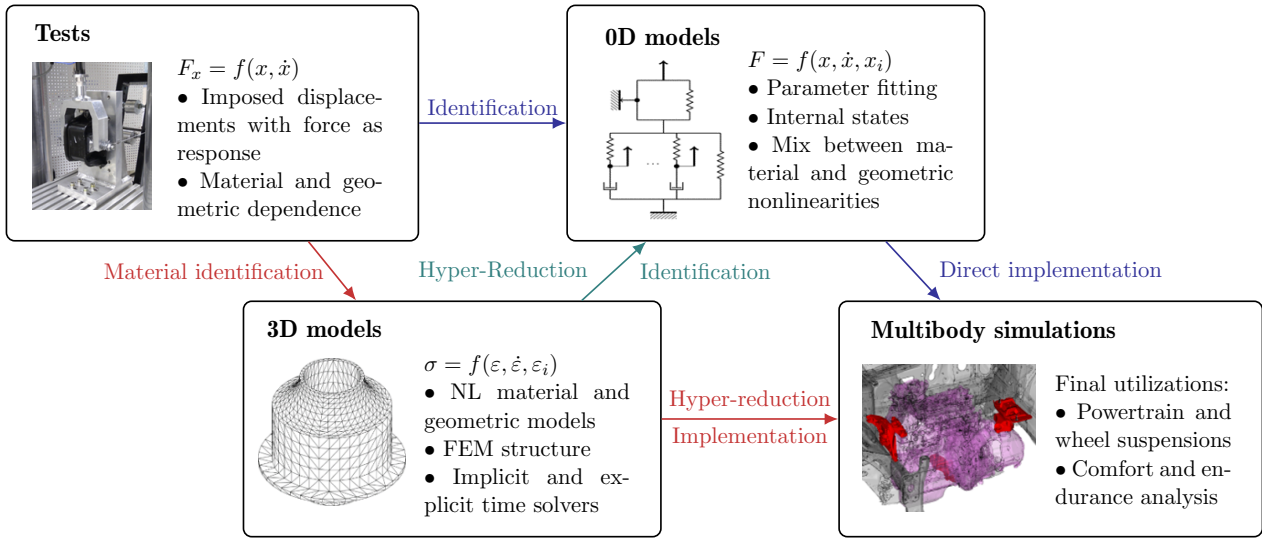


Figure 30: Strategies for the incorporation of rubber mounts and bushings models in multibody simulations.

Chapter 1 proposes a unified perspective on **system modeling of non-linear dissipative behavior** which applies to 0D models of both materials and bushings. Behavior is discussed in terms of three base contributions hyperelasticity, viscoelasticity and rate independent hysteresis, which are all non-linear when coupled. The key aspects of the discussion are the distinction between parametric and non-parametric approaches, the link between model order selection, internal states, and accuracy, and finally the analysis of order independent parametric models. The contributions are linked to the unified perspective which allows a classification of existing models, the novel uses of some tests: low speed triangular tests to characterize both the hyperelastic behavior and a non-parametric model for the hysteretic relaxation. The novel idea of instantaneous modulus extraction in sine tests, the selection of a model that appropriately represents the coupling between all three base behavior with a synthetic plot that illustrates behavior coupling and will be used for identification.

When uniaxial tests are performed to characterize a material, the next step is to develop a **3D constitutive material model** [6, 7] appropriate for finite element simulations which will allow separation of material and geometry effects in bushing simulations. Chapter 2 reviews the theory of continuum mechanics for finite strains and gives details on how the rubber material is represented by a non-linear hyperviscoelastic model. While this chapter mostly recalls established results, its contributions are a first documentation of the implementations in SDT [8] and extensions of novel propositions of chapter 1 to a model that captures amplitude and frequency dependence for finite strains.

With the selected order parametric models chosen, many practical aspects still need discussion. **Test campaigns** must be designed to gather knowledge on materials or parts. With an established test

campaign, **identification** methods are needed to obtain a model.

Chapter 3 describes the reasoning behind the design of the test campaign performed during this work, details its execution, and discusses two different identification campaigns: a classic approach, and a revised strategy based on the non-parametric curves introduced in chapter 1. Notable contributions are the campaign design, the analysis of the test results performed by the supplier Vibracoustic, the confirmation that both non-parametric and parametric models proposed earlier are relevant for material identification in traction and shear, and for bushing identification coupling both material and geometry effects.

When considering the lower branch of figure 30, the 3D models that combine non-linear material models and geometries of arbitrary complexity, simulation performance drives later uses. Direct use of a detailed mount model in a multibody simulation is at least 3 orders of magnitude slower than expected for multibody models and thus not applicable. Using the FEM model to identify a 0D model, is a possibility illustrated by the teal branch of the figure, but it suffers from the limitations of 0D models discussed earlier.

Chapter 4 thus demonstrates the feasibility of combining **kinematic reduction** and **hyper-reduction**, see the synthesis in [9] for example, to achieve high performance 3D model evaluations that would be compatible with multibody simulations and yet still be based on an arbitrary non-linear material model and detailed FEM geometry. Contributions are details on the implementation of finite strain non-linear material models in SDT, expression of kinematic and hyper-reduction techniques in terms of observation and command matrices allowing a very generic implementation of hyper-reduction developed during this thesis, and finally performance and extrapolation accuracy illustrations on a twist beam axle bushing test case.

Chapter 5 addresses **multibody simulations**, the end objective of figure 30. This is where system level assessments are made using the identified 0D models and/or the hyper reduced models and contributions are linked to the analysis of test cases.

A first test case, the stop/start simulation of an engine resting on rubber mounts, illustrate the need to accurately model dissipation, as classical equivalence for harmonic response give notably different transients and modal energy contributions. This illustration, while shown at the thesis end, was very important in developing the discussions of parametric models in chapter 1. It is detailed here to emphasize the need to analyze the notion of stored and dissipated energy for proper model validation.

A second case with a full vehicle multibody simulation is also presented, and data on the rear twist beam axle bushing (whose model and test were discussed in earlier chapters) is gathered. While multibody simulation with the new bushing models could not be obtained due to lack of time, load and power predictions are used to demonstrate that the current approach can already be shown to be

insufficient for accurate transient modeling of system level behavior.

Despite detailing each part of the problem in each chapter, the chronological order of the study was quite different, and directly impacted the direction of the work. After the review of a few 0D models, the multibody engine suspension case was analyzed and emphasized the needs on the accuracy of predicting dissipation at different instants, since two seemingly equivalent models led to notably different system level predictions. Design of the test campaign had to be performed with the available information and, with post-processing strategies radically different from those classically used, the test data proved to be quite relevant. While finding a partner able to test a part and the associated materials, Vibraoustic eventually, and waiting for the experiment to take place during the COVID crisis, the focus was placed on 3D material modeling and implementing a hyper-reduction strategy mixing kinematic reduction and reduced integration, and eventually showing that it would be possible to use it in a multibody routine. With the detailed analysis of test results, the need for a major effort on giving a clear perspective on 0D/material modeling, changed the focus once again and limited the time left for extended multibody analysis and confrontation of 0D and 3D hyper-reduced models.

The developments of chapter 1 correspond to a paper submitted to MSSP [3]. The chapter 4 implementation of hyper-reduction routines on the bushing model was presented at the ISMA 2020 conference [4]. Finally the first multibody study case of chapter 5 was presented at the ECCMR 2019 conference [5].



# Chapter 1

## 0D system models of bushings

### Contents

---

<b>1.1</b>	<b>Introduction</b>	<b>60</b>
<b>1.2</b>	<b>Hyperelasticity or non-linear static gain</b>	<b>62</b>
1.2.1	Instantaneous modulus	64
<b>1.3</b>	<b>Viscoelasticity</b>	<b>65</b>
1.3.1	Non-parametric transfer: complex and relaxation modulus	67
1.3.2	Selected order base representation: rational complex modulus	68
1.3.3	Order independent parametric models : fractional derivatives	71
<b>1.4</b>	<b>Rate independent hysteresis</b>	<b>73</b>
1.4.1	A non-parametric model: hysteretic relaxation	74
1.4.2	Selected order base representations : Iwan series model	76
1.4.3	Order independent parametric forms	79
1.4.4	Regularity in first order hysteretic cells	81
<b>1.5</b>	<b>Unified perspectives through environmental factors</b>	<b>82</b>
1.5.1	Classical temperature modeling	83
1.5.2	Intermediates between viscoelasticity and rate independent hysteresis	84
1.5.3	Combined behavior	86
<b>1.6</b>	<b>Experiment design perspectives and conclusions</b>	<b>88</b>

---

## 1.1 Introduction

The current approach for modeling elastic articulations is through testing and model identification. Identification is the usual name describing an inverse problem where a class of models is chosen and the associated values are selected to minimize a distance between test results and the model predictions. The test results used to illustrate this chapter were taken from test campaigns detailed in chapter 3, where the legends are also described. The main purpose behind the tests was to determine and separate as much as possible the different mechanisms that will be described here.

To illustrate the different kind of identifications and models, three base mechanisms are known to be important in rubber mount behavior [10, 11], and will be taken as references:

- **Hyperelasticity**, or the non-linear dependence of long term stress to the current value of strain;
- **Viscoelasticity**, or the dynamic dependence of stress on strain history;
- A last effect for which there is no consensus on whether it should be classified as a long term effect, or, as will be portrayed here as **rate independent hysteresis**, characterizing the dependence of stress to the strain path

Eventually, hyperelasticity, viscoelasticity and rate independent hysteresis are coupled. Figure 1.1 illustrates what the model should represent. The underlying hyperelastic behavior is visible as a thick red line. To that value a first additional stiffness contribution is associated with hysteretic behavior, visible as the green dashed hysteretic relaxation modulus that will be defined in section 1.4.1 and is derived from low speed triangular tests. Finally, sine testing leads to small colored maps (from low frequency in blue to high frequency in yellow) showing complex moduli measured through stepped sine tests and demonstrating further increase of modulus due to viscosity.

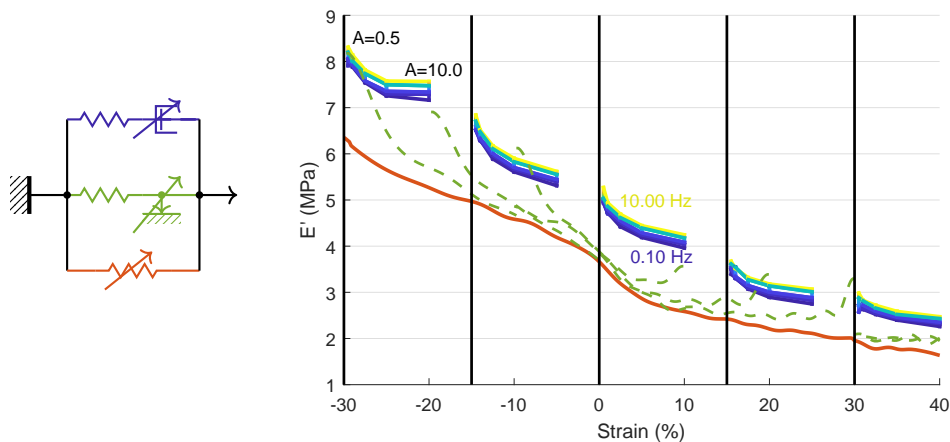


Figure 1.1: Tangent hyperelastic stiffness, hysteretic relaxation modulus, viscoelastic complex modulus

Beyond the three mechanisms, one will here distinguish non-parametric identification, where the model is described by a curve whose values can be derived from test, and parametric identification where the curve is described as a functional form using a finite number of parameters.

*Parametric* models are also often used in system dynamics with multiple forms of interest: rational fractions, pole-zero representations, state space models for which bidirectional transforms exist. In viscoelasticity, classical parametric forms are the generalized Maxwell, which is a subset of rational fractions (see [12] for example), and fractional derivative models (see [13]). While both are often considered as separate models, section 1.3.3 will sustain the argument that finite horizon approximations of the fractional derivative model (such as the Grünwald approximation [14, 15]) has an explicit expression as rational fractions. The fractional derivative model can thus be seen as an order independent parametrization of a subclass of Maxwell models. The literature in rate independent behavior is very rich from the mathematical point of view (see [16]), while low order parametric hysteretic models are often more specific implementations, such as the STS model for rubber mounts [17], and four parameter Iwan model for bolted joints proposed by Segalman [18].

Parametric forms have the advantage of being *high resolution*, meaning that they can be used to build non-parametric models with any degree of accuracy (frequency or time resolution). The inverse transformation from non-parametric to parametric models is called *identification* and is a numerical process that requires a choice of the parametric form and an optimization process to estimate the parameters. This work also distinguishes two forms of parametric models: selected order and order independent.

Selected order models are simpler to implement, as they are represented by an assembly of basic components and one may choose as many as the accuracy requires. Order independent models are normally based on physical assumptions of the material, thus, with a predefined type of behavior, they demand less data and less parameters for identification and may be used to extrapolate data. Despite the advantages, inconsistency with data will induce bias and thus be problematic. Model order and accuracy in the representation of the non-parametric data are also classical discussions which will be seen as a discretization problem.

This chapter will take a close look at the modeling of rubber bushings. For models assumed to represent a single material point, one will say that stress  $\sigma$  is a function of strain  $\varepsilon$  history. For models representing a macroscopic object, force  $F$  will be a function of displacement  $x$  and its history. It is assumed for now that the system stress and strain are scalar quantities (hence, the 0D denomination) and handling of cases where this is not true will be discussed in later chapters. One will also then seek to decouple geometric and material effects.

Section 1.2 shows that for every test there is a non-linear backbone that is attributed to hyperelastic effects, and also provides a manner to extract instantaneous modulus from sine tests which reinforce the idea of a hyperelastic behavior.

Section 1.3 reviews classic definitions of viscoelastic behavior and illustrates different features from these definitions, such as behavior in frequency domain and time domain implementation. Coupling with hyperelasticity is shown to be necessary to achieve reasonable representation.

Section 1.4 uses classical rules proposed by Madelung and Masing to describe rate independent hysteresis to motivate a non parametric model of hysteresis where force is obtained by integration of a hysteretic relaxation curve which is shown to be measurable in experiments. High and low order parametric models are then introduced and identification procedures are discussed.

Section 1.5, based on the structural temperature theory, provides perspectives unifying all the three behaviors, and illustrate methods used to take into account those variables.

Section 1.6 summarizes the conclusions from the previous sections and directs them towards test campaign design.

## 1.2 Hyperelasticity or non-linear static gain

Rubber materials may undergo very intense deformations. Linear elasticity (or constant static gain in LTI systems terminology) may not be suitable. It may be very hard to isolate an elastic backbone curve, but it is present in every test that is made.

Hyperelasticity may be characterized by multi-step relaxation tests [19], partially illustrated in figure 1.2 left. On the right part of the figure, another part of the test is illustrated along with other extractions of hyper-elasticity. The tests are further detailed in section 3.2. At the end of each step, one waits a *long time* (60 minutes, in this case) to obtain a reasonable estimate of the long term/low frequency elastic behavior. One can thus extract an asymptotic behavior shown in red in the right part of the same figure. However, the points on the upward and downward part of the experiment do not perfectly coincide. There is thus, either a path effect or a long term effect, which can be represented by either rate independent hysteresis or extremely slow relaxation, respectively. From this experiment, one identifies a 0D model simply given by a force/displacement curve, which combines both geometric and material effects, whose separation will be considered in chapter 4.

## 1.2. HYPERELASTICITY OR NON-LINEAR STATIC GAIN

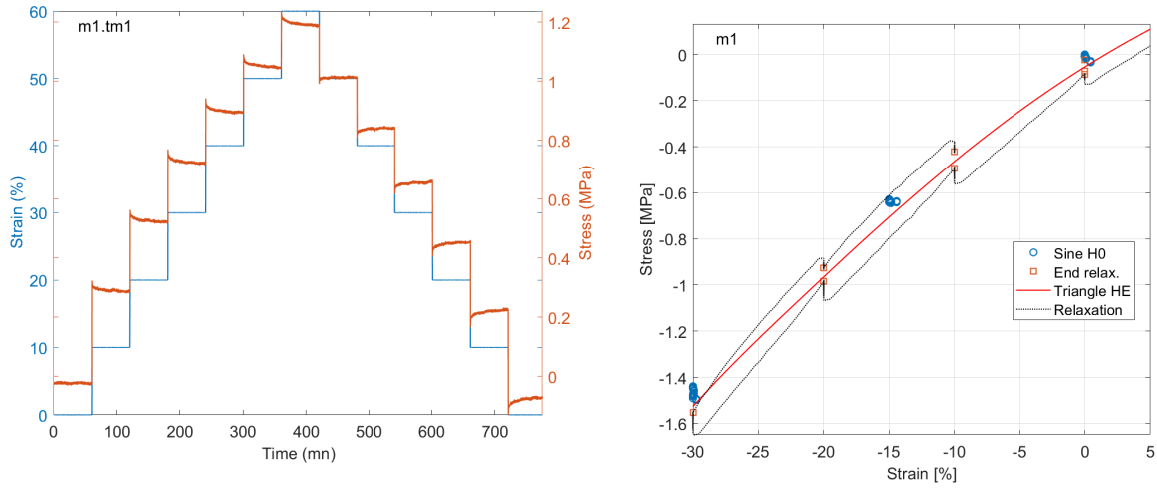


Figure 1.2: Left: Multi-step test profile and response. Right: Extracted hyperelastic behavior.

To illustrate the idea, sine or constant speed tests, which will also be detailed in section 3.2, illustrated in figure 1.3, the backbone is still clearly given by the hyperelastic behavior shown in red, despite the fact that those tests are designed to capture dynamic effects, which are visible in sine tests, specifically on the slopes higher than the backbone curve, and the rate-independent dissipation, present on the low speed triangular test, given by the surface defined by the loading and unloading phases. The compression end of the triangular tests is detached from the triangular one as it is only an extrapolation of multi-step tests.

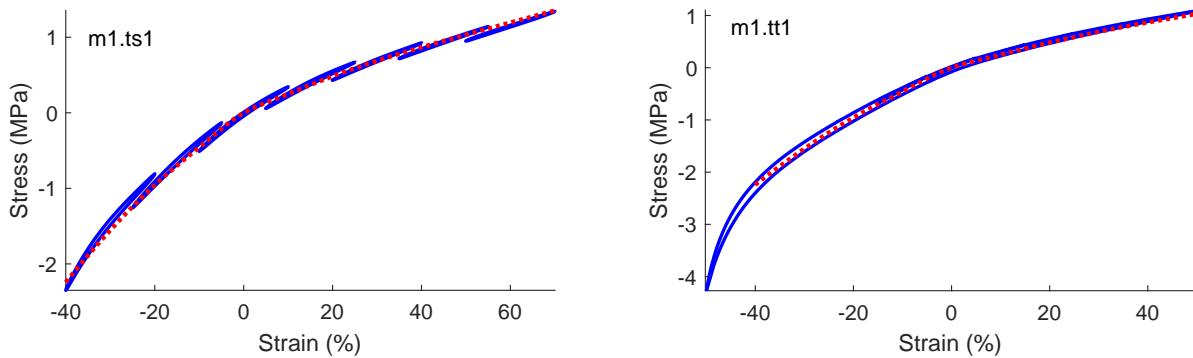


Figure 1.3: Left: stress/strain response of sine tests. Right: stress/strain response for triangular tests.

The points extracted may be seen as a non parametric representation of the hyperelastic behavior. A parametric representation would be the interpolation of those points with a polynomial or any other function. For 3D models, as will be shown in section 2.3, the parametric representations are based on polynomials of the invariants of the strain tensor.

### 1.2.1 Instantaneous modulus

For sine testing, the linear viscoelastic model is associated with the complex modulus (1.4), where the the time response of a signal containing harmonics 0 and 1 of  $\omega$  is of the form

$$u(t) = u_0 + \Re\left(u_1(\omega)e^{i\omega t}\right) = u_0 + \Re(u_1(\omega)) \cos(\omega t) - \Im(u_1(\omega)) \sin(\omega t), \quad (1.1)$$

where  $\Re$  denotes the real part and  $\Im$  denotes the imaginary part. If the system is linear time invariant, one can classically obtain the harmonic 1 coefficients  $u_1(\omega)$  through the mean over one period  $\Re(u_1(\omega)) = \int_0^{2\pi/\omega} 2u(t) \cos(\omega t) dt$ . Here however, the hyperelasticity is non-linear and the classic approach would be to consider harmonic balance where the signal would be composed of harmonics  $e^{ik\omega t}$ . But here, the point of view that the response is linear time-varying will be taken. One thus defines a zero mean signal

$$\bar{u}(t) = u(t) - \frac{\omega}{2\pi} \int_0^{2\pi/\omega} u(t) dt \quad (1.2)$$

and builds a sliding window of  $N$  points computing the instantaneous complex amplitude of a signal by solving the linear least squares problem

$$\min_{u_1(t_1)} \left\| \begin{bmatrix} \cos(t_1) & -\sin(t_1) \\ \vdots & \vdots \\ \cos(t_N) & -\sin(t_N) \end{bmatrix} \begin{Bmatrix} \Re(u_1(\omega)) \\ \Im(u_1(\omega)) \end{Bmatrix} - \begin{Bmatrix} \bar{u}(t_1) \\ \vdots \\ \bar{u}(t_N) \end{Bmatrix} \right\| \quad (1.3)$$

The instantaneous complex modulus is then obtained as the ratio  $E(\omega, t_1) = \sigma(\omega, t_1)/\varepsilon(\omega, t_1)$ . This approach is quite sensible to sampling and for current work, a quarter cycle window size was chosen. Residual of the minimization may also be taken to measure the approximation quality.

Figure 1.4 illustrates that cycles on the left are associated with stiffness variations on the right with these providing more information on the nonlinear behavior of the material combining both hyperelasticity and the Payne effect. It also clearly illustrates that the material cannot be considered as linear time invariant. The instantaneous complex stiffness also illustrates very well that the complex modulus is almost always higher than the hyperelastic modulus shown as a black dotted line.

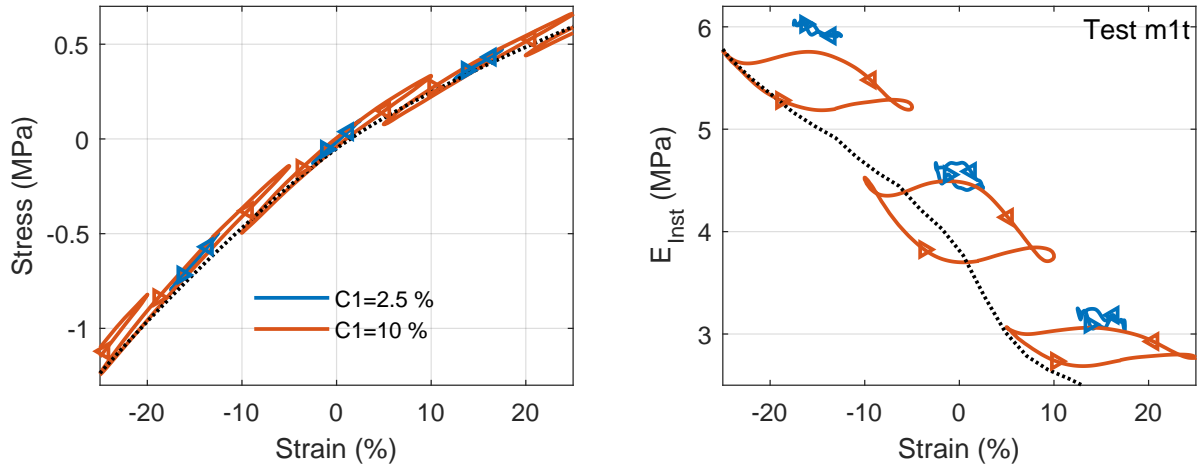


Figure 1.4: Amplitude dependence on uniaxial test for different amplitudes and preloads.

In terms of behavior, the modulus curve is at a maximum right after turning point due to the hysteretic relaxation, and starts to drop as it goes far from the turning point. Around the middle of the cycle, the stiffness rise again, as viscoelastic effects are more intense due to highest speeds. Towards the end of the cycle, the stiffness rise again due to the hysteretic effect of the turning point being anticipated through the sliding window.

### 1.3 Viscoelasticity

Dynamic dependence on strain history is first assumed to be linear. This is called viscoelasticity in the materials community and Linear Time Invariant (LTI) system in the control community. LTI systems have many equivalent representations. In particular, one distinguishes:

- Continuous time differential equations;
- Their transformation frequency domain transfers in the form of rational fractions characterized by their poles and zeros, or using the partial fraction expansion as a sum of first order rational fractions with associated gains;
- The inverse transform of the transfer function is a time domain impulse response and this can be exploited using convolution products;
- When performing numerical integration with a fixed time step, the  $z$ -transform (discrete time) of the transfer corresponds to a recursion equation with a finite number of steps

### 1.3. VISCOELASTICITY

The direct output of tests are *non parametric* representations that characterize LTI systems either through frequency dependent *transfer functions*, called *complex modulus* in the viscoelastic material literature [20]

$$\sigma(\omega) = E(\omega)\varepsilon(\omega) \quad \text{or} \quad F(\omega) = K(\omega)x(\omega) \quad (1.4)$$

or their inverse Fourier transform, known as a time domain impulse response, which corresponds to the time derivative of the relaxation function [21], as will be further detailed in section 1.3. Figure 1.5 left illustrates the time response of a step relaxation test extracted from the multi-step test. Figure 1.5 center, the amplitude of the corresponding estimated transfer ratio of frequency response of stress and strain. Naturally, the storage modulus increase with the frequency, while the decreasing loss factor indicates that the glass transition is located in frequencies/temperatures further below the analyzed transfer. The last part of the same figure corresponds to the classical characterization of complex moduli using sine testing in DMA (Dynamic Mechanical Analysis), which is only one of many possible approaches to characterize complex modulus. The dotted red line in figure 1.5c illustrates the fact that hyperelasticity and viscoelasticity are coupled as the slope of harmonic loops are clearly dependent on the static strain.

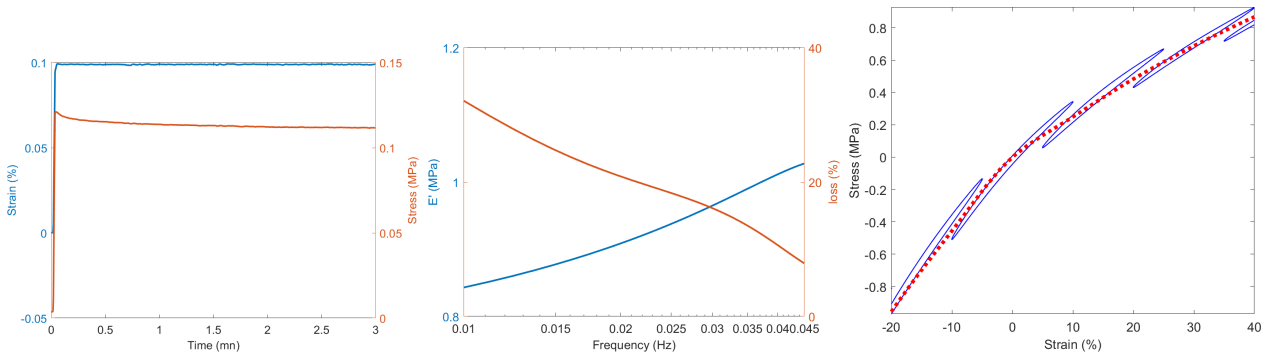


Figure 1.5: Left: Stress relaxation for a strain step. Center: Estimated transfer or complex modulus. Right: Sine testing with different initial strains.

Since relaxation functions and complex moduli are Fourier transform pairs, any experiment made at twice the speed should shift the input spectrum to twice higher frequencies and thus modify the response. Low speed triangular tests, shown in figure 1.6 indicate that the stress/strain trajectory is almost insensitive to speed. At low speeds, one still sees a behavior that differs from hyperelasticity but that does not correspond to viscoelasticity: rate-independent hysteresis. Section 1.4, will introduce a novel non-parametric representation of hysteresis, called the hysteretic relaxation modulus, which will be used to analyze low speed triangular tests where hysteresis plays a very important role.

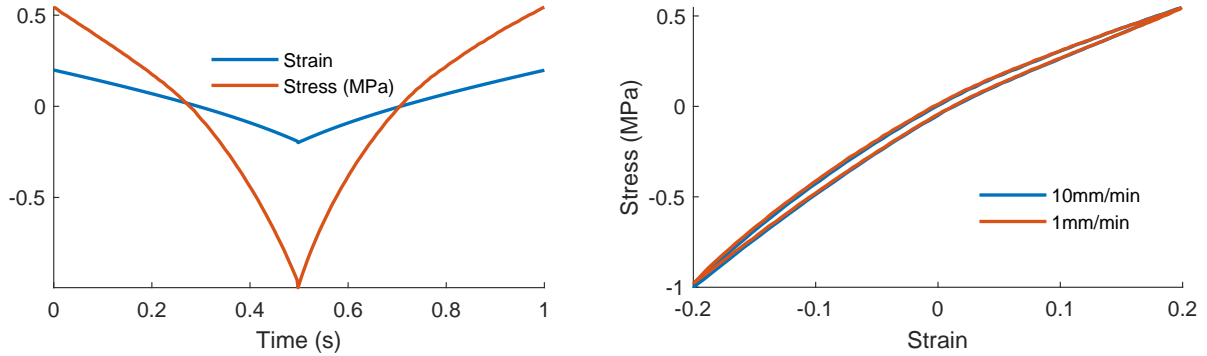


Figure 1.6: Triangular tests

In this section, the theory of viscoelasticity is reviewed and applied to macroscopic 0D models. First, the non parametric representation known as complex modulus is analyzed in a system perspective, then the transition to a selected order parametric model - rational fraction or Maxwell model - is detailed with its different implementations in frequency and time-domain. Finally an order independent model - the fractional derivative model - is presented, and discretization issues are discussed. Extension to 3D models will be illustrated in section 2.4.

### 1.3.1 Non-parametric transfer: complex and relaxation modulus

Three equivalent representations of viscoelasticity are considered: a transfer function in the frequency domain (1.5), an impulse response associated with convolution (1.6) or a differential equation in the time domain (1.11). In material analysis, the transfer is called complex modulus and one has

$$\sigma(\omega) = E(\omega)\varepsilon(\omega) = E'(\omega)(1 + i\eta(\omega))\varepsilon(\omega) = |E(\omega)| e^{i\delta} \varepsilon(\omega). \quad (1.5)$$

where the complex modulus may also be separated in its real part  $E'$  and its complex part  $E''$ , respectively named storage and loss modulus, and the loss factor  $\eta = E''/E' = \tan(\delta)$  is used here preferably to the transfer phase  $\delta$ .

Estimation of linear transfers is a classical process [22], which can be performed using broadband signals (impulse response) or stepped sine testing which is the classical approach in Dynamic Mechanical Analysis (DMA) tests. Estimation of transfers at a set of frequencies is called *non-parametric* in the sense that it only gives the estimate of the complex modulus at a selected set of frequencies.

The inverse Fourier transform of the complex modulus is the relaxation modulus

$$E(t) = R'(t) = \mathcal{F}^{-1}\{E(\omega)\} = \frac{1}{2\pi i} \int_{-\infty}^{+\infty} E(\omega) e^{i\omega t} d\omega, \quad (1.6)$$

which can be measured directly through relaxation testing. The relations between stress and strain can be obtained through convolution of either strain with relaxation modulus or strain rate with relaxation

function

$$\sigma(t) = \int_{-\infty}^{+\infty} E(t-r)\varepsilon(r)dr = \int_{-\infty}^{+\infty} R(t-r)\dot{\varepsilon}(r)dr \quad (1.7)$$

To ease handling of initial conditions, classical texts on viscoelasticity [21] use the Laplace-Carson transform and the relaxation function  $R(t)$ , but the Laplace transform can be used for  $E(t)$ .

The direct use of such curves is not very easy in transient simulation since it requires alternating between time and frequency domain, which is a very strong reason to prefer parametric models. Any system identification textbook will describe parametric models in terms of differential equations in time or rational fraction representations of transfers. But since viscoelasticity term comes from material modeling, the process is called rheologic modeling and will be detailed next.

### 1.3.2 Selected order base representation: rational complex modulus

Rational fraction representations of transfers are, in the frequency domain, classically characterized by poles  $p^i$  and zeros  $z^i$ , or separated in a sum of first order rational fractions with constant numerators called residues and first order denominators associated with poles.

$$K(s) = \frac{F(s)}{x(s)} = K^0 \prod_{i=1}^N \frac{1 - s/z^i}{1 - s/p^i} = K^\infty \left( 1 + \sum_{i=1}^N \frac{-g^i}{s/\omega^i + 1} \right) = K^\infty \left( g^0 + \sum_{i=1}^N g^i \frac{s}{s + \omega^i} \right). \quad (1.8)$$

In the present case, all the poles must have its real part negative, so the system is stable. They are thus associated with a characteristic time  $\tau^i = -2\pi/\omega^i$ , the low frequency asymptotic gain is noted  $K^0$ , the high frequency asymptote is noted  $K^\infty$  and the residue associated with each pole is expressed as fractions of the high frequency gain  $K^i = g^i K^\infty$ .

These two equations imply that there are two different manners to see the problem: either in total force, or in force rate, corresponding to the middle and the right parts, respectively.

In mechanics this standard LTI model is known as the generalized Maxwell model illustrated in figure 1.7, where the total load is the sum of a series of forces

$$F = \sum_{i=0}^N F^i, \quad (1.9)$$

each associated with a first order *relaxation equation* which contributes with a gain increase and dissipation maximum centered at the pole frequency. The gain increase is illustrated in figure 1.7 right, where the poles are put in increasing frequency, accordingly to the legend. This might as well be seen as the time domain differential equation equivalent to the frequency formulation stated above, and each equation corresponds to the equilibrium of the internal cell point  $F^i = c^i \dot{x}^i = K^i(x - x^i)$  and is classically given in terms of displacement,

$$\frac{c^i}{K^i} \dot{x}^i = \frac{\dot{x}^i}{\omega_i} = (x - x^i) \quad (1.10)$$

### 1.3. VISCOELASTICITY

but can also be written in terms of relaxation loads to be removed from the high frequency asymptotic force, as in the middle form of equation (1.8), leading to

$$\frac{\dot{F}^i}{\omega^i} + F^i = -g^i F^\infty(x) = -g^i K^\infty(x)x, \quad (1.11)$$

or written as loads added to low frequency asymptotic force, as in the last form of (1.8), leading to a load rate relaxation

$$\dot{F}^i + \omega^i F^i = g^i \dot{F}^\infty(x) = g^i K^\infty(x)\dot{x}. \quad (1.12)$$

The displacement formulation, given by center and right parts of equation (1.10) does not provide a simple manner to couple viscoelasticity to hyperelasticity, whereas the force formulations highlight the potentially nonlinear static gain term  $F^\infty(x)$ , or equivalently  $K^\infty(x)$ . The utilization of the variable or its rate for the formulation generates differences when the static gain is nonlinear. The fact that static gain multiplies  $\dot{x}$  instead of  $x$  in force rate formulation generates differences if using a non-linear expression. In terms of dissipation, the fact that  $\omega^i$  is always constant (meaning that  $K^i$  and  $c^i$  are not constant when using nonlinear static gain) implies that the loss modulus does not evolve with amplitude. Eventually, analysis of instant complex moduli in section 1.5.3, will show that the force rate formulation is the most relevant for building other nonlinear models, despite being a less usual formulation.

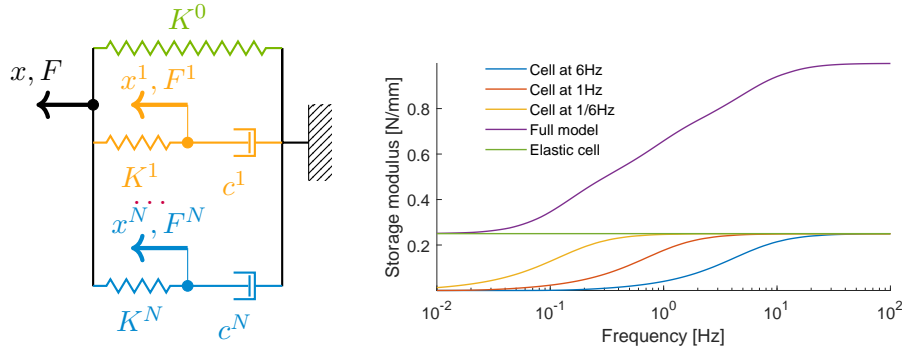


Figure 1.7: Generalized Maxwell model with linear components and associated frequency domain response.

*Order* refers to equivalent notions of number of Maxwell cells, number of poles in the model, or number of internal states. The relation between  $K^i, c^i$ , poles and zeros is given in the appendix of [12].

The term *selected order* is used here to emphasize the fact that identification of a Maxwell model should be viewed as a discretization problem. The modulus as a increasing function of frequency, the poles  $p^i = -2\pi/\tau^i$  are real and negative, and the rational fraction gains  $g^i K^\infty$  are positive. Renaud & al. [12] give a clear overview both graphical and numerical methods used for complex modulus

### 1.3. VISCOELASTICITY

approximation methods. Of particular interest, is the discussion that poles can be placed arbitrarily and the model accuracy is dependent on the number of poles per decade.

To illustrate the discretization argument, it is chosen to discretize the storage modulus interval and place poles accordingly. In figure 1.8, the order 4 model, illustrates the fact that low order models are less accurate on storage modulus and loss factors. Even though the 30% error on loss may appear poor for the order 4 model, the need for more accuracy is actually debatable considering all the other unknowns. In the end, our design rule is to use more than one pole per decade.

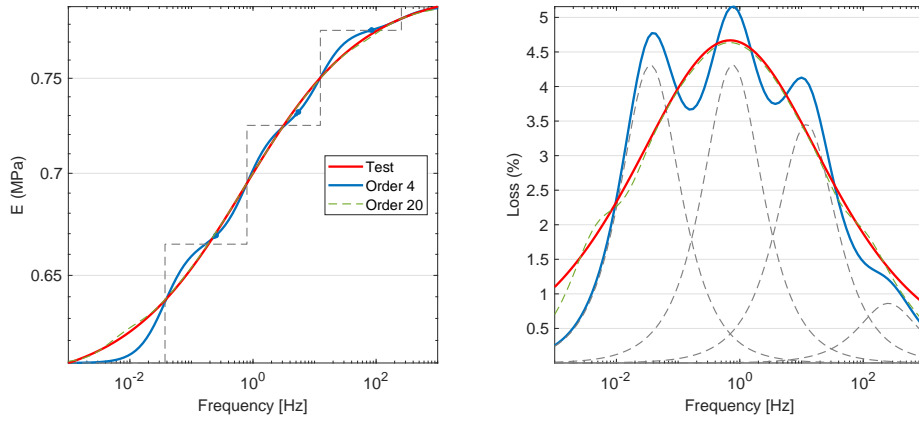


Figure 1.8: Impact of order on accuracy of storage modulus and loss factor

Time implementation comes through integration schemes. Using a fixed explicit time scheme based on the load relaxation equation (1.11), a first order *recursion equation* is given by

$$F_n^i = (1 - \omega^i \Delta t) F_{n-1}^i - \omega^i g^i \Delta t (F_n^\infty). \quad (1.13)$$

Applying the  $\mathfrak{z}$  transform (discrete time) to this scheme, one obtains.

$$\frac{F^i}{F^\infty}(\mathfrak{z}) = g^i \frac{-\omega^i}{1 - (1 - \omega^i \Delta t)\mathfrak{z}^{-1}}, \quad (1.14)$$

which means that the pole is given by  $1 - \omega^i \Delta t$ , and implies that the scheme becomes unstable for any  $\omega^i \Delta t \geq 1$ .

To find a more accurate integration scheme, one may depart from the *convolution form* of the problem, and from its solution, apply a recursive scheme and a trapeze rule to integrate forces leading to the second order accurate scheme given by

$$F_n^i = e^{-\omega^i \Delta t} F_{n-1}^i - \omega^i g^i \Delta t e^{-\frac{\omega^i \Delta t}{2}} \frac{F_n^\infty + F_{n-1}^\infty}{2} \quad (1.15)$$

which has the  $\mathfrak{z}$ -domain pole  $e^{-\omega^i \Delta t}$ , which is always stable, but may present numerical conditioning problems when too close to zero.

The alternative based on load rate relaxation (1.12) leads to a slightly different recursion,

$$F_n^i = (1 - \omega^i \Delta t) F_{n-1}^i + g^i (F_n^\infty - F_{n-1}^\infty). \quad (1.16)$$

As the term multiplying  $F_{n-1}^i$  is the same as the one in the previous scheme, the pole in the  $\mathfrak{z}$  domain is unchanged as the constraint  $\omega^i \Delta t < 1$ .

Again, to find the second order accurate scheme, one may use the same procedure to obtain

$$F_n^i = e^{-\omega^i \Delta t} F_{n-1}^i + g^i e^{-\frac{\omega^i \Delta t}{2}} (F_n^\infty - F_{n-1}^\infty). \quad (1.17)$$

### 1.3.3 Order independent parametric models : fractional derivatives

Fractional derivatives [20] are known to use a low number of parameters to represent viscoelastic behavior in broad bands. In such model, the differential equation describing a dissipative cell is expressed as

$$F + \frac{1}{\omega_c^\alpha} \frac{d^\alpha F}{dt^\alpha} = K^0 x + \frac{1}{\omega_c^\alpha} K^\infty \frac{d^\alpha x}{dt^\alpha}. \quad (1.18)$$

This equation in the Laplace domain is expressed by

$$\left(1 + \left(\frac{s}{\omega_c}\right)^\alpha\right) F(s) = \left(K^0 + \left(\frac{s}{\omega_c}\right)^\alpha K^\infty\right) x(s), \quad (1.19)$$

giving a direct expression for the complex modulus,

$$K(s) = K^\infty + \frac{K^0 - K^\infty}{1 + (s/\omega_c)^\alpha}, \quad (1.20)$$

with expressions of storage and loss moduli,

$$\begin{aligned} K'(\omega) &= \frac{K^0 + (K^\infty + K^0)(\omega/\omega_c)^\alpha \cos(\frac{\pi\alpha}{2}) + K^\infty(\omega/\omega_c)^{2\alpha}}{1 + 2(\omega/\omega_c)^\alpha \cos(\frac{\pi\alpha}{2}) + (\omega/\omega_c)^{2\alpha}} \\ K''(\omega) &= \frac{(K^\infty - K^0)(\omega/\omega_c)^\alpha \sin(\frac{\pi\alpha}{2})}{1 + 2(\omega/\omega_c)^\alpha \cos(\frac{\pi\alpha}{2}) + (\omega/\omega_c)^{2\alpha}} \end{aligned} \quad (1.21)$$

Storage and loss moduli for different values of  $\alpha$  are illustrated in figure 1.9. For smaller  $\alpha$ , the stiffness increase and loss peak bandwidth increases. The transition between  $K^0$  and  $K^\infty$ , now has a bandwidth dependent on the shape parameter  $\alpha$  and is thus independent of model order.

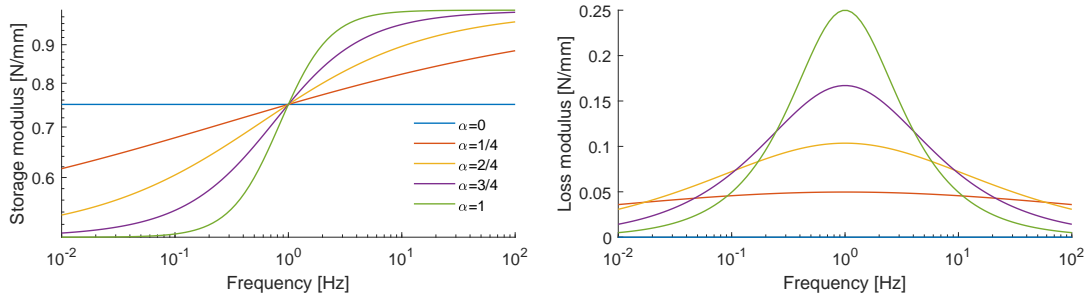


Figure 1.9: Storage and loss moduli evolution for fractional derivative model.

### 1.3. VISCOELASTICITY

---

Despite the advantage of using a low number of parameters, the implementation of such model in time domain is more complicated, as by definition, fractional derivatives require a full convolution to be computed, as the Riemann-Loiouville definition is expressed as

$$\frac{d^\alpha f(t)}{dt^\alpha} = \frac{1}{\Gamma(1-\alpha)} \frac{d}{dt} \int_0^t \frac{f(r)}{t-r} dr. \quad (1.22)$$

There are different approximations to estimate the fractional derivative value, and one of them is Grünwald approximation [14]

$$\frac{d^\alpha f(t)}{dt^\alpha} \approx \left(\frac{t}{N}\right)^{-\alpha} \sum_{j=0}^N A_{j+1} f(t-j\Delta t), \text{ with } A_j = \frac{\Gamma(j-\alpha-1)}{\Gamma(-\alpha)\Gamma(j)}, \quad (1.23)$$

with  $\Gamma$  the gamma (continuum factorial) function. Considering fixed values for  $\Delta t$ , one obtains a summation over values with a fixed delay, and it becomes interesting to analyze this model in the  $\mathfrak{z}$  domain. Applying equation (1.23) to (1.18), and the  $\mathfrak{z}$ -transform, one obtains

$$\left(1 + c \sum_{j=0}^N A_{j+1} \mathfrak{z}^{-j}\right) F(\mathfrak{z}) = \left(K^0 + K^\infty c \sum_{j=0}^N A_{j+1} \mathfrak{z}^{-j}\right) x(\mathfrak{z}), \quad (1.24)$$

with  $c = (\omega_c \Delta t)^{-\alpha}$ . Then, separating the ratio between force and displacement, one reaches to the polynomial transfer function

$$\frac{F}{x}(\mathfrak{z}) = \frac{K^0 + \sum_{j=0}^N (K^\infty c A_{j+1}) \mathfrak{z}^{-j}}{1 + \sum_{j=0}^N (c A_{j+1}) \mathfrak{z}^{-j}}, \quad (1.25)$$

Using any discrete to continuous approximation, such as Tustin transform  $\mathfrak{z} = \frac{1+s\Delta t/2}{1-s\Delta t/2}$ , it is possible to return to Laplace domain with a transfer function in the form

$$\frac{F}{x}(s) = K_0 \prod_{j=1}^N \frac{1-s/z^j}{1-s/p^j}, \quad (1.26)$$

where  $z^i$  and  $p^i$  the zeros and poles from the transfer function. The poles and zeros from this equation determine the fractions  $g^i$  and the characteristic frequencies  $\omega^i$  from the equivalent Maxwell model. It is also possible to affirm that the number of time steps used for the approximation is equivalent to the number of cells of the equivalent Maxwell model and thus, equivalent to the order of the model of (1.8).

Figure 1.10 illustrates the response of the equivalent Maxwell model of the Grünwald's approximation for a fractional derivative and the analytic response. It is clear that there is a narrow band defined by  $\Delta t$  and  $N\Delta t$  where the approximation is appropriate. Placing poles graphically around the fractional derivative curve might thus be a more effective manner to implement such model.

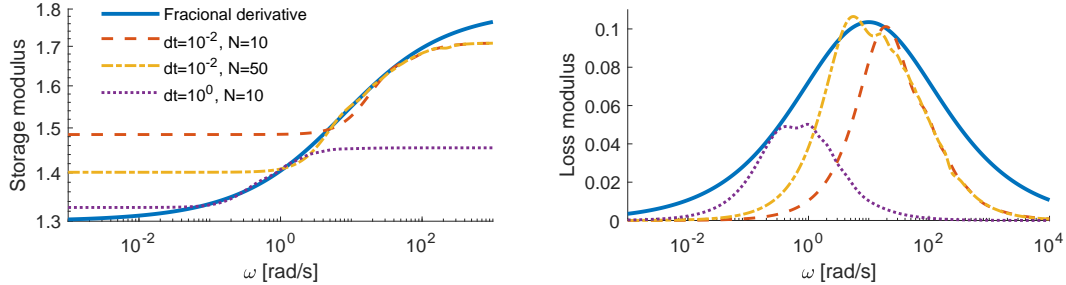


Figure 1.10: Numeric implementation of truncated Grünwald's approximation of a fractional derivative model.

This section has made a broad overview on viscoelasticity and its relation with system modeling. The difference between selected order and order independent models was detailed as a discretization problem, as the first may always represent the second one to any degree of accuracy. The different formulations, which are equivalent for linear elasticity are will differ when coupled with nonlinear elasticity. The force rate form (1.12) will be shown to be more appropriate in section 1.5.3.

As stated in section 1.1, viscoelasticity is not the only mechanism that drives dissipation, so the development of the same formalism for a position dependent dissipation will be made in the next section.

## 1.4 Rate independent hysteresis

Hysteresis is a system model assumption where stress is assumed dependent on strain history. As this definition is broad enough to fit viscoelastic effects, here, hysteretic behavior will refer to the effects that depend only on the system position and not on the deformation rate, hence, the term *rate independent hysteresis*. For the applications in the present work, hysteresis will always be associated to the force/displacement, or stress/strain.

As an example, figure 1.11 illustrates a low speed triangular test. Right after the turning point, one first has a relaxation phase with a tangent modulus higher than the hyperelastic one. Such relaxation will be referred as *hysteretic relaxation*. More details on the test are given in chapter 3. This is then followed by a relaxed phase where the tangent stiffness closely matches the hyperelastic response, shown as solid lines. The match is not perfect since this is test data and some integration is involved as will be detailed in section 1.4.

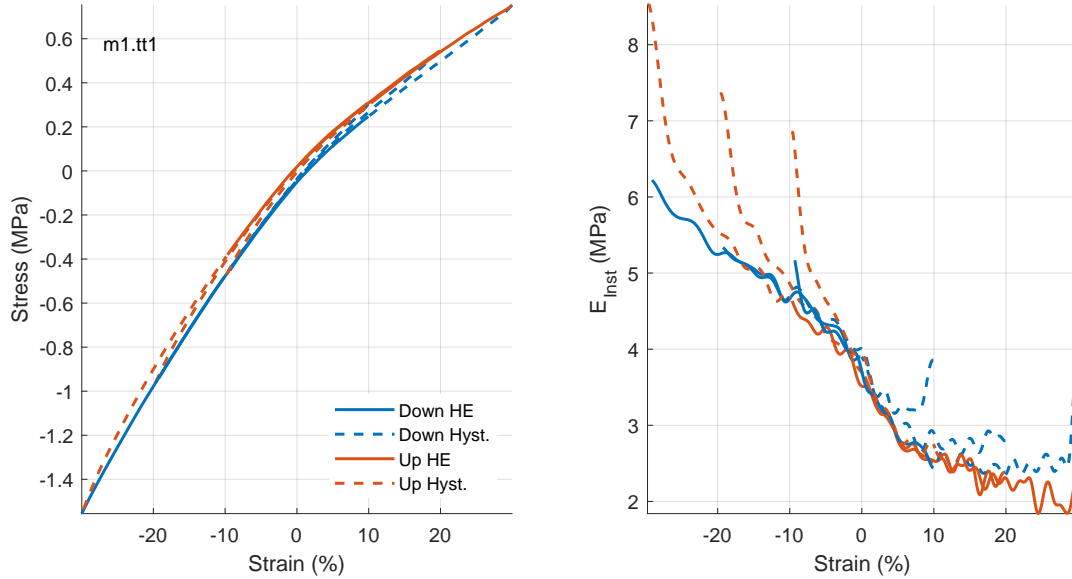


Figure 1.11: Triangular traction tests. Left: stress. Right: tangent modulus.

This section will review the base principles of hysteresis based on literature background, and then, as for the viscoelasticity, it will be shown that one may also introduce parametric models of selected order and order independent ones. Finally, other types of hysteretic approximations that do not perfectly respect the hysteresis hypothesis are discussed.

### 1.4.1 A non-parametric model: hysteretic relaxation

There is an extensive mathematical analysis of hysteresis in literature [16], but here, only the most basic assumptions will be applied to bushing models. The first one is the verification of the Madelung rules, which state that every loop closes itself where it started, no matter how many internal loops were made. In more precise terms, and using the illustration in figure 1.12:

- any curve  $\Gamma_1$  emanating from a turning point  $A$  of the input-output graph is uniquely determined by the coordinates of  $A$ ;
- if any point  $B$  on the curve  $\Gamma_1$  becomes a new turning point, then the curve  $\Gamma_2$  originating at  $B$  will eventually lead back to  $A$ ;
- if the curve  $\Gamma_2$  is continued beyond the point  $A$ , then it coincides with the continuation of the curve  $\Gamma$  which led to  $A$  before the  $\Gamma_1 - \Gamma_2$  cycle was traversed.

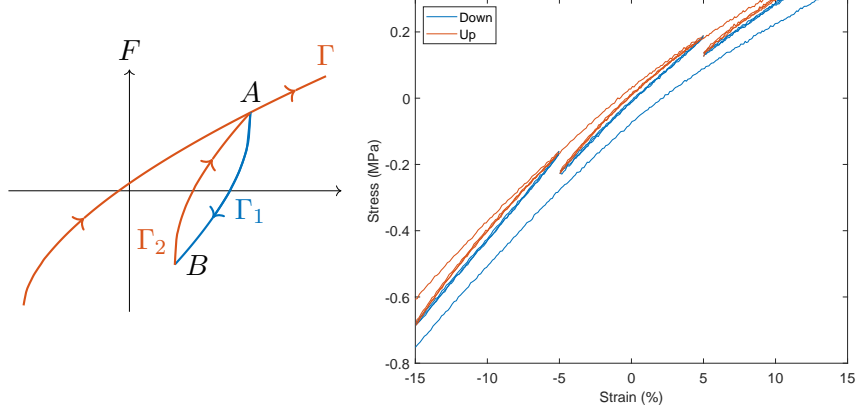


Figure 1.12: Illustration of Madelung rules. Left: Principles; Right: large deformation traction test.

The test result shown in the right part of the figure, drawn from experiments detailed in chapter 3, demonstrate a clear verification of the Madelung rules despite the presence of some noise and imperfect cycle repetition. The other feature of interest is the hyperelastic change of global slope around zero strain. One will thus seek to introduce a non-parametric model that allows the automatic verification of these rules while compatible with non-linear hyperelasticity.

To follow a process similar the one used in section 1.3 for viscoelasticity, the proposition made here is to state that a system that verifies Madelung's rules must have a force slope, or tangent stiffness, that only depends on distance to the turning point

$$\frac{dF}{dx}(x) = K_f(|x - x_{Turn}|) \quad (1.27)$$

The function  $K_f(x)$  will be called *hysteretic relaxation* stiffness or modulus since the force is obtained through

$$F(x) = F(x_{Turn}) + \int_0^{|x-x_{Turn}|} K_f(r) dr \quad (1.28)$$

which is similar to the relaxation modulus (1.7) of viscoelasticity.

If force evolution is expressed by (1.27), one can readily see that Madelung's rules are verified since the loop closure can be obtained from

$$0 = F(A) - F(B) + F(B) - F(A) = \int_0^{x_B-x_A} K_f(|x|) dx + \int_0^{x_A-x_B} K_f(|x|) dx \quad (1.29)$$

Figure 1.13 illustrates the different segments described during a force/displacement cycle (using the continuous STS model described in section 1.4.3). When ignoring coupling with hyperelasticity, this figure also illustrates that the downward and upward parts of the cycle have the same slope as

consistent with (1.28) but not with test shown in figure 1.11. Proper strategies for coupling with hyperelasticity will thus be discussed in the next section.

For the first branch starting from an initial null state, the same range of values is found, but with a horizontal scaling factor. Masing's law [23, 24], provides a classic procedure to deal with this branch. The statements are

- the first descending curve presents the same shape as the first ascending curve with an aspect ratio of two. Which considering the proposed formulation translates into the fact that when starting zero state, the convolution (1.28) must use  $2dr$  rather than  $dr$  for integration.
- subsequent curves present the same shapes as the last one, which is readily found here.

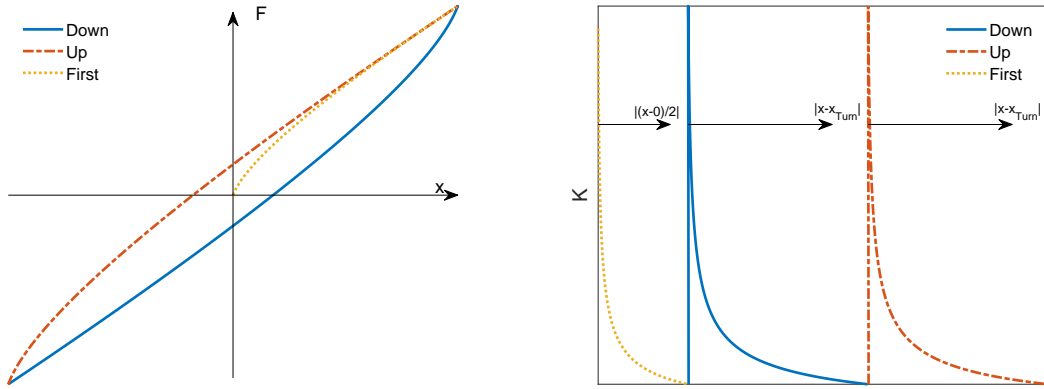


Figure 1.13: Hysteretic force/displacement cycle (left) and hysteretic stiffness (right) for model verifying Masing's law and Madelung rules.

### 1.4.2 Selected order base representations : Iwan series model

As for viscoelasticity and rational transfer functions presented in section 1.3.2, a discretization of the relaxation modulus is obtained using a series of first order friction elements. Using rheologic terminology, the equivalent of a Maxwell cell is a Jenkins cell where the damper is replaced by a friction element as shown in figure 1.14. Internal friction states  $x^i$  are introduced and the differential equation (1.27) is replaced by a set of non-linear evolution equations on displacement rate, distinguishing sticking and sliding states as

$$\begin{aligned} \dot{x}^i &= 0, \text{ if } \|x - x^i\| < F_f^i/K^i && \text{sticking state} \\ \dot{x}^i &= \dot{x}, \text{ if } \|x - x^i\| = F_f^i/K^i && \text{sliding state} \end{aligned} \quad (1.30)$$

Thus, realistic hysteretic models combine an elastic branch  $K^0$  (potentially hyperelastic), and a

## 1.4. RATE INDEPENDENT HYSTERESIS

series of Jenkins cells leading to a global force written as

$$F(x) = K^0 x + \sum_{i=1}^{N_{cell}} K^i (x - x^i) = \sum_{i=0}^{N_{cell}} F^i(x, x^i) \quad (1.31)$$

Rather than considering sliding points, the problem may be seen as load saturation, as for the Dahl model (detailed in section 1.4.4), which is more readily analyzed in a force rate formulation of the evolution equation

$$\begin{aligned} \dot{F}^i &= \frac{g^i}{g^0} \dot{F}^0, \text{ if } F^i \text{sign}(\dot{x}) < F_f^i = \frac{g^i}{g^0} K^0 x_f^i && \text{sticking state} \\ \dot{F}^i &= 0, \text{ if } F^i \text{sign}(\dot{x}) = F_f^i && \text{sliding/saturated state} \end{aligned} \quad (1.32)$$

Figure 1.14 illustrates two different discretizations of the order independent STS model that will be described in the next section. Starting from a turning point, the tangent stiffness begins at a high asymptote  $\sum_{i=0}^{N_{cell}} K^i$  and tends to the lower limit  $K^0$ . Assuming the Jenkins cells to be ordered by increasing saturation forces, the hysteretic relaxation stiffness for  $k$  sliding cells is

$$K_b^k = \sum_{i \leq k} K^i \quad (1.33)$$

with stiffness changes occurring at break points given by

$$x_f^k - x_{turn} = \frac{F_f^i}{K^i} \quad (1.34)$$

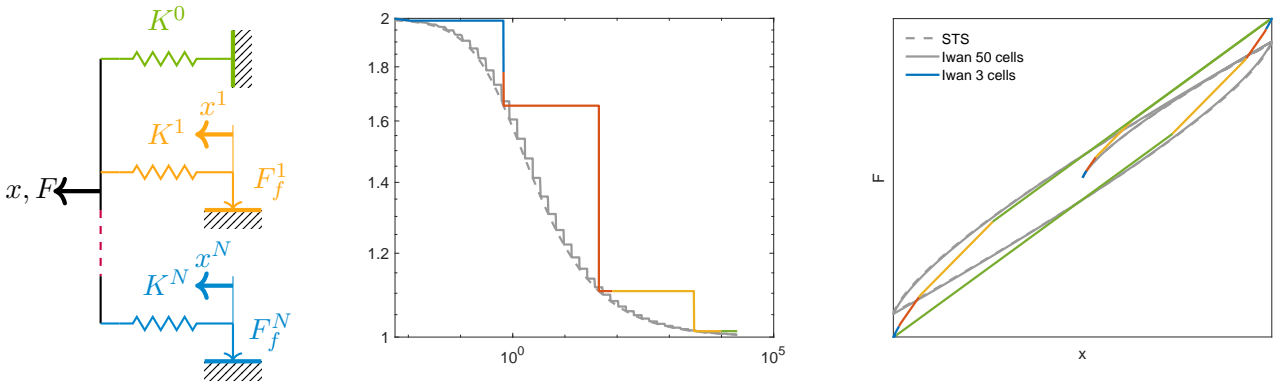


Figure 1.14: Scheme for Iwan model and respective response in terms of hysteretic relaxation and on force/displacement domain.

In figure 1.14 the hysteretic relaxation stiffness is represented using a log scale to emphasize the parallel with the complex modulus representation of figure 1.7. Choices in the discretization strategy will be linked to order and positioning of points on the hysteretic relaxation curve. Here the model

#### 1.4. RATE INDEPENDENT HYSTERESIS

with three cells does not fit the full data very well because the curve is set to be above the reference data. Obviously increasing the order gives a better control on the accuracy so that a non-parametric hysteretic relaxation curve may be fitted to the desired accuracy, just as complex moduli accuracy can be maintained under any threshold by using more cells.

When accounting for hyperelasticity, which is needed as clearly visible in figure 1.11 and figure 1.12 right, non-linear coupling needs to be considered. Figure 1.15 left clearly shows that the hysteretic stiffness is much higher for a turning point at -50% strain than at 50%. Considering  $K^i$  constant is thus not appropriate. The ratio of hysteretic by hyperelastic stiffness shown right seems much more constant despite experimental limitations stiffness estimation (one should notice the different scales).

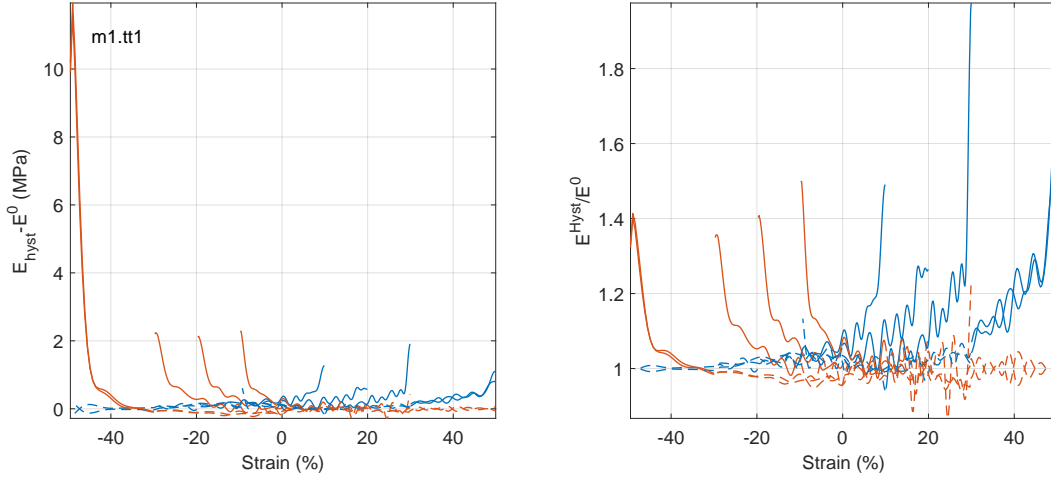


Figure 1.15: Difference (left) or ratio (right) of hysteretic and hyperelastic moduli.

Considering that the hysteretic stiffness depends on the local hyperelastic stiffness thus seems appropriate. Using the same definition of fractions (or gains)  $g^i$  of the hyperelastic part to describe each Jenkins cell as the one used in section 1.3.2 for viscoelastic models, the non-parametric formulation (1.27) can be revised to use a gain depending on distance to turning point instead (that equals the actual fraction of the cell before sliding and zero after sliding)

$$\dot{F}^i = g^i(|x - x_{\text{Turn}}|)\dot{F}^\infty. \quad (1.35)$$

With such coupling with hyperelasticity, a notable difference between the distance dependent relaxation (1.30) or load saturation (1.32) models is that the breakpoints positions do not depend on static strain as in the first case and are more widely spaced for lower hyperelastic stiffness in the second. This is illustrated in figure 1.16, where a voluntarily small order with 3 Maxwell and 3 Jenkins cells is considered in a triangular test.

At turning point, velocity changes very rapidly and the hysteretic modulus is discontinuous. It starts from a high value that relaxes rapidly because of the 3 viscoelastic cells. This relaxation is clearly something that was hard to see in the considered experiment because of too coarse time sampling and the procedure should be corrected.

After viscoelastic relaxation, hysteretic relaxation is seen as three sudden drops in the hysteretic stiffness as sliding/force saturation starts. The spacing of drops on the strain axis is more visibly different for the segments from -5% to 15% and from 5% to 15%, but happens to all the segments. This indicates that a stress saturation model was used and seems consistent with figure 1.15 where the relaxation distance is higher when going down and thus coming from a lower modulus.

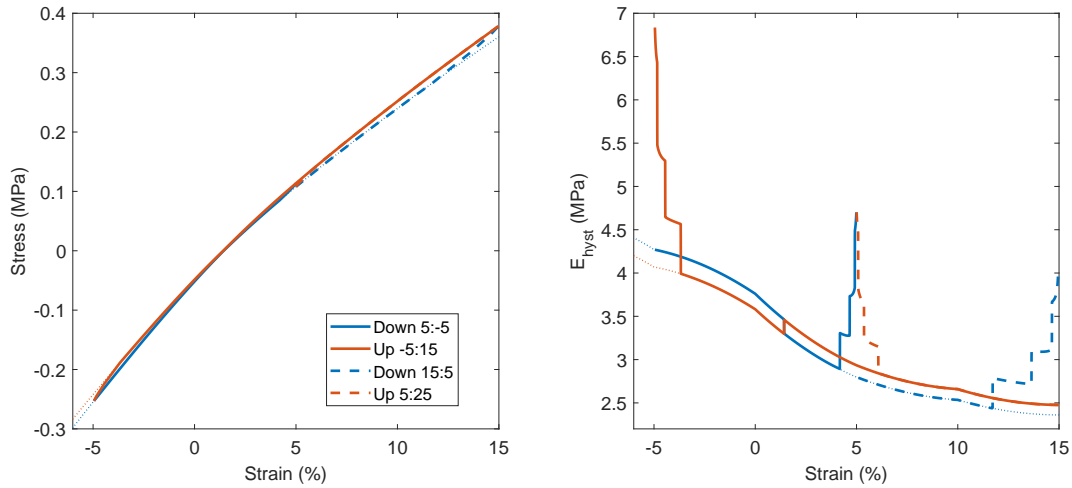


Figure 1.16: Simulated triangular test. Left: force displacement cycle, right: hysteretic relaxation modulus

### 1.4.3 Order independent parametric forms

The use of an Iwan model may be parameter intensive when trying to establish optimization routines, so there is a use for order independent models that use much fewer parameters.

Segalman [18] developed a four parameter model, to represent bolted connections and friction phenomena, but that it is a very appropriate model for representing the rate independent behavior of rubber bushings. Its force as function of displacement is expressed by

$$F = \int_0^{\phi_{max}} R(x - x^1(\phi))\phi^x d\phi + S(x - x^1(\phi_{max})) \quad (1.36)$$

with material parameters  $F_S, K_T, \chi, \beta$  and intermediate constants defined as

$$\begin{aligned} R &= \frac{F_S(\chi + 1)}{\phi_{max}^{\chi+2} \left( \beta + \frac{\chi+1}{\chi+2} \right)} \\ S &= \left( \frac{F_S}{\phi_{max}} \right) \left( \frac{\beta}{\beta + \frac{\chi+1}{\chi+2}} \right) \\ \phi_{max} &= \frac{F_S(1 + \beta)}{K_T \left( \beta + \frac{\chi+1}{\chi+2} \right)}, \end{aligned} \quad (1.37)$$

and the internal variable  $x^1$ , whose evolution is given by

$$\begin{aligned} \dot{x}^1 &= \dot{x}, \text{ if } \|x - x^i\| = \phi \text{ and } \dot{x}(x - x^1) > 0 \\ \dot{x}^1 &= 0, \text{ otherwise} \end{aligned} \quad (1.38)$$

Coveney [17], developed an extension to an infinite number of cells of an arrangement of identical springs and friction elements illustrated in figure 1.17. For the current development, they will be considered different at first, indexed accordingly to the figure.

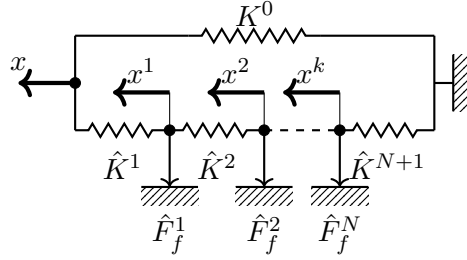


Figure 1.17: Standard triboelastic solid

For a finite order version of the same model, one may have the stiffness after sliding points defined by

$$K_b^i = K_0 + \left( \sum_{j=1}^i \hat{K}^{j-1} \right)^{-1} = \sum_{j=0}^{N-i} K^j \quad (1.39)$$

and the distance to the turning points, where the stiffness changes, is defined by

$$x_f^i = x_f^{i-1} + \frac{\hat{F}_f^i}{K_b^i} = \frac{F_f^i}{K^i} \quad (1.40)$$

which can be used to demonstrate that the finite order STS model has an exact Iwan equivalent.

To obtain an order independent model, the model is extended to an infinite number of cells by using  $\hat{F}_f^i = F_f^C \rightarrow 0$  and  $\hat{K}^i = K^C \rightarrow \infty$ , for  $i > 2$ , while keeping the product  $F_f^C K^C = C$  constant. The hysteretic force is then given by

$$F - F_{Turn} = \left( \sqrt{NC|x - x_{Turn}| + \left( \frac{NC}{2\hat{K}_0} \right)^2} - \frac{NC}{2\hat{K}_1} \right) \text{sign}(x - x_{Turn}), \quad (1.41)$$

where  $N$  is a variable that equals 2 when the level of force has already been reached before and 1, otherwise. This rule is quite difficult to implement, as there may be an infinite number of turning points to be stored, leading to a difficult management of internal states.

Ignoring the first loading conditions, the hysteretic relaxation curve is given by

$$K(x - x_{Turn}) = K_0 + \frac{C}{2} \left( C(x - x_{Turn}) + \frac{C^2}{4K_1^2} \right)^{-1/2} \quad (1.42)$$

For this order independent hysteretic relaxation, an equivalent Iwan series model can be obtained selecting breakpoints and the asymptotic behavior, using a maximum amplitude, placing forces using (1.42) and using (1.39) and (1.40) to obtain the Iwan parameters. Accuracy is, as shown in figure 1.14, clearly directly linked to the choice of number and position of breakpoints, which are the equivalent of order for the Iwan model.

#### 1.4.4 Regularity in first order hysteretic cells

The introduction of a discontinuity is often an issue for integration solvers. This is why different authors created other models to regularize the behavior of a friction element. One of the most used models with these properties is the Dahl model [25], whose evolution equation for force  $F^i$  as function of displacement  $x^i$  is given by

$$\dot{F}^i = K_d \left( 1 - \frac{F^i}{F_f^i} \text{sign}(\dot{x}^i) \right)^\alpha \dot{x}^i, \quad (1.43)$$

with  $\alpha$  a shape parameter, controlling the abruptness of transition between elastic and sliding states,  $K_d$  the initial stiffness and  $F_f^i$  the equivalent friction parameter.

The Bouc-Wen model [26] is another differential model often used in the representation of rate independent dissipative behavior. Its evolution equation is given by

$$\dot{F}^i = \alpha \dot{x}^i \left( A - \left( \gamma + \beta \text{sign}(\dot{x}^i) \text{sign}(F^i) \left\| \frac{F^i}{\alpha} \right\|^n \right) \right) \quad (1.44)$$

with  $\alpha$ ,  $\beta$ ,  $\gamma$ ,  $n$  and  $A$  model parameters, with the constraints  $n > 0$ ,  $\beta > 0$ ,  $A > 0$ ,  $-\beta < \gamma < \beta$ .

The Berg model [27] is another common attempt at regularization of Coulomb's friction model. Its behavior is described by the formula

$$F^i - F_{Turn} = \frac{x^i - x_{Turn}}{x_2 \left( 1 - \frac{(F^i - F_{Turn})}{F_{max}} \right) + |x^i - x_{Turn}|} (F_{max} - \text{sign}(x - x_{Turn}) F_{Turn}), \quad (1.45)$$

where  $x_2$  and  $F_{max}$  are model parameters.

Figure 1.18 illustrates the hysteretic relaxation curve for those models. All the models were fitted based on the dissipation and the apparent stiffness for triangular tests on a wheel suspension bushing. Clearly all the models begin in a higher stiffness, and Dahl and Berg models do not show perfect

superposition on loading and unloading. Bouc-Wen model present an unexpected peak in a specific distance to the turning point, which might be due to the fact that the hysteretic relaxation curve was not taken into account for the parameters identification, potentially leading to unrealistic choices.

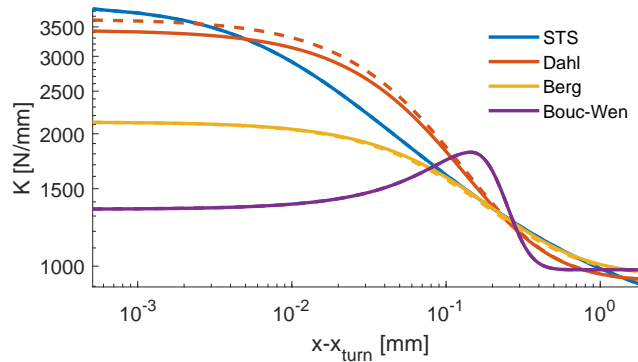


Figure 1.18: Masing curve for continuous hysteretic models.

The models described in this might be used instead of the Coulomb's friction elements in Jenkins cells to provide a continuous sliding, avoiding severe discontinuities throughout a sollicitation in single direction. However, the utilization of absolute and sign functions make that after turning points, discontinuities are still present. This work will not retain those implementations, but they may be useful for fitting non parametric models.

## 1.5 Unified perspectives through environmental factors

Beyond the three detailed mechanisms it is clear that there are other remarkable effects on rubber, the most notable being temperature effects and amplitude dependence, also known as Payne effect, that can be related to stress activation where characteristic times are lowered at higher stress amplitudes [15]. Figure 1.19 illustrates stabilized cycles for a different amplitudes. To properly visualize the trends, each cycle is divided by its amplitude so that one clearly sees how the mean slope decreases with amplitude.

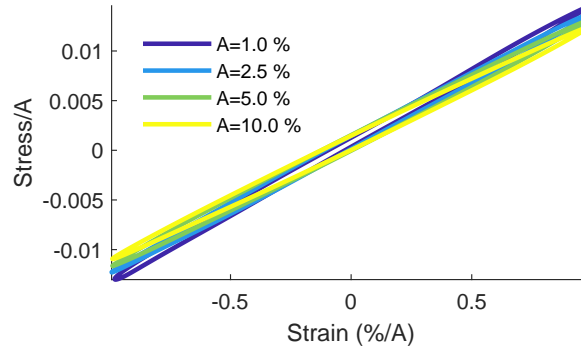


Figure 1.19: Amplitude dependence of shear test at 10 Hz with stress and strain divided by amplitude.

Assuming rate-independence for hysteresis or exactly linear behavior for viscoelasticity are obviously idealizations and one should not expect reality to match either behavior. For this reason, several authors were interested in developing intermediate models. For instance, [28] developed the STVS model, where the Jenkins cells were also tied to a non-linear damper, [29] developed a model that combines non-linear elasticity, non-linear hysteresis and non-linear viscoelasticity, [10] developed a model where these three branches were also present, [30] introduced viscoelastic dependence on the STS model, among other works.

On the hysteretic side, regularizations of friction behavior are often used to make the behavior more realistic. On the viscoelastic side, Heymans [15] convincingly argues that characteristic times depend on a structural temperature which evolves not only with temperature (whose effects will be explained in section 1.5.1), but also strain history.

These two approaches eventually converge into an attempt to simulate the behavior in a zone where it is difficult to identify and separate what is rate dependent and what is not, as will be shown in section 1.5.2. In the end, the combined behavior is assembled into a model, and its response is compared to test measures in section 1.5.3.

### 1.5.1 Classical temperature modeling

Temperature is classically considered as the major factor influencing viscoelastic behavior. For thermoreologically simple materials, one can regularly use the so called *frequency/temperature* equivalence principle [20, 31] that states that the complex modulus (viscoelastic transfer) does not depend separately on frequency and temperature but on a single coordinate called reduced frequency obtained as the product of frequency and a temperature shift factor  $\alpha(T)$ . Thus

$$E(\omega, T) = E(\omega_{red}) = E(\alpha(T)\omega) \quad (1.46)$$

where the complex modulus curve is called a master curve illustrated in figure 1.20. Its existence can be verified using Cole-Cole [32] or Wicket [1] plots (similar to a Nyquist diagrams in systems

theory). This assumption is consistent with the physical notion that frequency and temperature are equivalent in terms of particle excitation. Classical parametric expressions of the shift factor are the the Williams-Landel-Ferry, and Arrhenius models [20].

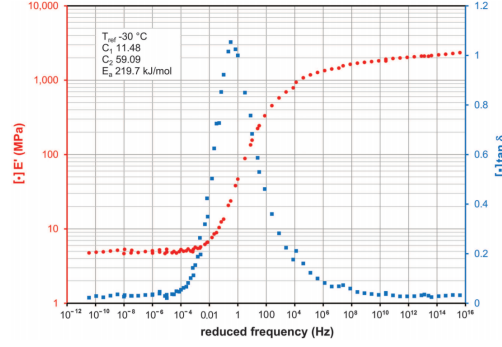


Figure 1.20: Utilization of master curves for polymeric materials. Source: [1]

The reduced frequency  $\omega_{red} = \alpha(T)\omega$  can directly be used in parametric models since characteristic relaxation times at a different temperature are simply obtained using

$$\omega^i(T) = \alpha(T)\omega^i(T_0) \quad (1.47)$$

where the reference temperature  $T_0$  is selected such that  $\alpha(T_0) = 1$ .

The frequency domain rational fraction model (1.8) thus becomes parametrized in temperature as

$$K(s, T) = K^\infty \left( 1 - \sum_{i=1}^N \frac{g^i}{\frac{s}{\alpha(T)\omega^i(T_0)} + 1} \right) = K^\infty \left( g^0 + \sum_{i=1}^N g^i \frac{s}{s + \alpha(T)\omega^i(T_0)} \right). \quad (1.48)$$

The implementation of the shift factor into viscoelastic schemes is very simple, as it only demands a change on the characteristic frequency.

### 1.5.2 Intermediates between viscoelasticity and rate independent hysteresis

Using a similar idea of viscous poles having a non-linear dependence on the material state, [33] proposed *reduced relaxation times*. This formulation can be rewritten as the non-linear stress relaxation equation

$$\dot{F}^i + \omega^i(1 + \beta \|\dot{x}\|)F^i = g^i \dot{F}^\infty \quad (1.49)$$

with a velocity dependent shift factor  $\alpha(\|\dot{x}\|) = (1 + \beta \|\dot{x}\|)$  which is clearly related to the structural temperature discussed in [15].

For  $\beta \|\dot{x}\| \gg 1$  and assuming a linear base branch  $F^0 = K^0 x = g^0 K^\infty x$ , the asymptotic value is a friction force

$$F^i \approx \frac{g^i K^\infty}{\beta \omega^i} \frac{\dot{x}}{\|\dot{x}\|} \quad (1.50)$$

leading to the expression using hysteretic constants

$$\beta = \frac{1}{\omega^i x_f^i} \quad (1.51)$$

and physically clearer form

$$\dot{F}^i + \left( \omega^i + \frac{\|\dot{x}\|}{x_f^i} \right) F^i = g^i K^\infty \dot{x} \quad (1.52)$$

where the parameters controlling behavior are the load fraction  $g^i$ , the viscous frequency  $\omega^i$  and the hysteretic relaxation distance  $x_f^i$  which provides a saturation for a force that is viscoelastic at low velocities and amplitudes. Such saturation may be seen in figure 1.21, where a linear gain of 1N/mm was used so the saturations are supposed to arrive at 0.1, 0.5, 1 and 3N, for a sine sollicitation of 1mm amplitude. Without any saturation, one would expect an ellipse, while for a pure friction element, one would have a rectangle. It is clear that for the first cell, the saturation is reached, but for the other cells, closer to the saturation, the transition is not fully made.

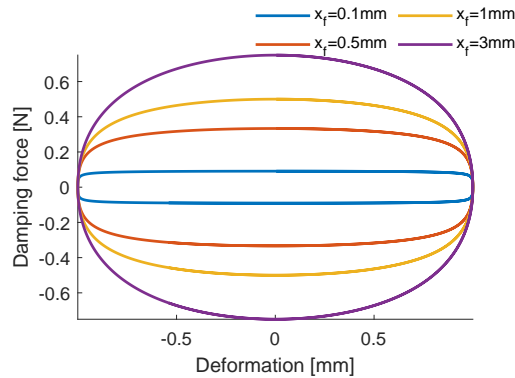


Figure 1.21: Damping force evolution for different values of  $x_f$ .

To illustrate the difference between different cells coupled with hyperelasticity, figure 1.22 displays the branch stress  $F^i$  and the instantaneous modulus first shown in figure 1.4. Two Jenkins cells are shown in blue.  $F^1$  shown as a solid line does not slide and its instant modulus shows a nearly constant value with the small changes due to coupling with the hyperelastic behavior.  $F^2$  shown with dashed lines has notable sliding and this induces a major drop of instant modulus during the period. The non-linear viscous version of the same load shown as a dot dashed line, follows (1.52). The drop for higher velocities is still very much visible but the transition is much smoother.

Two Maxwell cells are shown in red. The solid curve  $F^3$  has a relaxation frequency at 1Hz, so the modulus is relatively high and nearly constant, especially for 15% static strain where the hyperelastic modulus varies much less than at 0% (see figure 1.4 left). The dashed  $F^4$  has a much higher relaxation frequency at 25 Hz so the apparent modulus at 1 Hz is quite small.

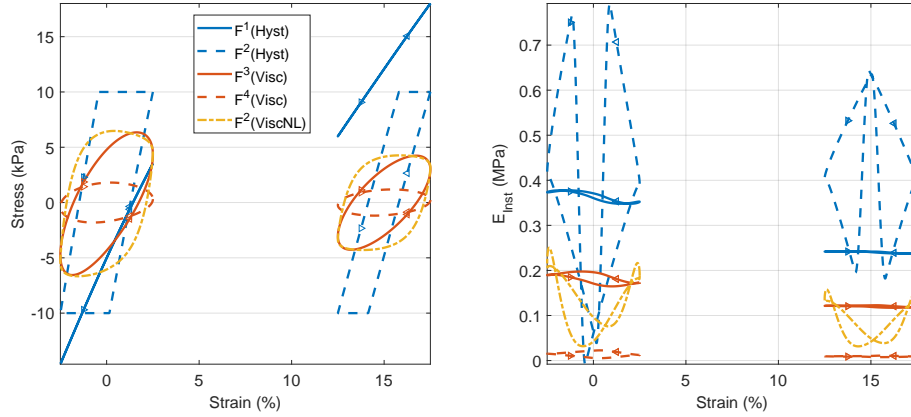


Figure 1.22: Branch stress and stiffness contributions for 1 Hz excitation, 10% strain amplitude and 0 and 15% static strain

In conclusion, non-linear viscoelastic representations such as (1.52) provide an appropriate transition between viscoelasticity and rate independent hysteresis. Detailing the evolution during harmonic periods, provides a clear path for the identification of parametric representations for known dependencies discussed in [15]: strain softening, anelastic deformation, stress activation, ...

### 1.5.3 Combined behavior

The first coupling of interest is with hyperelasticity. When adding viscoelastic branches, it is important to test whether the strain or stress relaxation forms are more relevant. Using the strain relaxation (1.10), viscous loads are not proportional to hyperelastic stiffness, which changes with pre-strain. In figure 1.23 left it appears that the modulus increase due to viscoelasticity varies by nearly a factor 2 between -30% and 30% static strain. In figure 1.23 right, however, the ratio with the hyperelastic modulus still varies but only by less than  $\pm 15\%$ . The data thus indicate that stress relaxation (1.12) based on fractions of the full hyperelastic part considered so far gives a more accurate representation, but the load fractions might need to be considered as slightly non-linear for even better accuracy.

## 1.5. UNIFIED PERSPECTIVES THROUGH ENVIRONMENTAL FACTORS

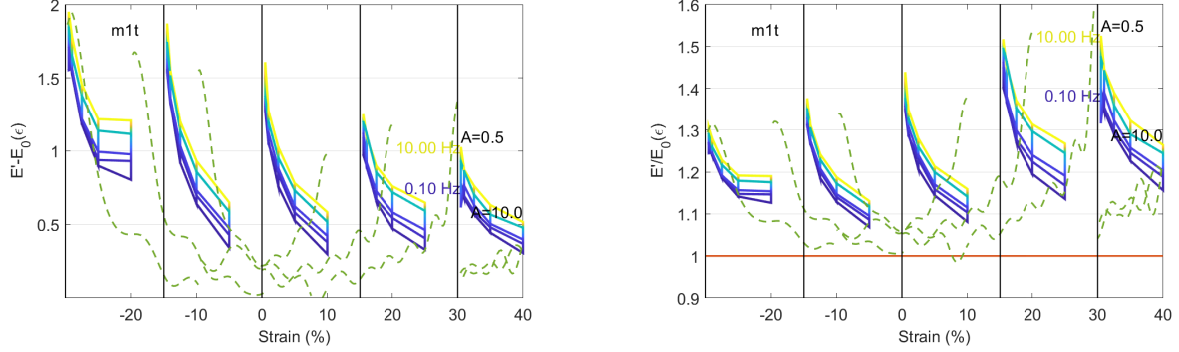


Figure 1.23: Left: viscoelastic and hysteretic modulus *difference* with hyperelastic modulus, right: modulus *ratio*.

The second coupling of interest is linked to the interaction between viscoelastic and rate independent hysteretic contributions. Using the instant modulus, figure 1.24 compares test and simulation results while focusing on amplitude variation at 1Hz. When comparing cycles with the same frequency and prestrain, the instant modulus is clearly lower in average for the test with larger amplitude. This is known as the Payne effect (also known as Fletcher-Gent effect) [34, 35]. This effect is quite notable for carbon black filled rubbers and has been extensively studied [36, 10, 37]. Figure 1.1 illustrated this using the classical first harmonic extraction, but this figure indicates that the effect is present at all instants.

The reproduction by the model in figure 1.24 right is quite clear. When removing the dependency of poles on velocity,  $x_f^i \rightarrow \infty$  in (1.52), the instant stiffness trajectories have the same mean. This confirms that the Payne effect is linked to rate independent hysteresis, which here is possibly not distinguishable from non-linear effects on very low frequency viscoelasticity.

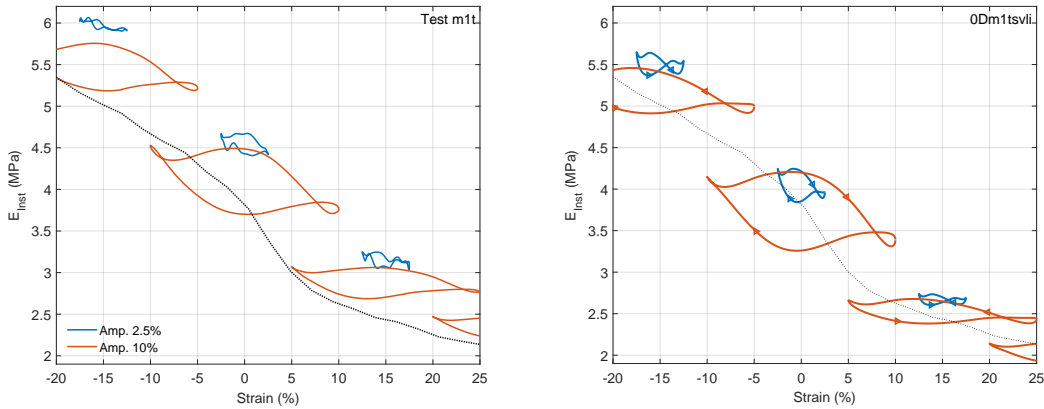


Figure 1.24: Sine test at 1Hz, 2.5 and 10% strain. Left: test. Right: model.

Figure 1.25 focuses on frequency variations. The modulus cycles only shift up while keeping a nearly identical shape. This is consistent with the fact that at higher frequencies the change in the behavior is essentially viscoelastic. The imperfect shift in the model can clearly be attributed to a fairly coarse identification with manual optimization of parameters.

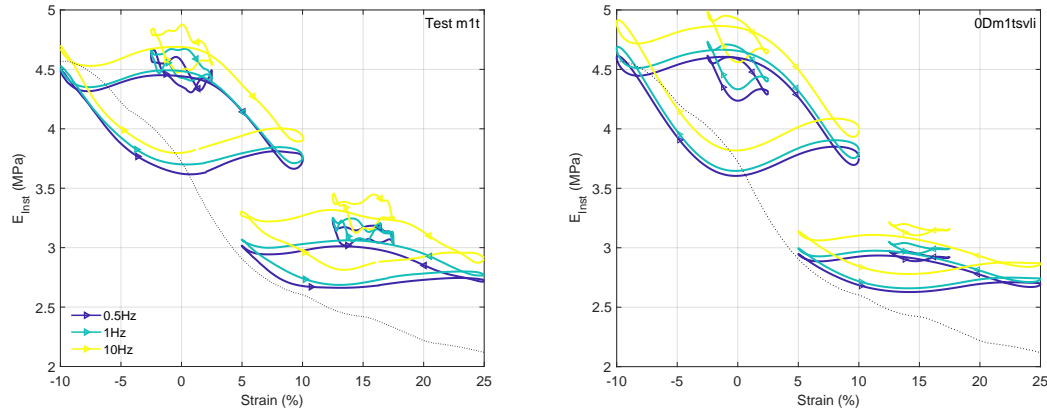


Figure 1.25: Sine test at 0.5, 1 and 10Hz at 10% strain. Left: test. Right: model.

## 1.6 Experiment design perspectives and conclusions

After the realization of the test campaign, in hindsight there are some clear adjustments and improvements to be made for the next campaigns.

The first fundamental result of the test campaign, was that low speed triangular tests effectively enabled the characterization of the hyperelasticity and the newly introduced hysteretic relaxation. Since this was not initially foreseen, the sampling rate was insufficient right after the turning point. Using faster sampling would improve filtering possibilities. Introducing smoother turning point trajectories seeking to minimize high frequency excitation and thus coupling with viscoelasticity, would give a better estimation of the hysteretic relaxation. Small loops, that were introduced to verify the Madelung rules are useful, but much less critical than the large amplitude triangles. An imperfect verification of Madelung rules seems consistence with presence of viscosity, but detailed analysis would require rework of sampling and trajectories.

The second major result was the introduction of instantaneous modulus as function of strain (figure 1.24, for instance) instead of the classical first harmonic modulus extraction. This corresponds to a major perspective change from considering linearization through mean over a cycle to linearization through the consideration of a time varying system. This gave a clearer view of the Payne effect and allowed detail analysis of model behavior during the cycle. Using direct time domain analytic signal estimation in an extended Kalman filter, would give better control of tests and final results.

Finally, multi-step tests were not found to be really helpful. Hyperelastic behavior is better char-

acterized using large triangular cycles, where one may disregard early hysteretic effects, and also easily characterized by taking the harmonic 0 from sine tests. Considering the ramp as a dynamic characterization of the relaxation function and its transform (as figure 1.5) was helpful and could be improved with faster sampling or shorter ramps to excite higher frequencies. On the other end, using even longer relaxation periods, one might have an interesting insight on very long term effects, as seen in figure 1.2, where loading and unloading do not converge to the same point. Mullins effect might also be included on such characterization.

In conclusion, it is very clear that the hyperelastic backbone is necessary for accurate modeling, whose coupling with other effects should be made with force rate formulations. The gain of the force rate model can only be considered linear at high frequencies where hysteresis can be neglected, or at very low velocities where viscoelasticity can be neglected. In the intermediate regime, an affine dependence of relaxation frequencies on velocity seems to be a good candidate even though more work is obviously needed.

Beyond the considered effects, there are also models that incorporate other effects such as first cycles softening [37, 7], plastic effects [6, 10, 38], damage effects [39], strain induced crystallization, preloading effects in fatigue [40], and amplitude effects [33] with modified viscoelastic models. The unified perspective proposed does not all of them into account, which may be a perspective for future work in the subject.

Chapter 2 will extend most of the concepts presented in this chapter to three dimensional tensorial models, appropriate for finite element implementation, and the test campaign that motivated and illustrated this chapter will be detailed in chapter 3.

## 1.6. EXPERIMENT DESIGN PERSPECTIVES AND CONCLUSIONS

---

# Chapter 2

## 3D material models

### Contents

---

<b>2.1</b>	<b>Introduction</b>	<b>92</b>
<b>2.2</b>	<b>Continuum mechanics</b>	<b>92</b>
2.2.1	Kinematics	92
2.2.2	Invariants, strain rates	93
2.2.3	Stress, equations of motion, time integration at a material point	94
<b>2.3</b>	<b>Hyperelasticity</b>	<b>95</b>
2.3.1	General properties: potential, polyconvexity	95
2.3.2	Compression or volume change behavior	96
2.3.3	Deviatoric behavior	96
2.3.4	Basic deformations used for material characterization	98
<b>2.4</b>	<b>Viscoelasticity in finite strains</b>	<b>100</b>
2.4.1	Finite strain deviatoric viscoelasticity - Simo formalism	100
2.4.2	Bulk viscoelasticity	101
2.4.3	Non-linear transition between viscoelasticity and hysteresis	102
<b>2.5</b>	<b>Perspectives and conclusions</b>	<b>103</b>

---

## 2.1 Introduction

As mentioned in the introduction, most of the time 0D models combine both material and geometric behaviors. For 3D models, geometry can be accurately modeled and material models need to account for the tensorial nature of large strain and stresses. Adaptations of results shown in chapter 1 are thus needed.

A brief review on continuum mechanics is made in section 2.2, focusing on the development of consistent material laws for finite strains. The review ends in the virtual work principle, and actual implementation of this principle to arbitrary geometries in a finite element code is made in the chapter 4.

The theory of hyperelasticity is also revisited, detailing usual strategies for rubber materials and test possibilities. A few invariant based models are fully developed and will be retained for implementation in section 2.3. Finally, the same relaxation schemes as the ones presented in section 1.3 are applied to the base hyperelastic behavior, with a nonlinear adaption to represent amplitude effects in section 2.4.

The implementation of purely hysteretic models in large strains with plastic-like models and kinematic hardening is still subject of discussion and there is no prevalent theory. The research made regarding this subject was ultimately not implemented and the research is documented in appendix A.

## 2.2 Continuum mechanics

This first section summarizes classical results of continuum mechanics, which are needed for later discussion of constitutive laws exhibiting hyperelasticity, viscoelasticity and rate independent hysteresis under large deformation [21, 41, 42].

### 2.2.1 Kinematics

Considering a three dimensional euclidean space with base  $e_1, e_2, e_3$ , a body  $\Omega$  may be described by a region from this space. Each point  $P$  of  $\Omega$  is called a material point and its coordinates are described by

$$\{x(t)\} = x_1 \{e_1\} + x_2 \{e_2\} + x_3 \{e_3\} \quad (2.1)$$

in the reference configuration of a Lagrangian description of the problem. The body position may evolve with time, and time derivatives give velocity  $v$  and acceleration  $a$  as

$$v = \frac{\partial x}{\partial t}, \quad a = \frac{\partial^2 x}{\partial t^2}. \quad (2.2)$$

The kinematic description is based on the knowledge of the initial and current positions of any material point. The difference between initial and current positions of material points is the displace-

ment vector  $\{u\}$ . Material behavior is typically described as a function of strains. The most basic strain measure is the deformation gradient tensor, given by

$$F = \frac{\partial \{x\}}{\partial \{x_0\}} = \delta_{ij} + \frac{\partial u_i}{\partial x_j} = \delta_{ij} + u_{i,j} \quad (2.3)$$

where  $\delta_{ij}$  denotes the Kronecker delta function. This tensor links the reference and the current configurations, making it a hybrid deformation description. It may be divided in two separate parts: rotation  $R$  and dilatation  $U$  in a polar decomposition

$$F = RU \quad (2.4)$$

where  $R$  is orthonormal, and  $U$  positive definite and symmetric. To obtain rotation independent deformation tensors, quadratic forms of the deformation tensor are used. For a Lagrangian description, the right Cauchy-Green tensor

$$C = F^T F \quad (2.5)$$

will be used. The Green Lagrange strain  $e_{ij} = 1/2(C_{ij} - \delta_{ij})$  is a common alternative. The main difference between the two is that  $C$  tends to the identity for nil deformation, while  $e$  tends to zero.

### 2.2.2 Invariants, strain rates

For isotropic materials, properties should not depend of orientation and behavior should not dependent on rotation  $R$ . Invariants of the strain tensors are often used in constitutive formulation to achieve rotation independence. The three classical invariants are

$$\{I_i\} = \left\{ \begin{array}{l} \text{tr}(C) \\ \frac{\text{tr}^2(C) - \text{tr}(C^2)}{2} \\ \det(C) \end{array} \right\} \quad (2.6)$$

where one should note that  $I_3 = \det(C) = \det^2(F)$  quantifies the square of the volume change at the material point, and  $J = \sqrt{I_3}$  the volume change. The derivatives of invariants with respect to deformations will also be necessary and are classically given by

$$\frac{\partial I_k}{\partial C_{ij}} = \left[ \delta_{ij} \quad I_1 \delta_{ij} - C_{ij} \quad I_3 C_{ij}^{-1} \right], \quad (2.7)$$

and

$$\frac{\partial I_k}{\partial C_{ij} \partial C_{kl}} = \left[ 0_{ijkl} \quad \delta_{ij} \delta_{kl} - 1_{ijkl} \quad I_3 \left( C_{ij}^{-1} C_{kl}^{-1} - 1/2 \left( C_{ik}^{-1} C_{jl}^{-1} + C_{il}^{-1} C_{jk}^{-1} \right) \right) \right] \quad (2.8)$$

where  $1_{ijkl} = 1/2(\delta_{ik}\delta_{jl} + \delta_{il}\delta_{jk})$ . For highly incompressible materials, it is usual to describe the potential associated with the deviatoric part of the strain using reduced invariants, defined by

$$\bar{I}_1 = J^{-2/3} I_1, \bar{I}_2 = J^{-4/3} I_2. \quad (2.9)$$

Deformation rate tensors are also often needed. The velocity gradient tensor is commonly used and given by

$$L = \frac{\partial v_i}{\partial u_j} = \frac{\partial v_i}{\partial x_j} \frac{\partial x_i}{\partial u_j} = \dot{F} F^{-1} \quad (2.10)$$

As this gradient is not rotation independent, it is handy to decompose it into strain rate and spin tensors, by taking its symmetric and the skew-symmetric parts,

$$D = \frac{1}{2} (L + L^T), W = \frac{1}{2} (L - L^T). \quad (2.11)$$

The strain rate tensor may be used in viscoelastic laws, as will be done in section 2.4, while the spin tensor is usually discussed in finite deformation plasticity models [43].

### 2.2.3 Stress, equations of motion, time integration at a material point

When computing work of deformable bodies the dual quantities (energy conjugate pair) are stress and strain, as force and displacement are dual for rigid body mechanics.

In the Lagrangian reference frame, the second Piola-Kirchhoff  $S$  tensor is used for stress. The hybrid reference tensor (initial frame for strains to current frame for stresses) is called first Piola-Kirchhoff II (or Boussinesq, or also nominal stress) and is not symmetric. In linearized conditions, the Eulerian description given by the Cauchy stress  $\sigma$  is used.

Stress and strain energy present different equivalent expressions, forming dual pairs

$$W = S : e = \Pi : F = \sigma : \varepsilon. \quad (2.12)$$

Material or constitutive models are laws that describe the evolution of stresses for an history of deformations and possibly internal states. They are system models of what happens at a material point. The parameters of these laws should be identified from experiments as discussed in chapter 1 and further detailed in chapter 3.

Given a displacement gradient tensor evolution, as the ones from section 2.3.4, stress at timestep  $n + 1$  must be an explicit function of the gradient displacement tensor and its internal states at the last timestep  $n$  (considering explicit implementation),

$$[S_{n+1}, u_{n+1}^{int}] = f(\nabla u_{n+1}, \nabla \dot{u}_{n+1}, u_n^{int}). \quad (2.13)$$

The development of material laws should typically be tested and tuned separately from the global structural application, which may be done by equation (2.13).

With material laws defined, equations of motion at the structure level are derived from the fact that the work of all forces for any kinematically acceptable virtual displacement field  $w$  is equal to zero. In other words,

$$\int_{\Omega_0} S : \delta e(w) - \int_{\Omega_0} \{f_v\} \delta w = 0. \quad (2.14)$$

The implementation for the virtual work principle in the scope of FE routines will be detailed on chapter 4.

## 2.3 Hyperelasticity

Following the usual strategy [41], one will distinguish the effects of compression or isotropic volume change in section 2.3.2 and deviatoric behavior in section 2.3.3.

### 2.3.1 General properties: potential, polyconvexity

A material is said to be hyperelastic if its stress only depends on the current strain. It is classically shown that this is verified if stress is obtained as the derivative of a potential  $\psi$  that depends on deformation tensors. Derivation from a potential is a sufficient condition to demonstrate that deformations are completely reversible, despite being nonlinear. The non-linearities involved are

- geometric: large deformations is typically involved requiring non-linear strain descriptions
- material: as the operating range can be large, there is no physical reason for materials to respond linearly

For an isotropic material, behavior must be independent of rotation. This can be used to demonstrate that the potential may always be expressed as a function of strain invariants. The stress is thus found as

$$S_{ij} = \frac{\partial \psi}{\partial e_{ij}} = 2 \frac{\partial \psi}{\partial C_{ij}} = 2 \frac{\partial I_k}{\partial C_{ij}} \frac{\partial \psi}{\partial I_k} \quad (2.15)$$

where the convention of summing repeated indexes is used. Other consequence of the expression of the potential in terms of the invariants is that it may always be written in the form [41]

$$\sigma = \beta_0(I_1, I_2, I_3) \mathbb{1} + \beta_1(I_1, I_2, I_3) F^T F + \beta_2(I_1, I_2, I_3) (F^T F)^2 \quad (2.16)$$

with  $\beta_i$  functions of the invariants that may be determined according to the model. These three  $\beta$  functions, therefore can be seen as a non parametric manner of modeling hyperelasticity. Since going through the whole space spanned by  $I_1$ ,  $I_2$  and  $I_3$  is unpractical, most common approaches are to use either selected order representations as polynomials on the invariants or order independent models that are not based on invariants, as will be described in section 2.3.3.

The only restriction on the energy potential is its polyconvexity [21, 44] which ensures stability. For scalar stress or 0D, the potential is the integral of the force/displacement curve seen in section 1.2. This function can be a polynomial or any convex function corresponding to the fact that the instantaneous stiffness or slope of the force/displacement curve is positive.

## 2.3. HYPERELASTICITY

---

In 3D, ensuring polyconvexity for a tensor is not straightforward but corresponds to the positive definite nature of the tangent material stiffness. For an isotropic material, this matrix can be expressed as [45, 46]

$$\mathcal{D}_{ijkl} = 4 \frac{\partial^2 \psi}{\partial C_{ij} \partial C_{kl}} = 4 \frac{\partial^2 I_n}{\partial C_{ij} \partial C_{kl}} \frac{\partial \psi}{\partial I_n} + 4 \frac{\partial I_n}{\partial C_{ij}} \frac{\partial^2 \psi}{\partial I_n \partial I_m} \frac{\partial I_m}{\partial C_{kl}} \quad (2.17)$$

### 2.3.2 Compression or volume change behavior

Materials used for bushings are typically incompressible. Compressibility is described by the isotropic part of strains and a specific discussion of constitutive laws is needed. Remaining behavior is associated with deviatoric strains and discussed separately.

To achieve this separation for hyperelastic models, one may divide the potential in a deviatoric and an isotropic part  $\psi = \psi^D + \psi^I$ , which means that the same decomposition applies to the stresses, aside from numerical issues. This implies the introduction of two separate models that are superposed in the end.

As the third invariant is the only one that has no deviatoric components, compression models are normally based on this invariant, or its square root  $J$ . The isotropic potential for linear models normally used is

$$\begin{aligned} \psi^I &= \frac{\kappa}{2} (J - 1)^2 \\ \frac{\partial \psi^I}{\partial J} &= \kappa (J - 1) = p \\ \frac{\partial J}{\partial J^2} &= \kappa \end{aligned} \quad (2.18)$$

This potential however allows full compression or volume suppression. For this reason, the Ciarlet-Geymonat [47] potential was developed with a logarithmic penalty term,

$$\begin{aligned} \psi^I &= \frac{\kappa}{2} (J^2 - \ln(J^2)) \\ \frac{\partial \psi^I}{\partial J} &= \kappa \left( J - \frac{1}{J} \right) = p \\ \frac{\partial^2 \psi^I}{\partial J^2} &= \kappa \left( 1 + \frac{1}{J^2} \right) \end{aligned} \quad (2.19)$$

The stress tensor resulting from the isotropic part may be computed as  $\sigma_p = p \delta_{ij}$  in an Eulerian reference frame, which may be transferred to a Lagrangian reference frame by  $S_p = F^{-1}(\sigma_p)F^{-T}$ .

### 2.3.3 Deviatoric behavior

Three main groups of hyperelastic potentials are typically [48] distinguished: invariant, principal strains and physic based potentials.

*Invariant based* formulations were developed first and are still widely used, because of their simpler formulation and low numerical cost.

### 2.3. HYPERELASTICITY

The neo-hookean model is a linear constitutive model applied to large deformation. One combines compression with a shear model given by

$$\begin{aligned} \psi^D &= \mu \bar{I}_1 = \mu I_1 I_3^{-1/3} \\ \frac{\partial \psi^D}{\partial I_i} &= \left\{ \begin{array}{ccc} \mu I_3^{-1/3} & 0 & -\frac{\mu I_1 I_3^{-4/3}}{3} \end{array} \right\} \\ \frac{\partial^2 \psi^D}{\partial I_i \partial I_j} &= \left[ \begin{array}{ccc} 0 & 0 & -\frac{\mu I_3^{-4/3}}{3} \\ 0 & 0 & 0 \\ -\frac{\mu I_3^{-4/3}}{3} & 0 & \frac{4\mu I_1 I_3^{-7/3}}{9} \end{array} \right] \end{aligned} \quad (2.20)$$

The Mooney-Rivlin model adds the second invariant to this formulation and is given by

$$\begin{aligned} \psi^D &= c_1 \bar{I}_1 + c_2 \bar{I}_2 = c_1 (I_1 I_3^{-1/3}) + c_2 (I_2 I_3^{-2/3}) \\ \frac{\partial \psi^D}{\partial I_i} &= \left\{ \begin{array}{ccc} c_1 I_3^{-1/3} & c_2 I_3^{-2/3} & -\frac{c_1 I_1 I_3^{-4/3}}{3} - \frac{2c_2 I_2 I_3^{-5/3}}{3} \end{array} \right\} \\ \frac{\partial^2 \psi^D}{\partial I_i \partial I_j} &= \left[ \begin{array}{ccc} 0 & 0 & -\frac{c_1 I_3^{-4/3}}{3} \\ 0 & 0 & -\frac{2c_2 I_3^{-5/3}}{3} \\ -\frac{c_1 I_3^{-4/3}}{3} & -\frac{2c_2 I_3^{-5/3}}{3} & \frac{4c_1 I_1 I_3^{-7/3}}{9} + \frac{10c_2 I_2 I_3^{-8/3}}{9} \end{array} \right] \end{aligned} \quad (2.21)$$

Stability requires  $\partial^2 \psi^D / \partial C^2$  to be a positive definite matrix, but the above potentials do not verify stability for all strain. A very simple potential featuring a very good fitting unconditional stability [49, 50] is the Carroll model given by

$$\begin{aligned} \psi^D &= \alpha \bar{I}_1 + \beta \bar{I}_1^4 + \gamma \bar{I}_2^{1/2} = \alpha I_1 I_3^{-1/3} + \beta I_1^4 I_3^{-4/3} + \gamma I_2^{1/2} I_3^{-1/3} \\ \frac{\partial \psi^D}{\partial I_i} &= \left\{ \begin{array}{ccc} \alpha I_3^{-1/3} + 4\beta I_1^3 I_3^{-4/3} & \frac{\gamma I_2^{-1/2} I_3^{-1/3}}{2} & -\frac{\alpha I_1 I_3^{-4/3}}{3} - \frac{4\beta I_1^4 I_3^{-7/3}}{3} - \frac{\gamma I_2^{1/2} I_3^{-4/3}}{3} \end{array} \right\} \\ \frac{\partial^2 \psi^D}{\partial I_i \partial I_j} &= \left[ \begin{array}{ccc} 12\beta I_1^2 I_3^{-4/3} & 0 & -\frac{\alpha I_3^{-4/3}}{3} - \frac{16\beta I_1^3 I_3^{-7/3}}{3} \\ 0 & -\frac{\gamma I_2^{-3/2} I_3^{-1/3}}{3} & -\frac{\gamma I_2^{-1/2} I_3^{-4/3}}{3} \\ -\frac{\alpha I_3^{-4/3}}{3} - \frac{16\beta I_1^3 I_3^{-7/3}}{3} & \frac{\gamma I_2^{-1/2} I_3^{-4/3}}{6} & \frac{4\alpha I_1 I_3^{-7/3}}{9} + \frac{28\beta I_1^4 I_3^{-10/3}}{9} + \frac{4\gamma I_2^{1/2} I_3^{-7/3}}{9} \end{array} \right] \end{aligned} \quad (2.22)$$

As the proof for the stability of invariant based models is not straightforward, the use of potentials associated with *principal strains*  $\lambda_i$  (equivalently, the eigenvalues of the matrix  $C$ ) ensures the stability, as the matrix  $C$  is symmetric (note that these correspond to the square of the singular values of  $F$ ). The Ogden model [48] is the most used model of this type

$$\psi^D = \sum_{n=1}^N \frac{\mu_n}{\alpha_n} (\lambda_1^{\alpha_n} + \lambda_2^{\alpha_n} + \lambda_3^{\alpha_n}) \quad (2.23)$$

## 2.3. HYPERELASTICITY

---

This open form ensures that the model is able to fit any curve, but it comes at the cost of a large number of parameters and the need to compute eigenvalues at each step.

So called *physic based* potentials are based on assumptions of how the elastomer behaves at a microscopic level. The main origin of this type of model is the chain model [48], which assumes that the elasticity of networked chains is due to the entropic changes, thus it may be determined by the number of possible states. This chain model gave origin to the widely used Arruda-Boyce model, which assumes that the chains are distributed in a form that 8 chains are attached to the center and to the vertices of a cube. More recently the assumption that the chain is restricted to a tube gave origin to the tube model, and finally the assumption that these chains are continually distributed in a sphere gave origin to the sphere models which are very good at capturing the behavior with few parameters.

### 2.3.4 Basic deformations used for material characterization

If behavior is described by 3 invariants, or 2 in the case of incompressible materials where  $I_3 \approx 1$  which is true for most rubbers, a single test is insufficient to map the input range. Multiple tests with independent variations of invariants are thus needed.

**Simple shear** deformation can be achieved by a “sandwich” test body. Figure 2.1 illustrates both the specimen and the assumed deformation gradient tensor, with a linear variation of strain through thickness.



Figure 2.1: Simple shear specimen and respective deformation tensor.

Applying the assumed shear deformation gradient in equation (2.16), one obtains a Cauchy stress tensor

$$\sigma = \begin{bmatrix} \beta_0 + \beta_1 + \beta_2(1 + \gamma^2) & \gamma(\beta_1 + \beta_2(2 + \gamma^2)) & 0 \\ \gamma(\beta_1 + \beta_2(2 + \gamma^2)) & \beta_0 + \beta_1(1 + \gamma^2) + \beta_2(1 + 3\gamma^2 + \gamma^4) & 0 \\ 0 & 0 & \beta_0 + \beta_1 + \beta_2 \end{bmatrix} \quad (2.24)$$

This stress does not verify the free edge conditions (this is known as Poynting effect [41]). The assumed strain is thus an approximation since the absence of deformations on the free edge is impossible to enforce exactly. The approximation used here was to neglect those effects and assume that only simple shear exists leading to

$$\sigma_{12} = \mathcal{F}/A \quad (2.25)$$

with  $\mathcal{F}$  the measured force, and  $A$  the surface of sheared material.

### 2.3. HYPERELASTICITY

---

**Uniaxial stress** is a state characterized by stretch in one direction while keeping others directions free of sollicitation. Figure 2.2 illustrates both the specimen and the deformation gradient that characterizes this state, when the model is assumed incompressible.



$$F = \begin{bmatrix} \lambda & 0 & 0 \\ 0 & \lambda^{-1/2} & 0 \\ 0 & 0 & \lambda^{-1/2} \end{bmatrix}$$

Figure 2.2: Tension/compression specimen and respective deformation tensor.

It is not simple to ensure a constant deformation gradient in this specimen. Therefore, Vibracoustic NE developed a specific specimen (with special attachments to the machine and fillet splines) that ensures a constant deformation on the central section of the specimen. The relation between machine displacement and strain  $\varepsilon$  in the central section is obtained using a polynomial spline generated by an image correlation procedure. Further details on the specimen are kept confidential.

The section in the middle of the sample sees an enforced  $F_{11} = \lambda$ , and the in plane  $F_{22} = F_{33} = \lambda^{-1/2}$ , for an isotropic material, result from the section surface change linked to the fact that edges are free and that there is no volume change.

The supposed stress tensor from the test has only the component  $\sigma_{11}$  as non zero, while the stress issued for the model has the  $\sigma_{11}$  and  $\sigma_{22} = \sigma_{33}$  components. To reach a stress tensor comparable to the test one, an arbitrary pressure (which does not affect the model, as it is supposed incompressible) may be added. Using a pressure of  $-\sigma_{22}$  to the tensor diagonal would generate the stress tensor with only one nonzero component, comparable to the supposed tested stress tensor, thus

$$\sigma_{11}^D = \mathcal{F}/A = \sigma_{11} - \sigma_{22} \quad (2.26)$$

with  $A$  the area of the section with constant deformation gradient.

**Equibiaxial** sollicitation may be obtained by an equal elongation in two directions. This state may be generated by the stretch of a plane band (this procedure may provide an uneven deformation gradient), or from bubble inflation [6]. The deformation gradient tensor that characterizes this state for an incompressible material is given by

$$F = \begin{bmatrix} \lambda & 0 & 0 \\ 0 & \lambda & 0 \\ 0 & 0 & \lambda^{-2} \end{bmatrix}. \quad (2.27)$$

Exactly like for the tension/compression load, the strain tensor is meant to be diagonal and, thus the stress as well. Again, as the machine imposes a pressure and model where the displacement gradient

## 2.4. VISCOELASTICITY IN FINITE STRAINS

---

is imposed does not generate pressure, the same strategy of using the difference between the principal stresses is used to relate the force to the stress,

$$\sigma^D = \mathcal{F}/A = \sigma_{11} - \sigma_{33} \quad (2.28)$$

where  $A$  designates the surface of the elastic band.

**Hydrostatic** strain requires an equal pressure over the whole specimen. It may be obtained by any specimen shape in a closed container. The deformation tensor should only have values on the diagonal. The force is thus related to the trace of the Cauchy stress matrix.

Figure 2.3 shows the evolution of the two reduced invariants with respect to each of those tests. As all of them present independent evolutions with respect to strain, any combination of two tests (except for the hydrostatic) should be enough to characterize the deviatoric behavior of an hyperelastic material.

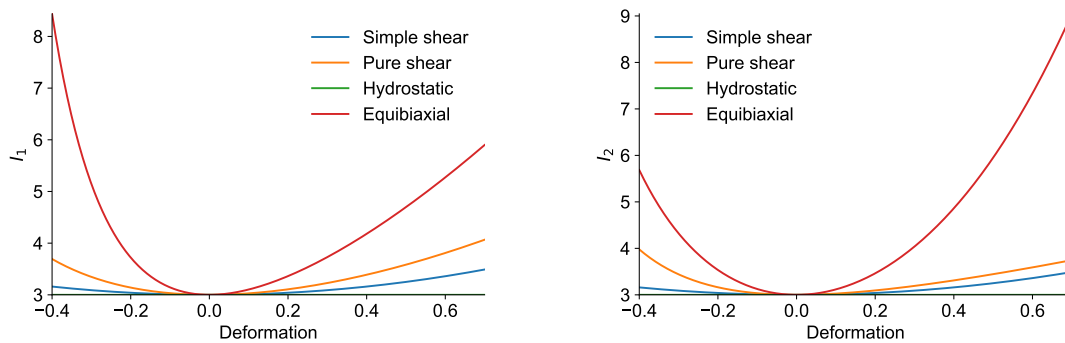


Figure 2.3: Evolution of invariants with deformation for standard tests.

The hydrostatic test acts only on the third invariant, so the values of  $I_1$  and  $I_2$  for this test remains constant at 3.

## 2.4 Viscoelasticity in finite strains

Viscoelasticity expresses the dependency of the behavior to the history of strains. Section 1.3 provided a full background for this behavior in scalar 0D models, and the results will here be extended to 3D finite strains. As large deformation and hyperelasticity is considered, the models are non linear and only time domain formulations will be covered in this section.

### 2.4.1 Finite strain deviatoric viscoelasticity - Simo formalism

The formulation proposed by Simo and Hughes in their book [42] is a generalization of the Maxwell model to deviatoric finite strains. The first step is to define the hyper-elastic potential that replaces

the non-dissipative branch of the Maxwell model, with deviatoric and isotropic contributions split, as illustrated in section 2.3, without restriction on a model choice. Then, the total stress is expressed as the sum of a deviatoric hyperelastic part  $S^0$ , deviatoric viscoelastic branch contributions  $S^i$  and isotropic stress  $S^p$

$$S = S^0 + \sum_{i=1} S^i + S^p. \quad (2.29)$$

Equation (2.15) is thus used to evaluate  $S^0 = g^0 S^\infty$ , and viscoelasticity is introduced by considering a stress relaxation equation for each branch, given by

$$[\dot{S}^i] + \omega^i [S^i] = g^i [\dot{S}^\infty] \quad (2.30)$$

where parameters are the branch fraction  $g^i > 0$ , and characteristic relaxation frequency  $\omega^i$ . Note that here the SDT convention, also used in (1.12), assumes load fractions such that  $\sum_{i=0}^{N_{cell}} g^i = 1$ , corresponding to the use the high frequency modulus as reference. But the Simo-Hughes model implemented in Abaqus uses a different scaling convention with  $\hat{g}^i = g^i/g^0$ .

Since this expression is directly comparable to (1.12), a fixed time step  $\Delta t$  recursion is simply given by

$$S_{n+1}^i = e^{-\omega^i \Delta t} S_n^i + g^i e^{-\omega^i \Delta t/2} (S_{n+1}^\infty - S_n^\infty) \quad (2.31)$$

with  $S_n^\infty$  and  $S_n^i$  hyperelastic and viscous stresses from the precedent time step, respectively stored as internal states.

To avoid round-off errors with hydrostatic pressure in these computations, the deviatoric constraint may be enforced by transforming the 2nd Piola Kirchhoff stress into the Cauchy stress ( $\sigma = F S F$ ) and removing its isotropic part ( $\bar{\sigma} = \sigma - \mathbb{1} = \text{dev}(\sigma)$ ) [42]. In other words using

$$\bar{S}^\infty = F^{-1} \text{dev} \left( F S^\infty F^T \right) F^{-T} \quad (2.32)$$

### 2.4.2 Bulk viscoelasticity

If viscoelastic dissipation is only applied to the deviatoric part, non-dissipative isotropic waves (p-waves) [51] are propagated without dissipation in the material, and as long as energy is injected, these waves will grow in amplitude and cause high frequency instabilities.

To mitigate this problem, one may either use a dissipative integration scheme, or impose viscoelastic dissipation on the isotropic component [52]. Here, the material level solution will be privileged to provide a proper response independently from solver adjustments. Given that this component is not identified, and this effect is only desired for numerical reasons, a single viscoelastic cell is implemented, so the full pressure can be computed by  $p = p^1 + p^0$  with  $p^0$  obtained from (2.19), and  $p^1$  relaxation described by

$$\dot{p}^1 + \omega^p p^1 = g^p \dot{p}^0 \quad (2.33)$$

or the recursion scheme,

$$p_{n+1}^1 = p_n^1 e^{-\omega^p \Delta t} + g^p e^{-\omega^p \Delta t/2} (p_n^0 - p_{n-1}^0) \quad (2.34)$$

where the parameters using exponent  $p$  are relative to the isotropic behavior.

To limit instabilities is it classical to place this cell near the p-wave frequency given by

$$f_{p\text{-wave}} = \frac{\sqrt{\frac{\lambda + 2\mu}{\rho}}}{l_{elt}^2} \quad (2.35)$$

where  $\lambda$  and  $\mu$  are the linearized Lamé coefficients,  $\rho$  the mass density, and  $l_{elt}$  element characteristic length. As each element has its own length, it is important that every element present a similar size to avoid a large dispersion on this value, or to impose this coefficient for each element.

### 2.4.3 Non-linear transition between viscoelasticity and hysteresis

As for 0D models, rate independent hysteresis would be interesting for 3D models. This corresponds to the use of plasticity models. This is a topic known to be difficult for finite strains. Significant effort was spent gaining understanding of the difficulties of kinematic hardening in the context of finite strains and some details are given in appendix A for future reference. Eventually, the conclusion of work on 0D models in section 1.5 was that non-linear viscosity gave very appropriate results.

This choice was in particular motivated by material modeling work in [33] where the idea was introduced using the term *reduced time*  $\xi_i$ , computed for each cell using

$$\xi^i = \Delta t \left( 1 + \sqrt{\frac{2}{3}} \beta^i \|d\| \right) \quad (2.36)$$

with  $d$  the deformation rate gradient given by

$$d = \frac{1}{2} F^{-T} (F^T \dot{F} + \dot{F}^T F) F^{-1} \quad (2.37)$$

Here we prefer to state, as in section 1.5, that relaxation frequencies are non-linear with a reference strain saturation given by

$$\epsilon_f^i = \frac{1}{\beta^i \omega^i \sqrt{2/3}} \quad (2.38)$$

leading to the stress relaxation is given by

$$[\dot{S}^i] + \left( \omega^i + \frac{\|d\|}{\epsilon_f} \right) [S^i] = g^i [\dot{S}^\infty] \quad (2.39)$$

To simplify equations, one may use

$$\hat{\omega}^i = \omega^i \left( 1 + \sqrt{\frac{2}{3}} \beta^i \|d\| \right) = \omega^i + \frac{\|d\|}{\epsilon_f^i} \quad (2.40)$$

## 2.5. PERSPECTIVES AND CONCLUSIONS

---

Leading to the recursion scheme

$$S_{n+1}^i = e^{-\hat{\omega}^i \Delta t} S_n^i + g^i e^{-\hat{\omega}^i \Delta t / 2} (S_{n+1}^\infty - S_n^\infty) \quad (2.41)$$

To avoid the computation of exponential functions at every time-step, one may assume small values for  $\hat{\omega}^i \Delta t$ , to obtain the first order relaxation scheme

$$S_{n+1}^i = (1 - \hat{\omega}^i \Delta t) S_n^i + g^i (S_{n+1}^\infty - S_n^\infty) \quad (2.42)$$

The pseudo-algorithm in figure 2.4 details the implementation made for 3D models.

<p><u>Hyperelastic computation</u></p> $F_{n+1}, \dot{F}_{n+1}, S_n^i, S_n^0, p_n^0, p_n^1$ $C_{n+1} = F_{n+1}^T F_{n+1}$ $d_{n+1} = \frac{1}{2} F_{n+1}^{-T} (\dot{F}_{n+1}^T \dot{F}_{n+1} + \dot{F}_{n+1}^T F_{n+1}) F_{n+1}$ $I_{1n+1} = \text{tr}(C_{n+1})$ $I_{2n+1} = \text{tr}^2(C_{n+1}) + \text{tr}(C_{n+1}^2)$ $J_{n+1} = \det(F_{n+1})$ $S_{n+1}^\infty = 2 \sum_k \frac{\partial I_k}{\partial C_{ij}} \frac{\partial \psi}{\partial I_k} (C_{n+1})$	<p>Get deformation and internal states</p> <p>Main deformation tensors</p>
<p><u>Relaxation of cells <math>i</math></u></p> $\hat{\omega}_{n+1}^i = \omega^i + \frac{\ d_{n+1}\ }{\epsilon_f^i}$ $S_{n+1}^i = e^{-\hat{\omega}_{n+1}^i \Delta t} S_n^i + g^i e^{-\hat{\omega}_{n+1}^i \Delta t / 2} (S_{n+1}^\infty - S_n^\infty)$	<p>Invariants</p> <p>Deviatoric hyperelastic stress</p> <p>Loop on viscous cells</p> <p>Non-linear relaxation frequency</p> <p>Viscous stress</p>
<p><u>Compressive stress</u></p> $p_{n+1}^0 = \frac{\partial \psi^I}{\partial J}$ $p_{n+1}^1 = p_n^1 e^{-\omega^p \Delta t} + g^p e^{-\omega^p \Delta t / 2} (p_{n+1}^0 - p_n^0)$ $S_{n+1}^p = (p_{n+1}^0 + p_{n+1}^1) F_{n+1}^{-1} F_{n+1}^{-T}$	<p>Elastic pressure</p> <p>Bulk viscosity</p> <p>Pressure</p>
<p><u>Output</u></p> $S_{n+1} = g^0 S_{n+1}^\infty + \sum_i S_{n+1}^i + S_{n+1}^p$ $U_{int} = \begin{Bmatrix} p_{n+1}^0 \\ p_{n+1}^1 \\ S_{n+1}^\infty \\ S_{n+1}^i \end{Bmatrix}$	<p>Output stress</p> <p>Internal state propagation</p>

Figure 2.4: Pseudo algorithm for constitutive law integration.

## 2.5 Perspectives and conclusions

The model developed illustrated in this chapter was fully integrated into SDT with robustness and stability ensured after verification tests. Computational time optimization of these routines are still a perspective.

## 2.5. PERSPECTIVES AND CONCLUSIONS

---

In terms of model development, a few of the same remarks applied to 0D models also apply here: damage can be taken into account in the long term, while kinematic plasticity may also be added to represent pure path effects, and the first steps in this direction are illustrated in appendix A. As for the 0D models, a single model of the transition between pure hysteresis and pure viscoelasticity is proposed.

Beyond these implementations, there is also the possibility to split the deviatoric potential to be able to independently identify the different tests for the same 3D model, as suggested in section 3.4.1.

# Chapter 3

## Identification

### Contents

---

<b>3.1</b>	<b>Introduction</b>	<b>106</b>
<b>3.2</b>	<b>Tests conception</b>	<b>106</b>
3.2.1	Introduction: test objectives	106
3.2.2	Specimen and testing machine	107
3.2.3	Test parameters	109
3.2.4	Low speed test: filtering	111
3.2.5	Sine tests: instantaneous modulus and 1st harmonic	113
3.2.6	Mullins and long term effects	115
<b>3.3</b>	<b>Classical material identification procedure</b>	<b>116</b>
3.3.1	Hyperelastic coefficients	117
3.3.2	Hysteretic rate independent dissipation	118
3.3.3	Viscoelasticity	120
3.3.4	Identification results	122
<b>3.4</b>	<b>Non-parametric and selected order identification</b>	<b>123</b>
3.4.1	Hyperelastic behavior	124
3.4.2	Hysteretic relaxation	125
3.4.3	Viscoelastic frequency evolution	127
<b>3.5</b>	<b>Synthesis and perspectives</b>	<b>129</b>
3.5.1	Test synthesis	129
3.5.2	Perspectives and conclusions	136

---

## 3.1 Introduction

Chapter 1 focused on model choices and used a few test results to gain understanding on their properties. This chapter seeks to compare results of the full test campaign and discuss identification procedures.

The conception of the tests began with what was sought to be modeled, which in the case was quite clear: frequency, amplitude, preload and path effects. The next step was the choice of the specimen, going from a specific vehicle part to its materials. Finally, the test parameters were set based on coherence between part solicitations and resources available. The conception procedure is detailed in section 3.2.

Few results were selected from the large pool of generated data to create a classic identification procedure, detailed in section 3.3. These few selected results were compared to a 3D model, as the one described in section 2.4, to create an objective function to be minimized. The results of such identification were compared to the selected results.

As the results from the classical identification routine were not completely satisfying, a novel identification routine is proposed in section 3.4. Such routine consists of the extraction of a base hyperelastic behavior, a hysteretic curve from triangular tests, and a viscoelastic contribution. The two dissipative branches are normalized with respect to the hyperelastic one and they are graphically identified using selected order parametric models, as described in sections 1.4.2 and 1.3.3. The obtained models are compared to the synthesis of the test results.

Finally, the test results are summarized in a single plot, already introduced in the first chapter, and the perspectives for future work in this field are discussed, in section 3.5.

## 3.2 Tests conception

### 3.2.1 Introduction: test objectives

As first analyzed for the 0D case in chapter 1, the main phenomena that one seeks to characterize through tests are hyperelasticity, rate-independent hysteresis, viscoelasticity and their non-linear dependencies. All these phenomena may be dependent on both material and geometry, so special attention must be made on the test body selection to limit sensitivity to geometric effects in material tests, while it is impossible to make this separation for part tests.

The first difficulty was to design and deploy of a test campaign able to capture all these effects. Later exploitation led to propositions in non-parametric and parametric identification phases that were detailed in chapter 1. It is however worth mentioning the initial choices used to design the test campaign. For hyperelastic identification, a sequence of relaxations or multi-step relaxation test was retained as suggested in ref. [10]. For hysteretic behavior, constant low speed tests (triangular

## 3.2. TESTS CONCEPTION

---

loading) were considered to allow a verification of insensitivity to strain rate. For viscoelastic response, sinusoidal sollicitation is the classical approach and was kept here. To visualize amplitude effects, the triangular and sine tests were performed at different amplitudes.

The preload effects are often studied for fatigue design, as statically loaded polymers present longer life cycles [53], but since this work focuses on multibody aspect, one also sought to visualize the nonlinear effects that preloading has on viscous and hysteretic behavior and interpret whether these are dependent on strain state.

### 3.2.2 Specimen and testing machine

To characterize materials, the test body should provide a known deformation field as function of the applied displacement, as discussed in section 2.3.4. As the material will be described with invariant based hyperelasticity and considered incompressible, at least two specimen should be used. The specimens chosen to characterize the deviatoric behavior are the simple shear and the tension/compression ones, also presented in section 2.3.4 and shown in figure 3.1a,b.

### 3.2. TESTS CONCEPTION

---

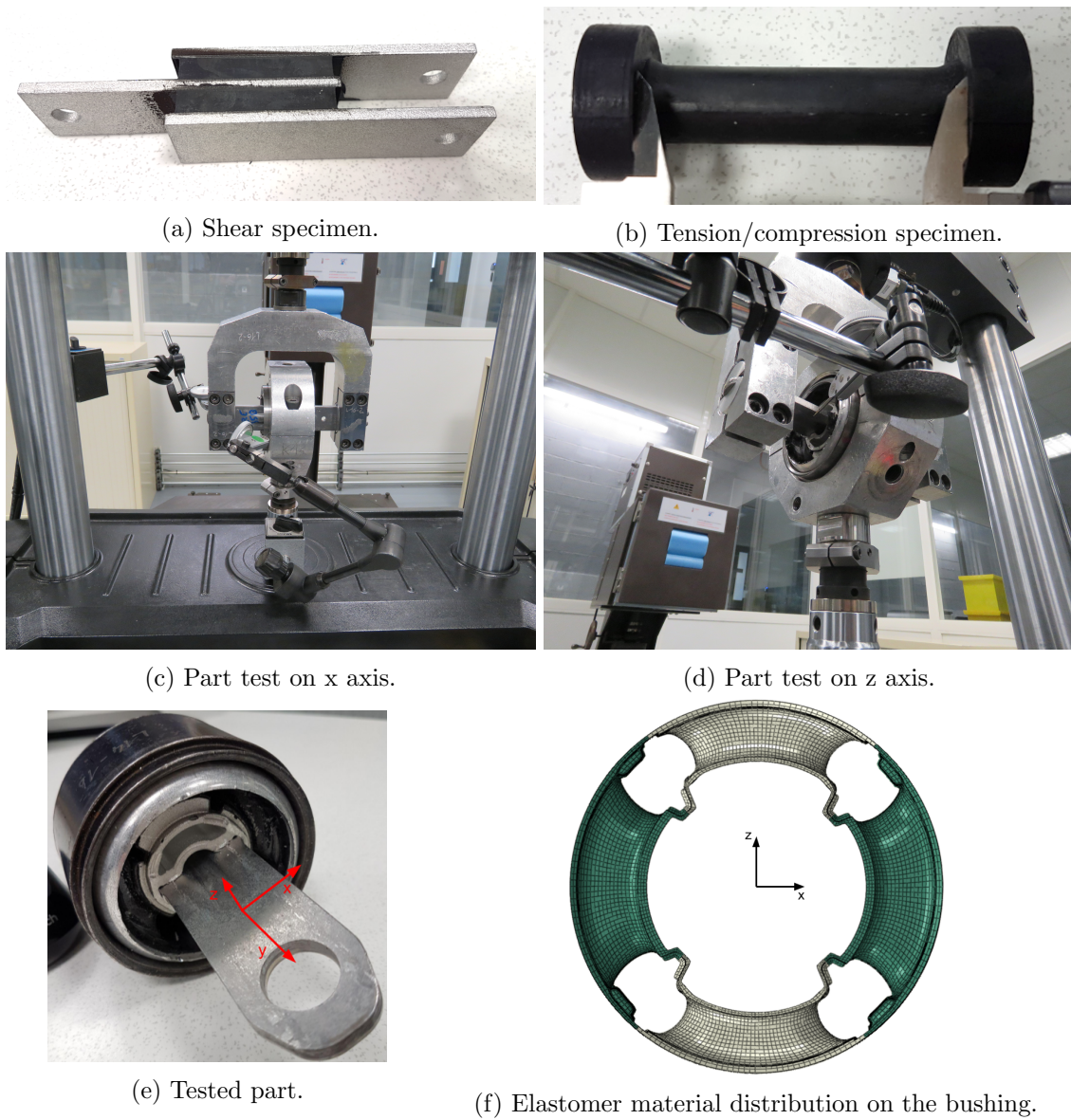


Figure 3.1: Specimens used and tested part illustration

For the part tests, a rear twist beam axle bushing shown in figure 3.1e will be considered. The selected part often undergoes coupled solicitations as it transmits lateral, longitudinal and vertical forces that may happen simultaneously, making it particularly interesting for the intended multibody implementations.

The bushing mesh illustrated in figure 3.1f concerns only the elastomer compounds. The outer edge is vulcanized into the external metallic interface, and the inner edge is vulcanized into the internal metallic interface connected to the blade. The colors in the scheme designate two different materials, later labeled **m1** and **m2**. Thus all material tests are made for both compounds, and the part will be

## 3.2. TESTS CONCEPTION

---

subjected to its two main working directions, denoted **px** and **pz**, as in figure 3.1c to f. The four voids are filled with a plastic piece that ensures contact generating a stiffening effect. Such piece was removed due to the fact that there were no short-term plans to consider contact effects and that the setup with the plastic limiter is too stiff for the testing machine.

One of the main solicitations in this part happens in the vertical direction where it transmits the road noise to the chassis. For this reason, the material in the z direction of this part is relatively less damped to avoid stiffening. As the other main solicitation direction is not perfectly aligned to the vehicle, a component between x and y directions (mainly in x axis) is responsible to transmit longitudinal forces to the chassis. The material in the x direction is thus more damped to dissipate undesired suspension lateral modes.

The machine used for material specimen tests is a MTS Landmark 200Hz Elastomer Test System, whose data sheet suggests a maximal load of 25kN and stroke of 120mm.

### 3.2.3 Test parameters

To select the parameter for the tests, each individual specimen was analyzed.

For the uniaxial tests, the base values for strains was set according to the ability of the specimen to sustain a constant section under loading/unloading, which is between -30% and 60%. Thus, multi-step tests for this specimen were set with 10% intervals between those values. Two relaxation times - 5min and 1h - were selected to verify if the material relaxes in a longer timescale. For the triangular tests, a few variations were defined: at null prestrain several amplitudes were tested in a logarithmic scale to verify Payne effect; at fixed amplitude several prestrains were tested to verify the Madelung rules; and finally, a few high amplitude cycles are made in fixed amplitude and varying prestrain and speed to verify rate-independence at those operation points. As this test was conceived with imposed displacements, the strain-rate is not perfectly constant (there is a confidential non-linear relation between displacement and strain for this specimen), conferring a different allure to the triangular tests. Finally for the sine tests, due to the long waiting time between each preload (waiting for relaxation), the steps between prestrain were set to 15% instead. For each prestrain, variations in amplitude and frequency were set. The prestrain restrictions were given by the specimen (-30%to 60%), while the lowest frequency was set to 0.1Hz (below this frequency effects are supposed to be considered rate-independent), while the highest one is set to 100Hz, which was already past the machines capabilities. In terms of amplitude, 0.1% was already on the edge of the machine sensing capacity and 10% is close to the dynamic limit of the machine (specially at 100Hz).

As all the verifications on the materials were meant to be in the tension/compression tests, and it was thought that the viscoelastic and hysteretic behavior would be similar for both specimen, the shear tests were significantly less sampled. For shear tests, the maximum of 100% of strain was selected, as strains are not supposed to reach this level on the selected part. Given the symmetry of the strain

### 3.2. TESTS CONCEPTION

---

tensor with respect to negative strains, the minimal strain was set to 0%. The same approach for the multi-step tests was used, with 10% strain steps. As the verification of the Payne effect and the Madelung rules were supposed to be made in the tension/compression specimen, it was decided to repeat only the last part of the triangular tests: two different speeds and two different prestrain, with amplitude variations for null prestrain. For the sine tests, the same amplitudes and frequencies as the tension/compression tests were applied, but this specimen was less sampled in prestrain (0, 45% and 90%).

The profiles for imposed strains are illustrated in figure 3.2, and a table describing specifically all the sampling points is available in appendix B.

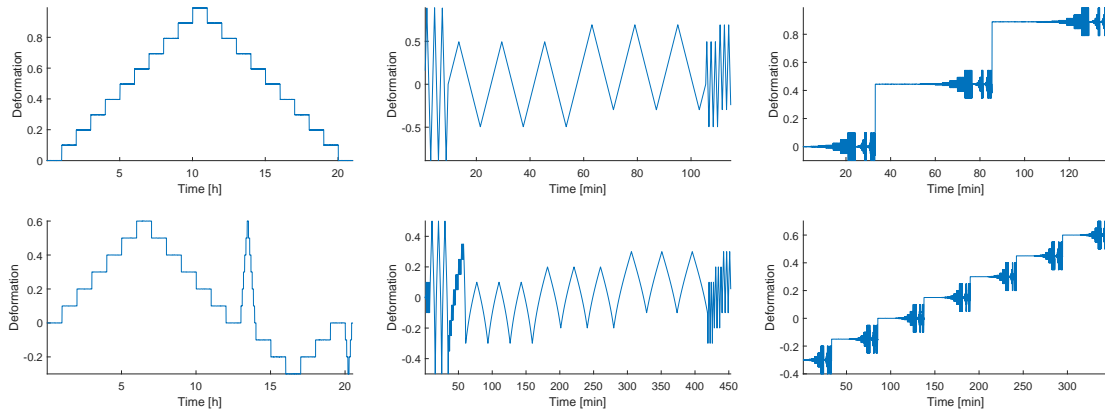


Figure 3.2: Strain profiles for each test: Multi-step, triangular and sine (columns) for shear and tension/compression specimen (lines).

Figure 3.3 zooms on the sine tests after an amplitude sweep at a fixed frequency.

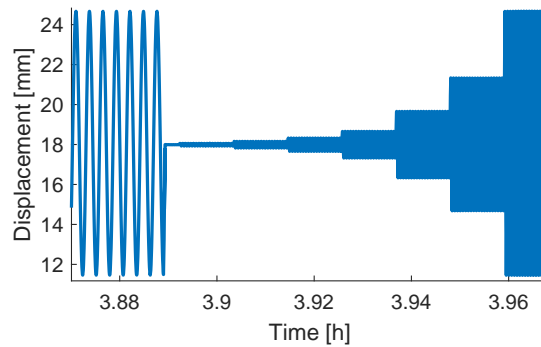


Figure 3.3: Detail on sine profile: changing frequency after amplitude sweep.

For the part tests, it was also sought to verify all the effects at part level. As the part is symmetric with respect to the x and z planes, the parameters were identically set. The multistep tests in the

## 3.2. TESTS CONCEPTION

---

part were limited by the machine capabilities at 4mm, while the minimum is set at 0mm due to the symmetry of the part. The steps for the multistep test were set at 0.5mm with 1h of relaxation time. For the triangular tests, the amplitude sweep was made at null prestrain, then a prestrain sweep at fixed amplitude, and finally the rate-independence test with two different speeds at two different prestrains, similarly to the tension/compression tests. For the sine tests, the same principles were used, but here, the prestrain steps were set to 1mm, while amplitudes were swept from 0.1mm (close to the sensing capacity) to 1mm (close to the machine dynamic capacity at 100Hz), finally, the same frequencies from material tests (0.1Hz to 100Hz) were retained. The enforced displacements for part tests is summarized in figure 3.4, while the detailed parameters for all the tests is also summarized in appendix B.

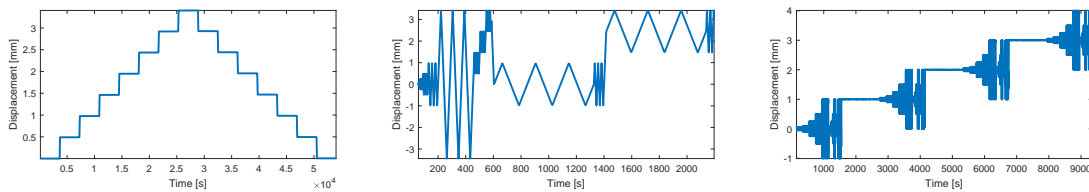


Figure 3.4: Displacement profiles for part tests: Multi-step, triangular and sine.

The acquisition rate for all multistep tests is set at 1Hz for the relaxation phase and 20Hz for the ramps. For the triangular tests, the acquisition rate is set at 3Hz for tests at 10mm/min and 0.3Hz for tests at 1mm/min. The acquisition frequency for sine tests is set at 50 times the solicitation frequency, and the relaxation phases after the prestrain change (which takes 20 minutes) have an acquisition rate of 1Hz.

### 3.2.4 Low speed test: filtering

The notion of hysteretic relaxation was introduced in chapter 1, and will be here discussed for low-speed triangular wave tests. As the machine was designed to measure force and not force variations, it was not obvious that measurements contained high frequency components. These are however strongly present as visible in figure 3.5 and must be filtered.

As first attempt, a double second order low-pass Butterworth filter (forward and backward to avoid phase differences) with a cutoff frequency of 1/10 of the acquisition rate was applied to the triangular test signals. With this approach, there is a significant loss of data near the turning points, where unreasonable values are found, illustrated in figure 3.5 in red. A better approach separates upward and downward parts of the cycle and filters each separately. The results, in figure 3.5 illustrates the application of both filters and its comparison with unfiltered data for one of the tests. Despite the fact that the hysteretic relaxation is not lost with the filter, the end of the curves are still quite noisy (not sufficiently sampled). For future tests, the acquisition rate should be increased right after the turning

### 3.2. TESTS CONCEPTION

points and work should be done on improving the noise levels.

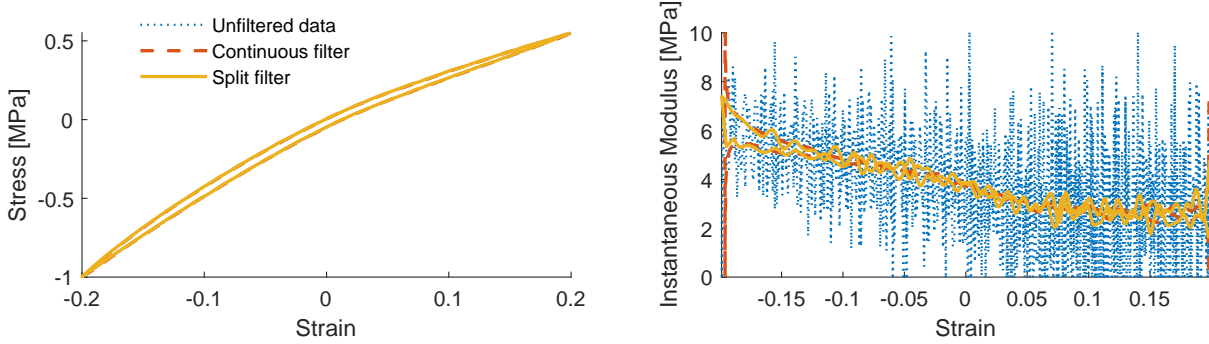


Figure 3.5: Difference between considered filters and unfiltered data.

In figure 3.6, one considers three tests with different initial offsets  $C_0 = -20, 0, 20\%$ . Interpreting the stress/strain curves is not obvious, but qualitatively away from the turning point, the slopes only depend on position - meaning an underlying hyperelastic behavior. And for some distance away from the turning point, the slope is higher. This phase was called hysteretic relaxation.

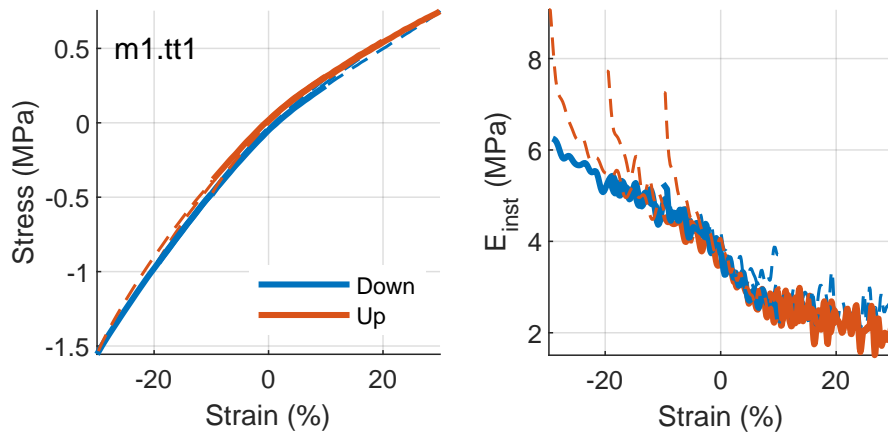


Figure 3.6: Triangular wave test results: underlying hyperelasticity and hysteretic relaxation

Distinguishing hysteretic relaxation and hyperelastic parts is somewhat arbitrary. But it is not quite clear whether the differences between various curves in the hyperelastic areas, seen in figure 3.6, are due to reproducibility issues or noise filtering effects. Thus a manual selection of distances was performed for identification, and thoroughly in section 3.4. On the part model, the separation is even less evident as strain is not uniform throughout the body, so the hysteretic relaxation is not the same as the materials.

### 3.2.5 Sine tests: instantaneous modulus and 1st harmonic

To extract data from sine tests, the classic strategy is to extract (or approximate) the first harmonic component of the response and consider non-linearities as frequency and amplitude dependence. These data will be used to identify models in sections 3.3 and 3.4.

Despite providing all the needed data, some tests in this elaborate campaign failed. The main issues are the small amplitudes and high frequencies in sine tests. Figure 3.7 illustrates that yellow and green points (50Hz and 100Hz for smaller amplitudes) in the storage modulus map are notably lower, indicating wrong data, which is not particularly surprising since high frequency excitation is always more difficult to enforce in a high load machine. These data were later removed from all identification and plots.

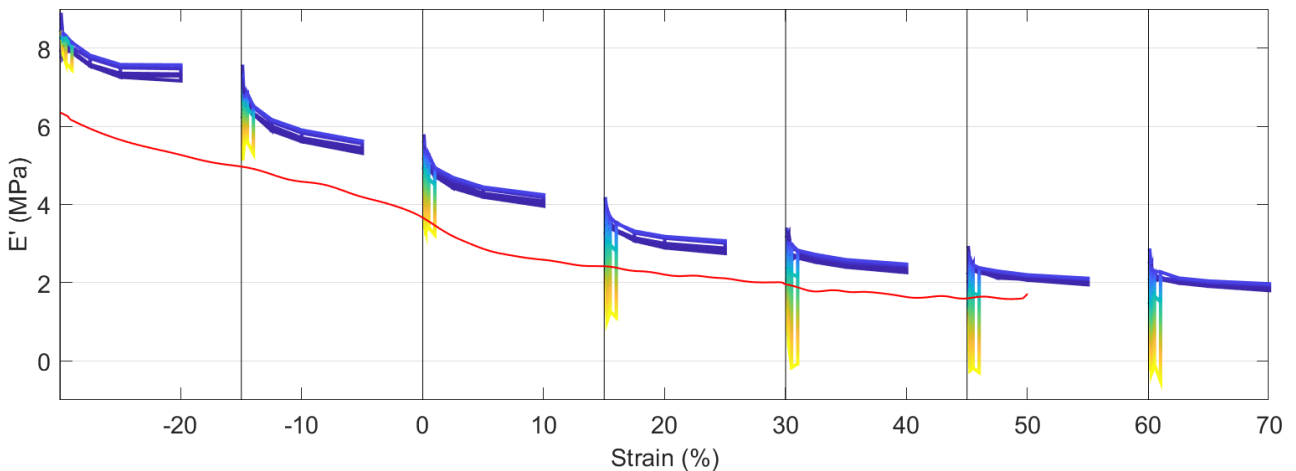


Figure 3.7: Failed HF tests

Looking at the stress-strain plot for the time domain reconstitution of the Fourier series for those results up to the fourth harmonic, in figure 3.8, the responses do not seem to provide a reasonable behavior for the material.

### 3.2. TESTS CONCEPTION

---

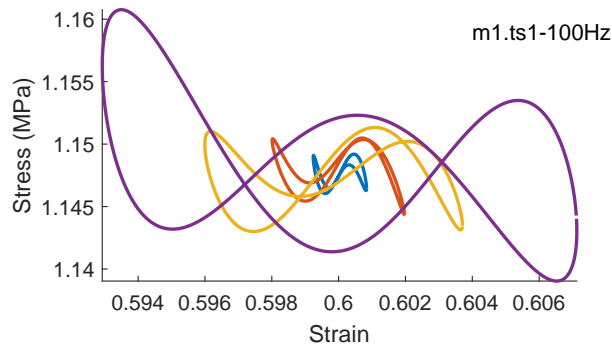


Figure 3.8: Stress-strain curves for failed HF tests.

Considering the system as linear time varying, the proposed instantaneous modulus illustrate fairly well how the non linearities of the system may be expressed, as was already shown in section 1.5.3. This is illustrated in figure 3.9 where the instantaneous modulus varies strongly within the cycle, also allowing to visualize the Payne effect by showing the modulus for lower amplitudes above the larger amplitude. The use of this modulus in terms of evaluation and identification will however remain as a perspective, though it provides a qualitative view on the modeled behavior.

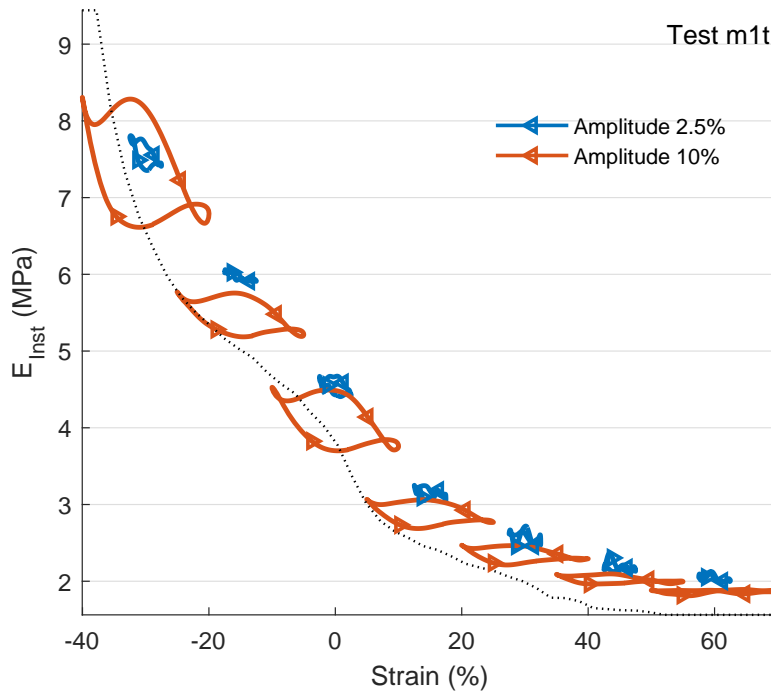


Figure 3.9: Instantaneous modulus extraction from sine tests.

### 3.2.6 Mullins and long term effects

Beyond effects that are viewed in a timescale of hours, the Mullins effect, which is commonly seen as the softening that filled rubbers go through after the first loading cycles, may also be present after a few *months* [54]. This effect is clearly visible in figure 3.10 illustrates, but after the first few cycles, it is completely negligible with respect to the other effects, so when emulating utilization conditions or a large number of cycles, it is often disregarded.

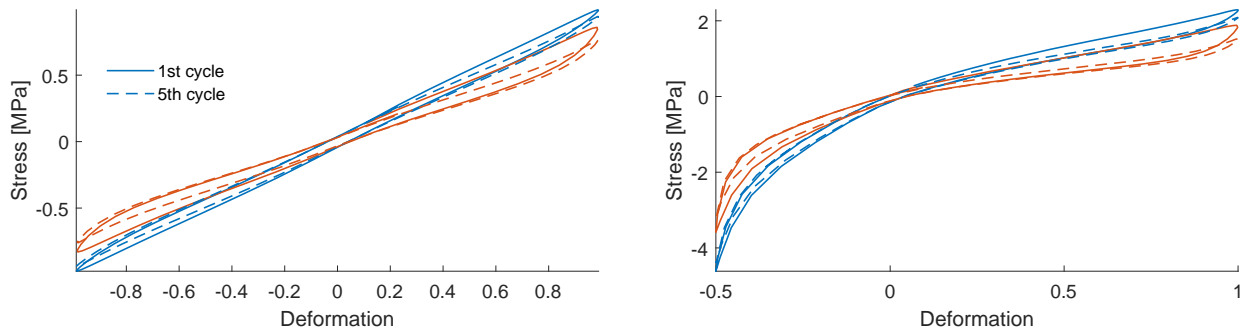


Figure 3.10: Mullins effect illustration for two materials in shear (left) and in tension/compression (right).

From a practical perspective this effect will be disregarded by loading the specimen with five cycles right before each test, with larger amplitudes than the ones associated to the tests.

Determining *long term* effects is not very simple due to the time scaling difficulty. From the viscoelastic point of view, relaxation tests like the steps of the multi-step tests are the simplest manner to extract the complex modulus in very long timescales. The steps are actually 20s ramps followed by an hour of relaxation. The relaxation associated with such ramps excites frequencies up to 0.05Hz, so that one can use standard transfer function estimation [22] to obtain the complex moduli. Figure 3.11 illustrates the extraction of this modulus for shear tests.

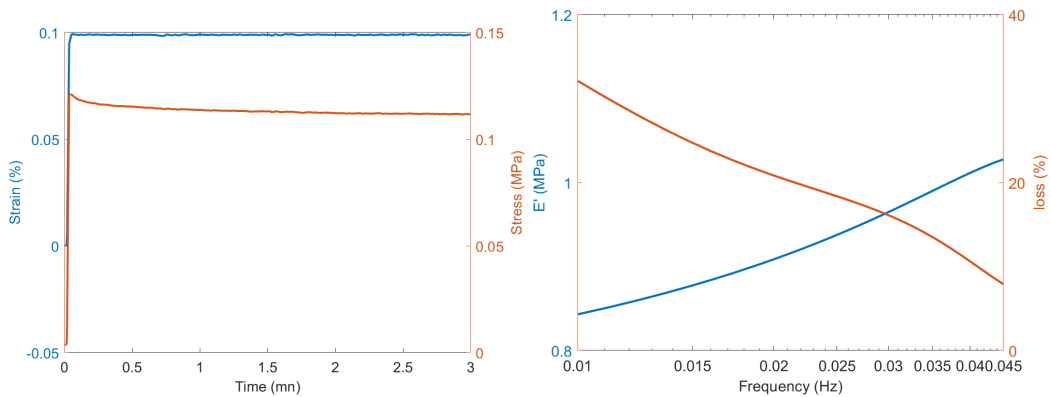


Figure 3.11: Relaxation modulus extraction for multi step tests.

### 3.3. CLASSICAL MATERIAL IDENTIFICATION PROCEDURE

In a different perspective, computing the storage and relaxation moduli for both specimen and plotting them as function of strain for multi-step tests, it is clear that the map is not symmetric with respect to loading and unloading, as seen in figure 3.12. This might be an indication that there is a history effect in the time scale of hours which might be related to the Mullins effect. Plots in section 3.5 illustrate how the relaxed modulus is placed with respect to the estimation of hyperelastic curve.

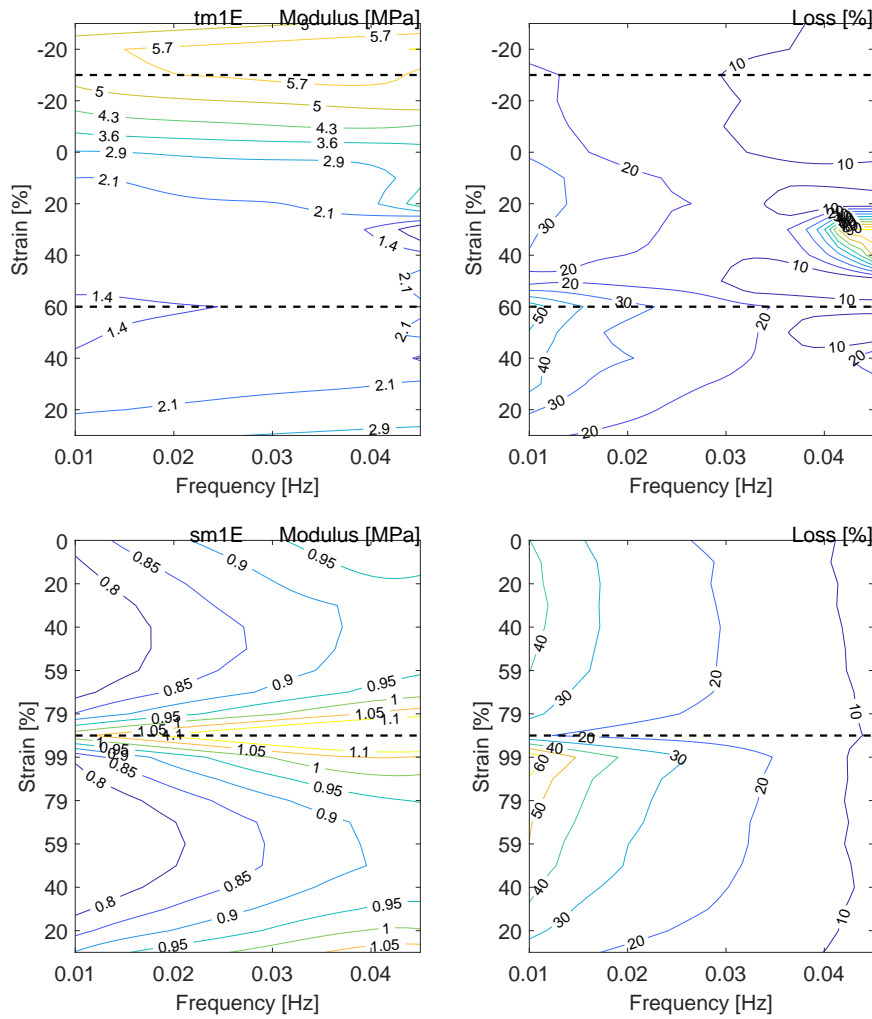


Figure 3.12: Maps for relaxation modulus in function of step amplitude. Top: tension/compression specimen. Bottom: shear specimen.

### 3.3 Classical material identification procedure

Classical material identification procedures are based on a few reference curves, i.e. *non parametric identification*, the choice of a model form and the definition of an objective function measuring the

difference between model and non-parametric test results. As three different tests with different identification goals were chosen, a different objective is established for each, with the initial idea that each should give different parameters.

The chosen model is the one presented in figure 2.4 and stress/strain curves are obtained using the evolution equation (2.13), for both tension/compression and simple shear solicitations. The base hyperelastic part is represented with Carroll deviatoric hyperelastic potential and Ciarlet-Geymonat bulk potential, presented in sections 2.3.3 and 2.3.2. Nonlinear viscoelastic coefficients are used for hysteretic behavior obtained with triangular tests. Finally viscoelastic fractions and frequencies are used for viscoelasticity obtained with sine tests.

#### 3.3.1 Hyperelastic coefficients

As detailed in section 2.3 the model contains a deviatoric part to be identified and a bulk part that is assumed almost incompressible - quite common assumption for elastomers. However, for numerical implementation it is much simpler to implement compressible models than perfectly incompressible ones. Thus, a bulk modulus was set to 30MPa for both materials, which is more than one order of magnitude larger than the expected linearized shear modulus, ensuring that the model behavior is almost incompressible.

The identification of hyperelastic coefficients  $c_1$ ,  $c_2$  and  $c_3$  is based on the average stress from the relaxed stresses of the multi-step tests (even though it later appeared that triangular tests give more information). For the simulation, all the viscous fractions were set to zero, so only one step is enough to compute the hyperelastic response. The objective function used is

$$f_{HE} = \sum_{n_{step}} \left( \sigma_{relax}^{calc} - \sigma_{relax}^{test} \right)^2, \quad (3.1)$$

where  $\sigma_{relax}^{calc}$  is the value simulated by the model and  $\sigma_{relax}^{test}$  represent the test results. Figure 3.13 shows points taken for stresses and the fitting results for both materials and both specimen.

### 3.3. CLASSICAL MATERIAL IDENTIFICATION PROCEDURE

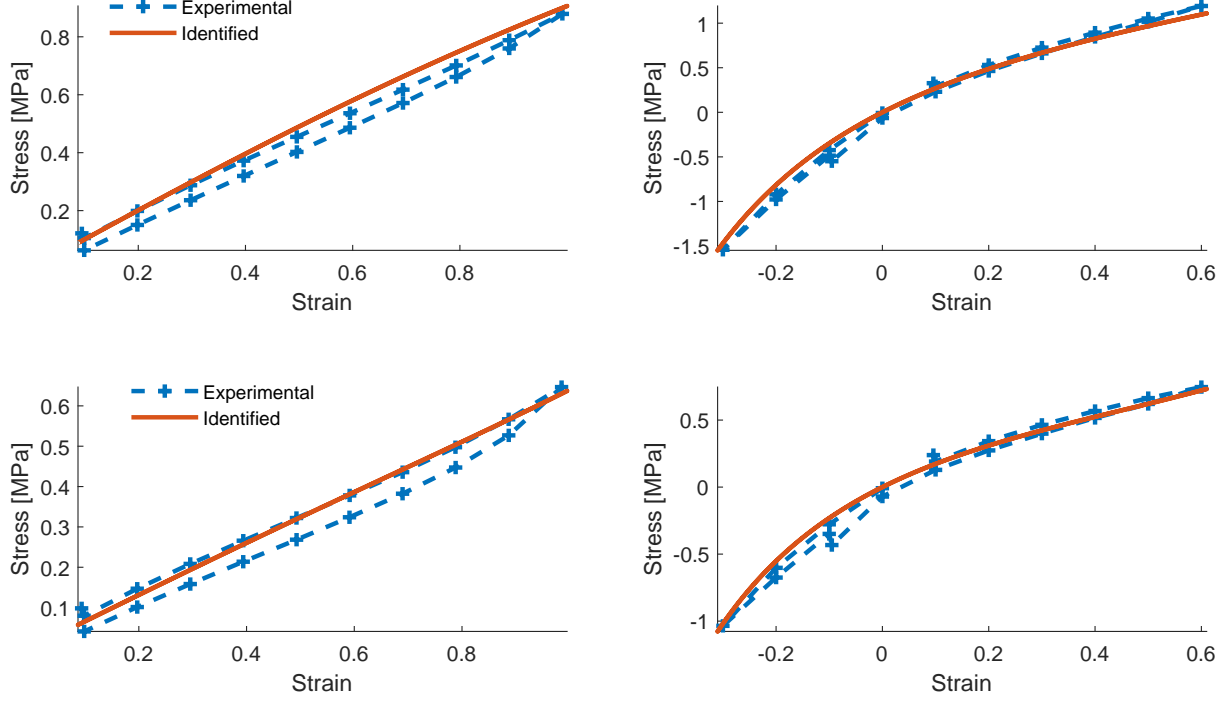


Figure 3.13: Comparison between hyperelastic identification and reference multi-step tests. Left: shear, right: tension/compression. Top: material 1, bottom: material 2

Further details on invariant based non-parametric identification will be given in section 3.4.1.

#### 3.3.2 Hysteretic rate independent dissipation

As discussed in section 2.4.3, the transition between viscoelasticity and pure hysteresis may be done with a nonlinear viscous cell, and its parameters  $g^1$  and  $\epsilon_f^1$  should be determined. At first, a single cell with a fixed frequency of 0.005Hz (more than a decade below the slowest sine test). The tests used for reference for this behavior are the triangular ones with no prestrain.

Since the two values are attached to the same cell, they must be determined simultaneously. Although, as they do have different natures, the objective must use features that are sensitive to different aspects: stiffness and dissipation. This defines a multiobjective optimization, meaning that the objectives must be normalized to avoid the possibility of one outweighing the other.

For dissipation, which is mostly sensitive to the load fraction  $g^1$ , one uses the dissipated power over one period

$$W_d = \int_0^T \sigma \dot{\epsilon} dt \quad (3.2)$$

### 3.3. CLASSICAL MATERIAL IDENTIFICATION PROCEDURE

and defines a objective as

$$f_{g_{LF}}(g^1, \epsilon_f^1) = \sum_{n_{amp}} \left( \frac{W_d^{comp}}{A_\sigma A_\epsilon} - \frac{W_d^{test}}{A_\sigma A_\epsilon} \right)^2, \quad (3.3)$$

with normalization with respect to stress and strain amplitudes given by

$$A_\sigma = \max(\sigma) - \min(\sigma), A_\epsilon = \max(\epsilon) - \min(\epsilon), \quad (3.4)$$

For the stiffness, which is sensitive to  $\epsilon_f^1$ , the secant modulus decreases with amplitude. The chosen objective is based on such secant modulus,

$$K_s = \frac{A_\sigma}{A_\epsilon} \quad (3.5)$$

and measures the drop in this modulus with amplitude using

$$f_{\beta_{LF}}(g^1, \epsilon_f^1) = \sum_{i=1}^{n_{amp}-1} \left( \left( K_t^{comp}|_{i_{amp}} - K_t^{comp}|_{i_{amp}+1} \right) - \left( K_t^{test}|_{i_{amp}} - K_t^{test}|_{i_{amp}+1} \right) \right)^2, \quad (3.6)$$

Figure 3.14 illustrates computed and tested evolution for secant modulus with the triangular cycles amplitudes for both tension/compression specimens, with differences below 15%.

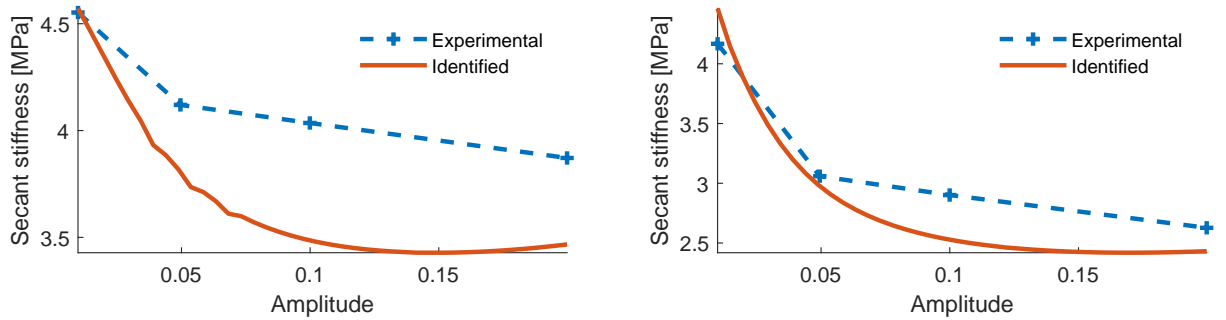


Figure 3.14: Comparison between tested and identified secant modulus softening with amplitude for tension/compression specimen. Left: material 1, right: material 2

A more visual evaluation for this identification is provided in figure 3.15, where the simulated triangular cycles in the strain/stress plane are plotted and compared with the tested ones for different amplitudes. The plot in shear present a good agreement for both tested amplitudes, meanwhile in tension/compression the model apparently highly overestimates the dissipation when in compression.

### 3.3. CLASSICAL MATERIAL IDENTIFICATION PROCEDURE

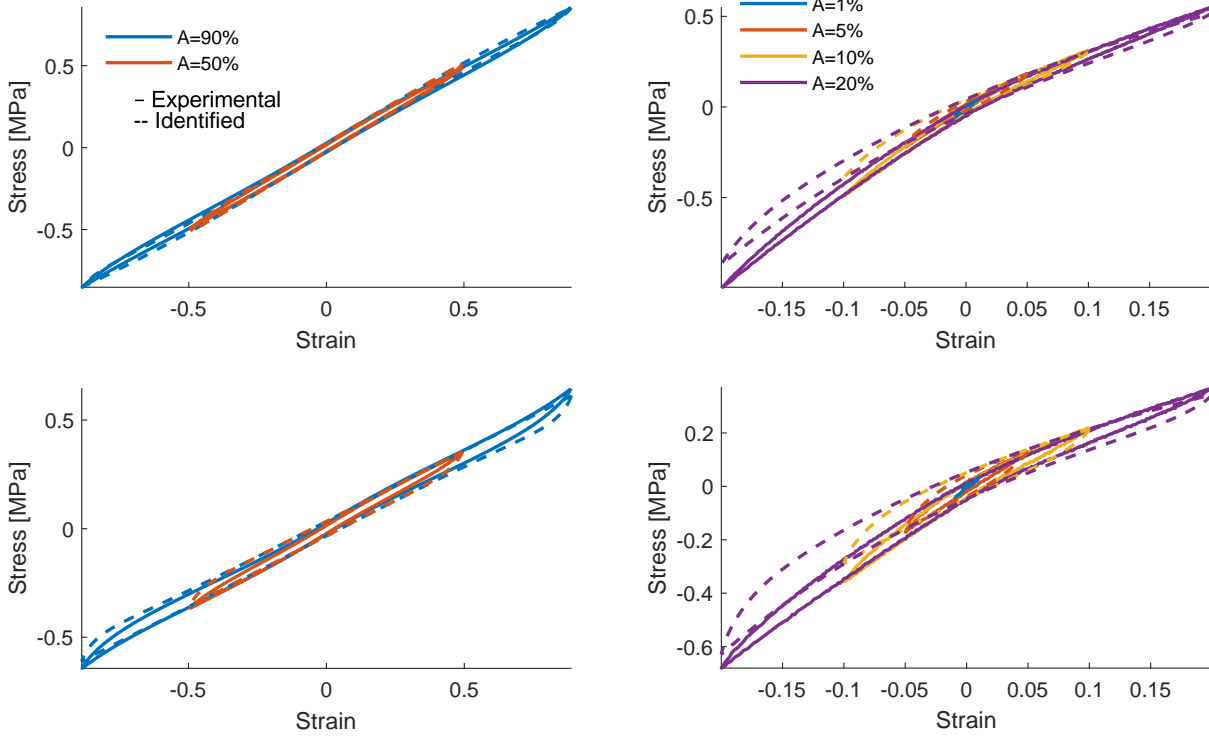


Figure 3.15: Comparison between tested and identified behavior for triangular solicitations. Top: material 1, bottom: material 2, left: shear specimen; right: tension/compression specimen.

A posteriori, the objective on secant stiffness dependence on amplitude also measures hyperelasticity for large amplitudes and better choices could be made, such as using ratios with respect to the hyperelastic stiffness, as used in section 1.5.3.

#### 3.3.3 Viscoelasticity

The deviatoric nonlinear Maxwell cells are fixed at 50Hz, 5Hz, 0.5Hz. As it was unclear if these cells should keep an intermediary behavior, they also kept the nonlinear part, meaning that the coefficients  $g^i$  and  $\epsilon_f^i$  should be determined here for the cells with higher frequency ( $i \geq 2$ ), in a second multi-objective identification. A bulk cell was also defined with a frequency at 1KHz (which may change depending on the FE model and the mean size of the elements) and a  $g^p = 10\%$  fraction.

The tests taken to compute the viscous fraction, are the ones with no prestrain, moderate amplitude (2.5%) and every available frequency. The first part of objective function is based on dissipated energy and is given by

$$f_{g_{HF}}(g_i, \beta_i) = \sum_{n_{freq}} \left( \frac{W_d^{comp}}{A_\sigma A_\epsilon} - \frac{W_d^{test}}{A_\sigma A_\epsilon} \right)^2. \quad (3.7)$$

For the second part of the functional, the tests used as reference were the ones with no prestrain,

### 3.3. CLASSICAL MATERIAL IDENTIFICATION PROCEDURE

moderate frequency (5Hz), and every amplitude available. The second part of this functional is based on the loss of secant modulus and may be expressed as

$$f_{\beta_{HF}} = \sum_{n_{amp}-1} \left( \left( K_t^{comp}|_{i_{amp}} - K_t^{comp}|_{i_{amp}+1} \right) - \left( K_t^{test}|_{i_{amp}} - K_t^{test}|_{i_{amp}+1} \right) \right)^2. \quad (3.8)$$

Again, both objective functions were normalized to avoid domination of one function over the other.

Figure 3.16 illustrates the experimental moduli used as reference for identification in frequency and its respective identified model curve.

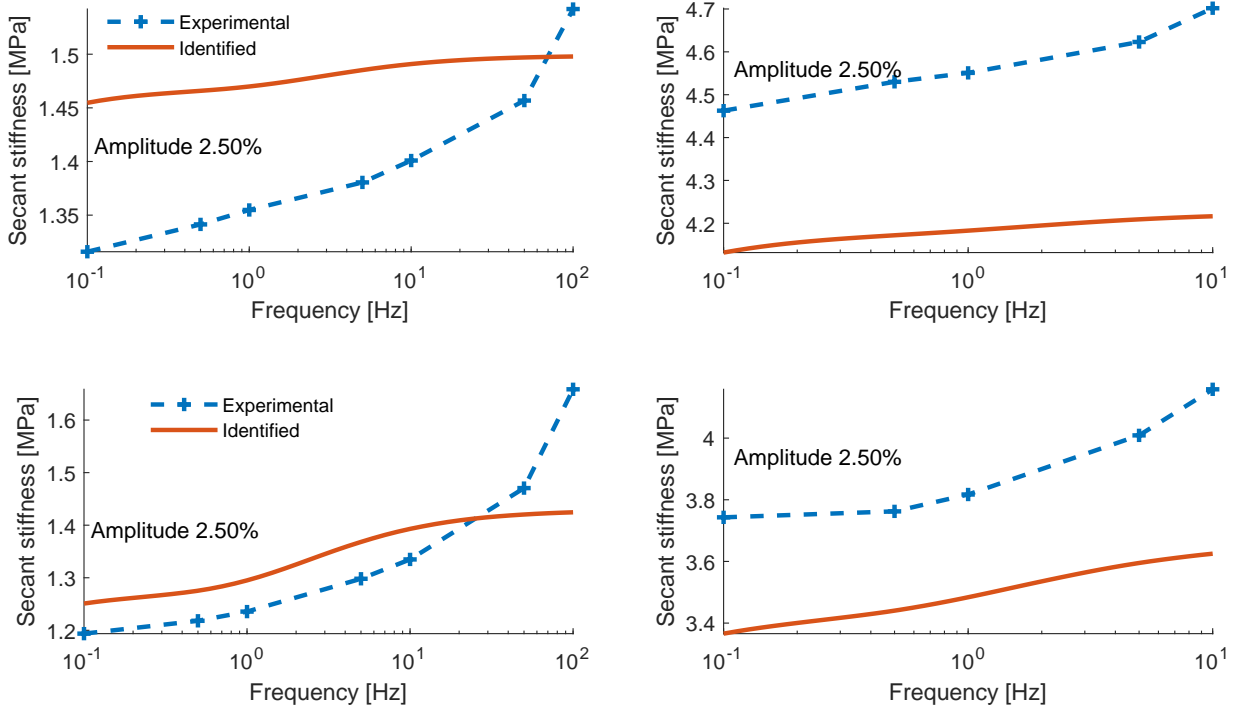


Figure 3.16: Comparison of tangent modulus evolution with frequency between identified model and experimental results. Left: shear specimen, right: tension/compression specimen. Top: material 1, bottom: material 2

Figure 3.17, on the other hand, illustrates the moduli evolution with amplitude and the comparison between identified model and experimental results.

### 3.3. CLASSICAL MATERIAL IDENTIFICATION PROCEDURE

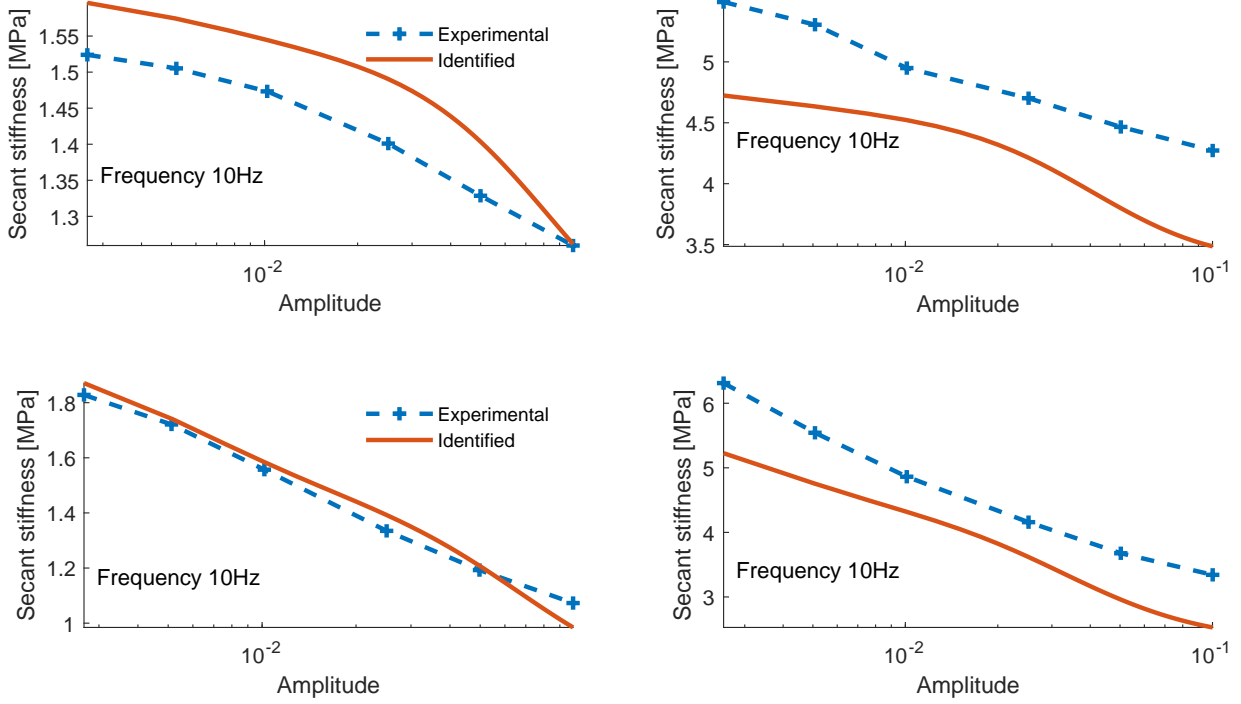


Figure 3.17: Comparison of tangent modulus evolution with amplitude between identified model and experimental results. Left: shear specimen, right: tension/compression specimen. Top: material 1, bottom: material 2

Despite not perfectly capturing perfectly the evolutions with frequency and amplitude, the errors are no larger than 15%, and the errors on the tension/compression specimens are more likely tied to the hyperelastic moduli difference rather than the viscoelastic cell identification itself. The stiffening with frequency and the softening with amplitude seem to be fairly well reproduced by the model.

#### 3.3.4 Identification results

To ensure the robustness and stability of the procedure, sequential optimization of the three objectives was performed until convergence. The final results are displayed in table 3.1.

The extremely low value for  $c_2$  in the two material indicate very low stiffening for large strains. Regarding the viscous cells, there is a clear concentration on the mid frequency cell, which may reflect too much weight on the second part of the viscoelastic functional (established at 5 Hz), which could be compensated with better weighting on the objective functions. The difference in the values of  $\epsilon_f$  also indicates that the high frequency cells are far from the hysteretic transition.

The higher dissipative fractions on the second material indicate that it is much more damped than the first one. The difference in the stiffening in shear and in tension/compression may justify another

Table 3.1: Identification results.

	$c_1$ [MPa]	$c_2$ [MPa]	$c_3$ [MPa]	$g$	$\epsilon_f$	$f$ [Hz]
Material 1	0.37	0	2.2	29.6%	$2.5 \times 10^{-2}$	0.005
				0	$4.4 \times 10^{-2}$	0.5
				9.2%	$2.6 \times 10^{-3}$	5
				0	$1.7 \times 10^{-4}$	50
Material 2	0	0	3.55	30.6%	$2.2 \times 10^{-2}$	0.005
				0	$1.9 \times 10^{-2}$	0.5
				39.5%	$2.3 \times 10^{-3}$	5
				0	$1.7 \times 10^{-4}$	50

separation of behaviors and the utilization of different Maxwell cells. The possibility to use different reference curves and place Maxwell cells accordingly may present better results while demanding a more elaborate model.

From a practical point of view, this kind of identification provided acceptable parameters to simulate realistically the material. More accurate parameters may be found using the same type of routine, by tweaking or changing the objective functions, using more cells and use more data for identification. Although, the utilization of more cells and more data for those routines deemed to be unpractical as the more data and parameters are added, the more local optima are added and more time is spent on the optimization. For these reasons, the focus was placed on a different identification method.

### 3.4 Non-parametric and selected order identification

Since the results of the initial classical optimization were not sufficiently convincing, the later developments detailed in chapter 1 were used. Non parametric identification was performed first and order selection allowed easier nearly graphical initialization of selected parametric models.

For the hyperelastic part, non parametric identification consists in the extraction of the instantaneous stiffness from different triangular tests, after the threshold of the hysteretic relaxation, as shown in section 3.4.1.

For hysteretic relaxation, section 3.4.2 considers relaxation phases extracted from triangular tests and proposed a low order Iwan model fit.

For viscoelastic behavior, instant modulus computations were still under developments and first harmonic complex modulus approximations were used to identify load fractions and choose appropriate frequencies.

### 3.4.1 Hyperelastic behavior

To obtain a continuous representation of the hyperelastic component, the triangular tests were used. The separation of hysteretic relaxation was made by defining a specific distance from the turning point. To generate a continuous model, a 3rd order polynomial piece-wise interpolation (ensuring 2nd derivative continuity) was made on these curves.

The link with 3D coefficients can be made by analytic developments tying the reduced invariants to the theoretic imposed deformations illustrated in 2.3.4, by using, for simple shear

$$C^{ss} = \begin{pmatrix} 1 & \gamma & 0 \\ \gamma & 1 + \gamma^2 & 0 \\ 0 & 0 & 1 \end{pmatrix} \quad (3.9)$$

$$\bar{I}_1^{ss}(\gamma) = \gamma^2 + 3 \quad (3.10)$$

$$\bar{I}_2^{ss}(\gamma) = \gamma^4 + 5\gamma^2 + 6 \quad (3.11)$$

and for tension/compression

$$C^{tc} = \begin{pmatrix} \lambda^2 & 0 & 0 \\ 0 & \lambda^{-1} & 0 \\ 0 & 0 & \lambda^{-1} \end{pmatrix} \quad (3.12)$$

$$\bar{I}_1^{tc}(\lambda) = \lambda^2 + 2\lambda^{-1} \quad (3.13)$$

$$\bar{I}_2^{tc}(\lambda) = \lambda^4 + 2\lambda + 3\lambda^{-2} \quad (3.14)$$

These equations imply that for a 3D model, any invariant based hyperelastic model may be seen as a parametric form that fits stress based on these deformation polynomials. By selecting specific models, such development can be made upto build stress in function of strain for both cases, and finally check if the model is capable to appropriately represent specific behaviors, such as the stiffness drop on simple shear specimen, and eventually tune the model to do so. This procedure should remain as a perspective.

The extracted non parametric curves for the materials is illustrated in figure 3.18, and used all the triangular tests available after the removal of the hysteretic relaxation.

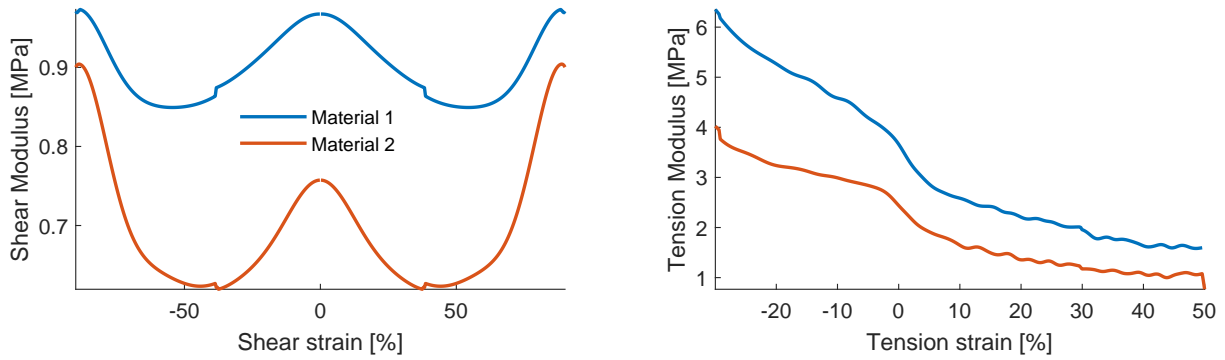


Figure 3.18: Non-parametric hyperelastic material models. Left: shear, right: tension/compression.

The same procedure was made to the part tests where all triangular tests were used after removal of hysteretic relaxation, yielding the curves in figure 3.19.

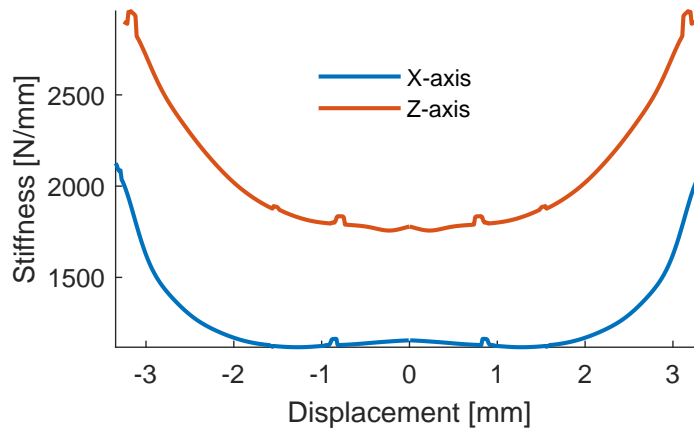


Figure 3.19: Non-parametric hyperelastic part models.

### 3.4.2 Hysteretic relaxation

The hysteretic curves are extracted from triangular tests. As section 1.4.2 illustrated, the best fit is made through ratios to the hyperelastic modulus. Indeed, normalizing those curves and plotting them altogether seems to provide proper reference non-parametric hysteretic model. The distance from the turning point where behavior is considered hysteretic is visible in figure 3.20, 50% for shear and 20% for tension/compression. In the figure, *all* the material triangular tests (instantaneous modulus as function of distance to the turning point normalized by the hyperelastic modulus) are plotted in gray dotted line, and the mean value for all of them is marked as the solid black line.

The discretization of this curve with a selected order model (Iwan model), may be done simply by choosing distances to the turning point and relaxation gains associated with drops. The placement

### 3.4. NON-PARAMETRIC AND SELECTED ORDER IDENTIFICATION

of the Jenkins cells is illustrated in figure 3.20 for the material specimens, in green, using the mean curve as reference. As found earlier with the first identification, the hysteretic dissipation is much more pronounced for the second material.

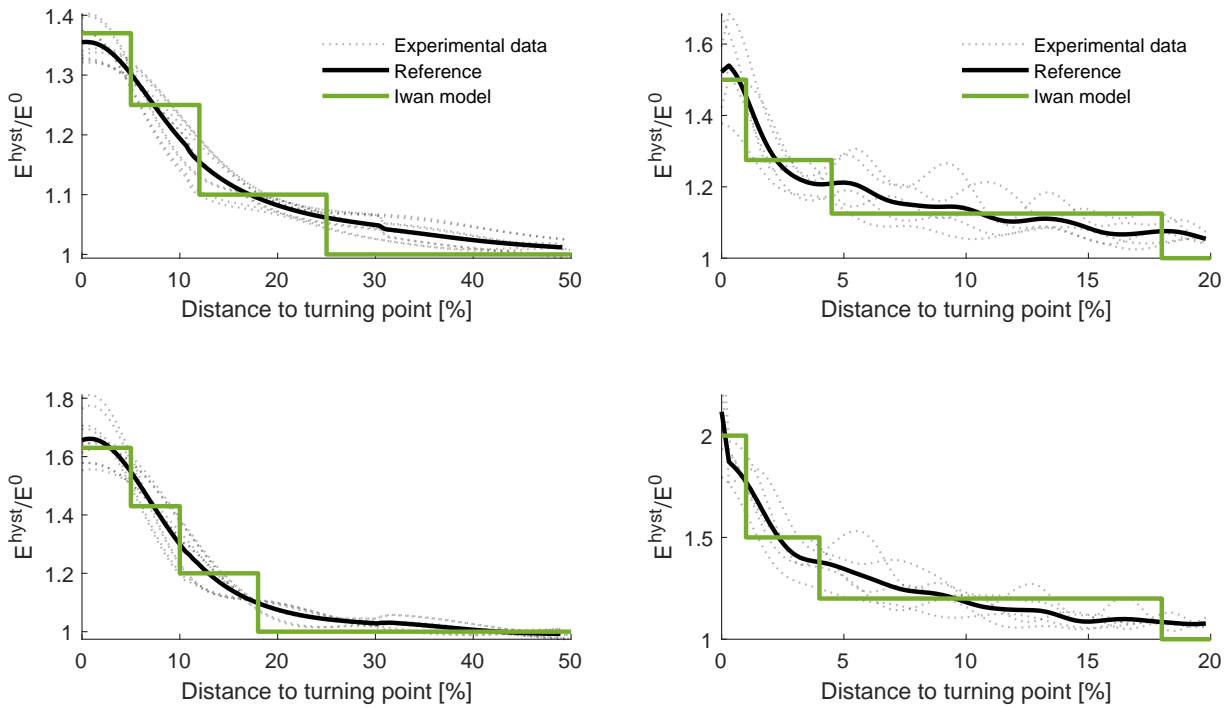


Figure 3.20: Hysteretic relaxation. Left: shear , right: tension/compression. Top: material 1, bottom: material 2

For the part test, the distance to the turning point used to separate the hyperelastic behavior is 1.5mm for both directions, as seen in figure 3.21. Again, *all* triangular test data is plotted in the figure as gray dotted line, with the black solid curve representing the mean value of all of them, used as reference for the green solid line, correspondent to the identified model behavior.

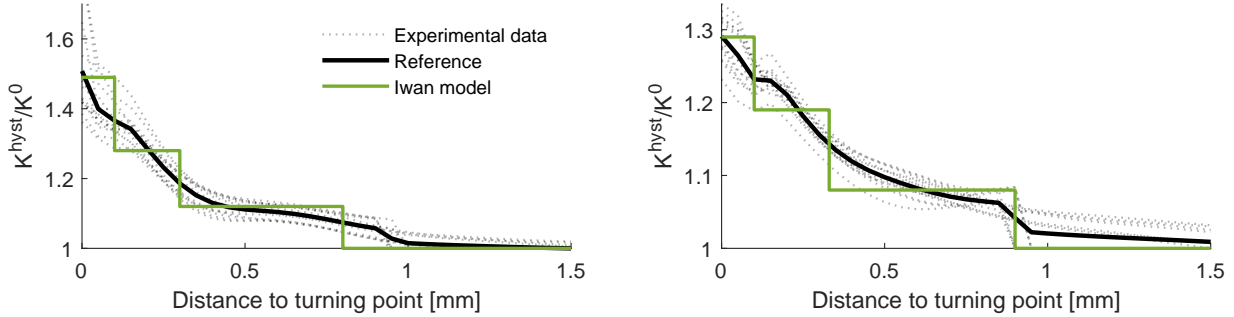


Figure 3.21: Hysteretic relaxation for part tests. Left: x axis, right: z axis.

### 3.4.3 Viscoelastic frequency evolution

For the sine tests, the viscoelastic behavior is always influenced by the hysteresis (Payne effect). It is thus not possible to obtain a non-parametric model of purely viscoelastic behavior. To circumvent the effects of hysteresis on sine tests, one may either try to compensate for the amplitude, or select a single low amplitude (as was made for the initial identification routine). The solution retained is first to normalize by the hyperelastic modulus as seen in figure 1.25 and second to work on viscoelastic gains by removing the low frequency offset at 0.1Hz. The identification is then performed on  $(E(s) - E_{(0.1Hz)})/E^0$ .

In figure 3.22, the first harmonic storage modulus (less the low frequency contribution, normalized by the hyperelastic modulus) extracted from *all* exploitable sine tests are plotted as light dotted lines. The mean moduli for all amplitudes at a given level of prestrain (denoted in the legend as  $C_0$ ) lead to thick dashed lines. The mean of all curves is shown as a solid black line, used as reference for the identification.

The selected order parametric representation may be achieved by a Maxwell cell placement which is largely discussed by [12]. Here, the Maxwell asymptotes, defined by a cell frequency and a gain were used to graphically place the cells. The solid green curve in figure 3.22 illustrates the expected asymptotic behavior in frequency for the material specimens.

Again, as for the hysteretic, the same conclusion may be drawn regarding the dissipation for the material 2. Here, though, the effect of prestrain is much more visible in the tension/compression test, which may suggest the utilization of a non-linear gain with static strain. Although, the utilization of a single curve was deemed to be accurate enough for the present work.

### 3.4. NON-PARAMETRIC AND SELECTED ORDER IDENTIFICATION

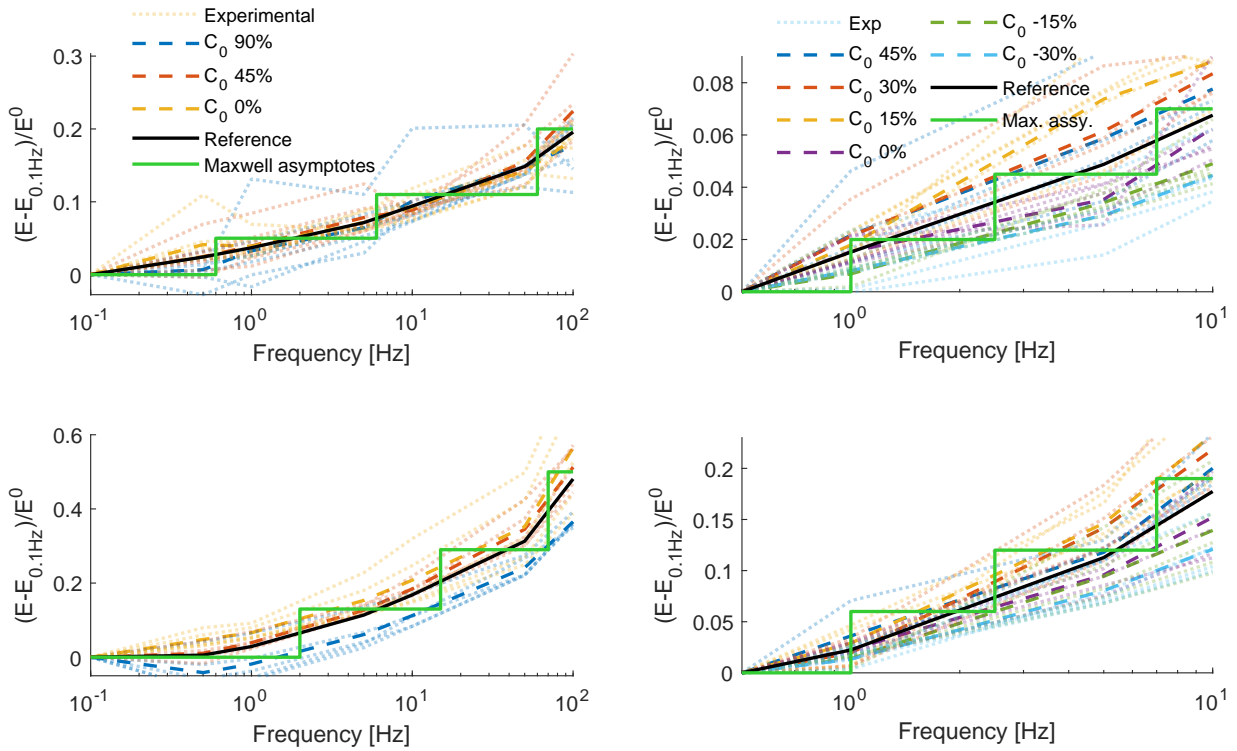


Figure 3.22: Viscoelastic fitting for materials. Left: shear , right: tension/compression. Top: material 1, bottom: material 2

The same procedure was applied to the part test, also using *all* exploitable sine tests, and illustrated in figure 3.23, but here the results are much less dispersed as function of the prestrain. This might be an indication that that areas with high strain levels inside the part are sufficiently small to have smaller global effect than seen in material tests.

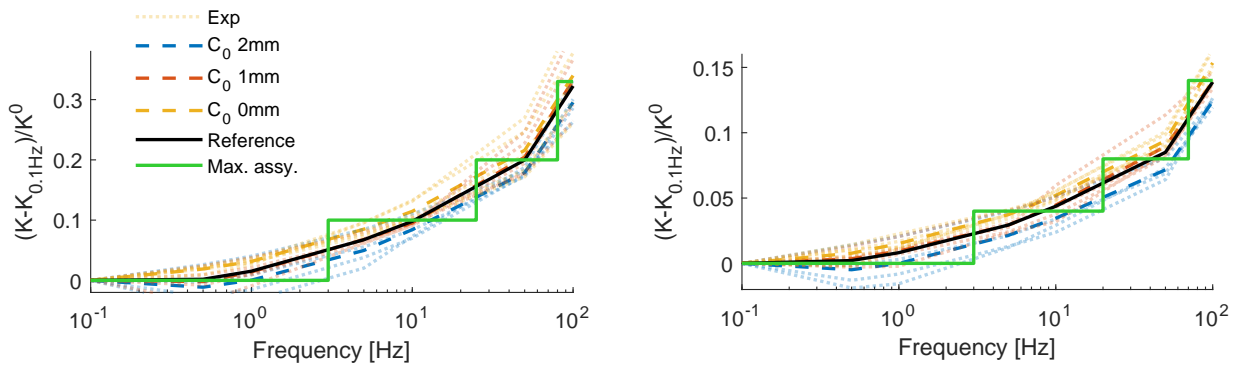


Figure 3.23: Viscoelastic fitting for part. Left: x axis, right: z axis.

Despite retaining almost all data, there are a few points in the part test with low amplitude and

high prestrains that show negative modulus evolution with frequency, which means an unrealistic behavior, and should be examined.

### 3.5 Synthesis and perspectives

#### 3.5.1 Test synthesis

To synthesize all the data collected from each test, a synthetic plot is proposed in figures 3.24 to 3.29. In the top, in a kind of *map*, one sees the results of the mean first harmonic of sine tests, with the amplitude depicted in the x-axis, and the frequencies illustrated in the color scale. The red solid lines shows the hyperelastic curve extracted from the triangular tests, with an averaged value for the ranges with more than one test. The green dashed ones shows the hysteretic relaxation, also associated to triangular tests, which were used to determine the associated non-parametric model. The dotted lines show two different extraction points from the relaxation modulus (two different points of the curve in figure 3.11 right for all the steps). The data for the first material is shown in figures 3.24 and 3.25.

### 3.5. SYNTHESIS AND PERSPECTIVES

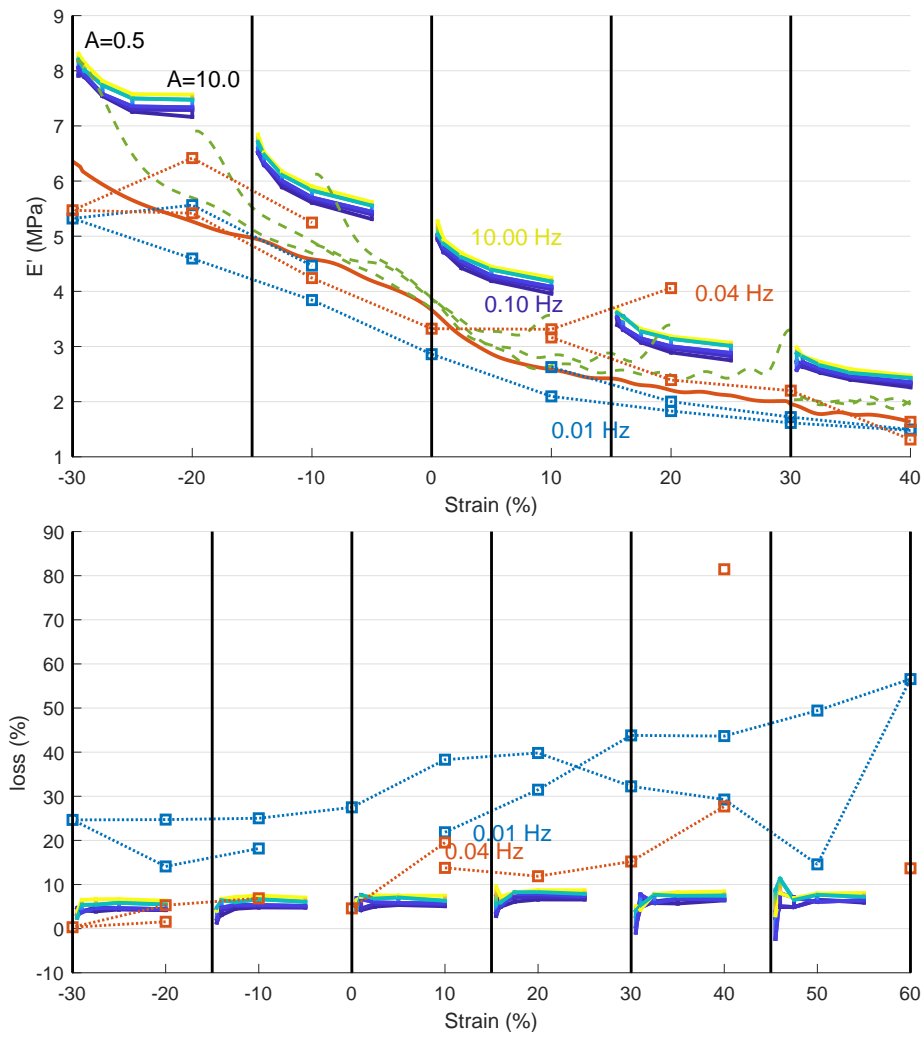


Figure 3.24: Summary of tension/compression tests for material 1 **m1t**. Top: Storage modulus. Bottom: loss factor.

### 3.5. SYNTHESIS AND PERSPECTIVES

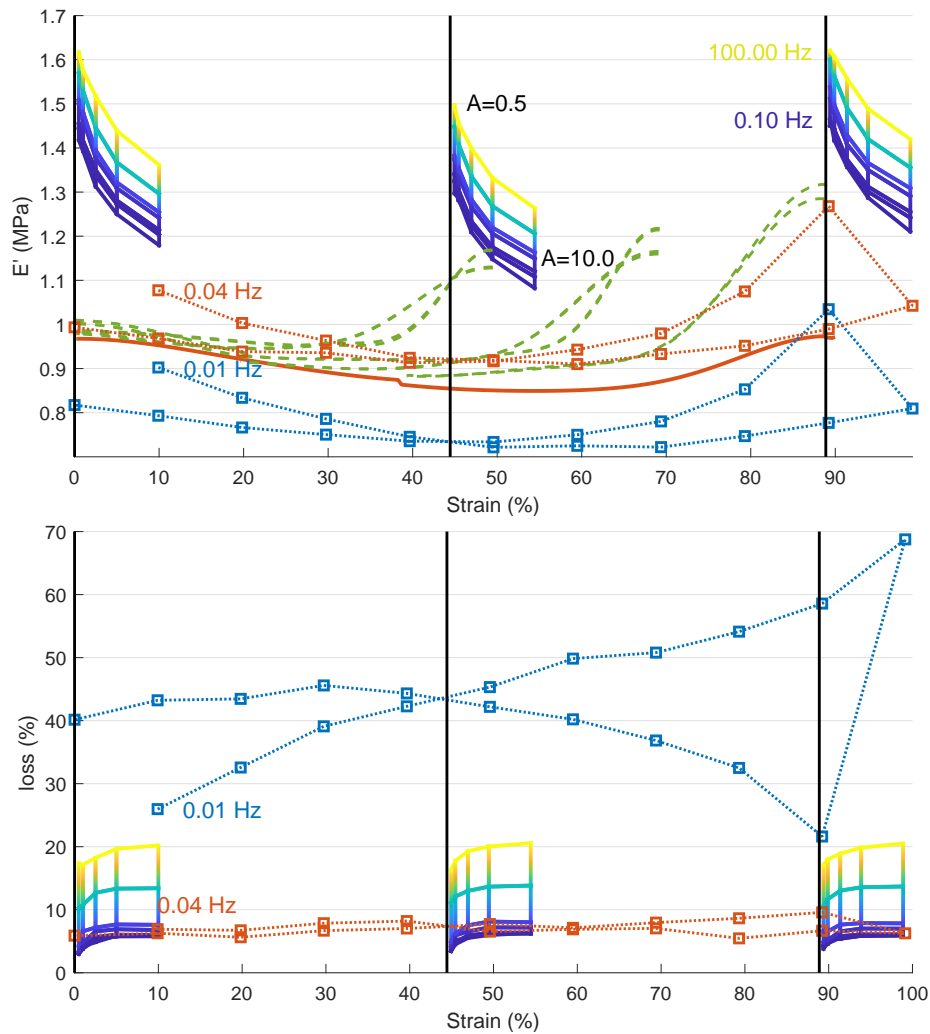


Figure 3.25: Summary of shear tests for material 1 *m1s*. Top: storage modulus. Bottom: loss factor.

The points extracted from the relaxation functions are only reasonable representations for the higher frequency (0.04Hz) in shear. The fact that there are several outliers and unreasonable values (especially those with more than 20% in loss) indicate that viscoelasticity is not an appropriate hypothesis for those levels of frequency.

Figures 3.26 and 3.27 summarize the test results for the second material.

### 3.5. SYNTHESIS AND PERSPECTIVES

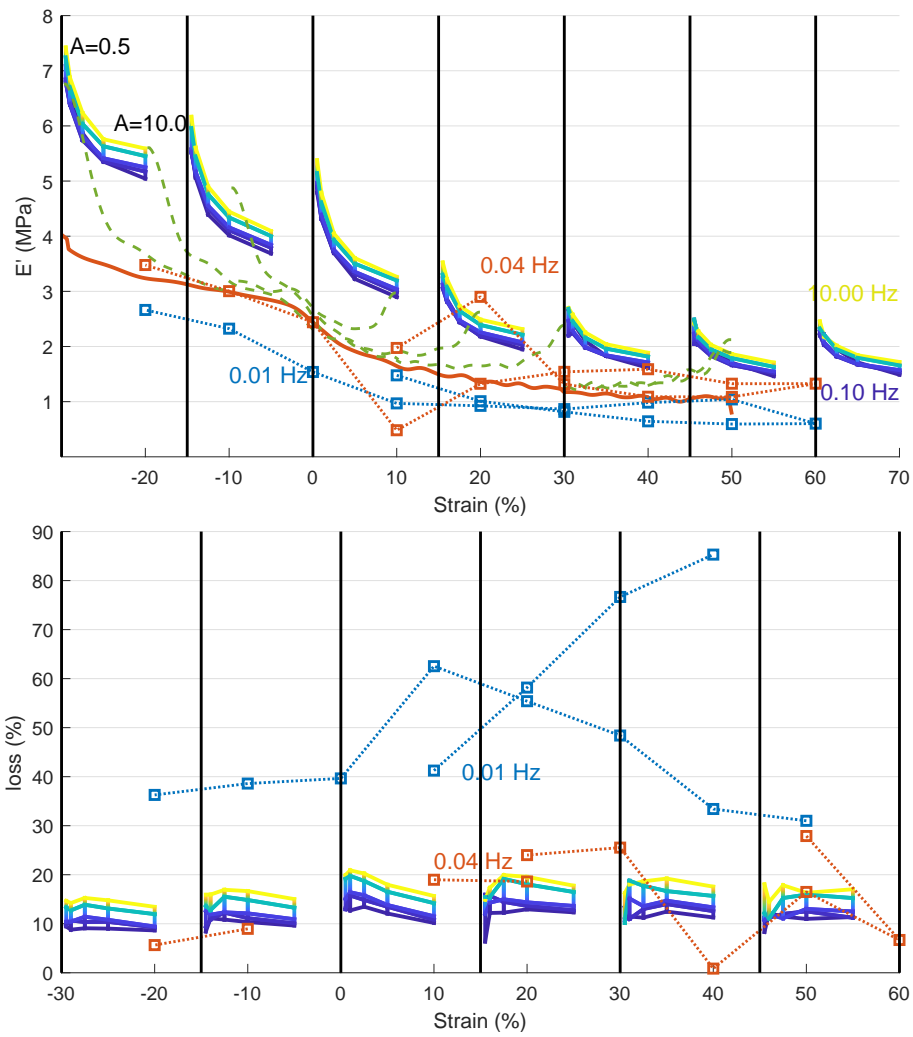


Figure 3.26: Summary of tension/compression tests for material 2 *m2t*. Top: storage modulus. Bottom: loss factor.

### 3.5. SYNTHESIS AND PERSPECTIVES

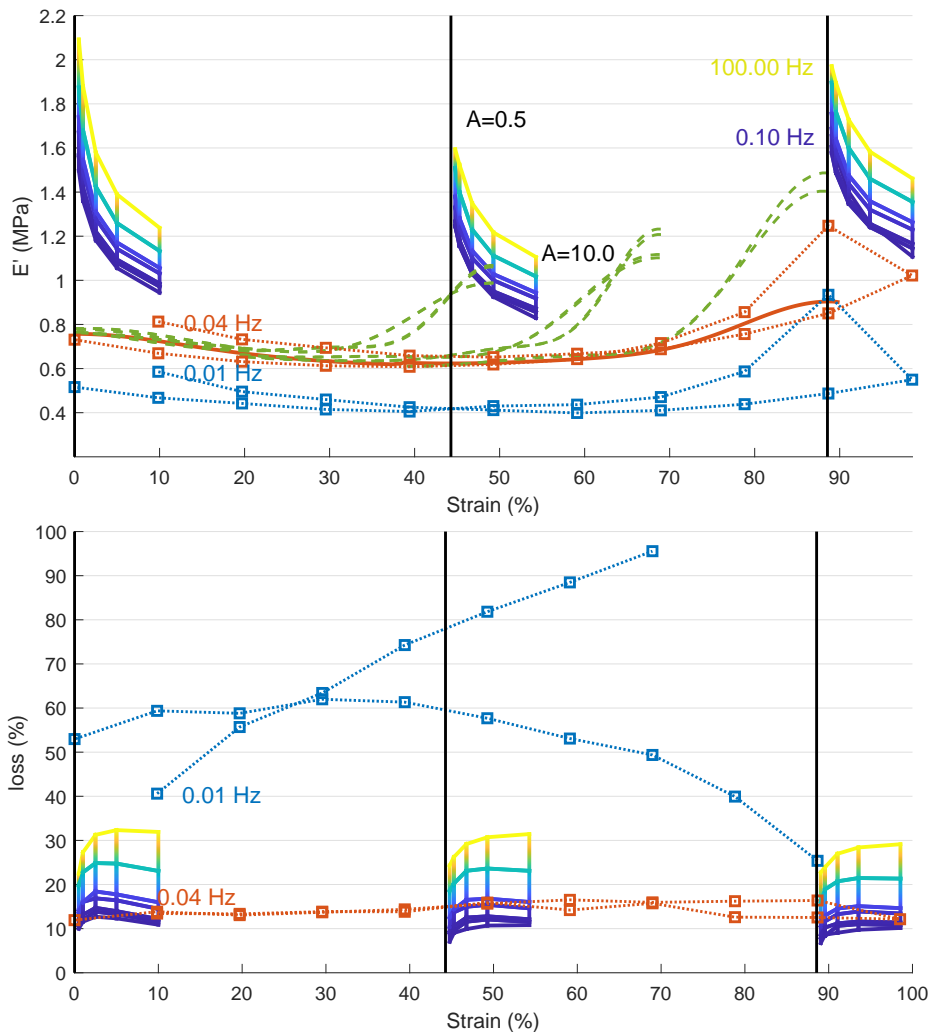


Figure 3.27: Summary of shear tests for material 2  $m2s$ . Top: storage modulus. Bottom: loss factor.

The second material show much higher loss factors and modulus drop more than the first material, which indicates a much stronger material damping. The same take may be made on the multi-step relaxations extracted as for the first material.

Figures 3.28 and 3.29 illustrate the summary from the part tests in x and z axis, respectively.

### 3.5. SYNTHESIS AND PERSPECTIVES

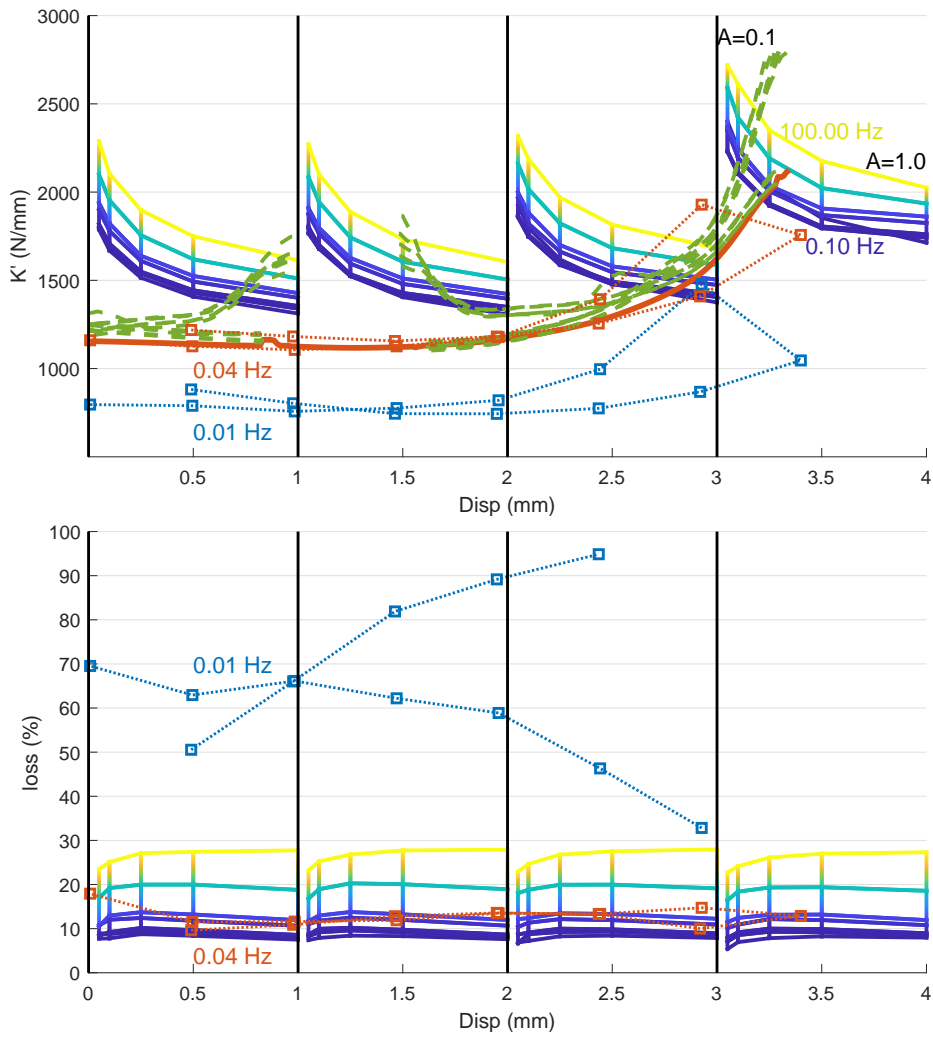


Figure 3.28: Stiffness and loss summary for part test in x px. Top: storage stiffness. Bottom: loss factor.

### 3.5. SYNTHESIS AND PERSPECTIVES

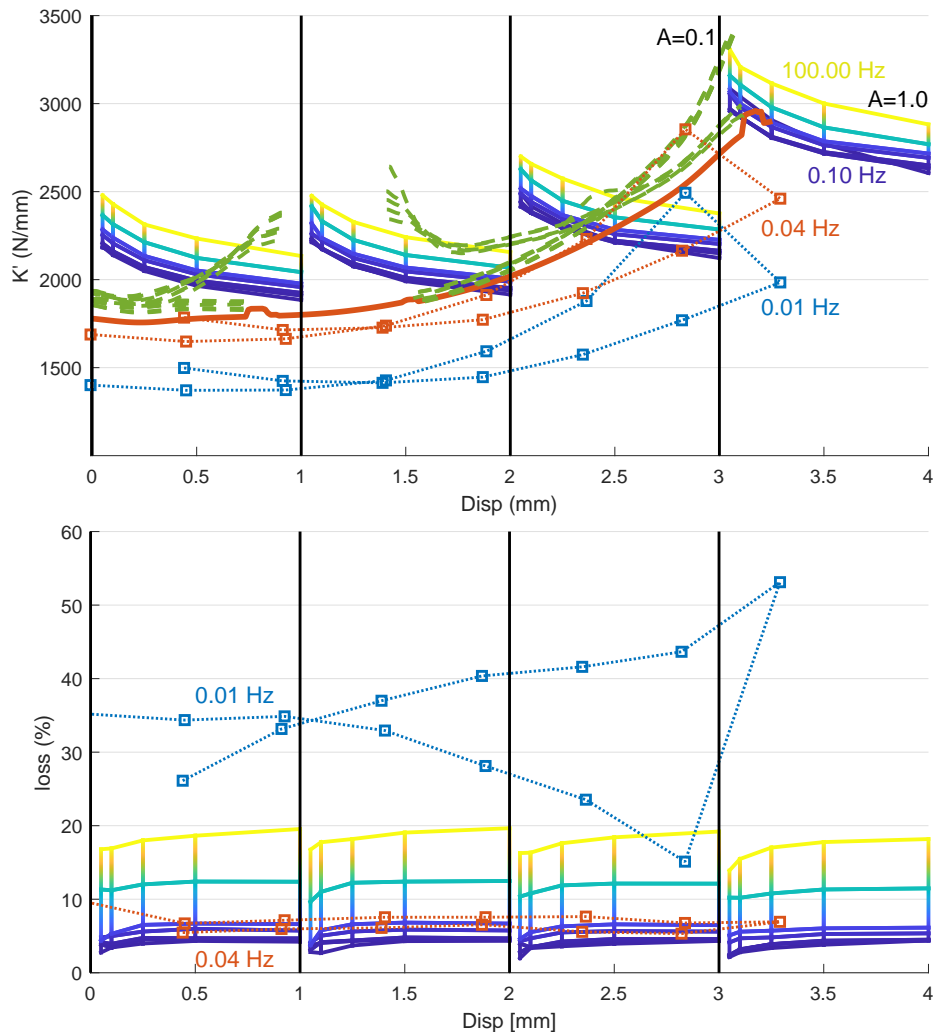


Figure 3.29: Stiffness and loss summary for part test in  $z$   $pz$ . Top: storage stiffness. Bottom: loss factor.

The behavior at 0.04Hz for the part is in line of what is seen in the literature of viscoelasticity, while the behavior at lower frequency (0.01Hz) does not seem to respect this hypothesis, indicating that the slowest relaxation cells should be put in the range between these two frequencies, if one seeks a very refined representation of viscoelasticity. One may see that the  $x$  axis is more dissipative, and it is due to the fact that the second material  $m2$  is mostly oriented in this direction. This direction is aligned to the vehicle longitudinal direction and it is more damped to dissipate the energy injected by step obstacles. Meanwhile, the other direction is aligned to the vertical direction and is less damped to avoid stiffening in low amplitudes and thus filter HF road noises that would otherwise be transmitted to the chassis.

### 3.5.2 Perspectives and conclusions

The obtained results from classical identification routines may be directly exploitable into finite element models. The proposed non-parametric routine, on the other hand provides results readily implementable as 0D models into multibody models.

The utilization of a single material to emulate the different behaviors (in simple shear and tension/compression) means that the material would have to split contributions, and instead of analyzing the model in terms of a single deviatoric core, from where the relaxation is computed, one may divide in two different deviatoric parts. For instance use as potentials  $\psi(f(\gamma))$  and  $\psi(g(\lambda))$ , and associate different viscoelastic and hysteretic relaxations to them.

Beyond the extension of the proposed identification to 3D models, the tests should be verified. Hypothesis made on the constant state within a section must be verified, which can be made via a finite element model. The other major simplification was the assumption of incompressibility for both material tests, which can also be addressed with a FE simulation, by testing different bulk moduli.

Validation of the identified chosen materials could be made with a part simulation that could be directly compared to tests, if one accounts for pre-strain. The utilization of hyper-reduction techniques, which will be described and illustrated in chapter 4 should be used to enable the possibility to simulate the whole test campaign.

In terms of extrapolation, the simulation of the whole bushing in coupled loads (displacements imposed in several directions/angles at the same time, for instance) could be generated to emulate real use conditions, as will be shown in chapter 5. These conditions are quite difficult to replicate in controlled conditions or even in testbeds, albeit they are necessary for generating 0D models capable of representing such coupling effects. Other perspective would be to add contact, as the removed plastic limiter plays a fundamental role when it comes to the stiffening within larger displacements, generating a bump stop effect.

# Chapter 4

## From 3D to 0D

### Contents

---

<b>4.1</b>	<b>Introduction</b>	<b>138</b>
<b>4.2</b>	<b>Finite element method</b>	<b>138</b>
4.2.1	Principles	138
4.2.2	Implicit schemes	141
4.2.3	Explicit schemes	142
<b>4.3</b>	<b>Kinematic reduction</b>	<b>143</b>
4.3.1	Motivation	143
4.3.2	Learning methods	144
4.3.3	Basis generation	145
<b>4.4</b>	<b>Hyper reduction: lower cost integration of non-linear terms</b>	<b>147</b>
4.4.1	Discrete Empirical Interpolation Method (DEIM)	147
4.4.2	Energy Conserving Sampling and Weighting (ECSW)	148
<b>4.5</b>	<b>Sample application</b>	<b>149</b>
4.5.1	Model description	149
4.5.2	Performance and accuracy of base implementation	150
4.5.3	Extrapolations	152
<b>4.6</b>	<b>Perspectives and conclusions</b>	<b>153</b>

---

## 4.1 Introduction

The finite element method (FEM) is the most established tool for solid structural analysis. It provides a direct well controlled process to address simulation accuracy by accounting for spatial detail and wavelengths. Following the system model perspective used for FEM implementations throughout the MATLAB based SDT [8], section 4.2 summarizes classical development of FEM formulation using the notion of strain observation and stress command with a focus on configurations where materials undergo large deformation which were first discussed for material behavior in section 2.2. The section then discusses the respective advantages and limitations of implicit and explicit time integration schemes.

The model size of FEM model is driven by geometric detail, gradient sizes and wavelengths which decrease with frequency. In terms of system response, the driving factors are spatial distribution of loads and frequency content of the associated inputs. As a result, the actual kinematics can typically be represented by a subspace that is orders of magnitude smaller than the model size. Section 4.3 discusses classic techniques to learn kinematics, build bases and thus generate reduced order models with a lower number of generalized degrees of freedom.

When considering non-linear material behavior, possibly including internal states as discussed in chapter 2, kinematic reduction still leaves the costly evaluation of material evolution laws at a large number of points. Hyper-reduction is thus introduced as a second phase of model reduction, where one seeks a sparse set of integration hyper-points allowing an accurate approximation of non-linear dependencies at a much lower numerical cost. Section 4.4 reformulates existing Discrete Empirical Interpolation Method (DEIM) and Energy Conserving Sampling and Weighting (ECSW) method in the light of the input/output formulation detailed in section 4.2.

After the first contribution of reformulating kinematic reduction and hyper-reduction methods in a input/output perspective, the chapter ends with an application section 4.5 where the potential of the proposed methods is evaluated for the case of a rear twist beam axle articulation (this corresponds the ISMA 2020 Paper [4]). Details of the actual implementation are analyzed, performance is discussed and capabilities for extrapolation are illustrated. With the experience drawn from this example, the chapter ends with discussion of perspectives.

## 4.2 Finite element method

### 4.2.1 Principles

The finite element method is detailed in many texts [55, 52]. The objective of this section is to clarify the input/output formalism used for non-linear simulations in SDT [8]. The method combines a kinematic description of fields and a derivation of equations of motion using the virtual work

principle (2.14).

Within elements whose shape is simple enough to use piecewise polynomial shape functions  $N$  that depend only on position, kinematic fields are described as a linear combination of shape functions with time dependent degrees of freedom (DOF). In other words, displacements  $u$  are linearly related to time dependent degrees of freedom  $q$  by shape functions so that

$$u_i^g(t) = [N_i^g] \{q(t)\}, \quad (4.1)$$

with  $g$  the sample points, which are typically taken to be those of a Gauss quadrature. For strain, the base operation is to observe the deformation gradient at a given observation point. As it is also a linear function of degrees of freedom, it can be written as a time independent linear observation equation or matrix product

$$F_{ij}^g = \delta_{ij} u_{i,j} = \sum_{i \in \Omega} [N_{i,x,y,z}^g] (x^g, y^g, z^g) \{q\} = \delta_{ij} + [\mathbb{C}_{ij}^g] \{q\} \quad (4.2)$$

with  $\mathbb{C}$  the constant observation matrix that gives the polynomial derivatives at the integration points.

The virtual work principle (2.14) derives equations of motion from the fact that the difference between internal forces and external plus inertial forces must be zero. In other words, one has

$$\{r\} = \sum_g w^g J_g \left( [\mathbb{C}_{ij}^g]^T [\hat{F}(q)]^T S^g - [N_i^g]^T \{f_{vi}\} \right) = 0 \quad (4.3)$$

with  $w_g$  the weights of the chosen integration rule,  $J^g$  the Jacobian of the geometric transformation from the reference geometry to the current one, and

$$[\hat{F}(u(q))^g] = \begin{bmatrix} 1 + u_{1,1} & 0 & 0 & u_{2,1} & 0 & 0 & u_{3,1} & 0 & 0 \\ 0 & u_{1,2} & 0 & 0 & 1 + u_{2,2} & 0 & 0 & u_{3,2} & 0 \\ 0 & 0 & u_{1,3} & 0 & 0 & u_{2,3} & 0 & 0 & 1 + u_{3,3} \\ u_{1,2} & 1 + u_{1,1} & 0 & 1 + u_{2,2} & u_{2,1} & 0 & u_{3,2} & u_{3,1} & 0 \\ 0 & u_{1,3} & u_{1,2} & 0 & u_{2,3} & 1 + u_{2,2} & 0 & 1 + u_{3,3} & u_{3,2} \\ u_{1,3} & 0 & 1 + u_{1,1} & u_{2,3} & 0 & u_{2,1} & 1 + u_{3,3} & 0 & u_{3,1} \end{bmatrix} \quad (4.4)$$

or equivalently, extending the 4th order index to further lines and columns,

$$\hat{F} = 1_{ijkl} F_{kl} = \begin{bmatrix} F_{11} & 0 & 0 & F_{21} & 0 & 0 & F_{31} & 0 & 0 \\ 1/2 F_{12} & 1/2 F_{11} & 0 & 1/2 F_{22} & 1/2 F_{21} & 0 & 1/2 F_{32} & 1/2 F_{31} & 0 \\ 1/2 F_{13} & 0 & 1/2 F_{11} & 1/2 F_{23} & 0 & 1/2 F_{21} & 1/2 F_{33} & 0 & 1/2 F_{31} \\ 1/2 F_{12} & 1/2 F_{11} & 0 & 1/2 F_{22} & 1/2 F_{21} & 0 & 1/2 F_{32} & 1/2 F_{31} & 0 \\ 0 & F_{12} & 0 & 0 & F_{22} & 0 & 0 & F_{32} & 0 \\ 0 & 1/2 F_{13} & 1/2 F_{12} & 0 & 1/2 F_{23} & 1/2 F_{22} & 0 & 1/2 F_{33} & 1/2 F_{32} \\ 1/2 F_{13} & 0 & 1/2 F_{11} & 1/2 F_{23} & 0 & 1/2 F_{21} & 1/2 F_{33} & 0 & 1/2 F_{31} \\ 0 & 1/2 F_{13} & 1/2 F_{12} & 0 & 1/2 F_{23} & 1/2 F_{22} & 0 & 1/2 F_{33} & 1/2 F_{32} \\ 0 & 0 & F_{13} & 0 & 0 & F_{23} & 0 & 0 & F_{33} \end{bmatrix} \quad (4.5)$$

In this expression, the link with command matrix  $\mathbb{B}$ , defined as

$$\mathbb{B} = \mathbb{C}^T w_g J_g, \quad (4.6)$$

## 4.2. FINITE ELEMENT METHOD

---

is obtained considering the integration of all stress components as inputs in a large  $\{S^g\}$ , giving internal forces,

$$\mathcal{F}^{int} = \mathbb{B}S^g. \quad (4.7)$$

Considering the inertia forces, virtual work principle can be written as a set of structural equations given by

$$[M] \{\ddot{q}\} + [\mathbb{B}] f_{material}([\mathbb{C}] \{q\}, \{\mathcal{U}^I\}) = \mathcal{F}^{ext} \quad (4.8)$$

where stress observations give the  $f_{material}$  vector and  $\mathcal{U}^I$  are the material internal states which are associated with spatially independent material evolution equations such as 2.42, which use strains  $[\mathbb{C}] \{q\}$  as inputs.

For a number of iterative algorithms it is useful to compute the derivative of the residual with respect to states. For the material laws this corresponds to the model tangent stiffness.

The derivative of the stress with respect to its dual strain yields a fourth order tensor, called material tangent stiffness tensor, expressed as

$$\mathcal{D}_{ijkl} = \frac{\partial S_{ij}}{\partial e_{kl}}, \quad (4.9)$$

which may be transformed into a second order tensor using the engineering notation,

$$S = \begin{pmatrix} S_{11} & S_{12} & S_{13} \\ S_{21} & S_{22} & S_{23} \\ S_{31} & S_{32} & S_{33} \end{pmatrix} \rightarrow \left\{ \begin{array}{c} S_{11} \\ S_{22} \\ S_{33} \\ S_{23} \\ S_{31} \\ S_{12} \end{array} \right\}, \quad (4.10)$$

as both  $S$  and  $e$  are symmetric. For linear materials, this tensor is constant and defines completely the material law, while for nonlinear models, the material stiffness tensor must be updated at the current point which depends on displacements and internal states.

The derivative of the residual with respect to degrees of freedom is called the tangent stiffness, given by

$$\begin{aligned} [K_G] &= \int_{\Omega_0} S_{ij} \delta u_{k,i} du_{l,j} + \int_{\Omega_0} \delta e : \frac{\partial S}{\partial e} : de \\ &= \sum_g w_g J_g [\mathbb{C}^g]^T \left( [\hat{F}]^T [\mathcal{D}] [\hat{F}] + \hat{S} \right) [\mathbb{C}^g] \end{aligned} \quad (4.11)$$

where  $\hat{S}$  is the injection of the components of the second Piola-Kirchhoff stress tensor into the following

matrix

$$\hat{S} = \begin{bmatrix} S_{11} & 0 & 0 & S_{12} & 0 & 0 & S_{13} & 0 & 0 \\ 0 & S_{11} & 0 & 0 & S_{12} & 0 & 0 & S_{13} & 0 \\ 0 & 0 & S_{11} & 0 & 0 & S_{12} & 0 & 0 & S_{13} \\ S_{21} & 0 & 0 & S_{22} & 0 & 0 & S_{23} & 0 & 0 \\ 0 & S_{21} & 0 & 0 & S_{22} & 0 & 0 & S_{23} & 0 \\ 0 & 0 & S_{21} & 0 & 0 & S_{22} & 0 & 0 & S_{23} \\ S_{31} & 0 & 0 & S_{32} & 0 & 0 & S_{33} & 0 & 0 \\ 0 & S_{31} & 0 & 0 & S_{32} & 0 & 0 & S_{33} & 0 \\ 0 & 0 & S_{31} & 0 & 0 & S_{32} & 0 & 0 & S_{33} \end{bmatrix}. \quad (4.12)$$

In the implementation of (4.11), the computation of the gradient as  $[\mathbf{C}] \{q\}$  is a base functionality of the FEM code, while the computation of the inner matrix  $\left( [\hat{\mathbf{F}}]^T [\mathcal{D}] [\hat{\mathbf{F}}] + \hat{S} \right)$  is considered to be part of the constitutive law implementation which thus includes the large deformation effect.

For solving the remaining differential equation in time, there are two main types of integration schemes - explicit and implicit, and each one has its pros and cons.

### 4.2.2 Implicit schemes

Implicit schemes [56] are the ones where the integration depends not only on the last time-steps, but also on the next one, which allows the use of larger timesteps. There are several different explicit schemes, and the one implemented for this work is a Newmark scheme with Newton iterations. Figure 4.1 summarizes the implementation made for the implicit scheme.

<u>DoStep</u>	
$t_{n+1} = t_n + \Delta t$	Time step
$q_{n+1}^0 = q_n + \Delta t \dot{q}_n + \left(\frac{1}{2} - \alpha\right) \Delta t^2 \ddot{q}_n$	Predict displacements
$\dot{q}_{n+1}^0 = \dot{q}_n + (1 - \beta) \Delta t \ddot{q}_n$	Predict velocity
$\ddot{q}_{n+1}^0 = 0$	Predict acceleration
<u>Iter <math>k</math></u> : while $\ r_{n+1}^k / \mathcal{F}_{n+1}^{ext}\  > tol$	Iteration loop
If (Jacobian update criterion), $J_N = \frac{\partial r_n}{\partial q_n}$	Compute Jacobian
<u>Residual</u>	// loop on for each NL
$\nabla u_{n+1}^k = \mathbb{C} q_{n+1}^k$	Compute strains and get internal states
$[S_{n+1}^k, \mathcal{U}_{n+1}^k] = f_{material}(\nabla u_{n+1}^k, \mathcal{U}_n^I)$	Compute stresses and internal states
$r^k = \mathbb{B} S_{n+1}^k + M \ddot{q}_{n+1}^k - \mathcal{F}_{n+1}^{ext}$	Compute residuals on DOF
$q_{n+1}^{k+1} = q_{n+1}^k + J_N^{-1} r^k$	Compute corrections
$\dot{q}_{n+1}^{k+1} = \dot{q}_{n+1}^k + \frac{\beta}{\Delta t \alpha} J_N^{-1} r^k$	
$\ddot{q}_{n+1}^{k+1} = \ddot{q}_{n+1}^k + \frac{1}{\Delta t^2 \alpha} J_N^{-1} r^k$	
<u>StoreState</u>	increment storage strategy
$q_{n+1} = q_{n+1}^k, \dot{q}_{n+1} = \dot{q}_{n+1}^k, \ddot{q}_{n+1} = \ddot{q}_{n+1}^k$	Propagate DOF values
$\mathcal{U}_{n+1}^I = \mathcal{U}_{n+1}^k$	Propagate internal states

Figure 4.1: Implementation of the implicit Newmark scheme in SDT

It is important to remind [57] that the values of  $\alpha = 0.5$  and  $\beta = 0.25$  ensure the unconditional stability of the scheme and there is no extra dissipation or energy injected on the differential equation, but those may be changed if one seeks different convergence parameters.

Implicit schemes may have severe convergence issues, especially on stiffening conditions, like contact or high compression. Jacobian matrix may be assembled either by taking the derivative of the residual or by assembling the geometric stiffness matrix  $K_G$ , taking into account inertial and external forces terms. Both methods of assembly are very costly both in time and memory. Thus, Jacobian update criterion is the most critical issue for this type of scheme as it involves a delicate tradeoff between radius of convergence and implementation time.

Other characteristic from implicit schemes is that its larger timesteps also act as a filter to high frequency oscillations. Due to the use of larger timesteps, models require formulations that are accurate relatively far from linearization point.

### 4.2.3 Explicit schemes

Explicit schemes [56] depend only on the last timestep to predict the next one, by using iterations based on acceleration and a Jacobian corresponding to a mass matrix built as diagonal by using integration at nodes.

<p><u>DoStep</u></p> $t_{n+1} = t_n + \Delta t$ $q_{n+1} = q_n + \Delta t \dot{q}_{n+1/2}$ <p><u>Residual</u></p> $\nabla u_{n+1} = \mathbb{C} q_{n+1}$ $\left[ S_{n+1}, \mathcal{U}_{n+1}^I \right] = f_{material} \left( \nabla u_{n+1}, \mathcal{U}_n^I \right)$ $r_{n+1} = \mathbb{B} S_{n+1} - \mathcal{F}^{ext}$ $\ddot{q}_{n+1} = M^{-1} (-r_{n+1})$ $\dot{q}_{n+1} = \dot{q}_n + \frac{dt}{2} \ddot{q}_{n+1} + \frac{dt}{2} \ddot{q}_n$ $\dot{q}_{n+\frac{3}{2}} = \dot{q}_{n+1} + \frac{dt}{2} \ddot{q}_{n+1}$ <p><u>StoreState</u></p> $\mathcal{U}_{n+1}^0 \leftarrow \left\{ \begin{array}{c} 0 \\ \mathcal{U}_{n+1}^I \end{array} \right\}$	<p>Time step</p> <p>Compute displacements</p> <p>// loop on for each NL</p> <p>Compute strains and get internal states</p> <p>Compute stresses and evolve internal states</p> <p>Compute residuals on DOF</p> <p>Compute accelerations</p> <p>Compute velocities</p> <p>Estimate speed</p> <p>increment storage strategy</p> <p>Propagate internal states to <math>\mathcal{U}^0</math></p>
--	---

Figure 4.2: Implementation of the explicit Newmark scheme in SDT.

The use of a diagonal Jacobian and lack of need to evaluate the geometric stiffness makes timestep evaluations considerably faster than for implicit schemes, but comes at the price of a conditionally stable schemes. Time steps must be smaller than the inverse highest characteristic frequency in the model, dependent on the smallest element size and the wave speed. A classic evaluation [52] is done

at element level using

$$\delta t = \min \left( \frac{2}{\omega_{elt}^{max}} \right) = \min \left( \frac{L_e}{c_d} \right) = \frac{\min(L_e)}{\max \left( \sqrt{\frac{\lambda + 2\mu}{\rho}} \right)} \quad (4.13)$$

with  $\omega_{elt}^{max}$  the greatest eigenvalue for an element,  $c_d$  the dilatational wave speed,  $\mu$  and  $\lambda$  are Lamé's parameters,  $L_e$  is the element length, and  $\rho$  the density. Since nonlinear models have evolving stiffness, the linearized parameters also evolve, and the time step given by the formulation above applied to the initial position may be too large for some points of the trajectory.

Explicit schemes have frequency content up to the maximum element frequencies and thus present high frequency waves/modes that are not representative of the physical behavior and should be damped, either using numeric dissipation of the time scheme [58, 59], or damped through material laws, or filtering the results. In particular, bulk waves must be treated as described in section 2.4.2.

## 4.3 Kinematic reduction

### 4.3.1 Motivation

In order to make the computations faster, the first approach is to reduce the number of degrees of freedom (DOF) of a model. The kinematic reduction, more commonly known as model order reduction in the literature, consists of defining base  $T$  such that

$$\{u(t)\}_N = [T]_{N \times NR} \{q(t)\}_{NR}. \quad (4.14)$$

The choice of a proper subspace restraining the response  $u$  to the subspace spanned by a selected base  $T$  using reduced coordinates  $q$ , has been historically viewed using ad hoc techniques combining static, eigenvalue and various iterative approaches, but would now often be placed in the broad category of subspace classification problems.

Finite element models are a first level of reduction where  $T$  is built as a union of piecewise polynomials. Other techniques [60, 9, 61] can be analyzed by considering a learning, a basis generation phase and possibly iterative methods combining the two phases as will be detailed in the next sections.

With the subspace selected, the same Ritz approach as the one used for FEM is used. Equation (4.14) gives the kinematic reduction and the principle of virtual work which led to (4.8) is reused to obtain a reduced set of equations of the same form

$$[M_R] \{\ddot{q}_R\} + [\mathbb{B}_R] f_{material}([\mathbb{C}_R] \{q_R\}, \{\mathcal{U}^I\}) = \mathcal{F}^{ext} \quad (4.15)$$

with reduced observation given by  $\mathbb{C}_R = [\mathbb{C}] [T]$ , reduced command given by  $\mathbb{B}_R = T^T \mathbb{B}$ , reduced mass given by  $M_r = T^T M T$ . Mass normalization of the base  $T$  is a good strategy to accelerate computations in explicit schemes where  $M^{-1}$  is needed, as with the normalization, one has  $M_r = \mathbb{1}$ .

### 4.3. KINEMATIC REDUCTION

---

While kinematic reduction limits the number of kinematic states (degrees of freedom), it does not change the size of  $f_{material}$  which is defined at all material points used for full model integration. Thus if integrating material evolution equations represents a significant time, the model cost is still great. Generating a sparse approximation of  $f_{material}$  by using a limited number of material points, reduces the number of columns of  $\mathbb{B}$  and rows of  $\mathbb{C}$ , will be the object of the next section on hyper-reduction.

#### 4.3.2 Learning methods

Learning phases should reproduce behavior of interest. The learning phase is thus a tradeoff between numerical cost and representativity of trajectories to be reproduced by the reduced model. Classical component mode synthesis uses a combination of static and eigenvalue computations for learning. More recently, the use of snapshots extracted from transients has gained interest. It is worth noting that using snapshots is the principle of experimental modal analysis and has been used for much more time than for numerical applications.

When the behavior is static and described by displacements at a restricted number of points Guyan condensation [62] or Schur complement is used. Separating the model in master and slave DOF and considering a linearized model, one has

$$\begin{bmatrix} K_{mm} & K_{ms} \\ K_{sm} & K_{ss} \end{bmatrix} \begin{Bmatrix} q_m \\ q_s \end{Bmatrix} = \begin{Bmatrix} \mathcal{F} \\ 0 \end{Bmatrix}, \quad (4.16)$$

leading to the reduced basis given by

$$\begin{Bmatrix} q_m \\ q_s \end{Bmatrix} = \begin{bmatrix} I \\ K_{ss}^{-1} K_{sm} \end{bmatrix} \{q_m\} = [T] \{q_m\}. \quad (4.17)$$

Note that static responses to loads have also been considered with marginal differences in the presence of rigid body modes [63].

When the only available information is bandwidth, modal truncation is relevant. The modes, solution of the eigenvalue problem

$$\left[ K - M\omega_j^2 \right] \{\phi_j\} = \{0\}, \quad (4.18)$$

form an ordered series and one can keep the vectors associated with frequencies within the band of interest.

Since load locations and simulation bandwidth are typically known, component mode synthesis methods [63] combine static responses and modes. Classical combinations are enforced static displacement and fixed interface loads, the Craig-Bampton method, and applied load static and free interface

modes, the McNeal method. Extensions of these methodologies are linked to the consideration of additional loads for parameter or non-linear changes [64].

While combining static and eigenvalue solution is very practical for linear systems, choosing linearization points can be a difficulty. A number of authors have thus considered transient based learning assuming that a reasonable reduction subspace is generated by the span of a number of snapshots [65]

$$\text{span}[T] = \text{span} \left[ q(t_1) \quad \dots \quad q(t_N) \right] \quad (4.19)$$

Finally, it is worth noting that a last traditional approach is to introduce error evaluation as a basis enrichment mechanism. A first reduced model is used to obtain an approximation of the response and a residue evaluation is used to enrich the basis in a direction allowing error minimization, see for example [66] for applications to component mode synthesis.

#### 4.3.3 Basis generation

From a set of vectors, possibly combination of static, eigenvalue and transient learning methods, the second phase is to build a basis. Basis generation algorithms must guarantee vector independence even in the presence of round off errors and possibly order contributions to allow truncation or seek to induce sparsity by generating vectors with disjoint support.

For basis independence, Gram Schmidt algorithms or partial LU decomposition are the classical approaches. To combine orthonormal bases with the idea of ordering contributions, the Singular Value Decomposition SVD is the classical approach. Thus the combination of snapshot learning and SVD is typically known as a POD (Proper Orthogonal Decomposition) [65].

Using a learning phase, which yields  $n$  displacement  $q_l$ , containing  $m$  DOF, the singular value decomposition of the response is given by

$$[q_l]_{m \times n} = \sum_i U_i(x) (\Sigma_i V_i(t)), \quad (4.20)$$

where  $U^T U = \mathbb{1}_m$ ,  $\Sigma$  is diagonal, and  $V^T V = \mathbb{1}_n$ . Each vector of the left singular shapes  $U_i$  is a spatial base vector, while the product from the singular values  $\Sigma_i$  with the right singular shapes is a degree of freedom that describes the evolution of each of the left singular shapes in time. Numeric procedures for the decomposition will not be discussed here, though a visual interpretation is illustrated in figure 4.3.

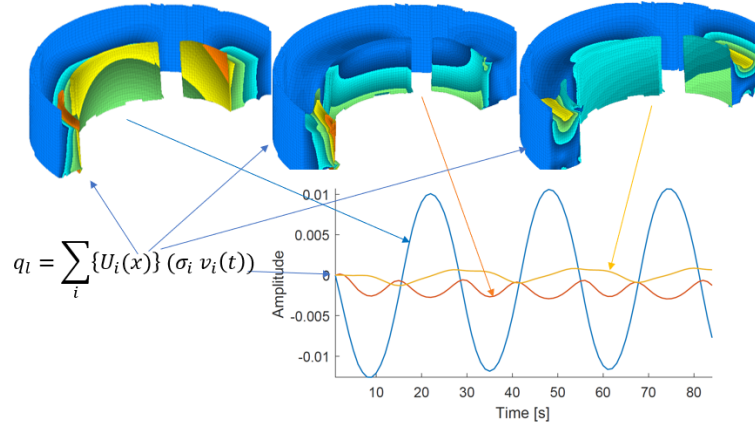


Figure 4.3: Visual interpretation of a singular value decomposition.

With a proper choice of norms [67], SVD and modal decomposition can be shown to be equivalent. Thus as high frequency modes were truncated as being not relevant because less likely to be excited by low frequency signals, shapes associated with low singular values are often truncated to generate a small rank base. Sometimes this reduction is called principal component analysis.

For parametric problems described by a large number of dimensions, higher order variable separation like

$$u^r(t, x, p^1, \dots, p^n) \approx \sum_i f_i(x) g_i(t) \prod_{k=1}^n h_i^k(p^k) \quad (4.21)$$

provides a framework which received a lot of attention. For a parametric set of data  $u^r$  that could be computed using a full FEM model, one seeks a separated variable approximation (4.21). Taking only time and space as the only separate functions, one has exactly a singular value decomposition, if one sees  $f_i(x)$  as each vector of the retained base and  $g_i(t)$  as their evolution in time.

The argument of the proper generalized decomposition (PGD) method [68] is that it can be less costly to approximate parametric evolution of responses in the form (4.21) than to restrict the assumption using a linear combination of  $f_i(x)$  spatial shapes. This argument has motivated a body literature on iterative procedures to build separated variable approximations.

The gain can be significant when using more parameters, where one needs to compute the response only for each value  $i$ . If such separation is not used, one must compute the whole response for each parameter. But the approach may be completely impractical if the parameters correspond to transient excitation signals for which no small order separated variable approximation exists.

For the application considered in this work, the choice to retain the material behavior on the model representation, and the necessity to run the model on transient inputs of multibody models, for which variable separation will have a large order, motivates the use of classical reduction based on spatial

bases.

## 4.4 Hyper reduction: lower cost integration of non-linear terms

As expressed in section 4.2, for both explicit and implicit schemes, the residual computation involves the evaluation of the material law on every integration point, despite the kinematic reduction involving the base  $T$ . Thus, a second layer of reduction is needed and it is usually called hyper-reduction. The main idea is to compute the internal forces with reduced computational cost.

These methods build reduced integration routines to compute stress only in a few points and rebuild internal forces accurately for displacements spanned by the reduced base. In the present work, the DEIM method will be described, and the ECSW method will be used, as it ensures stability.

### 4.4.1 Discrete Empirical Interpolation Method (DEIM)

The idea of Chaturantabut and Sorensen [69] is to project the forces exerted by the elements into a reduced base,

$$\mathcal{F}_l^{int} = \mathbb{B}S \approx Af \quad (4.22)$$

where  $\mathcal{F}_l^{int}$  is the internal forces yielded from a learning simulation,  $A$  is the projection base and  $f$  corresponding amplitudes obtained from SVD of  $\mathcal{F}_l^{int}$ .

Choosing to observe internal forces on only a few DOF by using a Boolean observation matrix  $E$ , leads to

$$E^T \mathcal{F}_l^{int} = E^T Af \quad (4.23)$$

so the reduced force amplitudes may thus be estimated using

$$f \approx (E^T A)^{-1} E^T \mathcal{F}_l^{int}. \quad (4.24)$$

As a result, in reduced simulations, the internal forces may be computed using the form

$$\mathcal{F}_r^{int} \approx A(E^T A)^{-1} E^T \mathcal{F}_l^{int} \quad (4.25)$$

which is sparser since non-linear material behavior is only computed at elements selected by matrix  $E$ . Those elements may be optimally selected by algorithms specialized on rebuilding the full internal forces.

There are iterative variants, for this method, such as the one proposed by [70] whose idea is to generate a base for each internal variable field, introduce a residual evaluation and possibly perform some full steps when this evaluation indicates notable error levels.

#### 4.4.2 Energy Conserving Sampling and Weighting (ECSW)

As the DEIM only relies on ensuring that internal forces are properly projected, it does not ensure accuracy or stability. This motivated the method proposed in [71] to affordably compute the nonlinear forces, also with the idea to select only few integration points to compute the internal forces, but now with the objective that the computed work of deformations in the reduced base is approximately the same as the work for the full model in the learning conditions.

From the learning conditions, one retains the stresses  $S_l$ , and the assembly matrices  $\mathbb{B}$  and  $\mathbb{C}$ . From a kinematic reduction on such learning conditions, one obtains a kinematic reduction base  $[T]_{N \times NR}$ . The work contribution  $\{b^r\}$  for the  $NR$  reduced DOF at  $NT$  time snapshots may then be written in different forms,

$$\begin{aligned}
 \{b^r\}_{NR \times NT} &= [T^T \mathbb{B}]_{NR \times NG} \{S_g^l\}_{NG \times NT} \\
 &= [[\mathbb{C}T]^T S_g(t)]_{(NR \times NT) \times NG} \{J_g w_g\}_{NG \times 1} \\
 &= [G]_{(NR \times NT) \times NG} \{J_g w_g\}_{NG \times 1}
 \end{aligned} \tag{4.26}$$

The first form is the one actually used in the FE routines with  $T^T \mathbb{B}$  giving the work of each strain component on the reduced basis. The second form explicits the relation between the  $\mathbb{B}$  at the weights  $w_g$  associated with each integration point. The last form rewrites the same reduced work components  $\{b^r\}$  as a linear combination of weights. This last form motivates the proposed algorithm. One seeks a minimum set  $E$  of columns of  $G$ , or hyper integration points, and the associated positive weights  $w_g^*$  that give a good approximation of the learning work contributions  $\{b^r\}$ . In other words, one seeks

$$\text{Find } w_g^* \text{ that minimizes } \|w_g^*\|_0, \text{ subject to } \|\{b^r\} - [G] \{w_g^*\}\|_2 < \varepsilon_{tol} \text{ and } w_g^* > 0. \tag{4.27}$$

Although, a minimization with a zero-norm is a problem with NP complexity, a sub-optimal approach, called Sparse non negative least square method (SNNLSQ), consists in finding the point that contributes the most to represent the matrix  $G$ , and then perform a regular LSQ with this point and all previously added, until the constraints are satisfied. A summary of the implementation is shown in figure 4.4.

<p>Learning simulation</p> $\mathbb{B}, \mathbb{C}, w_g, S_g^l, T, G$ $\{\mathcal{F}_{int}^l\} = [G] \{w_g\}$ Initialize $E = \emptyset, w_g^* = \{0\}$ Initialize $\varepsilon_{tol}, r = 1$ SNNLSQ <p>While <math>r = \left\  \frac{\mathcal{F}_{int}^l - G \{w_g^*\}}{\mathcal{F}_{int}^l} \right\  &gt; \varepsilon_{tol}</math></p> <p>    <math>r_0 = \mathcal{F}_{int}^l - [G] \{w_g^*\}</math>                 <math>\mu = [G]^T r_0</math>                 Find index <math>j_\mu</math> of <math>\max(\mu)</math>                 <math>E = E \cup j_\mu</math>                 <math>\eta = \min_{w_g^*} \left( \left\  \mathcal{F}_{int}^l - [G] w_g^* \right\ _2 \right)</math>                 Find index <math>j_{neg}</math> of <math>\eta &lt; 0</math>                 <math>E = E \setminus j_{neg}</math>                 <math>w_g^*(\bar{E}) = 0</math> and <math>w_g^*(E) = \eta</math>  <math>\mathbb{B}_R^E = T^T \mathbb{B}(E) w_g^*, \mathbb{C}_R^E = \mathbb{C}(E) T</math></p>	<p>Assembly, learning, kinematic reduction</p> <p>Get internal forces for training conditions</p> <p>Initialize set of active points and weights</p> <p>Initialize hyper-reduced command and tolerance</p> <p>Optimization loop</p> <p>Get difference from full internal load learning points</p> <p>Compute points contributions for current residue</p> <p>Get point with most contribution</p> <p>Add Gauss point to active points set</p> <p>Least square method to find optimal weights</p> <p>Find computed negative weights</p> <p>Remove negative weights from active set</p> <p>Assign weights to active elements</p> <p>Update observation and command</p>
---	---

Figure 4.4: Implemented hyper reduction scheme

Using the relations in equation (4.26), with the selected integration points  $E$ , one may define a different assembly matrices  $\mathbb{B}^E$  and  $\mathbb{C}^E$ , so the numeric schemes defined in figures 4.1 and 4.2 remain unchanged.

Another interpretation of this method is to consider the whole structure as a single element, with the kinematic reduction giving the element shape functions and the selected points, the integration rules [72].

Other developments on this method were made, such as [73] for contact implementation, [74] with a *on the fly* reduction method and [75] which uses the DEIM method to expand the values of internal variables to the whole structure.

## 4.5 Sample application

### 4.5.1 Model description

The full model is based on a rear suspension twist beam axle bushing shown in figure 3.1. It has 77mm of outer diameter and 45.5mm of inner diameter. It is composed of two different elastomer materials surrounded by metal plates, but for this sample application (which happened earlier than the identifications) a single material model was used.

Metal parts are considered rigid and the elastomer volume is modeled by the constitutive law pre-

## 4.5. SAMPLE APPLICATION

sented in section 2.4, without the nonlinear viscous coefficients with an underlying deviatoric Mooney-Rivlin potential and linear isotropic model. The simulation constants are given in table 4.1. To reduce the learning phase computational cost, the model is cut in four using its symmetry planes. The retained model uses 24530 hexahedric elements with eight integration points each and a total of 76084 DOF. The exterior shell is fixed and a force is applied to the inner shell.

Table 4.1: Material constants used in simulation.

$c_1$	$c_2$	$\kappa$	$\kappa_v$	$g$	$\tau$	$\rho$
1MPa	2MPa	20MPa	0.2MPa	$1/3, 1/3$	$1/12s, 1/50s$	$2.33 \text{ ton/m}^3$

### 4.5.2 Performance and accuracy of base implementation

The retained learning phase consists in the simulation of 3 cycles at 20Hz, with the explicit scheme described in figure 4.2. The computation took 27.7 hours in a Core i5-6300HQ CPU at 2.3GHz. Timestep used is 30% smaller than that computed by equation (4.13), based on the high frequency asymptote. The constitutive law was called  $49.06 \times 10^9$  times, for  $250 \times 10^3$  timesteps. The peak deformation is 37%. 30 snapshots per cycle are kept for the hyper-reduction step.

The SVD from the learning phase results takes only a few seconds as less than a hundred snapshots are used. For kinematic reduction, 6 shapes are retained, defined by a threshold of 1% from the most significant singular value. The first five shapes are shown in figure 4.5 along with the decrease of singular values. The least important singular shapes already show localized deformations, which indicates that retained shapes should be enough to capture global deformations in the model.

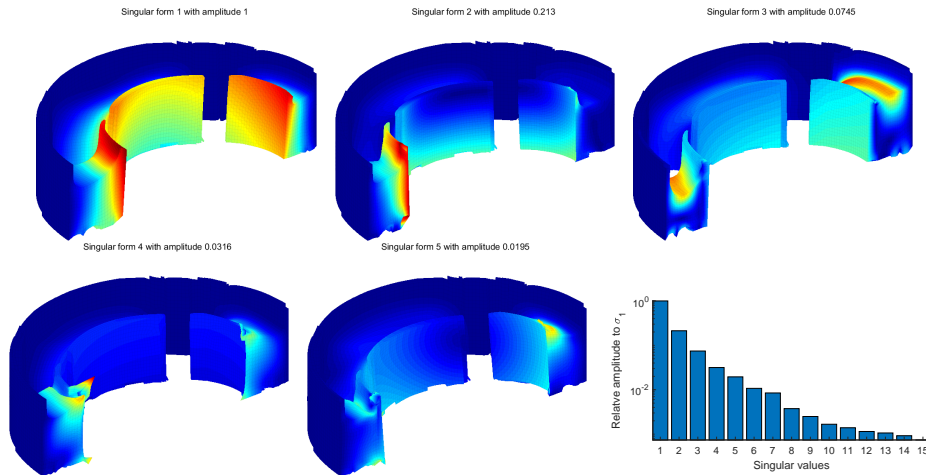


Figure 4.5: First 5 vectors from the reduced model base and singular values amplitudes

For the hyper-reduction, a few minutes are needed to converge with the chosen kinematic base and a tolerance of  $10^{-4}$  on full internal work contributions. The final model retains 139 Gauss points

## 4.5. SAMPLE APPLICATION

---

out of 196240, meaning a 3 orders of magnitude reduction, which can be directly translated to CPU time as illustrated in table 4.2. An important remark is that the error may be reduced to zero if one decides to perfectly constrain the vector  $b^r$ , by using  $N_t \times N_r$  points (540 in the present case).

Table 4.2: Model characteristics. CPU time is for 3 cycle transient.

	Number of DOF	Number of Gauss points	CPU time
Full model	76084	196240	27.7h
HR with 3 cycles	6 ( $10^{-2}$ on tolerance)	139 ( $10^{-4}$ on tolerance)	29s
HR with half cycle	4 ( $10^{-2}$ on tolerance)	48 ( $10^{-4}$ on tolerance)	12s

Figure 4.6 illustrates the distribution of the chosen integration points. They are mainly concentrated on tension/compression zones, indicating, as expected, that these regions are those where the material behavior is more non-linear, and that most of the energy is concentrated there. The point concentration would likely change if there were solicitations of the same magnitude in the transverse direction.

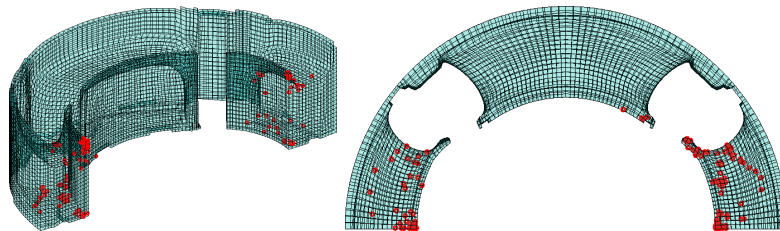


Figure 4.6: Localization of integration points selected by the hyper-reduction.

Simulation on the hyper-reduced model takes less than 30 seconds on the same CPU, corresponding to a speedup factor above 2000 (as shown in table 4.2). Figure 4.7 shows the very good match of the global displacement of the full and hyper-reduced models.

A second hyper-reduction was made for only half cycle, from 1/4 cycle to 3/4 cycle, of the full simulation to evaluate the possibility of using less data on learning phase. Figure 4.7 illustrates that outside the transition associated with the first quarter cycle, the match is still quite accurate. The differences in the first 1/4 cycle and the up part of the cycle are rather limited.

## 4.5. SAMPLE APPLICATION

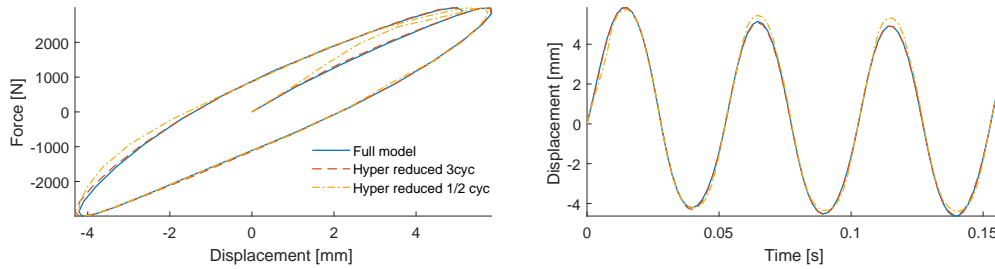


Figure 4.7: Comparison between the force displacement diagram and the displacement on time for full and hyper-reduced models.

The hyper reduced model is also accurate for predicting local deformations and stresses in the selected points, as illustrated by figure 4.8.

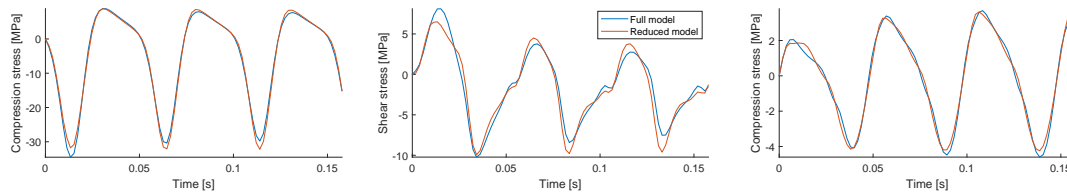


Figure 4.8: Stress comparison on three different points. The first on the center of the compressed zone, the second on the sheared zone and the last in the edge of the compressed zone.

### 4.5.3 Extrapolations

Harmonic loading at low frequency is an interesting tool for performance assessment in terms of comfort analysis, but there are other fields that require different solicitations. For example, lower amplitude and higher frequency solicitations may be pertinent for evaluating vibro-acoustic behavior when going over a rough road. Figure 4.9 show the response of the articulation at 100Hz and 50N of amplitude. Both local and global behaviors are well represented by the hyper-reduced model, even if these conditions are very far from the learning conditions.

Another benefit of hyper-reduction for explicit integration is the increased stability over timestep size, since smallest element length is no longer taken into consideration, and also, high frequency modes are filtered by the kinematic reduction. To illustrate the difference, articulation response to a force impulse in Ricker form with 5kN amplitude and 5ms duration is shown in figure 4.10. For the hyper-reduced model an explicit integration with a timestep increased by a factor 20 leads to a response with no visible difference.

## 4.6. PERSPECTIVES AND CONCLUSIONS

---

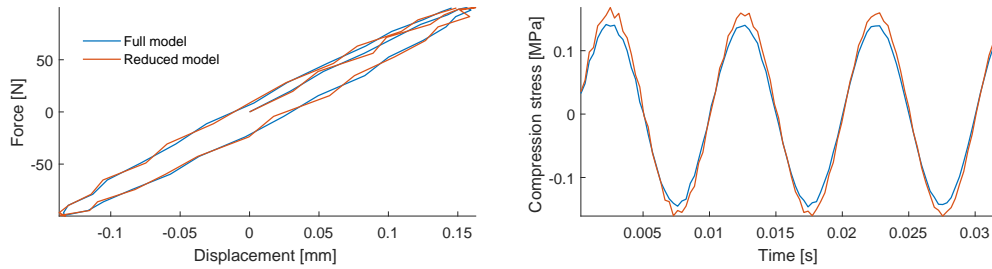


Figure 4.9: Articulation response to high frequency and low amplitude: global behavior on the left and localized stress on the right.

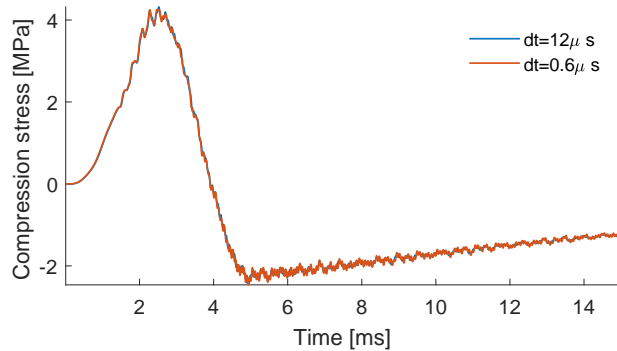


Figure 4.10: Articulation impulse response.

## 4.6 Perspectives and conclusions

A first clear perspective is to perform the simulation in the full model (6 directions) and verify if the responses are consistent on the hyper reduced model. Linear combinations of initial solicitations (angle and compression for instance) could also be used to check the validity domain of the hyper reduced model.

Another foreseeable possibility is to use the linearized geometric stiffness around a few different points to build modal bases to generate the first reduction, and static solutions to span the stresses to be used in a hyper-reduction attempt. Other possibility is the use of substructuring techniques [9] to perform reductions in smaller and simpler subsections of the whole volume. Enrichment of the objective function by weighting the energy at the interfaces also seems to be a good perspective for multibody representation.

In terms of the model, one may try extrapolations on material parameters and possibly change material models. Implementation of the materials developed in chapter 2 and identified in chapter 3 is a very clear perspective in sight, with different post processing techniques such as computing instantaneous dissipation, whose importance will be shown in chapter 5.

#### 4.6. PERSPECTIVES AND CONCLUSIONS

---

In further perspectives, the utilization of the nominal pre-stress that is imposed to the material by the manufacturing procedure should be accounted for. Other main unaccounted feature of the part is the plastic limiter, which ensures the contact to the rubber earlier, generating a severe increase in stiffness, and thus is vital for accurate models in large deformations, which was already developed in [76, 73].

# Chapter 5

## Multi-body simulations

### Contents

---

<b>5.1</b>	<b>Introduction</b>	<b>156</b>
<b>5.2</b>	<b>Dissipated power: Powertrain suspension case</b>	<b>156</b>
5.2.1	Model description	156
5.2.2	Bushing models	157
5.2.3	Dissipated power	160
5.2.4	Stop/start transient	163
5.2.5	Modal responses	164
<b>5.3</b>	<b>Steps for a complete multibody integration: rear twist beam axle bushing case</b>	<b>165</b>
5.3.1	Current model description	166
5.3.2	Integrating 0D models	168
5.3.3	Integrating 3D hyper-reduced models	169
5.3.4	Validation data for consistence checks	170
5.3.5	Consistence of mount forces	173
<b>5.4</b>	<b>Perspectives and conclusions</b>	<b>176</b>

---

## 5.1 Introduction

Multibody simulation is a method of numerical simulation where systems are composed of various bodies, normally with few DOF each (unlike for FEM, where hundreds of thousands of DOF are usual). Connections between bodies may be modeled with kinematic constraints (such as planar joints, universal joints, etc.) or force elements (such as springs, dampers or more elaborate user models, as control elements). There is also the possibility of imposing boundary conditions in the joints and on the bodies. There are also several types of solvers (static, kinematics, dynamics, eigensolvers, etc.) enlarging the amount of information that can be extracted from such models.

This work is particularly interested on the force elements that connects the bodies and the instantaneous dissipation on these elements is particularly addressed in section 5.2. The instantaneous dissipation is introduced for hysteretic models, and is proven to be a crucial feature to be addressed with a sample application on a powertrain suspension case, where two models with different instantaneous dissipations lead to different system-level behaviors.

In a second example, the simulation of a full vehicle going through obstacles was performed. The computed forces on the twist beam axle articulation were directly compared to test results. Meanwhile, the theoretic bases for an implementation of a hyper-reduced model are set and the forces are computed for a 0D model identified in 3. The detailed reasoning for this case is presented in section 5.3. The perspectives are discussed in 5.4 the first steps to integrate the developed models in chapters 1 and 2 are made.

## 5.2 Dissipated power: Powertrain suspension case

A new development is used here to clarify energy dissipation computations. The dissipation either in time-domain or in frequency domain for linear viscoelasticity is well known and established [20]. For hysteretic dissipation, subsection 5.2.3 illustrates how it can be computed, while subsection 5.2.4 compares both dissipations for selected order models.

### 5.2.1 Model description

The first multibody application will be a thermal powertrain suspension. For the chosen vehicle, the suspension consists of three mounts, located left right and below the engine. The ones at the top hold the weight of the powertrain unit, and the one below (called anti-torque) transmits part of the torque from the unit to the chassis. The scheme and the vehicle 3D model are shown in figure 5.1.

Those vibrations are usually predicted by a multi-body simulation of the powertrain unit, where its components are simplified for faster implementation. For the current application the powertrain is modeled by its inertia matrix and its gravity center. It is attached to a left mount, a right mount and

## 5.2. DISSIPATED POWER: POWERTRAIN SUSPENSION CASE

---

an anti torque mount, which is located under the engine as figure 5.1 shows. Those three mounts are attached to the chassis which is supposed to be fixed.

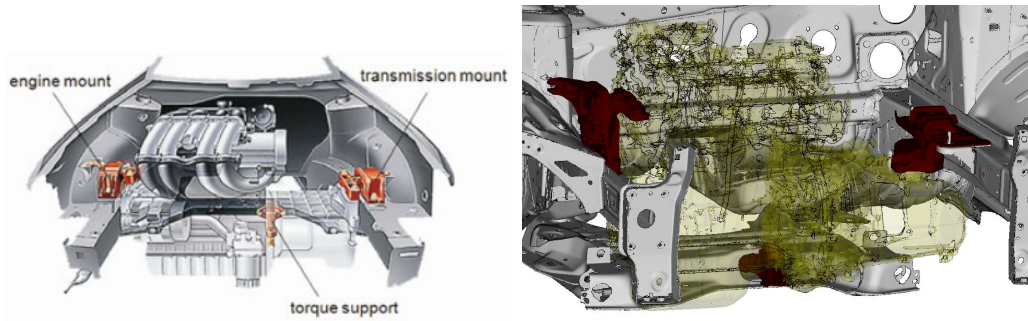


Figure 5.1: Left: Schematic positioning of engine mounts. Source: [2]. Right: 3D model of the engine suspension

The powertrain suspension is meant to filter the engine vibrations above the idle engine regimen, and thus limit noise and vibrations in the vehicle cabin. Therefore, the six rigid modes of the powertrain unit are determined by these mounts and intentionally placed below the idle engine frequency. While starting/stopping the engine, the ramp up/down of the regimen excites different frequencies that may cause comfort issues. The parameters that are normally tuned to limit this issue are the ramp speed and the modal damping, which means that the mounts dissipations need to be appropriately modeled to accurately predict vibrations on the cabin.

### 5.2.2 Bushing models

The test on three mounts that compose the powertrain suspension were made before this work and the understanding gained in chapter 1 and are thus not perfectly suitable, yet still quite relevant. Low speed 10mm/min triangular displacement was enforced, and the results are illustrated by figure 5.2.

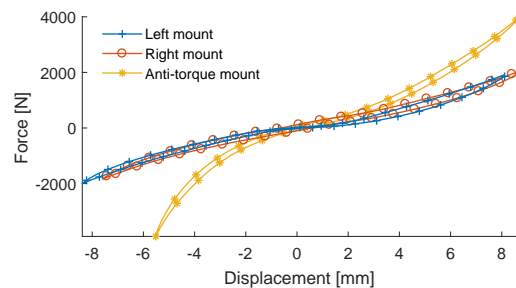


Figure 5.2: Force/displacement response for the three tested mounts

A nonlinear elastic model was built using the mean test load for each displacement and is shown in figure 5.3 left. An a posteriori view indicates that it would be a better approach to discard the

beginning of the curves for a hyperelastic behavior.

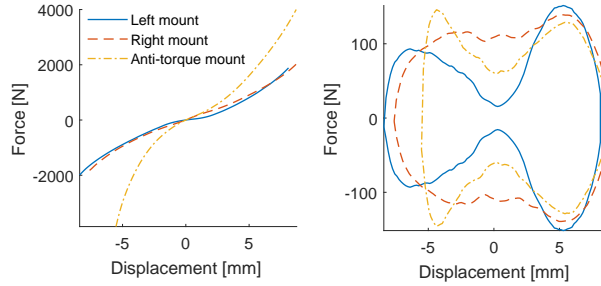


Figure 5.3: Non-linear elastic response (left) and dissipative forces (right) for the tested mounts

The remaining forces, shown in figure 5.3 right, computed subtracting the nonlinear elastic model (figure 5.3 left) from the test raw results (figure 5.2) and are supposed to be the generated by a dissipative model in parallel with the nonlinear elastic model. The left mount and the anti torque mount, on a smaller scale, present significantly less dissipation around null displacement. It is probably because a significant part of the rubber is not excited within small displacements, and after a certain level, it is solicited by a self-contact. Such increase in stiffness coupled with increased dissipation might actually be captured by the models proposed in chapter 1 with a proper test campaign.

Plotting the stiffness as function of distance to the turning point without the nonlinear elastic contribution, in figure 5.4, as it was suggested in section 1.4.2, one can see that its evolution for small distances to the turning point is quite similar to the ones provided by hysteretic models. The absence of dissipation around zero displacement creates bumps in the curves between 6 and 10 mm, more visible for the left mount. The end of the curve shows strong negative stiffness, due to the removal of the poorly extracted nonlinear elastic part.

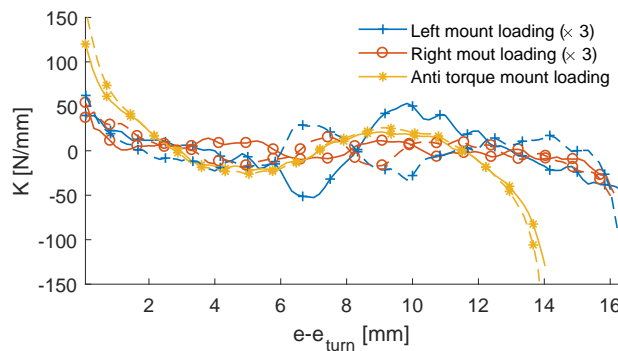


Figure 5.4: Stiffness as function of the distance to the last turning point without non-linear elastic component.

Considering the mean curve as the hyperelastic part was shown to be a poor approach chapter 1

## 5.2. DISSIPATED POWER: POWERTRAIN SUSPENSION CASE

and in section 3.4, as it illustrates that removing hysteretic relaxation is a more accurate way to do it. Using the strategy proposed in those parts, one reaches the curves illustrated in figure 5.5. Although, all further analysis were carried using the mean hyperelastic model, with dissipation in parallel.

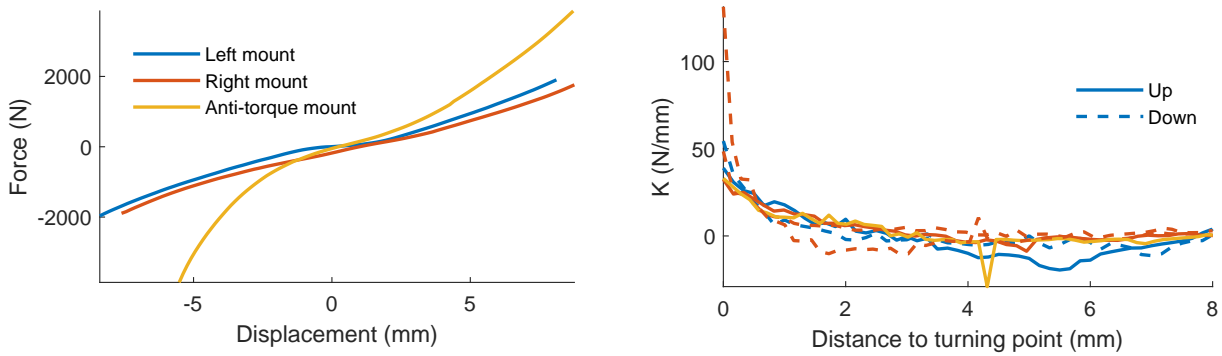


Figure 5.5: Nonlinear elastic force and stiffness as function of turning point with new extraction strategy.

To emulate the dissipation in parallel of the non-linear elasticity, two different models were used: a viscous dissipation or mount force of the form  $f(u) + c\dot{u}$  and a hysteretic STS model, equation (1.42). Both models were tuned to dissipate the same amount of energy for a harmonic solicitation with frequency close to the powertrain idle frequency (around 10Hz), with the same amplitude as the identification tests.

Figure 5.6 shows the dissipated power for both models of the right mount under the stated load, and even if the total dissipation is the same, the profiles during the period notably differ. More details on the computation of dissipated power for different models will be given in the following section.

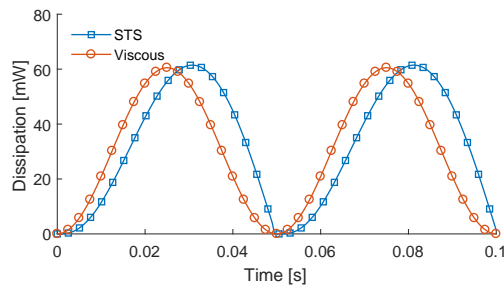


Figure 5.6: Dissipated power for a STS model and a viscous model under harmonic solicitation

The procedure provides a satisfactory fitting on both the right and the anti-torque mounts, though for the left mount the difference is quite visible, as it is possible to see in figure 5.7. The left mount present a different hysteretic loop, probably due to a contact that changes abruptly the stiffness. This contact may have its non-linear elastic part modeled by the proposed procedure, but the associated

## 5.2. DISSIPATED POWER: POWERTRAIN SUSPENSION CASE

dissipation cannot be modeled by viscous or hysteretic models uncoupled with non-linear stiffness. The viscoelastic effects are concentrated right after the turning point due to the slow imposed velocity.

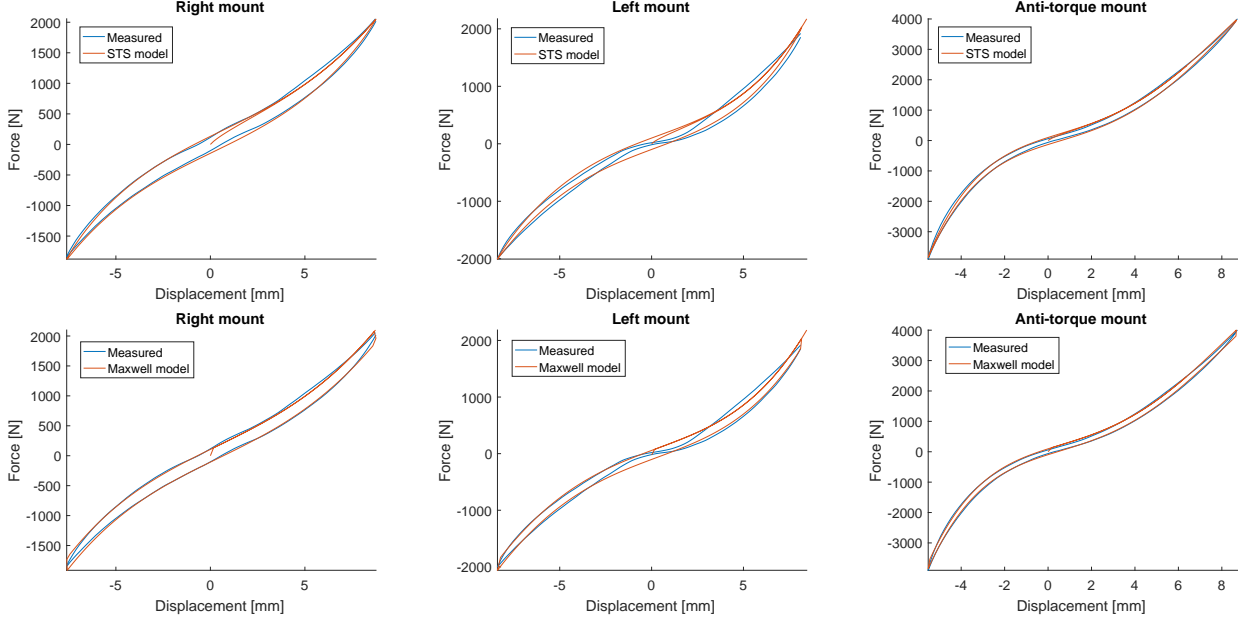


Figure 5.7: Rubber mount test data and fitting with non linear stiffness and hysteretic or viscous dissipation.

The parameters for each model are summarized in table 5.1.

Table 5.1: Model parameters

Mount	STS	Viscous
Right mount	$K^1 = 246.9N/mm$ $C = 23381N^2/mm$	$c = 638.66Ns/m$
Left mount	$K^1 = 321.6N/mm$ $C = 8842.5N^2/mm$	$c = 477.84Ns/m$
Anti-torque mount	$K^1 = 2239.3N/mm$ $C = 11959N^2/mm$	$c = 578.4Ns/m$

### 5.2.3 Dissipated power

As shown in figure 5.6 dissipated power notably depends on the model and understanding how to compute and separate stored and dissipated energy is important.

Time domain instant power computation for a Maxwell model is quite simple, as one has for each cell

$$P_d^i = F^i \dot{x}^i = c^i \dot{x}^{i2} \quad (5.1)$$

which transcribes the fact that all the power injected into the damper is dissipated.

Figure 5.8 shows that dissipation for a Maxwell model responds with twice the solicitation frequency, since both loading and unloading generate dissipation peaks. Power reaches a maximum that depends on the gap between solicitation frequency and cell resonance (positioned at  $1Hz$ ). For solicitations below the cell resonance, the dissipation occurs at maximum speed (or low displacements). For a solicitation far beyond the cell resonance, the dissipation peaks at low deformation rates (max displacements), and for a solicitation at the relaxation frequency, the dissipation peaks exactly at a quarter period of deformation. This delay/phase shift is due to the the fact that above relaxation frequency, the dashpot becomes stiffer on average than the spring. It is also worth noticing that if the cell is forced into its resonance, dissipation is much more intense, as seen in the bell-shaped curves in figure 1.8.

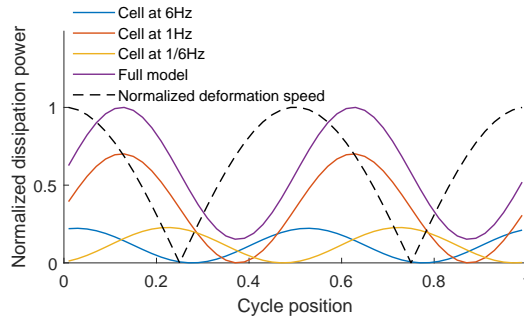


Figure 5.8: Dissipation as function of cycle position for different solicitation frequencies for 1Hz solicitation.

For a model with multiple cells and thus different characteristic frequencies, the dissipated power is always strictly positive, as there is always phase difference between one of the cells and the solicitation. In the previous section a viscous cell was placed in parallel to the spring, dynamic stiffness of the form  $K + Cs$ , and adjusted to dissipate the same energy over a period, that is have the same transfer or complex modulus at that frequency. But with this model, dissipated power is strictly null for no velocity. This implies that just having the phase difference between force and displacement is insufficient to properly predict instantaneous power dissipation which will be shown to have a role in transients.

For rate independent hysteretic models, first discussed in section 1.4, friction elements dissipate energy while elastic elements store it. For a given power injected into the mount, it is thus interesting to distinguish the power that is stored as purely (hyper)elastic energy and the dissipated power.

For the selected order parametric model (1.32), computation of dissipated power is quite simple, as for every friction element one has

$$P_d^i = F_f^i \dot{x}^i. \quad (5.2)$$

which describes the fact that all energy injected into the friction element is dissipated.

For a sinusoidal cycle on a 3 cell model, the power dissipated in each cell and in the full model is illustrated in figure 5.9. The energy is dissipated for sufficient distance from the last turning point. For example 0.25 is a turning point, and one sees the blue cell dissipate first, the red second, ... The total dissipation is thus concentrated in the second half of the half cycle that ends at 0.75. This is not like the viscous model where peak dissipation changed position within the period depending on frequency.

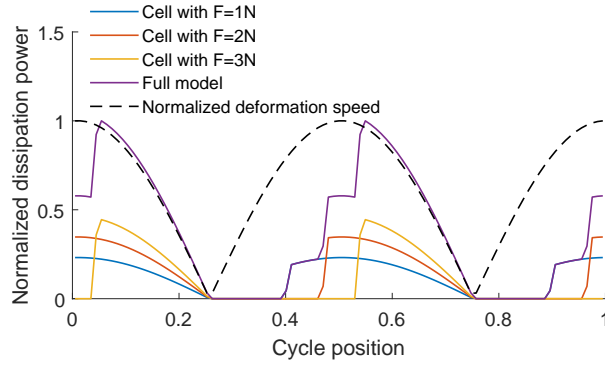


Figure 5.9: Instant dissipation on an Iwan model under sine solicitation

For the non-parametric model discussed in section 1.4.3, some assumptions are needed. The energy dissipation must depend only on the distance to the turning point, as it is composed only by friction elements. Thus, the model dissipates half the energy it would dissipate in a complete one. So the dissipated energy in a complete loop is given by

$$\begin{aligned}
 E_d(x - x_{turn}) &= \frac{\int_{x_{turn}}^x K^{hyst}(x - x_{turn})dx}{2} + \frac{\int_x^{x_{turn}} K^{hyst}(x_{turn} - x)dx}{2} \\
 &= \int_{x_{turn}}^x K^{hyst}(x - x_{turn})dx
 \end{aligned}
 \tag{5.3}$$

This means that supposing slow speeds, to disregard viscoelastic effects, for a hysteretic model one might simulate a closing cycle to compute the theoretical dissipation. Thus, half of this theoretic dissipation is the amount of energy that was dissipated in the supposed half cycle. Figure 5.10 presents a visual interpretation of the dissipated energy for a supposed closed cycle.

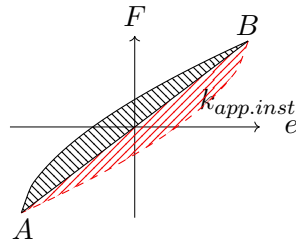


Figure 5.10: Dissipated power on a half cycle, supposing perfect closure.

### 5.2.4 Stop/start transient

To analyze the impact of the dissipation model in a realistic setting, one considers a stop/start transient. The model input is the engine torque, applied in the direction of the torque roll axis, which is the axis around where the powertrain turns when there are no efforts acting. Its time and frequency domain evolution are illustrated in figure 5.11. The model outputs are the forces exerted by the three mounts on the chassis.

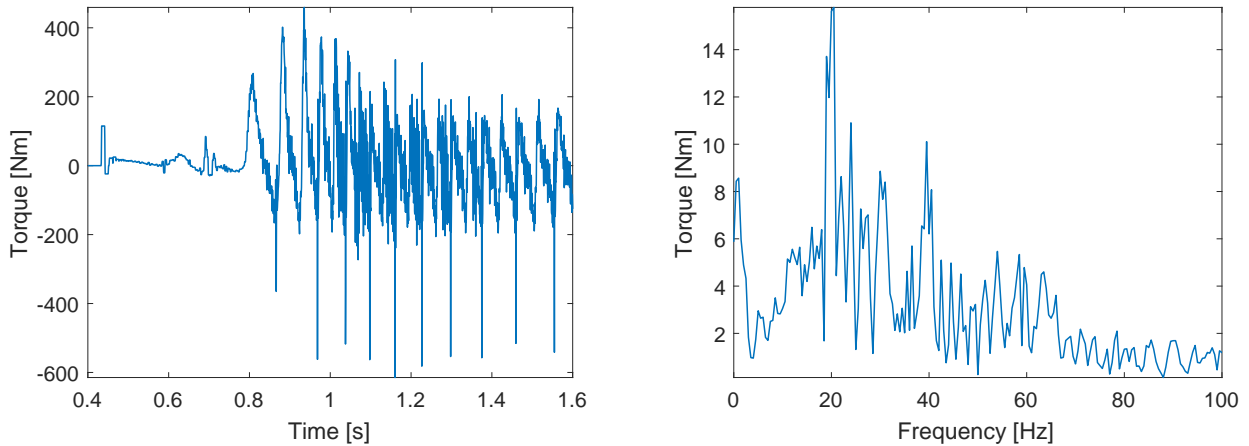


Figure 5.11: Measured engine torque used as an engine for the simulation.

The torque was measured in starting engine situation. Its components in frequency domain are very well spread in the spectrum, with strong components at 20Hz and 40Hz, which should correspond to the idle engine frequency and its first harmonic. A significant amount of residue is also present in all the considered spectrum (up to 4kHz).

Figure 5.12 shows the experimental results along with computed forces for both dissipative models in the direction of the vehicle motion. The models are quite accurate for predicting the highest loads on left and right mounts, and an error of the order of 30% is made for the estimated forces acting on the anti-torque mount. The viscous response tend to underestimate the forces with respect to the measurements, while STS model has a tendency to slightly overestimate the response.

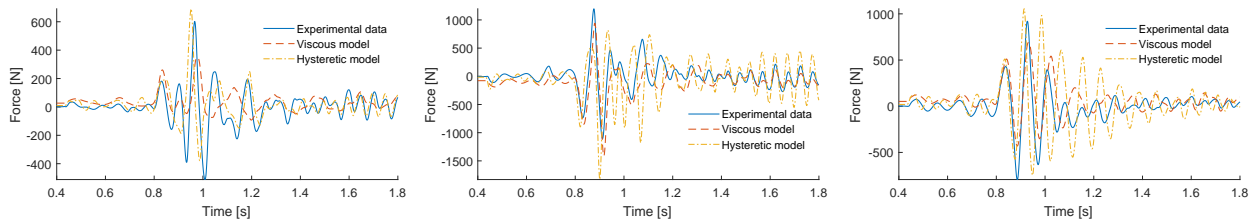


Figure 5.12: Measured and computed forces at the mounts. Left: Left mount. Middle: Anti-torque mount. Right: Right mount

## 5.2. DISSIPATED POWER: POWERTRAIN SUSPENSION CASE

To illustrate the importance of considering dissipated power computations, the approaches discussed in section 5.2.3, were computed for the two models considered. In figure 5.13, both models indicate a larger dissipation on the right mount, with left mount being the least dissipative. But dissipated energy totals present a considerable difference, around 30%.

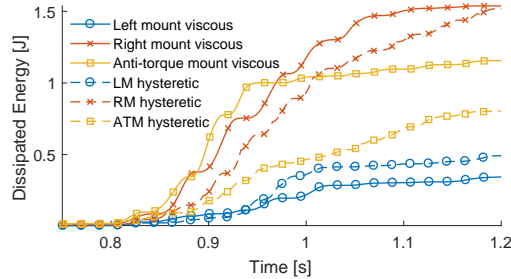


Figure 5.13: Dissipated energy for each model

### 5.2.5 Modal responses

The differences in terms of local behavior illustrated so far do not seem to justify the need for more detailed characterization, but system level should also be addressed. Hence, a modal analysis was carried around the resting position of the engine. As expected, the six powertrain modes are mainly three translational modes and three rotational modes. Considering as x-axis the one aligned to the crankshaft, and z the vertical one, the modes are listed in table 5.2.

Table 5.2: Powertrain suspension modes

Mode description	Frequency
Translation in x	4.00Hz
Translation in y	6.04Hz
Translation in z	7.13Hz
Powertrain pitch x	9.18Hz
Powertrain yaw	11.66Hz
Powertrain roll	13.38Hz

Translation in y and z correspond to rigid displacements in the directions perpendicular to the vehicle motion. Translation in x is a rigid displacement in the direction of the vehicle motion. Powertrain pitch represent the engine turning around its crankshaft axis, and the other ones represent the other powertrain rotations.

Modal amplitudes [77] are the decomposition of the displacement on the directions of the eigenvectors. This decomposition of the displacement vector  $q$  is given by

$$q_j = \phi_j^T M \{q\} \quad (5.4)$$

### 5.3. STEPS FOR A COMPLETE MULTIBODY INTEGRATION: REAR TWIST BEAM AXLE BUSHING CASE

with  $\phi$  the mass normalized eigenvectors and  $M$  the mass matrix, and  $q_j$  the amplitude associated to the mode  $j$ .

The time derivative of those amplitudes yield the modal speeds, which are also necessary for estimating modal energies as

$$2E_j = \dot{q}_j^2 + \omega_j^2 q_j^2 \quad (5.5)$$

with  $E_j$  the energy and  $\omega_j$  the frequency. This information is useful to analyze where the energy flows before its dissipation. Modal energy evolution through time is shown in figure 5.14, for both hysteretic and viscous models.

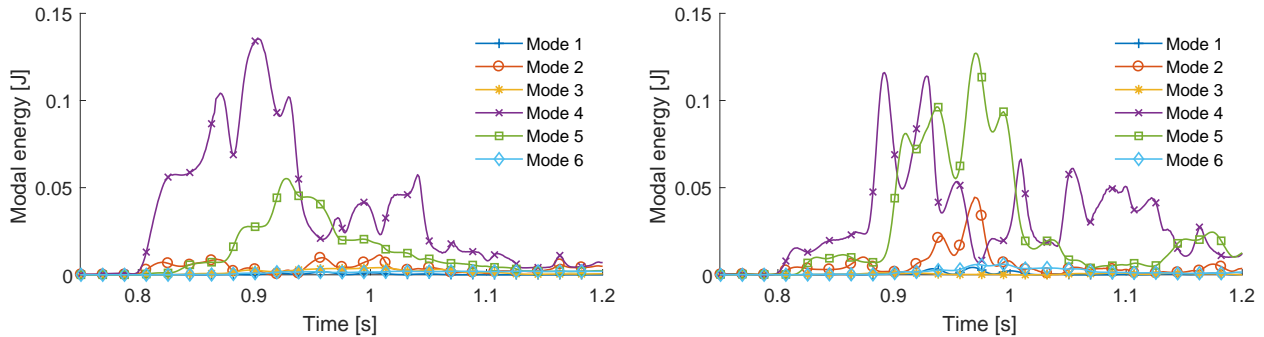


Figure 5.14: Modal energies for each model. Left: Viscous model; Right: Hysteretic model

Modes 4 and 5 take most of the imposed energy on the system, which is natural, as they represent the rotations along the direction of the imposed torque. The different dissipation models impact strongly on how the energy is transmitted to modes. For the viscous model, the fourth mode is clearly the only one which should be taken into account, while the fifth mode is equally important for the hysteretic dissipation.

Despite both models being acceptable in terms of local behavior, the differences regarding the type of dissipation lead to very different conclusions in terms of system level response. Such difference illustrate the demand for more elaborate identification techniques, aiming to describe both dissipative behaviors, as made afterwards in chapters 1 and 3.

### 5.3 Steps for a complete multibody integration: rear twist beam axle bushing case

The second multibody case studied in this work is that of a twist beam axle articulation. The part was first described in section 3.2.2 and will be used here again. The twist beam axle is a beam that aims to change cinematic behavior between roll and pumping to have better handling responses. The beam and the bushing are illustrated in figure 5.15.

### 5.3. STEPS FOR A COMPLETE MULTIBODY INTEGRATION: REAR TWIST BEAM AXLE BUSHING CASE

---



Figure 5.15: Twist beam axle with highlighted bushings.

A full vehicle simulation of the car going through different maneuvers was performed internally in Stellantis group on Dassault Simpack environment, which can be compared to equivalent tests on an instrumented vehicle.

This section will analyze the data collected by those simulations on the bushing model (theoretically the one described in chapter 2), test different OD models for the trajectory obtained on the multibody simulation.

#### 5.3.1 Current model description

The multibody model consists on a full vehicle description with rigid bodies except for the twist beam axle, which is described by a reduced finite element structure with modes up to 3kHz (130 modes) with 0.13% modal damping. A scheme of the model is shown in figure 5.16

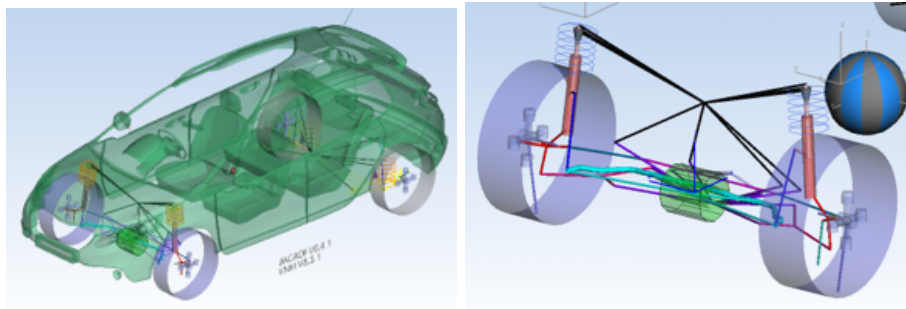


Figure 5.16: Full vehicle multibody model and suspension substructure (screenshots taken from Simpack).

The bushing model combines a nonlinear stiffness in three directions and the three rotations and a linear viscous dissipation on each of the 6 DOF. The nominal forces are set to zero. The force/displacement curves and stiffness in  $x, y, z$  directions are shown in figure 5.17, and the rotational stiffness in  $\alpha, \beta$  and  $\gamma$  are plotted in figure 5.18. The stiffness was estimated with prior quasi static tests. The viscous coefficients are given in table 5.3 and derived from a comparison with test at the

### 5.3. STEPS FOR A COMPLETE MULTIBODY INTEGRATION: REAR TWIST BEAM AXLE BUSHING CASE

roll mode frequency.

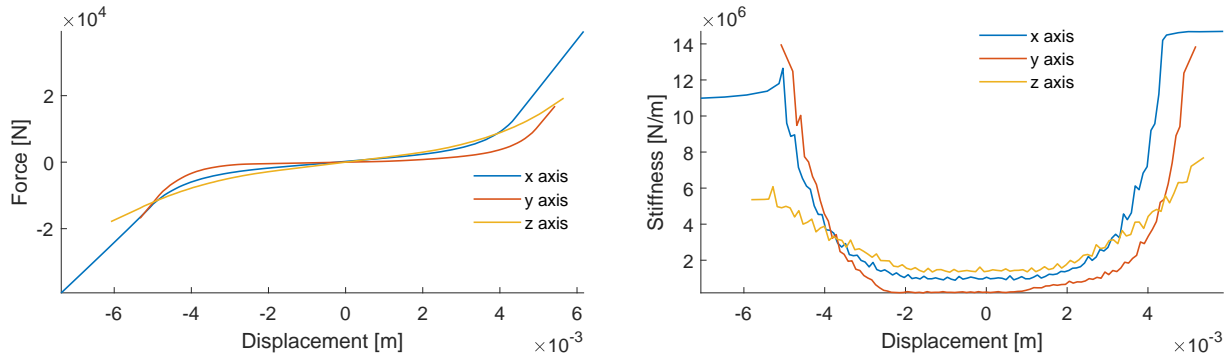


Figure 5.17: Force and stiffness as function of displacement from bushing in the MBS.

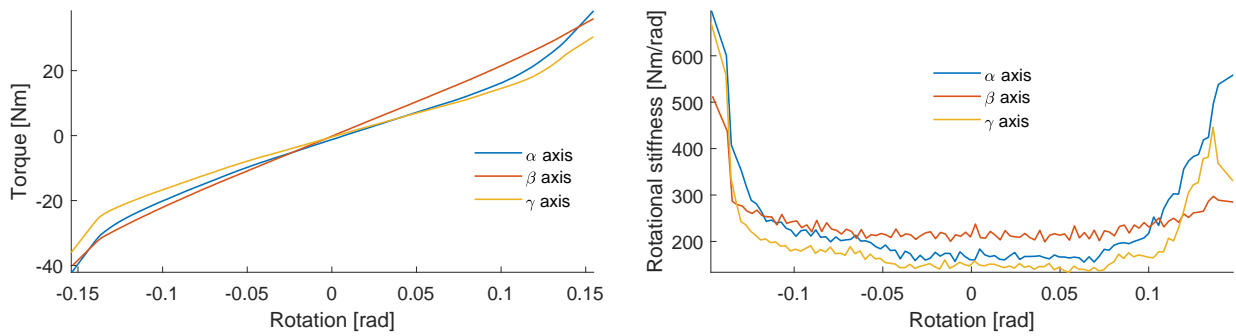


Figure 5.18: Torque and rotational stiffness as function of angle from bushing in the MBS.

Table 5.3: Viscous coefficient value for each direction

Direction	Coefficient value
x	1386.3 Ns/m
y	294.64 Ns/m
z	1763.8 Ns/m
$\alpha$	0.20347 Nm/sm
$\beta$	0.26306 Nm/sm
$\gamma$	0.18777 Nm/sm

As the articulation corresponds to the one identified in chapter 3, but without the plastic limiter, one compares the hyperelastic curves in figure 5.19. For low displacements, the x axis is almost superposed between both models. At larger amplitudes, the lack of measurements in the identified model is shown as a constant. For the z axis, the identified model is a bit stiffer than the model present in Simpack.

### 5.3. STEPS FOR A COMPLETE MULTIBODY INTEGRATION: REAR TWIST BEAM AXLE BUSHING CASE

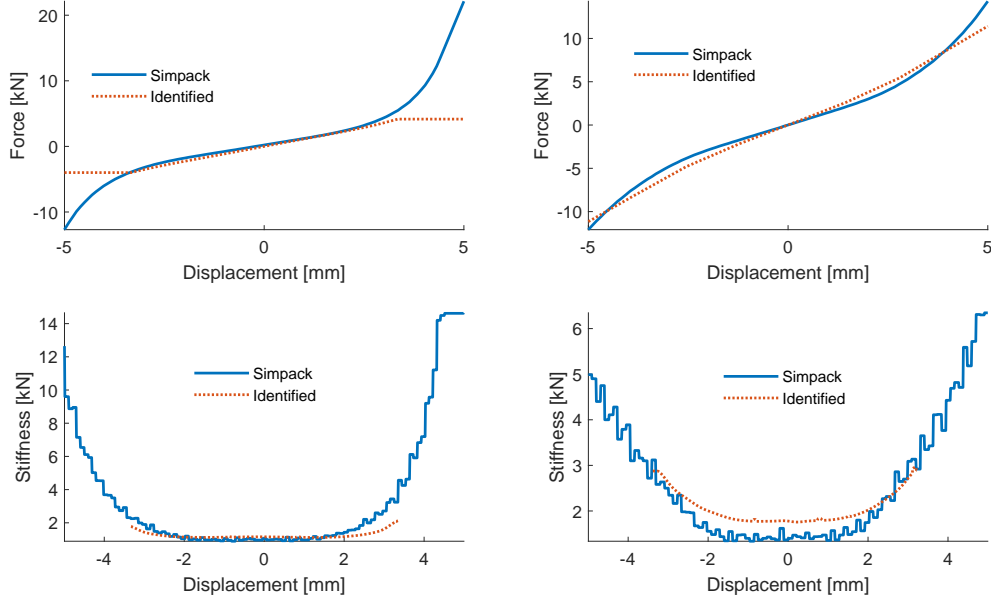


Figure 5.19: Hyperelastic models compared for  $x$  axis (left) and  $z$  axis (right).

#### 5.3.2 Integrating 0D models

In the Simpack [78] environment used by Stellantis, rubber articulations are represented as *bushing components* detailed in Simpack documentation and user interface. The standard setup for these components is to be defined with respect to two reference frames, each one attached to a body, and those frames are called **From Marker** and **To Marker**. The opposite forces and torques are applied to the To Marker body at location  $X_B(t)$ , also in the coordinate directions of the **From Marker** reference. For the **From Marker** body, forces must still be applied at the same location so that additional reaction torques  $F \wedge (X_A - X_B)$  are needed to account for the fact that forces are assumed applied at  $X_B$ .

The angular velocities are computed in the so called Cardan order  $\alpha - \beta - \gamma$  as

$$\omega_{rel} = \begin{Bmatrix} \dot{\alpha} + \sin(\beta)\dot{\gamma} \\ -\sin(\alpha)\cos(\beta)\dot{\gamma} + \cos(\alpha)\dot{\beta} \\ \cos(\alpha)\cos(\beta)\dot{\gamma} + \sin(\alpha)\dot{\beta} \end{Bmatrix}, \quad (5.6)$$

based on the transformation matrix

$$A(\alpha, \beta, \gamma) = \begin{Bmatrix} \cos(\beta)\cos(\gamma) & -\cos(\beta)\sin(\gamma) & \sin(\beta) \\ \cos(\alpha)\sin(\gamma) + \sin(\alpha)\sin(\beta)\cos(\gamma) & \cos(\alpha)\cos(\gamma) - \sin(\alpha)\sin(\beta)\sin(\gamma) & -\sin(\alpha)\cos(\beta) \\ \sin(\alpha)\sin(\gamma) - \cos(\alpha)\sin(\beta)\cos(\gamma) & \sin(\alpha)\cos(\gamma) + \cos(\alpha)\sin(\beta)\sin(\gamma) & \cos(\alpha)\cos(\beta) \end{Bmatrix} \quad (5.7)$$

which presents gimbal locks for  $\cos(\beta) = 0$ .

One thus obtains a generalized strain vector  $\Delta x, \Delta y, \Delta z, \Delta \alpha, \Delta \beta, \Delta \gamma$ , and its time derivative or velocity  $\Delta \dot{x}, \Delta \dot{y}, \Delta \dot{z}, \Delta \dot{\alpha}, \Delta \dot{\beta}, \Delta \dot{\gamma}$ . The Simpack bushing, then expresses bushing loads and moments

in the form

$$\begin{Bmatrix} F_x \\ F_y \\ F_z \\ T_\alpha \\ T_\beta \\ T_\gamma \end{Bmatrix} = \begin{Bmatrix} f_{kx}(\Delta x) + f_{vx}(\Delta \dot{x}) \\ f_{ky}(\Delta y) + f_{vy}(\Delta \dot{y}) \\ f_{kz}(\Delta z) + f_{vz}(\Delta \dot{z}) \\ f_{k\alpha}(\Delta \alpha) + f_{v\alpha}(\Delta \dot{\alpha}) \\ f_{k\beta}(\Delta \beta) + f_{v\beta}(\Delta \dot{\beta}) \\ f_{k\gamma}(\Delta \gamma) + f_{v\gamma}(\Delta \dot{\gamma}) \end{Bmatrix} \quad (5.8)$$

where the values of  $f_{ki}$  and  $f_{vi}$  may be given as a table or be assigned as a constant value that multiplies the displacement/angle. Offsets or nominal forces and moments can also be present as  $f_{ki}(0)$ .

This does not allow for cross coupling (an expression such as  $f_{kx}(\Delta x, \Delta y, \Delta z)$  or for behavior that depends on history as in the 0D models discussed in chapter 1. Indeed history dependence requires the integration of an evolution equation that contains internal states. Strategies envisioned to generate such behavior are Fortran or C++ coded user functions or co-simulation calling SDT via Simulink or calling Abaqus.

### 5.3.3 Integrating 3D hyper-reduced models

The kinematic reduction considered as the first phase of hyperreduction in section 4.3, assumed the existence of a constant basis  $T$  and associated degrees of freedom  $q_R$  leading to

$$\{q\} = [T] \{q_R(t)\} \quad (5.9)$$

The typical representation of a multibody model considers a body frame undergoing large rotations and small deformations within this frame. The node position field  $X(t)$  in the body coordinate system is thus given by

$$\{X_B(t)\}_{3N_p} = \{x_B\} + [T_F] \{q_F(t)\} \quad (5.10)$$

where the index B designates the body coordinates and the index F designates the flexible body. The global position is then obtained by translating and rotating the positions in the the body frame

$$\{X_{Global}(t)\}_{3N_p} = \{u_B(t)\} + [R_B(t)] \{X_B(t)\} = \{u_B(t)\} + [R_B(t)] \left( \{x_B\} + [T_F] \{q_F(t)\} \right) \quad (5.11)$$

where  $\{u_B(t)\}$  is the translation of the body origin and  $[R_B(t)]$  its non-linear rotation.

When considering a body/bushing interface as rigid, the motion of a point can be described using a marker point leading to

$$\{X_{Global}(t)\} = \{u_{Marker}(t)\} + [R_{Marker}(t)] \{x_{Local} - x_{Marker}\} \quad (5.12)$$

where the relative positions  $x_{Local} - x_{Marker}$  are constant in the marker frame.

The ability to introduce hyper-reduced models in multibody simulations is thus dependent on the possibility to reconcile (5.10) to (5.12), or in other words, rewrite (5.12) using a constant basis. This

### 5.3. STEPS FOR A COMPLETE MULTIBODY INTEGRATION: REAR TWIST BEAM AXLE BUSHING CASE

---

is indeed possible by reordering the linear product in (5.11). The time dependent variables, to be used as degrees of freedom, enforced on the edge of the hyper-reduced bushing model, are given by

$$\{q_{LR}\}^T = \{u_i \ R_{ij}\}^T = \{x \ y \ z \ \cos(\alpha)\cos(\beta) \ \cos(\beta)\sin(\gamma) \ \dots\}^T \quad (5.13)$$

and the constant basis combining all the constant terms of (5.12) is given by

$$[T_A]_{3Np \times 12} = \begin{bmatrix} \delta_x & \delta_y & \delta_z & \delta_{i1x1p} & \delta_{i2x1p} & \delta_{i3x1p} & \delta_{i1x2p} & \delta_{i2x2p} & \delta_{i3x2p} & \delta_{i1x3p} & \delta_{i2x3p} & \delta_{i3x3p} \end{bmatrix} \quad (5.14)$$

where it appears that the subspace dimension associated with large angle rigid rotations is 12.

In a multibody learning phase, generating 12 independent vectors on the two rigid surfaces of a mount can be simply obtained by selecting appropriate trajectories for the full system model learning phase. The current proposition, that could not be fully implemented within the scope of this work, would be to focus non-linear simulations on the main solicitation axes and only add a few snapshots to complete the order 12 basis needed on the edges. Singular value decomposition used for basis generation should also separate edge and interior as done in [79] for example. The final implementation would have the form

$$\{q\} = \begin{bmatrix} T^A & 0 & 0 \\ 0 & T^C & 0 \\ 0 & 0 & T^B \end{bmatrix} \begin{Bmatrix} q_{LR}^A \\ q_R \\ q_{LR}^B \end{Bmatrix} \quad (5.15)$$

where  $T^A$  with 12 columns gives the interface between the first marker and the articulation FEM, and  $T^B$ , again with 12 columns, the interface between the articulation and the second marker in a similar structure, while  $T^C$  keeps the internal motion resulting from the kinematic reduction.

Integration of hyper-reduced models into a generic multibody simulation package would thus simply require to have the ability to write a user defined constitutive model with internal states. Marker coordinates can then be transformed to generalized edge coordinates enforcing  $q_{LR}^A$  and  $q_{LR}^B$ , using (5.13), and the evolution of other internal variables  $q_R$  and material states at integration points kept by the hyperreduction could be managed inside the user defined model. The roadmap for an hyper-reduced multibody solver is thus quite clear.

#### 5.3.4 Validation data for consistence checks

As the project development did not give time to really implement the mount models chosen in the end within a multibody simulation environment, consistence checks were performed as validations. The simulations can only be accurate if mount forces are correctly predicted. Using displacements obtained from multibody simulations with the reference mount representation, forces and power are computed and consistence between the reference and detailed force models gives an indication of the current model validity and need for refinement.

### 5.3. STEPS FOR A COMPLETE MULTIBODY INTEGRATION: REAR TWIST BEAM AXLE BUSHING CASE

---

The reference inputs are the forces which were measured with an instrumented tire on a course track presenting different obstacles, and for the current implementation, the output was considered to be the measured forces in the bushing  $x$  and  $z$  directions.

It was chosen here to represent two different parts of the tests/simulations, one that brings the bushing to its saturation (in the vertical direction with the the car passing through 3 metal bars **BM**), and one where the bushing is forced in more than one direction (with three curves to the left in maximum lateral acceleration **TR**). The obstacles are illustrated in figure 5.20.



Figure 5.20: Tested and simulated obstacles **BM** (left), **TR** (right).

Test response is illustrated in figure 5.21 and compared with the Simpack simulation. The response is satisfactory for the **BM** test, while there is a significant difference in the **TR** test for the  $x$  axis. From the Simpack displacement response (figure 5.23), one may see that the strong angles might be the source of this difference, possibly due to coupling between angular solicitation and translation solicitations. Such difference justifies the need for better characterization, but coupled tests can be very costly and difficult to make.

### 5.3. STEPS FOR A COMPLETE MULTIBODY INTEGRATION: REAR TWIST BEAM AXLE BUSHING CASE

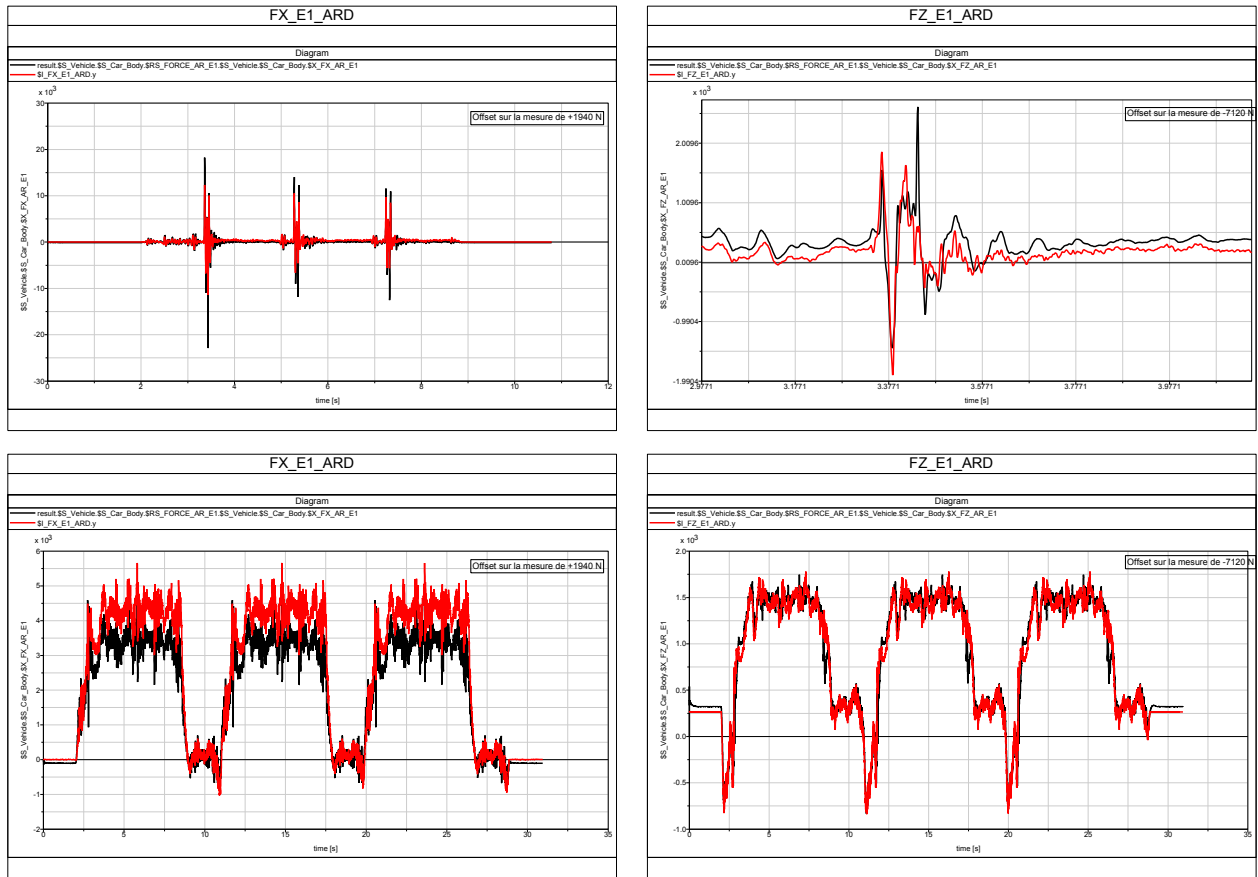


Figure 5.21: Comparison of tested (red) and Simpack (black) results in  $x$  (left) and  $z$  (right) directions. Top: BM. Bottom: TR

Displacement and force displacement diagrams for the multibody simulation are shown in figures 5.22 and 5.23.

### 5.3. STEPS FOR A COMPLETE MULTIBODY INTEGRATION: REAR TWIST BEAM AXLE BUSHING CASE

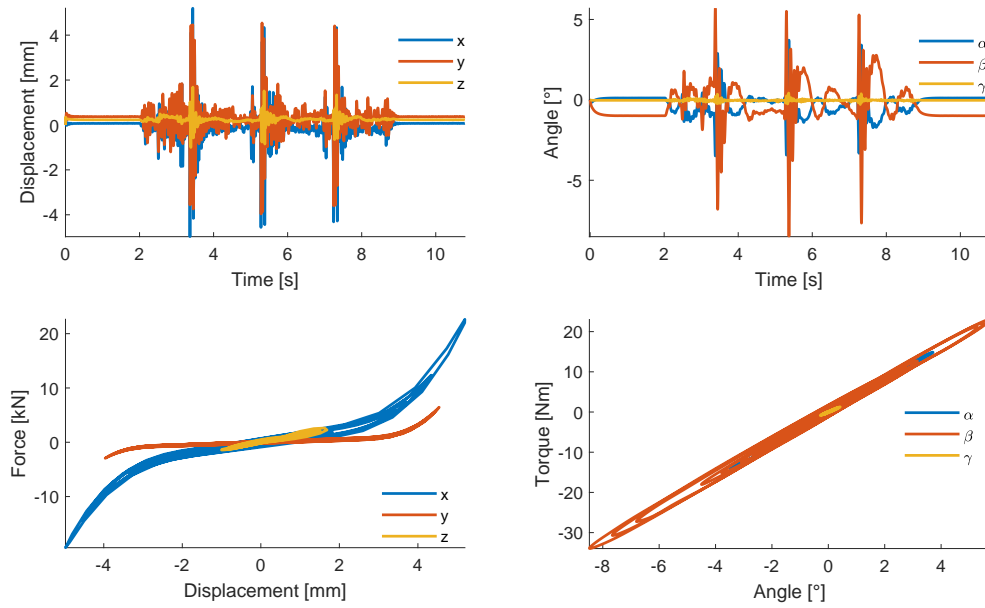


Figure 5.22: Responses from simulation of passing over a metallic bar **BM**.

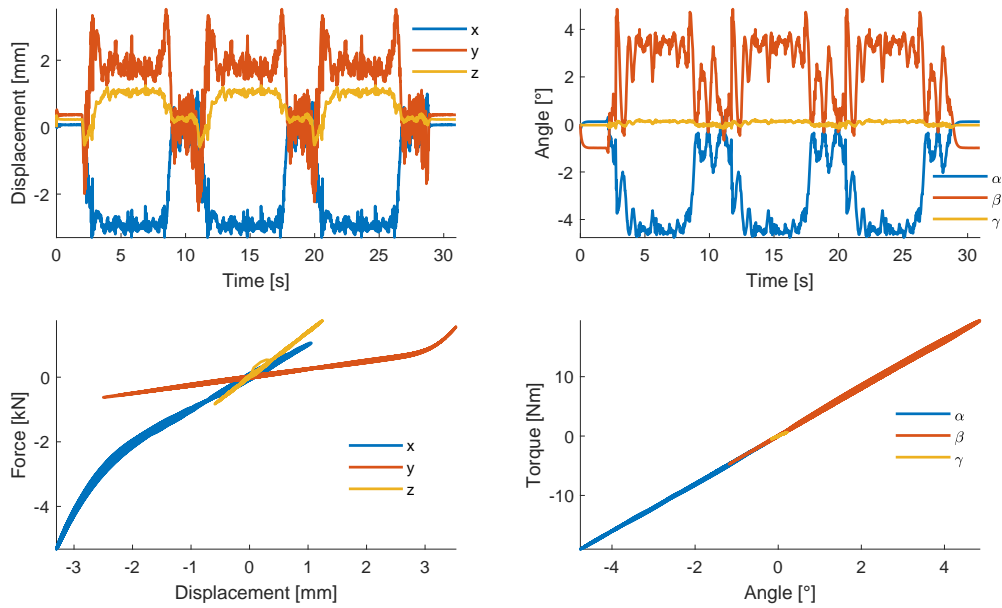


Figure 5.23: Responses from simulation of three left turns **TR**.

#### 5.3.5 Consistence of mount forces

A first consistence check was performed on the Simpack model itself. From the bushing parameters detailed in section 5.3.1 the forces were rebuilt in a SDT environment with a **cbush** element. Figure 5.24

### 5.3. STEPS FOR A COMPLETE MULTIBODY INTEGRATION: REAR TWIST BEAM AXLE BUSHING CASE

---

shows that values are not coincident with difference mainly found for the static loads and the largest peaks. This indicates that some processing of the input data occurs before actually getting the model truly used by Simpack.

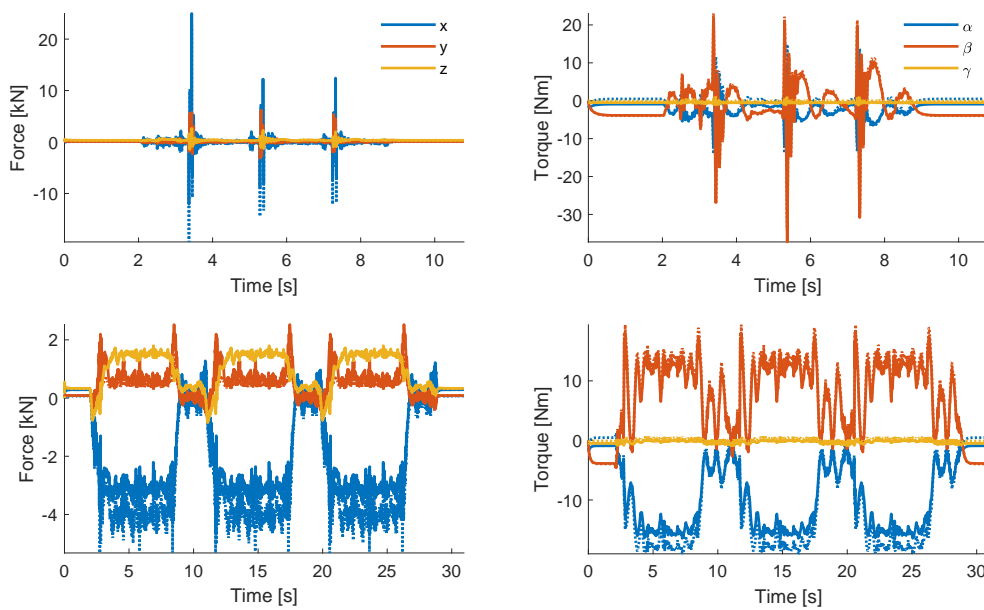


Figure 5.24: Comparisons for simulated forces. Solid lines: post-processed forces. Dotted line: Simpack results.

For the second consistence check, the model with 3 Maxwell and 3 Jenkins cells identified in section 3.5 is used to predict forces. In this consistence check, the displacements extracted from Simpack were imposed to the identified `cbush` element in the SDT environment, where the extracted forces are compared to the ones computed in Simpack.

For the `BM` test, the results are compared in figure 5.25. For the x direction, the peaks are quite poorly correlated. The difference is due to the fact that the identification did not reach contact levels, so the model was capped in force to avoid false extrapolations. For the z axis, the responses are much closer.

### 5.3. STEPS FOR A COMPLETE MULTIBODY INTEGRATION: REAR TWIST BEAM AXLE BUSHING CASE

---

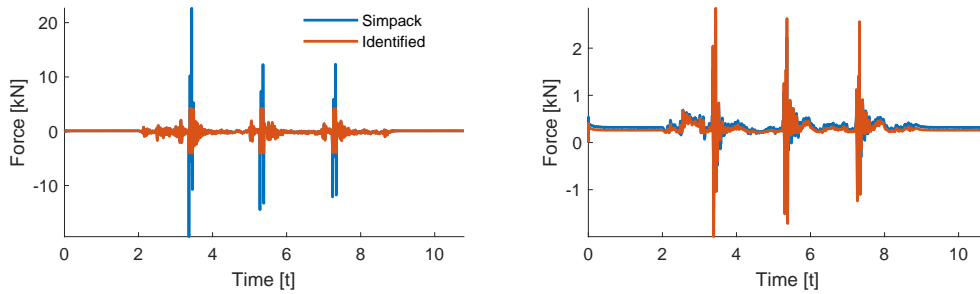


Figure 5.25: Comparisons for simulated forces for **BM** test. Left: x axis. Right: z-axis.

The response comparison for the **TR** test is shown in figure 5.26. For the x axis direction, the identified model is softer than the Simpack model. For the z direction, the identified model is considerably stiffer than the Simpack model, as it stays far from saturation points, and figure 5.19 illustrates.

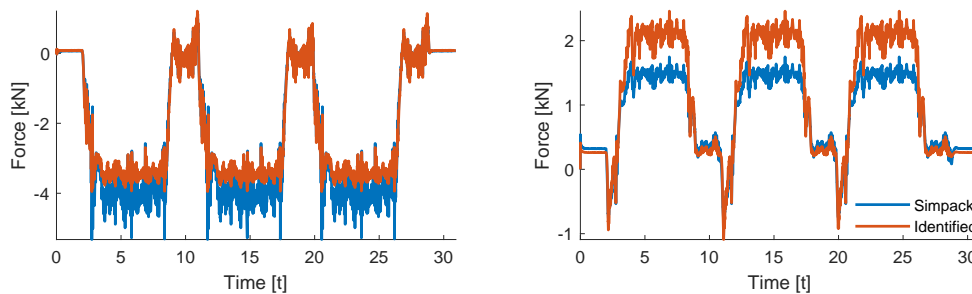


Figure 5.26: Comparisons for simulated forces for **TR** test. Left: x axis. Right: z-axis.

A last interesting result is linked to the analysis of inelastic forces (total forces less the hyperelastic ones) and the associated power which gives an indication of instant dissipation. Figure 5.27 illustrates these quantities for **BM** test on the z axis. It is interesting to see that one of the Iwan cells locks in a deformed position leading to an inelastic force offset close to -200 N. The cell locking could be resolved by using the nonlinear viscoelastic model, though very long stabilization times might occur. Confrontation with experiment seems necessary to really validate whether this is actually found or is an artefact of coarse order selection.

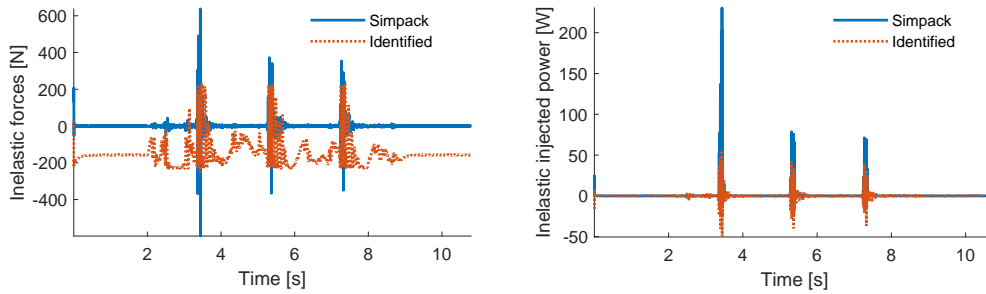


Figure 5.27: Inelastic forces (left) and injected power (right) for BM simulation in z direction.

The inelastic injected power plots illustrate that with the purely viscous cell from Simpack model, all energy injected is dissipated while with the more general identified model, some of the energy is stored and then released back into the system. One can thus expect notable difference in transient simulations.

## 5.4 Perspectives and conclusions

For the powertrain suspension case, the most obvious approach to ensure better representation would be to conceive better identification routines to extract both viscoelastic and hysteretic behaviors separately. The modal computations seems to be a solid approach to assess system behavior and a good approach to adjust the compromise between comfort and stiffness. Beyond those perspectives, one of the main outcomes from this case is the illustration that hysteretic and viscoelastic dissipation models may provide very different responses in transient state, even if they are equivalent in terms of stationary regime.

The twist beam axle case is considerably more complex. As the models are not connected as spherical joints, one must consider the six directions and their coupling. The preexisting test campaign focused on obtaining the full model characteristics. The one presented in this work focused on the validation of the material models and the FE implementation while confirming results for a limited range in two axes. Neither of the test campaigns give results on directional coupling which appears to be very important in the vehicle test shown in figure 5.21. The main foreseeable method to obtain a reasonable estimate of this coupling is to implement a FE model. To obtain reasonable performance, this would certainly need to be a hyper-reduced model based on the material tests of the second campaign. Regarding the full vehicle test, the force as the only output is not necessarily the most pertinent manner to evaluate the validity of the model, as the mount plays a smaller role in the full dynamics of the vehicle. A better approach would be to view and compare force/displacement trajectories, which should be captured in the test.

As the theoretical background for integrating hyper-reduced models into multi-body routines is

presented, its implementation in SDT is a short-term perspective. In the long term, the proposed bushing models should communicate with the Simpack solver. A first strategy would be the elaboration of user defined routines, but their development is often very time consuming, as it involves the programming in a different language (C++ or Fortran) and meeting all the template restrictions. A more promising lead is the communication of SDT with Simpack via the Simulink environment, as SDT is native to Matlab, and Simpack supports the integration. Another final possibility is to use the fact that Simpack supports co-simulation with Abaqus, but this would require the implementation of the developments made in this work into it, which might present unexpected issues in both implementation and performance.

#### 5.4. PERSPECTIVES AND CONCLUSIONS

---

# Conclusion

For all models, the first step is to determine the type of input/output relation that needs to be represented. Based on Stellantis experience and internal reports, whose results are illustrated in the introduction, it was determined that it is important to represent hyperelastic, viscoelastic and path dependency effects, while also being able to couple different solicitation directions. This requires a notable change from the current design practice that considers hyperelasticity in parallel with a viscous damper without directional coupling.

To address this broad problematic, subproblems were considered: optimization of test procedures to characterize and identify selected behaviors, investigation of different 0D models capable of representing all the sought effects, elaboration of models compatible with multibody simulation going through 3D models, and also the evaluation of these models inside a multibody routine.

### Outcomes and contributions

While 0D modeling, discussed in chapter 1, is the base of all modeling efforts, availability of the Vibracoustic test data and the relatively poor results of the initial identification efforts discussed in section 3.3 meant that the last 6 months were actually focused on this chapter. The results, submitted as an article to MSSP [3], give a clear unified framework of the non-linear coupling of a base hyperelastic behavior to which hysteretic, or saturated viscoelastic, forces are first added and non-linear viscoelastic forces affect higher frequencies.

On the test side, a first novel proposition was to use and exploit *low speed triangular tests* to extract non-parametric models of both hyperelastic stiffness and the hysteretic relaxation modulus. The use of a non-parametric representation of hysteresis associated with a relaxation modulus is fairly original and allows a clear link with the established concept of viscoelastic relaxation.

A second important contribution associated with tests was the introduction of the computation of an instantaneous modulus using the ratio of analytic input/output signals. The resulting exploitation of classical sine tests was fundamental in understanding coupling between the three base non-linear behavior and thus the end choice of a model form based on the relaxation of load fractions depending on *force rate*, with non-linear viscoelasticity used to represent hysteresis. For this last aspect, a notable contribution was to use the concept of load saturation instead of the much less intuitive notion of reduced times. The analysis of the Payne effect as a coupling between viscoelasticity and hysteresis is then much clearer than the classical first harmonic handling of sine tests. The assumption that the fractions are constant throughout the whole tested domain is not perfect, but still provide a reasonable fit for the tests.

On the modeling side, selected order models were shown to correspond to a generic discretization strategy that applies to both the classical viscoelastic case and the more original hysteretic relaxation. Graphical strategies were shown to give a simple control on the order/accuracy trade-off.

## CONCLUSION

---

For order independent models, such as fractional derivatives, the contribution was to demonstrate that order selection is the result of a numerical implementation, so that the real interest of such models is in the separation of parametrization and discretization phases, thus allowing a simpler access to design problems such as defining a class of realistic materials.

Chapter 2 is a natural sequel to chapter 1, as it extends to 3D and finite strains the proposed 0D parametric models. A problem in this transition is that the purely hysteretic model has a three dimensional equivalent (kinematic plasticity) that is not fully established for finite strains. As one of the contributions of chapter 1 was that hysteresis may actually be an idealization of non-linear viscoelasticity, the latter was fully implemented and judged satisfactory, without going through plastic formulations, which is an important outcome from the work. The research on the subject of kinematic plasticity was thus placed in appendix A.

In terms of numerical developments, the major contribution was to implement, test, and participate in the optimization of these finite-strain non-linear laws into the FEM software SDT used for 3D simulations. This involved management of implementation details, special attention to numeric scheme, timestep size, analysis of dissipation ... The written chapter is a first documentation of the actual implementation.

Chapter 3 gives the details of the experimental campaign that was designed during the thesis, realized by Vibracoustic, and whose post-processing led to the many propositions given in chapter 1. Since much insight was gained and a major outcome was the proposition of a new unified framework, the presentation details initial choices and documents the various tests to confirm the generality of propositions made in chapter 1.

Test design guidelines can be drawn from the experience. Using *low speed triangular tests* proved particularly insightful as it enabled the identification of the hysteretic relaxation and a quite fine description of the base hyperelastic modulus. With the current hindsight, better sampling right after the turning points would provide better non parametric identifications. Smaller loops on triangular tests also gave the possibility to verify Madelung rules, but better sampling and possibly a smoother transition would be needed for accurate understanding of behavior very close to the turning point. The most time consuming tests (multi-steps) are really not very useful as hyperelastic behavior was considered to be based on triangular tests. They could find some use if Mullins effect (and/or *very* long term effects) characterization was sought. Sine tests were properly chosen but the data extracted should be much richer than the usual first harmonic.

A classical identification routine was performed, and despite the fact that the results could represent the material reasonably, they were judged unsatisfactory. Indeed, a large amount of data that could be used was dropped to generate the objective function and the extrapolation of the obtained model to the dropped data was far from perfect. For such reason, a novel non parametric identification, based on

## CONCLUSION

---

the developments in chapter 1 was also made, selecting non-parametric curves (both viscoelastic and hysteretic) and providing discretization strategies. Results were analyzed for the material specimens and the part. The results from the novel identification provide 0D models readily implementable in multibody solvers, while some supplementary work is needed for a full 3D implementation.

Having addressed issues with 0D and material modeling, chapter 4 considers finite element formulations, which are needed to allow predictions of the impact of geometry changes or directional coupling (change of properties in a direction when another is loaded). Since such computations take hours when the requirement for practical multibody design simulations is seconds, the objective was to demonstrate that model reduction schemes could achieve the performance gain while retaining the use of arbitrary geometries and material laws. The conclusion is that the approach is clearly feasible and the contribution was to implement and document the use of standard kinematic reduction to reduce the number of degrees of freedom and hyper-reduction to provide a fast approximation of the work of non-linear materials. The development follows the originality of SDT where non-linearities are expressed through notions of observation and command matrices which are classical in control theory but not in mechanics and gives a fairly direct image of implementation.

Validation of the implementation for the tested bushing with a hyperviscoelastic model was presented at ISMA 2020 [4]. The main conclusions were that the hyper-reduced model has a performance compatible with multibody simulations and that extrapolations made on the material parameters, on solicitation shape and amplitude all provided very good agreements.

Chapter 5 comes back to the global objective of multibody simulations by analyzing two test cases: an engine suspension and a full vehicle simulation.

The first case, performed at the project beginning and presented at the ECCMR 2019 conference [5], gives a clear motivation for much of the work. An insufficient characterization of the mounts led to two different, yet at first glance equivalent, models. For a transient system level evaluation, the dissipated power profiles and modal responses are completely distinct. As this could affect major design decisions, characterization and identification are clear needs.

The second case of a twist beam axle bushing corresponds to the parts tested by Vibracoustic and demonstrating the ability to use the results of earlier chapter was needed for closure. As integration with Simpack was not possible due to time constraints, the work focused on clarifying future implementation needs and analyzing bushing models using forces and power. The extraction of the displacements, angles, forces and torques imposed on the bushing through the obstacles enabled the verification of consistency between model and results on Simpack. Surprisingly, force predictions were not perfectly consistent with the input model indicating some transformation within Simpack.

The models resulting from identification efforts of earlier chapter notably differ from the non-linear elasticity in parallel to viscous dissipation. The simulation of inelastic power being very notably

different, it appears that the conclusion of the engine case still applies: having a detailed model of the bushing is important for transient simulations.

## Perspectives

The results of the test campaign open a number of perspectives. The standard protocol should now include large amplitude triangular tests and the classical sine tests, while dropping multi-step relaxation except if seeking characterization of first cycles (Mullins effect) or longer time frames. The data processing should automate the novel extraction strategies for hyperelastic modulus, relaxation modulus and the associated ratio, as well as instant modulus characterization and extend the proposed synthetic representation of results within stress/strain maps. Incorporating the proposed strategy in standard DMA testing would clearly improve the characterization of both materials and mounts.

For the triangular tests, detailed analysis close to the turning points, with increased sampling and possibly smoother transitions, seems a path to understanding the transition between hysteretic or saturated viscoelastic loads and viscoelastic relaxation. Small amplitude triangular tests that were introduced to verify Madelung rules will need to be reworked with a detailed understanding of the transient very close to the instant where the strain direction changes.

The notion of instant modulus obtained by computing the ratio of analytic signals opens a major range of applications to non-linear systems. A time domain analytic signal estimation using an extended Kalman filter was already shown to give better estimators. Applications to other forms of non-linearity at the bushings, but also the structure levels using modal coordinates seem promising perspectives. The link with LPV (linear parameter varying) systems considered in control theory will also need to be established.

For 3D material models, a missing step is the ability to link the multiple non-parametric test curves to a three dimensional, invariant-based hyperelastic model. An eventual separation of the hyperelastic potential into one for each non-parametric model (one for each specimen) would also enable the utilization of the different identified cells within the same material model. This will be key to the desirable extension of selected order parametric models.

Consistence analysis of material testing configurations through detailed FE simulations of tests are also necessary to understand test limitations. Indeed, in the traction/compression specimen one uses the assumption that states are constant within a section, that the material is perfectly incompressible and that power dissipation can be approximated by behavior at the mid section, despite taking place at the whole specimen. This is essentially the same as performing hyper-reduction with a single Gauss point at the mid section, an assumption whose validity needs to be demonstrated. For the shear specimen, one neglects transverse stresses and still assumes incompressibility, which is only imperfectly true. Such consistence analysis are in particular expected to lead to geometric corrections

## CONCLUSION

---

of the hyperelastic curves obtained from test.

It is worth citing a few longer term or less critical to multibody simulation issues. Implementing a stable routine that represents pure hysteresis is of interest even though nonlinear hyperviscoelasticity is probably a more physically accurate representation. Purposes like comfort and road behavior also lead to other modeling needs: first cycles softening, plastic effects, damage effects, strain induced crystallization, preloading effects in fatigue. Implementation of those characteristics in 0D models is simpler than for 3D models, but there should be tests aiming to characterize them and non-vibration design groups are interested in the results.

For the implementation of hyper-reduced models compatible multibody simulations, a number of further steps are identified. The current learning phase based on explicit time integration is quite costly (the demonstration used a quarter model). Implicit and/or iterative methods considering local linearizations, piecewise kinematic reduction, ... are fairly obvious and need testing. Designing the learning strategy, accounting for all directions and for the presence of prestress, and building the associated generalized integration scheme requires working out a number of important implementation details.

Testing robustness of the hyper-reduced model for the simulation of the whole bushing in conditions that cannot be easily reproduced in testbeds or are outside learning conditions seems important. Other extrapolations on material parameters (or even models), cell sensibility, solicitation frequency, transient loads, ... for the same learning space should also be understood.

Contact should also be considered in the reduced model. The real part contains plastic limiters which increase stiffness through contact occurring in high amplitude deformations and must be considered in practice.

Finally for multibody applications, 0D large rotation models are now deployed in SDT for the engine suspension case which only involves two bodies and has been well tested. But the generalization to a generic multibody solver such as Simpack is needed for the twist beam axle application. Using cosimulation seems the easiest implementation route but, as always, software communication may be a problem despite the emergence of standards. Extending the number of easily accessible cases will allow running analysis such as the engine mount case where the importance of mount modeling and the usefulness of non-classical criteria such as power dissipation and modal energies clearly appeared.

Testing 0D models against hyper-reduced 3D models will also be needed to gain understanding of the impact geometric effects and prepare the way for an ideal configuration where tests would lead to material models and geometries that could be modified at will in the design phase.

# Bibliography

- [1] D. Price and J. Duncan, “Thermomechanical, Dynamic Mechanical and Dielectric Methods,” in *Principles of Thermal Analysis & Calorimetry*, Feb. 2016, pp. 164–213.
- [2] B. Heißing and M. Ersoy, Eds., *Chassis Handbook: fundamentals, driving dynamics, components, mechatronics, perspectives ; with 75 tables*, 1st ed., ser. ATZ. Wiesbaden: Vieweg + Teubner, 2011, oCLC: 845641128.
- [3] R. Penas, E. Balmes, and A. Gaudin, “A unified non-linear system model view of hyperelasticity, viscoelasticity and hysteresis exhibited by rubber,” *MSSP*, vol. Submitted, p. 25, Jun. 2021.
- [4] R. Penas, A. Gaudin, and E. Balmes, “Hyper-reduced models of hyperelastic dissipative elastomer bushings,” Leuven, 2020, p. 9.
- [5] R. Penas, A. Gaudin, A. Kreis, and E. Balmes, “Dissipation in hysteretic rubber mount models,” in *Constitutive Models for Rubber XI*, Jun. 2019. [Online]. Available: <https://www.taylorfrancis.com/>
- [6] R. Österlöf, “Modelling the viscoplastic properties of carbon black filled rubber,” Ph.D. dissertation, KTH, Stockholm, 2016. [Online]. Available: <http://www.diva-portal.org/smash/get/diva2:917398/FULLTEXT01.pdf>
- [7] F. Vincent, “Du modèle matériau à la mécanique des systèmes : étude dynamique d’une liaison souple en silicone chargée de silice,” Ph.D. dissertation, École Nationale Supérieure des Mines de Paris, 2011. [Online]. Available: <https://pastel.archives-ouvertes.fr/pastel-00584332>
- [8] E. Balmes, *Structural Dynamics Toolbox (for Use with MATLAB)*. SDTools, Paris, Sep. 1995.
- [9] M. S. Allen, D. Rixen, M. van der Seijs, P. Tiso, T. Abrahamsson, and R. L. Mayes, “Model Reduction Concepts and Substructuring Approaches for Nonlinear Systems,” in *Substructuring in Engineering Dynamics: Emerging Numerical and Experimental Techniques*, ser. CISM International Centre for Mechanical Sciences, M. S. Allen, D. Rixen, M. van der Seijs, P. Tiso, T. Abrahamsson, and R. L. Mayes, Eds. Cham: Springer International Publishing, 2020, pp. 233–267. [Online]. Available: [https://doi.org/10.1007/978-3-030-25532-9\\_6](https://doi.org/10.1007/978-3-030-25532-9_6)

## BIBLIOGRAPHY

---

- [10] A. Bhuiyan, Y. Okui, H. Mitamura, and T. Imai, “A rheology model of high damping rubber bearings for seismic analysis: Identification of nonlinear viscosity,” *International Journal of Solids and Structures*, vol. 46, pp. 1778–1792, 2009.
- [11] P.-E. Austrell, *Extending the visco-frictional branched modeling of filled rubbers to include coupling effects between rate and amplitude dependence*. CRC Press, 2019.
- [12] F. Renaud, J.-L. Dion, G. Chevallier, I. Tawfiq, and R. Lemaire, “A new identification method of viscoelastic behavior: Application to the generalized Maxwell model,” *Mechanical Systems and Signal Processing*, vol. 25, no. 3, pp. 991–1010, Apr. 2011. [Online]. Available: <http://www.sciencedirect.com/science/article/pii/S0888327010003079>
- [13] R. Koeller, “Application of fractional calculus to the theory of viscoelasticity,” *Journal of Applied Mechanics*, vol. 51, pp. 229–307, Jun. 1984.
- [14] A. C. Galucio, J.-F. Deu, and R. Ohayon, “Finite element formulation of viscoelastic sandwich beams using fractional derivative operators,” *Computational Mechanics*, vol. 33, no. 4, pp. 282–291, Mar. 2004. [Online]. Available: <http://link.springer.com/10.1007/s00466-003-0529-x>
- [15] N. Heymans, “Fractional Calculus Description of Non-Linear Viscoelastic Behaviour of Polymers,” *Nonlinear Dynamics*, vol. 38, no. 1-4, pp. 221–231, Dec. 2004. [Online]. Available: <http://link.springer.com/10.1007/s11071-004-3757-5>
- [16] M. Brokate and J. Sprekels, *Hysteresis and phase transitions*. Place of publication not identified: Springer, 2012, oCLC: 968504944.
- [17] V. A. Coveney, D. E. Johnson, and D. M. Turner, “A Triboelastic Model for the Cyclic Mechanical Behavior of Filled Vulcanizates,” *Rubber Chemistry and Technology*, vol. 68, no. 4, pp. 660–670, Sep. 1995. [Online]. Available: <https://doi.org/10.5254/1.3538765>
- [18] D. J. Segalman, “Using Series-Series Iwan-Type Models for Understanding Joint Dynamics,” *Journal of Applied Mechanics*, vol. 72, no. 5, Sep. 2005.
- [19] A. Lion, “On the large deformation behaviour of reinforced rubber at different temperatures,” *Journal of the Mechanics and Physics of Solids*, vol. 45, no. 11-12, pp. 1805–1834, Nov. 1997. [Online]. Available: <http://linkinghub.elsevier.com/retrieve/pii/S0022509697000288>
- [20] R. Lakes, *Viscoelastic Materials*. United States of America: Cambridge University Press, 2009.
- [21] J. Salençon, *Viscoélasticité*. Presse des Ponts et Chaussées, Paris, 1983.
- [22] W. Heylen and P. Sas, *Modal Analysis Theory and Testing*. Katholieke Universteit Leuven, Departement Werktuigkunde, 2006.

## BIBLIOGRAPHY

---

- [23] G. Masing, “Eigenspannungen und verfestigung beim messing,” *Proceedings of the 2nd International Congress of Applied Mechanics*, pp. 332–335, 1926.
- [24] H. Festjens, “Identification and modeling of jointed structures for dynamic analysis,” Ph.D. dissertation, Ecole Centrale Paris, Mar. 2014.
- [25] N. Aguirre, F. Ikhouane, J. Rodellar, and R. Christenson, “Parametric identification of the Dahl model for large scale MR dampers,” *Structural Control and Health Monitoring*, vol. 19, no. 3, pp. 332–347, 2012, eprint: <https://onlinelibrary.wiley.com/doi/pdf/10.1002/stc.434>. [Online]. Available: <https://onlinelibrary.wiley.com/doi/abs/10.1002/stc.434>
- [26] M. Ismail, F. Ikhouane, and J. Rodellar, “The Hysteresis Bouc-Wen Model, a Survey,” *Archives of Computational Methods in Engineering*, vol. 16, pp. 161–188, Jun. 2009.
- [27] M. Berg, “A model for rubber springs in the dynamic analysis of rail vehicles,” *Proceedings of the Institution of Mechanical Engineers, Part F: Journal of Rail and Rapid Transit*, vol. 211, no. 2, pp. 95–108, Mar. 1997. [Online]. Available: <http://journals.sagepub.com/doi/10.1243/0954409971530941>
- [28] B. Bourgeteau, “Modélisation numérique des articulations en caoutchouc de la liaison au sol automobile en simulation multi-corps transitoire,” Ph.D. dissertation, Ecole Centrale Paris, 2009.
- [29] M. Sjöberg, “On dynamic properties of rubber isolators,” Ph.D. dissertation, KTH, Stockholm, 2002. [Online]. Available: <http://www.diva-portal.org/smash/get/diva2:9268/FULLTEXT01.pdf>
- [30] V. A. Coveney and D. E. Johnson, “Rate-Dependent Modeling of a Highly Filled Vulcanizate,” *Rubber Chemistry and Technology*, vol. 73, no. 4, pp. 565–577, Sep. 2000. [Online]. Available: <https://doi.org/10.5254/1.3547606>
- [31] A. Nashif, D. Jones, and J. Henderson, *Vibration Damping*. John Wiley and Sons, 1985.
- [32] C. Dae Han and J. K. Kim, “On the use of time-temperature superposition in multicomponent/multiphase polymer systems,” *Polymer*, vol. 34, no. 12, pp. 2533–2539, Jan. 1993. [Online]. Available: <https://linkinghub.elsevier.com/retrieve/pii/003238619390585X>
- [33] P. Höfer and A. Lion, “Modelling of frequency- and amplitude-dependent material properties of filler-reinforced rubber,” *Journal of the Mechanics and Physics of Solids*, vol. 57, no. 3, pp. 500–520, Mar. 2009. [Online]. Available: <https://linkinghub.elsevier.com/retrieve/pii/S0022509608001981>
- [34] L. Mullins, “Softening of Rubber by Deformation,” *Rubber Chemistry and Technology*, vol. 42, no. 1, pp. 339–362, Mar. 1969, publisher: Allen Press. [Online]. Available: <https://meridian.allenpress.com/ret/article/42/1/339/87399/Softening-of-Rubber-by-Deformation>

## BIBLIOGRAPHY

---

- [35] W. P. Fletcher and A. N. Gent, “Nonlinearity in the Dynamic Properties of Vulcanized Rubber Compounds,” *Rubber Chemistry and Technology*, vol. 27, no. 1, pp. 209–222, Mar. 1954. [Online]. Available: <https://doi.org/10.5254/1.3543472>
- [36] M. Rendek and A. Lion, “Amplitude dependence of filler-reinforced rubber: Experiments, constitutive modelling and FEM – Implementation,” *International Journal of Solids and Structures*, vol. 47, pp. 2918–2936, 2010.
- [37] S. Cantournet, R. Desmorat, and J. Besson, “Mullins effect and cyclic stress softening of filled elastomers by internal sliding and friction thermodynamics model,” *International Journal of Solids and Structures*, vol. 46, pp. 2255–2264, Jan. 2009. [Online]. Available: [https://ac.els-cdn.com/S0020768309000080/1-s2.0-S0020768309000080-main.pdf?\\_tid=cde0d765-b399-4e3d-b7d6-7c3420df4c40&acdnat=1530276324\\_8cda1cb58f4a0167c3f08ca025130189](https://ac.els-cdn.com/S0020768309000080/1-s2.0-S0020768309000080-main.pdf?_tid=cde0d765-b399-4e3d-b7d6-7c3420df4c40&acdnat=1530276324_8cda1cb58f4a0167c3f08ca025130189)
- [38] S. G. Bardenhagen, M. G. Stout, and G. T. Gray, “Three-dimensional, finite deformation, viscoplastic constitutive models for polymeric materials,” *Mechanics of Materials*, vol. 25, no. 4, pp. 235–253, May 1997. [Online]. Available: <https://www.sciencedirect.com/science/article/pii/S0167663697000070>
- [39] J. Diani, M. Brieu, and P. Gilormini, “Observation and modeling of the anisotropic visco-hyperelastic behavior of a rubberlike material,” *International Journal of Solids and Structures*, vol. 43, no. 10, pp. 3044–3056, May 2006. [Online]. Available: <http://linkinghub.elsevier.com/retrieve/pii/S0020768305003811>
- [40] A. N. Gent and H. J. Kim, “Tear Strength of Stretched Rubber,” *Rubber Chemistry and Technology*, vol. 51, no. 1, pp. 35–44, Mar. 1978. [Online]. Available: <https://doi.org/10.5254/1.3535725>
- [41] I. Doghri, *Mechanics of Deformable Solids*. Berlin, Heidelberg: Springer Berlin Heidelberg, 2000. [Online]. Available: <http://link.springer.com/10.1007/978-3-662-04168-0>
- [42] J. C. Simo and T. J. R. Hughes, *Computational inelasticity*, 2nd ed., ser. Interdisciplinary applied mathematics Mechanics and materials. New York, NY: Springer, 2000, no. 7.
- [43] J. C. Simo and R. L. Taylor, “Consistent tangent operators for rate-independent elastoplasticity,” *Computer methods in applied mechanics and engineering*, vol. 48, pp. 101–118, 1985.
- [44] J. Schröder and P. Neff, “Invariant formulation of hyperelastic transverse isotropy based on polyconvex free energy functions,” *International Journal of Solids and Structures*, vol. 40, no. 2, pp. 401–445, Jan. 2003. [Online]. Available: <http://www.sciencedirect.com/science/article/pii/S0020768302004584>

## BIBLIOGRAPHY

---

- [45] INRIA and <http://www.sdtools.com/pdf/sdt.pdf> SDTools, *OpenFEM, a Finite Element Toolbox for Matlab and Scilab*, <http://www.openfem.net> *www.openfem.net*. INRIA, Rocquencourt, SD-Tools, Paris, France, 2004.
- [46] E. Code\_Aster Open Source, *General FEA software*.
- [47] D. Chapelle, J.-F. Gerbeau, J. Sainte-Marie, and I. E. Vignon-Clementel, “A poroelastic model valid in large strains with applications to perfusion in cardiac modeling,” *Computational Mechanics*, vol. 46, no. 1, pp. 91–101, Jun. 2010. [Online]. Available: <http://link.springer.com/10.1007/s00466-009-0452-x>
- [48] G. Marckmann and E. Verron, “Comparison of hyperelastic models for rubber-like materials,” *Rubber Chemistry and Technology*, vol. 79, no. 5, pp. 835–858, 2006. [Online]. Available: <https://hal.archives-ouvertes.fr/hal-01004680>
- [49] H. Dal, Y. Badienia, K. Açıkgöz, F. A. Denli, Y. Badienia, K. Açıkgöz, and F. A. Denli, “A comparative study on hyperelastic constitutive models on rubber: State of the art after 2006,” in *Constitutive Models for Rubber XI*, Jun. 2019. [Online]. Available: <https://www.taylorfrancis.com/>
- [50] M. M. Carroll, “A Strain Energy Function for Vulcanized Rubbers,” *Journal of Elasticity*, vol. 103, no. 2, pp. 173–187, 2011. [Online]. Available: <https://doi.org/10.1007/s10659-010-9279-0>
- [51] P. Boulanger, M. Hayes, and C. Trimarco, “Finite-amplitude plane waves in deformed Hadamard elastic materials,” 1994.
- [52] ABAQUS/Standard, *User’s Manual*. Hibbit, Karlsson, Sorensen, Inc., vol. 1.
- [53] P. Santharam, Y. Marco, V. Le Saux, M. Le Saux, G. Robert, I. Raoult, C. Guévenoux, D. Taveau, and P. Charrier, “Fatigue criteria for short fiber-reinforced thermoplastic validated over various fiber orientations, load ratios and environmental conditions,” *International Journal of Fatigue*, vol. 135, p. 105574, Jun. 2020. [Online]. Available: <https://www.sciencedirect.com/science/article/pii/S0142112320301055>
- [54] S. Wang and S. A. Chester, “Modeling thermal recovery of the Mullins effect,” *Mechanics of Materials*, vol. 126, pp. 88–98, Nov. 2018. [Online]. Available: <https://www.sciencedirect.com/science/article/pii/S0167663618301066>
- [55] O. Zienkiewicz and R. Taylor, *The Finite Element Method*. MacGraw-Hill, 1989.
- [56] M. Géradin and D. Rixen, *Mechanical Vibrations. Theory and Application to Structural Dynamics*. John Wiley & Wiley and Sons, 1994, also in French, Masson, Paris, 1993.

## BIBLIOGRAPHY

---

- [57] G. Vermot des Roches, “Frequency and time simulation of squeal instabilities. Application to the design of industrial automotive brakes.” Ph.D. dissertation, Ecole Centrale Paris, 2011.
- [58] D. Doyen, A. Ern, and S. Piperno, “A Semi-Explicit Modified Mass Method for Dynamic Frictionless Contact Problems,” in *Trends in Computational Contact Mechanics*, ser. Lecture Notes in Applied and Computational Mechanics, G. Zavarise and P. Wriggers, Eds. Berlin, Heidelberg: Springer, 2011, pp. 157–168. [Online]. Available: [https://doi.org/10.1007/978-3-642-22167-5\\_9](https://doi.org/10.1007/978-3-642-22167-5_9)
- [59] N. Nsiampa, J. P. Ponthot, and L. Noels, “Comparative study of numerical explicit schemes for impact problems,” *International Journal of Impact Engineering*, vol. 35, no. 12, pp. 1688–1694, 2008. [Online]. Available: <https://www.sciencedirect.com/science/article/pii/S0734743X08001310>
- [60] E. Balmès, “PARAMETRIC FAMILIES OF REDUCED FINITE ELEMENT MODELS. THEORY AND APPLICATIONS,” *Mechanical Systems and Signal Processing*, vol. 10, no. 4, pp. 381–394, Jul. 1996. [Online]. Available: <http://www.sciencedirect.com/science/article/pii/S0888327096900278>
- [61] K. Vlachas, K. Tatsis, K. Agathos, A. R. Brink, and E. Chatzi, “A local basis approximation approach for nonlinear parametric model order reduction,” *Journal of Sound and Vibration*, vol. 502, p. 116055, Jun. 2021. [Online]. Available: <https://www.sciencedirect.com/science/article/pii/S0022460X21001279>
- [62] R. Guyan, “Reduction of Mass and Stiffness Matrices,” *AIAA Journal*, vol. 3, p. 380, 1965.
- [63] R. J. Craig, “A Review of Time-Domain and Frequency Domain Component Mode Synthesis Methods,” *Int. J. Anal. and Exp. Modal Analysis*, vol. 2, no. 2, pp. 59–72, 1987.
- [64] E. Balmes, “Shapes & DOF: On the use of modal concepts in the context of parametric non-linear studies,” in *ISMA*, Leuven, 2018, p. Keynote.
- [65] G. Kerschen, J.-c. Golinval, A. F. Vakakis, and L. A. Bergman, “The method of proper orthogonal decomposition for dynamical characterization and order reduction of mechanical systems: An overview,” *Nonlinear dynamics*, vol. 41, no. 1, pp. 147–169, 2005.
- [66] A. Bobillot, “Méthodes de réduction pour le recalage : Application au cas d’Ariane 5,” Ph.D. Thesis, Châtenay-Malabry, Ecole centrale Paris, Jan. 2002.
- [67] E. Balmes, “Optimal Ritz vectors for component mode synthesis using the singular value decomposition,” *AIAA Journal*, vol. 34, no. 6, pp. 1256–1260, 1996.

## BIBLIOGRAPHY

---

- [68] F. Chinesta, A. Leygue, F. Bordeu, E. Cueto, D. Gonzalez, A. Ammar, and A. Huerta, “PGD-Based Computational Vademecum for Efficient Design, Optimization and Control,” *Archives of Computational Methods in Engineering*, vol. 20, no. 1, pp. 31 – 59, 2013, publisher: Springer Verlag. [Online]. Available: <https://hal.archives-ouvertes.fr/hal-01515083>
- [69] S. Chaturantabut and D. C. Sorensen, “Nonlinear Model Reduction via Discrete Empirical Interpolation,” *SIAM Journal on Scientific Computing*, vol. 32, no. 5, pp. 2737–2764, Jan. 2010, publisher: Society for Industrial and Applied Mathematics. [Online]. Available: <https://epubs.siam.org/doi/10.1137/090766498>
- [70] D. Ryckelynck and D. Missoum Benziane, “Multi-level A Priori Hyper-Reduction of mechanical models involving internal variables,” *Computer Methods in Applied Mechanics and Engineering*, vol. 199, no. 17–20, pp. 1134–1142, Mar. 2010. [Online]. Available: <http://www.sciencedirect.com/science/article/pii/S0045782509004022>
- [71] C. Farhat, P. Avery, T. Chapman, and J. Cortial, “Dimensional reduction of nonlinear finite element dynamic models with finite rotations and energy-based mesh sampling and weighting for computational efficiency: NONLINEAR MODEL REDUCTION AND ENERGY-CONSERVING SAMPLING AND WEIGHTING,” *International Journal for Numerical Methods in Engineering*, vol. 98, no. 9, pp. 625–662, Jun. 2014. [Online]. Available: <http://doi.wiley.com/10.1002/nme.4668>
- [72] J. Hernández, M. Caicedo, and A. Ferrer, “Dimensional hyper-reduction of nonlinear finite element models via empirical cubature,” *Computer Methods in Applied Mechanics and Engineering*, vol. 313, pp. 687–722, Jan. 2017. [Online]. Available: <https://linkinghub.elsevier.com/retrieve/pii/S004578251631355X>
- [73] M. Balajewicz, D. Amsallem, and C. Farhat, “Projection-based model reduction for contact problems,” *International Journal for Numerical Methods in Engineering*, vol. 106, no. 8, pp. 644–663, 2016. [Online]. Available: <https://onlinelibrary.wiley.com/doi/abs/10.1002/nme.5135>
- [74] P. Phalippou, S. Bouabdallah, P. Breitkopf, P. Villon, and M. Zarroug, “‘On-the-fly’ snapshots selection for Proper Orthogonal Decomposition with application to nonlinear dynamics,” *Computer Methods in Applied Mechanics and Engineering*, vol. 367, p. 113120, Aug. 2020. [Online]. Available: <https://www.sciencedirect.com/science/article/pii/S0045782520303054>
- [75] F. Casenave, N. Akkari, F. Bordeu, C. Rey, and D. Ryckelynck, “A nonintrusive distributed reduced-order modeling framework for nonlinear structural mechanics—Application to elastoviscoplastic computations,” *International Journal for Numerical Methods in Engineering*, vol. 121, no. 1, pp. 32–53, Jan. 2020. [Online]. Available: <https://onlinelibrary.wiley.com/doi/abs/10.1002/nme.6187>

- [76] J. Fauque, I. Ramière, and D. Ryckelynck, “Hybrid hyper-reduced modeling for contact mechanics problems: Hybrid hyper-reduced modeling for contact mechanics problems,” *International Journal for Numerical Methods in Engineering*, vol. 115, no. 1, pp. 117–139, Jul. 2018. [Online]. Available: <https://onlinelibrary.wiley.com/doi/10.1002/nme.5798>
- [77] J. Bianchi, E. Balmes, G. Vermot des Roches, and A. Bobillot, “Using modal damping for full model transient analysis. Application to pantograph/catenary vibration,” in *ISMA*, Leuven, Sep. 2010.
- [78] SIMPACK, “SIMPACK Documentation.”
- [79] H. Pinault, E. Arlaud, and E. Balmes, “A general superelement generation strategy for piecewise periodic media,” *Journal of Sound and Vibration*, vol. 469, p. 115133, Mar. 2020. [Online]. Available: <https://www.sciencedirect.com/science/article/pii/S0022460X19306960>
- [80] K. Hashiguchi, “Multiplicative Hyperelastic-Based Plasticity for Finite Elastoplastic Deformation/Sliding: A Comprehensive Review,” *Archives of Computational Methods in Engineering*, vol. 26, no. 3, pp. 597–637, Jul. 2019. [Online]. Available: <http://link.springer.com/10.1007/s11831-018-9256-5>
- [81] M. Wallin and M. Ristinmaa, “Deformation gradient based kinematic hardening model,” *International Journal of Plasticity*, vol. 21, no. 10, pp. 2025–2050, Oct. 2005. [Online]. Available: <https://linkinghub.elsevier.com/retrieve/pii/S0749641905000185>
- [82] M. Wallin, M. Ristinmaa, and N. S. Ottosen, “Kinematic hardening in large strain plasticity,” *European Journal of Mechanics - A/Solids*, vol. 22, no. 3, pp. 341–356, May 2003. [Online]. Available: <https://linkinghub.elsevier.com/retrieve/pii/S0997753803000263>
- [83] Y. F. Dafalias and E. P. Popov, “Cyclic loading for materials with a vanishing elastic region,” *Nuclear Engineering and Design*, vol. 41, no. 2, pp. 293–302, 1977. [Online]. Available: <https://www.sciencedirect.com/science/article/pii/0029549377901170>

## **Appendix A**

### **Rate independent 3D models**

As for 0D models, it is useful to represent rate independent behavior, but this is difficult because it implies extending the concept of turning point to three dimensions.

The most appropriate extension of Jenkins cells seems to be the kinematic hardening plasticity models. Such models are often used for metals under the plastic zone, but they might as well be appropriate for elastomers [6]. A brief discussion of these models will be given here.

## A.1 Plasticity formalism

Before illustrating the problems with finite strains, a review of a few concepts on plastic models is needed.

To define the moment where a tridimensional material will plastify - or equivalently, where the friction element is activated - a criterion  $f$  must be defined as a function of the stress tensor [41]. This criterion is defined by a yield surface

$$f = f(\sigma, (A; V)) \quad (\text{A.1})$$

where  $\sigma$  is the stress and  $(A; V)$  is a dual pair of thermodynamic forces and internal states, respectively. Thermodynamic consistency demands the evolution laws to be written in the form

$$\dot{\varepsilon}^p = \dot{\Lambda} \frac{\partial P}{\partial \sigma}, \quad \dot{V} = -\dot{\Lambda} \frac{\partial P}{\partial A}, \quad (\text{A.2})$$

with  $P$  the plastic potential,  $\Lambda$  the plastic multiplier and  $\varepsilon^p$  the plastic deformation. The equation that describes the evolution of the plastic deformation is called plastic flow. If the plastic potential is exactly the same as the yield criterion,  $P = f$ , the model is said to have an associated flow.

Hardening may be defined as the stress rule that takes place beyond the elastic domain. Classically there are two forms in material modeling: isotropic and kinematic, which respectively consist in an expansion of the yield surface and a displacement of the yield surface as illustrated in figure A.1.

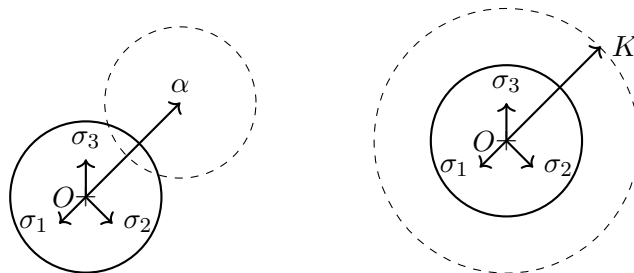


Figure A.1: Kinematic and isotropic hardening surface evolution.

For isotropic hardening, the internal variable to be stored is the size or the yield surface, denoted  $K$ , while for kinematic hardening, the internal variable is the center of the yield surface, denoted  $\alpha$ .

The determination of the plastic multiplier is done based on the maximal dissipation principle (Hill), which is mathematically equivalent to Karush-Kuhn-Tucker (KKT) optimization conditions,

$$\Lambda \geq 0, \quad f(\sigma, (A; V)) \leq 0, \quad \text{and} \quad \Lambda f = 0. \quad (\text{A.3})$$

Beyond this constraint to compute those values, there is also the Prager consistency condition, which states that the model should always remain in the elastic domain after hardening,

$$\Lambda df(\sigma, (A; V)) = 0, \quad \text{if} \quad f(\sigma, (A; V)) = 0; \quad (\text{A.4})$$

These conditions make the radial return algorithm the most interesting choice for implementation.

This formulation is well posed for infinitesimal strains, as all stress and strain rates are objective (rotation independent) allowing an additive strain decomposition  $\varepsilon = \varepsilon^{el} + \varepsilon^{pl}$ . Finite strain plasticity is a more complicated subject as an additive decomposition must involve objective stress rates (leading to problematic hypoelastic models), and multiplicative decomposition involves unicity issues due to the plastic spin. As consequence of those issues, there is a large number of theories and none is prevalent. After presenting the case of kinematic hardening for infinitesimal strains, this work will only present two specific implementations in finite strains.

## A.2 Kinematic hardening model - infinitesimal strains

Kinematic hardening models are used to simulate inelastic dissipative behavior of materials subjected to cyclic loading (also known as Bauschinger effect) [52]. If several yield surfaces are used, it may be seen as a 3D version of an Iwan model.

The classical yield criterion for this model is the second invariant  $I_2$ , which is also known as the von Mises criterion, which defines a maximal shear energy. As elastomers are nearly incompressible, this criterion is also adequate here. The yield criterion is given by

$$f = \sigma^{vm} - \sigma^y - \alpha \leq 0, \quad (\text{A.5})$$

with  $\sigma^{vm}$  the second invariant of the deviatoric part of the linearized stress tensor  $\sigma$ .

The second characteristic is the flow rule, and here we take an associative one

$$\varepsilon^{pl} = \Lambda \frac{\partial f}{\partial \sigma}. \quad (\text{A.6})$$

The third part is the hardening rule which describes the evolution of the yield surface with the inelastic strains, such that the yield function  $f$  remains always semi-definite positive. In the case, the

## A.2. KINEMATIC HARDENING MODEL - INFINITESIMAL STRAINS

---

hardening rule chosen will be kinematic linear, which means that the yield surface will not expand with strain increments, and the center of the yield surface (the so called backstress  $\alpha$ ) will evolve linearly with the plastic strains,

$$\alpha = \mu^h \varepsilon^{pl}, \quad (\text{A.7})$$

with  $\mu^h$  the hardening modulus.

The implementation is made, firstly with an elastic trial stress

$$\sigma_{tr} = 2\mu(\varepsilon - \varepsilon^{pl}) + \lambda \text{tr}(\varepsilon - \varepsilon^{pl}), \quad (\text{A.8})$$

with  $\lambda$  and  $\mu$  the Lamé parameters. This stress is used for the criterion evaluation

$$f = \text{vm}(\sigma^{tr}) - \sigma^y \quad (\text{A.9})$$

If  $f$  is negative or null, there is no plastic flow, and the problem is analog to the elastic case, with no evolution of internal states and the output stress is simply  $\sigma^{tr}$ . If  $f$  is positive, one needs to compute the plastic flow and verify the Prager's condition. As equation (A.6) implies, the flow must be perpendicular to the yield surface, the flow direction is taken to be as the direction of  $\text{dev}(\sigma^{tr}) - \alpha$ , named  $\hat{n}$ . With a known direction, the flow amplitude is computed by solving for  $\Lambda$  the consistency conditions,

$$\text{vm}(\sigma^{tr} - \lambda \hat{n}) - \sigma^y = 0. \quad (\text{A.10})$$

where  $\Lambda$  is the amplitude of the plastic flow, and the term  $\Lambda \hat{n}$  is the evolution of the backstress  $\alpha$ .

Equation A.10 may be solved with any nonlinear solving algorithm, which may be heavily time consuming, depending on the size of the model and the quality of the initial guess.

With the Lagrange multipliers computed, the value of  $d\varepsilon$  is taken as

$$d\varepsilon^{pl} = \frac{\Lambda \hat{n}}{\mu^h} = \frac{d\alpha}{\mu^h} \quad (\text{A.11})$$

The scheme for the model in the stress space may be seen in figure A.2.

This model responds in a quite similar form to the Iwan model for both shear and uniaxial sollicitations, as figure A.3 illustrates.

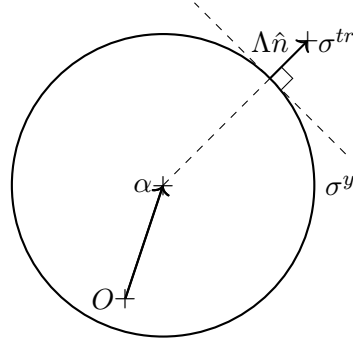


Figure A.2: Kinematic hardening scheme on the stress space

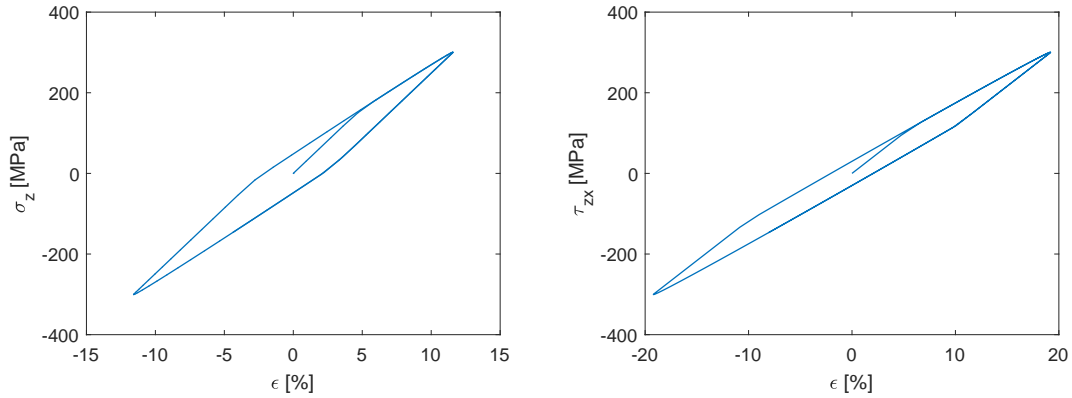


Figure A.3: Response for uniaxial stress and simple shear for kinematic plasticity model.

### A.3 Finite strains

For finite strains, there must be an objective description of the elastic-plastic strains. Additive split only works for hypoelastic formulations, which are often problematic due to parasite dissipations and the imposition of non physical objective rates [41, 80, 81]. Multiplicative decomposition decomposition is the most seen in literature

$$F = F^e F^p. \quad (\text{A.12})$$

This decomposition implies that  $\dot{C}^p$  is not objective, which poses problems on the unicity of the solution. So [82] introduces an intermediate ‘stres-free’ configuration is introduced, associated to a fictional displacement gradient  $\tilde{F}$ , leading to the kinematic conditions

$$\begin{aligned} F^e &= F F^p^{-1} \\ C^e &= F^e F^{eT} \\ \tilde{C} &= \tilde{F}^T \tilde{F} \end{aligned} \quad (\text{A.13})$$

### A.3. FINITE STRAINS

---

with the constitutive relations,

$$\begin{aligned}\Sigma &= 2C^e \frac{\partial \psi}{\partial C^e} \\ B &= 2\tilde{C} \frac{\partial \psi}{\partial \tilde{C}} \\ K &= \frac{\partial \psi}{\partial \kappa_\alpha}\end{aligned}\tag{A.14}$$

and as evolution laws (plastic flows),

$$\begin{aligned}\dot{F}^p &= \Lambda \left( -\frac{\partial g}{\partial \Sigma} + \frac{l^{p,n}}{\Lambda} \right) F^p \\ \dot{\tilde{F}} &= \Lambda \tilde{F} \left( -\frac{\partial g}{\partial P} + \frac{\beta^n}{\Lambda} \right) \\ \dot{\kappa} &= -\Lambda \frac{\partial g}{\partial K}\end{aligned}\tag{A.15}$$

and the consistency condition of  $\dot{f} = 0$ , with  $f$  being the yield criterion,  $\psi$  the energy potential,  $\Sigma$  the Mandel stress, dual to the velocity gradient tensor  $l$ ,  $B$  the kinematic hardening Mandel-like backstress,  $\beta$  its dual strain-like variable, where the exponent  $n$  designates its skew symmetric part (spin),  $K$  the isotropic hardening yield parameter,  $\kappa$  its dual strain variable,  $\Lambda$  the plastic multiplier and  $g$  the plastic potential

For the current implementation, there is no interest on the modeling of isotropic hardening or particular forms of spin tensors, which are, thus set to zero, and choosing an associated flow, so the equations remaining are

$$\begin{aligned}F^e &= F F^p{}^{-1} \\ C^e &= F^e F^{eT} \\ \tilde{C} &= \tilde{F}^T \tilde{F} \\ \Sigma &= 2C^e \frac{\partial \psi}{\partial C^e} \\ B &= 2\tilde{C} \frac{\partial \psi}{\partial \tilde{C}} \\ \dot{F}^p &= \lambda \left( -\frac{\partial f}{\partial \Sigma} \right) F^p \\ \dot{\tilde{F}} &= \lambda \tilde{F} \left( -\frac{\partial f}{\partial B} \right)\end{aligned}\tag{A.16}$$

In terms of implementation, as for the linearized model, one imposes at first the elastic stress

$$\Sigma^e = C^e 2 \frac{\partial \psi}{\partial C^e}\tag{A.17}$$

Linear backstress

$$B = \tilde{J}^{-4/3} \tilde{C} \mu^h\tag{A.18}$$

Then verify criterion

### A.3. FINITE STRAINS

---

$$f = \text{vm}(\Sigma^e - B) - \sigma^y \quad (\text{A.19})$$

Again, if  $f \leq 0$ , there is no plastic flow, so the elastic trial is the actual response. If  $f > 0$ , then there is plastic flow and the plastic evolution that satisfies the Prager's condition should be sought. For this purpose, one must find the value of the plastic multiplier that makes  $f = 0$ . To do this, an iterative process on a function that computes  $f$  in function of  $\Lambda$  must be used. This function is described by the equations A.20 to A.26 below

First an auxiliary scalar is defined as

$$A = \frac{3}{2\sigma^y} (B(\Sigma^e - B) - (\Sigma^e - B)B) \quad (\text{A.20})$$

Then, the spin plastic velocity gradient and backstress are computed

$$l^{p*} = \eta_l A \quad \beta^* = \eta_{beta} A \quad (\text{A.21})$$

with  $\eta_l$  and  $\eta_\beta$  material parameters. The total plastic deviatoric velocity gradient and backstress are thus computed with the plastic multiplier

$$l^{pn} = \Lambda \frac{3}{2} \sigma^y (\Sigma - B) + l^{p*} \quad \beta = \Lambda \frac{3}{2} \sigma^y (\Sigma - B) + \beta^* \quad (\text{A.22})$$

With the total evolution from both backstress and plastic velocity gradient, the update on both plastic deformation gradient the intermediate one may be computed, as well as the elastic deformation

$$\dot{F}^p = l^{pn} F^p \quad F_n^p = F_{n-1}^p + \dot{F}^p dt \quad (\text{A.23})$$

$$\dot{\tilde{F}} = \tilde{F} \beta \quad \tilde{F}_n = \tilde{F}_{n-1} + \dot{\tilde{F}} dt \quad (\text{A.24})$$

elastic deformation update

$$F^e = F F^p{}^{-1} \quad (\text{A.25})$$

With the elastic gradient, it is finally possible to verify the criterion again

$$f = \text{vm}(\Sigma(F^e) - B(\tilde{F})) - \sigma^y \quad (\text{A.26})$$

With the proper value of  $\Lambda$ , one can use equations A.20 to A.25 again, along with A.17 to compute the stress output.

This model was not fully tested, but early tests on integration point shows that this model seems to be capable of properly representing kinematic plasticity in large strains, as figure A.4 illustrates.

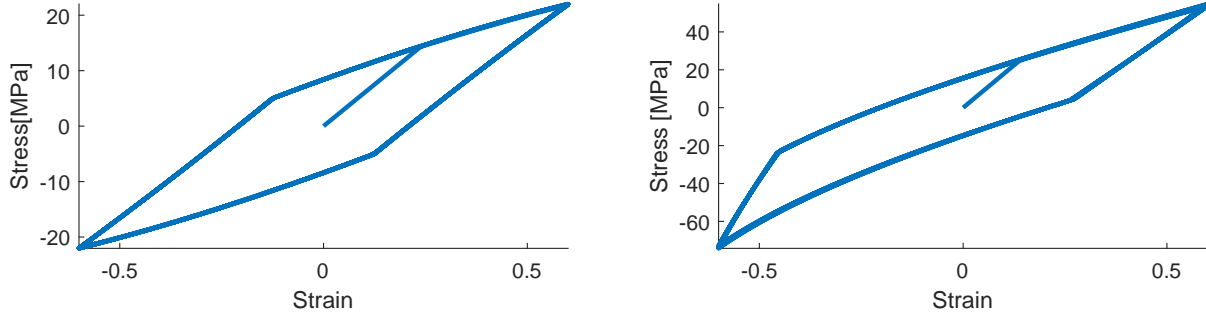


Figure A.4: Response of described finite strain kinematic hardening model in shear and uniaxial strains.

#### A.4 Kinematic hardening model + viscoelastic model in series

Other interesting model is proposed by [6], which might be symbolically represented by a rheologic assembly with a friction cell (kinematic hardening) in series with a viscoelastic Maxwell assembly, as figure A.5 illustrates.

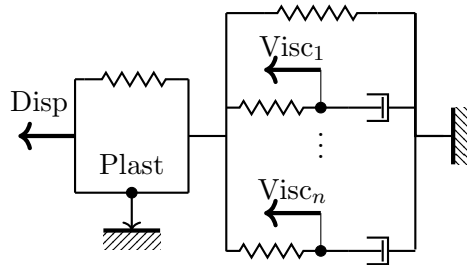


Figure A.5: Österlöf model

The model uses a neo-Hookean model for the deviatoric hyper-viscoelastic part and a model analog to the works of [83] for kinematic hardening plasticity, where the hardening modulus is a function of distance to the yield surface.

Regarding implementation, the first step is to decompose the strain into pure deformation and rotation, as  $F = RU$  with a polar decomposition. This might be done by taking  $R = uv^T$ , and  $U = vsv^T$ , with  $u, v, s$  the left and right singular vectors and the singular values of  $F$ , respectively.

Thus one have  $\Delta U = U_n - U_{n-1}$ , and the strain rate

$$D_n = \frac{\Delta U U_n^{-1} + U_n^{-1} \Delta U}{2\Delta t}. \quad (\text{A.27})$$

This model makes a difference between the displacements at each Maxwell cell, thus, one recovers the

#### A.4. KINEMATIC HARDENING MODEL + VISCOELASTIC MODEL IN SERIES

deformation on each Maxwell cell

$$C^i = \frac{\tau^i}{\mu^i} \quad (\text{A.28})$$

with  $\mu^i$  the shear coefficient for each cell, and  $\tau^i$  the Kirchhoff stress for each cell. The hydrostatic component to be removed from each viscoelastic deformation  $C^i$  is the only positive root from the polynomial on  $q$ ,

$$\det(C^i + q^i \mathbb{1}) = 1 \quad (\text{A.29})$$

Thus, the deformation for each Maxwell cell is taken as

$$U_e^i = \sqrt{C^i - \mathbb{1}q^i} \quad (\text{A.30})$$

With the pure dilation on each cell, one can compute the viscoelastic prediction, to be corrected by the plastic part evolution,

$$Pred = \sum_i \text{dev} \left( 2\mu^i \Delta t U_e^i \left( D - \frac{\tau^i}{\eta^i} \right) U_e^i \right) \quad (\text{A.31})$$

with  $\eta^i$  the loss factor for each cell.

The first part is to compute plastic part is to compute the direction of the predictor  $m = \frac{Pred}{\|Pred\|}$ . Then, the tensor that gives the distance from the stress to center of the plastic zone on current prediction is  $\tau^* = \sum_i(\tau^i) - \beta$ . The projection from this tensor on the viscoelastic predictor direction is given by  $b_0 = m : \tau^*$ , and  $b_1 = \tau^* : \tau^*$ , its norm. Thus, the distance between the current stress and the yield surface is expressed by

$$\delta = \sqrt{b_0^2 + R^2 - b_1} - b_0 \quad (\text{A.32})$$

where  $R$  is the size of the elastic limit. Finally the flow direction is computed

$$n = \frac{\sum_i \tau^i + \delta m - \beta}{\|\sum_i \tau^i + \delta m - \beta\|} \quad (\text{A.33})$$

The scheme in figure A.6 presents a graphical interpretation of all the norms and distances introduced for this model

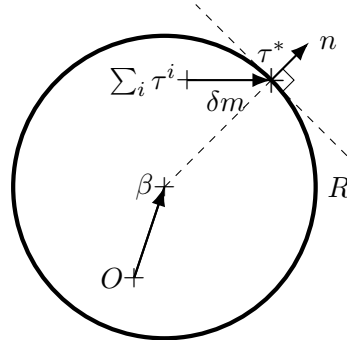


Figure A.6: Österlöf flow model.

#### A.4. KINEMATIC HARDENING MODEL + VISCOELASTIC MODEL IN SERIES

After computing directions and norms, the correction is computed, firstly by the factor

$$G = \sum_i 2\mu^i \text{trace} \left( n \text{dev} \left( U_e^i n U_e^i \right) \right) \quad (\text{A.34})$$

and then by the factor

$$H = h_0 + h \frac{\delta}{\delta_{ch} - \delta + \epsilon} \quad (\text{A.35})$$

where  $h_0$  represents the initial hardening modulus,  $h$  a parameter that tunes its evolution,  $\epsilon$  a numeric parameter that prevents singularities on turning points and  $\delta_{ch}$  another parameter that tunes the hardening evolution.

The plastic multiplier change is given by

$$\Delta\Lambda = \frac{\text{trace}(nPred)}{H + G} \quad (\text{A.36})$$

Now the center of elastic domain is updated

$$\beta_{n+1} = \beta + H\Delta\Lambda n \quad (\text{A.37})$$

And finally, viscoelastic stresses are computed with the plastic correction

$$\tau_{n+1}^i = \tau^i 2\mu^i \text{dev} \left( U_e^i \left( D - \frac{\tau^i}{\eta^i} - \frac{n\Delta\Lambda}{\Delta t} \right) U_e^i \right) \Delta t \quad (\text{A.38})$$

Hydrostatic pressure is computed separately by

$$p = \frac{\kappa}{2} (J - J^{-1}) \quad (\text{A.39})$$

The total stress is the computed by

$$S = F^{-1} J \left( p \mathbb{1} + J^{-1} R \sum_i \tau_{n+1}^i R^T \right) F^{-T}. \quad (\text{A.40})$$

As expected the model is perfectly capable of capturing the Payne effect as seen in figure A.7, and frequency evolution as well.

#### A.4. KINEMATIC HARDENING MODEL + VISCOELASTIC MODEL IN SERIES

---

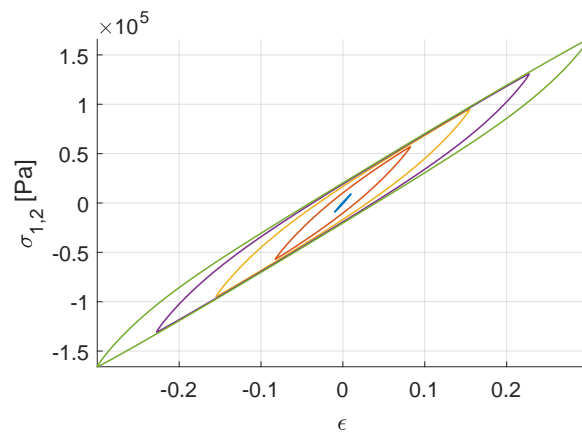


Figure A.7: Payne effect in Österlöf model

#### A.4. KINEMATIC HARDENING MODEL + VISCOELASTIC MODEL IN SERIES

## Appendix B

### Test parameters

Tables B.1 and B.2 give the parameter for material specimen and part tests.

Table B.1: Matrix of test conditions on specimens

<b>Sine</b>			
Specimen	Pre loads (%)	Frequencies (Hz)	Amplitudes (%)
Shear	0 , 45, 90	0.1, 0.5, 1, 5, 10	0.01, 0.05, 0.1, .5, 1
		50, 100	0.01, 0.05, 0.1, .5, 1, 5, 10
Traction	-30, -15, 0, 15, 30, 45, 60	0.1, 0.5, 1, 5, 10	0.01, 0.05, 0.1, .5, 1
		50, 100	0.01, 0.05, 0.1, .5, 1, 5, 10
<b>Triangular</b>			
Specimen	Test speed (mm/min)	Pre loads (%)	Amplitude (%)
Shear	1, 10	0, 20	50
	10	0	90
Traction	1, 10	-10, 0, 10	20
	10	-30 -20 -10 0 10 20 30	5
		0	0.1, 0.5, 1, 10, 50
<b>Multi step</b>			
Specimen	Relaxation times (s)	Amplitude levels (%)	
Shear	360	0, 10, 20, 30, 40, 50, 60, 70, 80, 90, 100	
Traction	360, 3600	-30, -15, 0, 15, 30, 45, 60	

Table B.2: Individual part tests

<b>Sine</b>		
Preloads (mm)	Frequencies (Hz)	Amplitudes (mm)
0, 1, 2, 3	0.1, 0.5, 1, 5, 10, 50, 100	0.05, 0.1, 0.25, 0.5, 1
<b>Triangular</b>		
Test speed (mm/min)	Pre loads (mm)	Amplitude (mm)
1, 10	1,2,3,4	0.05, 0.1, 0.25, 0.5, 1, 4.5
<b>Multi step</b>		
Relaxation time (s)	Amplitude levels (mm)	
3600	0.5, 1, 1.5, 2, 2.5, 3, 3.5, 4, 5	



**Résumé :** Les simulations multi-corps sont utilisées dans l'industrie automobile pour garantir le respect des principaux objectifs de conception. Un point clé de la précision de ces simulations est la modélisation des articulations élastomères. En effet, elles nécessitent une modélisation précise des grandes déformations pour les manœuvres à fortes sollicitations, généralement associées à la sécurité active, et une modélisation correcte de la dissipation, pour la plupart des applications de confort. Le processus actuel de modélisation de ces articulations utilise des essais séparés dans chaque direction pour générer des modèles 0D avec une dissipation visqueuse linéaire. Les essais proposés et réalisés dans ce travail ont été utilisés pour caractériser séparément les effets des grandes déformations, de l'hystérésis indépendante de la vitesse et de la viscoélasticité. Les modèles pour chacun de ces comportements sont classés en modèles non-paramétriques, extraits directement des données, modèles paramétriques d'ordre ajustable, dont la précision dépend du nombre d'états internes, et modèles indépendants de l'ordre. L'utilisation de ratios de la branche statique non-linéaire avec les autres branches s'avère être un moyen efficace de modéliser le couplage entre la dissipation et les grandes déformations. La transition entre l'hystérésis et la viscoélasticité est présentée comme une conséquence de la viscoélasticité non linéaire et conduit à un bon accord avec les essais, démontré par la comparaison du module instantané proposé. L'influence du chargement dans les directions transversales à un axe donné est très difficile à obtenir à partir d'essais, mais nécessaire pour des modèles d'articulation précis. Les calculs par éléments finis sont tout à fait appropriés pour telles études, et comme ils nécessitent des modèles 3D, la transformation du modèle 0D proposé en un modèle matériau 3D est détaillée. Deux routines d'identification différentes pour les modèles 3D et 0D ont été proposées : une avec des fonctions objectif classiques pour le modèle de matériau et une graphique avec sélection d'ordre basée sur les modèles non-paramétriques. Malgré l'utilité des routines FE pour relier la géométrie et le comportement matériau, leurs temps de calcul caractéristiques sont trop importants pour être acceptables pour les applications multi-corps envisagées. Une combinaison de réduction cinématique et d'intégration hyper-réduite des équations du modèle est donc détaillée et il est démontré qu'elle atteint une précision suffisante et l'accélération nécessaire des temps de calcul. Le cadre mathématique pour l'intégration des modèles 3D réduits dans les routines multi-corps est décrit. Finalement, deux illustrations multi-corps sont détaillées. Le premier cas met en évidence le fait que les dissipations hystérique et visqueuse peuvent conduire à des réponses transitoires sensiblement différentes, confirmant la nécessité des propositions réalisées pour les modèles 0D. Le deuxième cas montre que le remplacement des modèles 0D actuels, relativement grossiers, par ceux développés dans ce travail devrait engendrer des modifications importantes sur les réponses.

**Mots clés :** Elastomère, Hystérésis, Hyper-élasticité, Viscoélasticité, Identification paramétrique, MEF non-linéaire, Hyper-réduction, Multi-corps

**Abstract:** Multibody simulations are used in the automotive industry to ensure that important design targets are met. A key point in the accuracy of such simulations is the proper modeling of rubber bushings and mounts. Indeed, they do require precise modeling of large deformation for high loading maneuvers, typically associated with active safety, and a correct modeling of dissipation, for most comfort applications. The current modeling process of these mounts and bushings considers tests to generate 0D models in each separate direction with linear viscous dissipation. The tests proposed and realized in this work were used to characterize the effects of large deformation, rate independent hysteresis and viscoelasticity separately. Models for each one of those behaviors are categorized into non-parametric models, extracted directly from data, selected order parametric models, whose accuracy depend on the number of internal states, and order independent models. Utilization of ratios of the nonlinear static branch for all the other branches is shown to be an effective way to model coupling of dissipation with large deformations. Transition between hysteresis and viscoelasticity is presented as a consequence of nonlinear viscoelasticity and provides good agreement with tests demonstrated by the comparison of the proposed instant modulus. The influence of loading in transverse directions on a given axis is very difficult to obtain from tests, yet necessary for accurate bushing models. Finite element computations are quite suitable for such studies, and as they require 3D models, the translation of the proposed 0D model into a 3D material model is detailed. Two different identification routines for both the 3D and 0D models were proposed: one with classic objective functions for the material model and a graphic one with order selection based on the non-parametric models. Despite the usefulness of FE routines to link geometry and material behavior, their typical computation times are orders of magnitude too large to be acceptable for the envisioned multibody applications. A combination of kinematic reduction and hyper-reduced integration of the model equations is thus detailed and shown to provide sufficient accuracy and the needed speedup in computation times. The mathematical frame for integrating the reduced 3D models into multibody routines is described. Finally, two multibody illustrations are detailed. The first case highlights the fact that hysteretic and viscous dissipations may lead to notably different transient responses, confirming the need for the propositions made for 0D models. The second one shows that replacing the current relatively coarse 0D models with those developed in this work should induce notable modifications of the response.

**Keywords:** Elastomer, Hysteresis, Hyperelasticity, Viscoelasticity, Parametric identification, Non-linear FEM, Hyper-reduction, Multibody